Joachim Wegener *Editor*

Measuring Biological Impacts of Nanomaterials

Springer

5
Bioanalytical Reviews

Aims and Scope

Bioanalytical Reviews is the successor of the former review journal with the same name, and it will complement Springer's successful and reputed review book series program in the flourishing and exciting area of the Bioanalytical Sciences.

Bioanalytical Reviews (BAR) publishes reviews covering all aspects of bioanalytical sciences. It therefore is a unique source of quick and authoritative information for anybody using bioanalytical methods in areas such as medicine, biology, biochemistry, genetics, pharmacology, biotechnology, and the like.

Reviews of methods include all modern tools applied, including mass spectrometry, HPLC (in its various forms), capillary electrophoresis, biosensors, bioelectroanalysis, fluorescence, IR/Raman, and other optical spectroscopies, NMR radiometry, and methods related to bioimaging. In particular the series volumes provide reviews on perspective new instrumental approaches as they apply to bioanalysis, and on the use of micro-/nano-materials such as micro- and nanoparticles. Articles on μ-total analytical systems (μ-TAS) and on labs-on-a-chip also fall into this category.

In terms of applications, reviews on novel bioanalytical methods based on the use of enzymes, DNAzymes, antibodies, cell slices, to mention the more typical ones, are highly welcome. Articles on subjects related to the areas including genomics, proteomics, metabolomics, high-throughput screening, but also bioinformatics and statistics as they relate to bioanalytical methods are of course also welcome. Reviews cover both fundamental aspects and practical applications.

Reviews published in BAR are (a) of wider scope and authoratively written (rather than a record of the research of single authors), (b) critical, but balanced and unbiased; (c) timely, with the latest references. BAR does not publish (a) reviews describing established methods of bioanalysis; (b) reviews that lack wider scope, (c) reviews of mainly theoretical nature.

More information about this series at http://www.springer.com/series/11663

Joachim Wegener

Editor

Measuring Biological Impacts of Nanomaterials

With contributions by

C. Bantz · S. Beyazit · D. Docter · J. Domey · M. Dwivedi ·
K.A. Eslahian · H.-J. Galla · B. Goricnik · I. Grau ·
L. Haslauer · K. Haupt · I. Hilger · N. Hinterreiter · T. Hirsch ·
C. Hupf · R. Keller · M. Kettering · T. Lang · M.-M. Lemberger ·
S. Lukic · M. Maskos · J. Maximilien · M. Oberleitner · C. Rossi ·
A.K. Sachan · M. Sperber · R. Sperling · R. Stauber · J.A. Stolwijk ·
C. Strobel · B. Tse Sum Bui · J. Wegener

Springer

Editor
Joachim Wegener
University of Regensburg
Regensburg
Germany

Preface

Over the last two decades, nanotechnology has produced a myriad of different nanosized structures with enormously interesting material properties and potential applications. Quantum dots (QDs), carbon nanotubes (CNTs), carbon dots (CDs), gold nanoparticles, and pigment particles are among the most well-known representatives. But also less 'famous' nanomaterials made from polymers, noble metals, or inorganic materials have raised considerable interest for applications in the biomedical field and other areas of our daily life. Despite of their undisputed usefulness in certain areas, there is a constant and justified concern that these nanomaterials may have unwanted biological effects on cells and organisms that have not yet been discovered and understood entirely. Thus, research into the biological impact of nanoparticles on human and animal health as well as possible hazards for the environment is of outmost importance. As a deeper and more systematic understanding about the potential impact of nanomaterials on living cells, tissues, or ecosystems is in many ways based on state-of-the-art bioanalytical techniques, this volume of *Bioanalytical Reviews* is entirely devoted to this topic.

The first chapter of the book, written by Eslahian and colleagues, provides a concise summary of the most prominent, highly tailored approaches to physically characterize nanomaterials. The various techniques are described in principle before their individual analytical performance is highlighted and critically compared to other methods. Special emphasis is placed on material characterization under physiological conditions to describe the particles as they are when they encounter biological systems like cells, tissues, or organs.

The second chapter provided by Domey and coauthors addresses biochemical assays that are used extensively in labs around the globe to study the cytotoxicty or other cell responses to nanomaterials. Besides presenting model studies, this contribution critically highlights the pitfalls and possible artifacts that might be associated with these assays due to an interaction of the nanomaterials with the assay constituents. Often the possible artifacts can be accounted for by a carefully thought-out experimental design and proper controls. But the evidence accumulates that label-based assays should be used with great care to avoid misleading conclusions from cytotoxicity studies.

Following up on this discussion on the pros and cons of label-based biochemical assays to assess the impact of nanomaterials, the subsequent chapter by Sperber et al. discusses the use of label-free approaches for this purpose. After a more general introduction to the field of label-free detection techniques for cell observation, focus is placed on impedance analysis as one of its major representatives. The chapter describes the general concept of impedance-based cell monitoring, introduces the physical background, and illustrates its performance on a set of examples. These examples highlight that noninvasive impedance measurements can be used to monitor a huge variety of different cell-based assays including the analysis of cell adhesion and proliferation, time-resolved observation of cytotoxicity, or the quantitative examination of cell migration. After these introductory paragraphs, the article summarizes in how far these assays have been used already to describe the impact of nanomaterials on animal cells and tissues at these very different points of cell physiology. Inspired by the possibilities of impedance analysis to study one cell type subsequently in different physiological settings, the authors suggest a new perspective for nanotoxicology: instead of interpreting just one assay, we should establish response profiles for a given nanomaterial derived from a sequence of individual assays.

As the airways are one major route of nanomaterial invasion into the human body, the fourth chapter addresses a set of model systems to study the impact of nanomaterials on the alveolar lung surfactant that is literally of vital importance to our breathing cycle. Here Dwivedi et al. describe model systems from simple lipid monolayers to more complex model surfactants and their response to nanoparticle encounter. The impact of nanoparticles on lipid organization is mostly demonstrated by Langmuir film-balance measurements and state-of-the-art microscopy.

As one example of nanomaterials that do not only raise health and environmental concerns but show very interesting bioanalytical applications, Lemberger et al. summarize in the fifth chapter what is known about carbon nanodots (CDs), a member of the emerging class of photoluminescent carbon-based nanomaterials that can be produced from rather simple and cheap starting materials using low-tech equipment. The various strategies of CD synthesis are grouped and discussed. Deeper inside the article, the authors provide a concise summary of the particles' spectroscopic properties together with their most established bioanalytical application as a label in microscopic imaging.

The final chapter provided by Maximilien and coauthors takes it to the next level: nanomaterials as drug delivery vehicles in biomedicine. The authors start their discussion with lipid-based nanomaterials (liposomes) and their reversible loading with drugs. This discussion is followed by a concise overview of the available inorganic nanoparticles including quantum dots (QDs) and upconverting nanoparticles (UCNPs) with their inherent capability of absorbing two or more NIR photons before a photon of shorter wavelength in the visible range (higher energy) is emitted. This upconversion has several distinct advantages. Most prominently it provides a fluorescence labeling of biological specimens without producing an unwanted and disturbing background fluorescence of biomolecules as the latter

require excitation by UV/VIS. The description of polymeric nanoparticles as drug delivery vehicles starts with nanomaterials made from natural polymers. Within the class of nanoparticles produced from synthetic polymers, the authors highlight those materials that are either responsive to temperature, pH, or light because of their outstanding potential to allow for a localized unloading of the vehicle. The final paragraph describes polymeric nanoparticles with imprinted recognition sites for different low-molecular-weight analytes (MIPS) that provide many new opportunities for nanoparticle-based sensors or the specific separation and enrichment of complex samples.

The current volume of *Bioanalytical Reviews* presents a blend of different aspects that tackle the problem of measuring the biological impact of nanomaterials. This timely collection of articles will hopefully help to oversee the fast-developing field of nanotoxicology and emphasize its tight connection to bioanalysis. New instrumental developments, analytical assay formats, and new means of data deconvolution are needed to get a few steps closer to the big goal of a conceptual understanding about the bioresponse to nanoscale particles. This is particularly important as this topic is likely to stay relevant throughout the next decades given the increasing integration of nanomaterials in our daily lives.

This book would not have been possible without the fine work of all authors and coauthors to whom I would like to express my deepest gratitude. I hope you all agree that this big effort and the long hours of work have been worthwhile. Moreover, I would like to thank Dr. Rudolf Hutterer for his constant support in general and the editorial preparation of several chapters in particular.

Regensburg (G) in summer 2015. Joachim Wegener

Contents

Characterization of Nanoparticles Under Physiological Conditions

K.A. Eslahian, T. Lang, C. Bantz, R. Keller, R. Sperling, D. Docter, R. Stauber, and M. Maskos

Abstract In this article, well-established characterization methods for nanoparticles (NPs) are discussed, in particular their application under physiological conditions. The impact of different media, mimicking physiological conditions, on NP stability in terms of physiological ionic strength and formation of the NP–protein corona is described. In order to characterize NPs under physiological conditions, we distinguish between scattering and correlation methods, microscopy-based methods, and methods based on hydrodynamic separation. Features and limitations of relevant characterization methods are reviewed, as well as challenges arising in physiological media from enhanced aggregation tendency and the presence of proteins. We conclude that no available method for NP characterization in physiological media is able to describe the colloidal system completely and satisfactory. On the contrary, combining well-chosen analytical methods by taking benefits and disadvantages into account may provide detailed characterization results.

Keywords Characterization methods · Nanoparticles · Physiological media · Protein corona

Contents

K.A. Eslahian, T. Lang, C. Bantz, R. Keller, R. Sperling, and M. Maskos (✉)
Fraunhofer ICT-IMM, Carl-Zeiss-Straße 18-20, 55129 Mainz, Germany
e-mail: Michael.Maskos@imm.fraunhofer.de

D. Docter and R. Stauber
Molecular and Cellular Oncology/Mainz Screening Center, University Medical Center of Mainz, Langenbeckstraße 1, 55101 Mainz, Germany

1 Nanoparticles: Definition

Commonly, nanoparticles (NPs) are defined as dispersed particle species in the size range between 1 and 100 nm. These particles consist of a very large surface-to-volume ratio, and the physical properties of NPs vary markedly from well-known macroscopic behavior all the way to properties of molecular species. One may furthermore distinguish between natural nanoparticles (NNPs) and engineered nanoparticles (ENPs).

In industrial applications, the amount of NP-containing products is rising rapidly, and ENPs are nowadays found in cosmetics, special clothing, and industrial food products. To provide clear safety regulations, the EU commission has defined nanomaterials as "a natural, incidental or manufactured material containing particles, in a bound state or as an aggregate or as an agglomerate and where, for 50% or more particles in the number size distribution, one or more external dimensions is in the size range 1–100 nm" [1]. Additionally, NPs are discussed to serve as tools in many biomedical applications, for example, as drug carriers, MRI contrast agents, and synthetic "viral" systems for gene delivery. Consequently, exposure of NPs to the environment is propagating, and an improved understanding of their behavior in biological environment is necessary to estimate risks and avoid potential harm. In this context and considering medical therapy, the term biocompatibility is defined as the ability of a material to perform desired functions without undergoing undesired reactions or property changes [2].

Physicochemical properties of nanoparticles being suspended in aqueous media are determined by their size distribution and shape, as well as by their surface properties including surface potential, roughness, and functional groups [3]. The large surface area-to-volume ratio of NPs provides an enormous reactive interface between the particle and the local environment which can lead to significant modifications of the NPs' surface via physical adsorption or chemical reactions. As a result, it is crucial to understand the behavior of NPs under conditions mimicking their final application such as in the environment or body. Currently, the majority of NPs designed for human therapy or industrial use have been characterized with respect to their physicochemical properties in nonphysiological conditions prior to investigating their cytotoxicity. To improve comparability of experiments in this field, standardized characterization methods under physiological conditions must be developed and applied [4].

In this article, a brief introduction into nanoparticle properties, their interactions with biological environments, and the state of the art of characterization under physiological conditions is provided.

2 Nanoparticles: Stability and Interactions

Nanoparticle stability is an interplay of attractive (e.g., van der Waals type) and repulsive forces (e.g., Coulomb repulsion), with stable suspensions being achieved when repulsive forces are dominant.

Attractive van der Waals (VDW) forces, arising from dynamic interactions of fluctuating dipoles, act between nanoparticles and give rise to a tendency for particle aggregation. To prevent aggregation, particles can be stabilized by steric hindrance, electrostatic repulsion, or depletion forces. The surface of most nanoparticles contains charged groups that generate a surface potential which results in repulsive forces between particles of the same kind. The sum of attractive VDW forces and repulsive electrostatic forces is known as electrostatic stabilization potential and can qualitatively be described by the *Derjaguin–Landau–Verwey–Overbeek* (DLVO) theory [5]. As illustrated in Fig. 1a, the interaction potential between two particles is strongly repulsive at very short distances due to Born repulsion of atomic electron density. Moving particles away from each other, the net potential becomes strongly attractive at nm distances due to VDW forces and undergoes a repulsive maximum at a certain interparticle distance. This electrostatic repulsion potential acts as a hindrance barrier, preventing two particles from approaching and aggregating. As a measure for the effective electrostatic potential, the zeta potential ς is experimentally accessible.

Distance and amount of the electrostatic hindrance potential are dependent on the ionic strength of the solution (Fig. 1b). Increasing salinity gives rise to more effective screening of the surface potential, thus reducing the *Debye length* which describes how far the electrostatic repulsion potential persists into the solution. In *Lifshitz* theory of VDW forces, the zero frequency term is affected by high ionic strengths whereas higher frequency dispersion forces remain unaffected [6, 7].

Consequently, at high electrolyte concentrations, the repulsive potential vanishes and particle aggregation emerges. Steric stabilization occurs when macromolecules are attached onto the colloidal surface. The layer of steric hindrance lowers the probability of two NPs to collide. In addition, the approach of two colliding particles is impeded by a loss of conformation entropy. In case of polyelectrolytes or other strongly charged molecular layers, the combination of both effects is summarized as electro-steric repulsion, meaning that the respective species provide both steric and electrostatic hindrance.

Besides repulsive electrostatic forces and steric hindrance, solvation plays an important role in the stabilization of nanoparticles in aqueous solvents by forming a hydration shell around the nanoparticles. This layer hinders two nanoparticles from adhering and thus increases particle stability. When the relative affinity between the
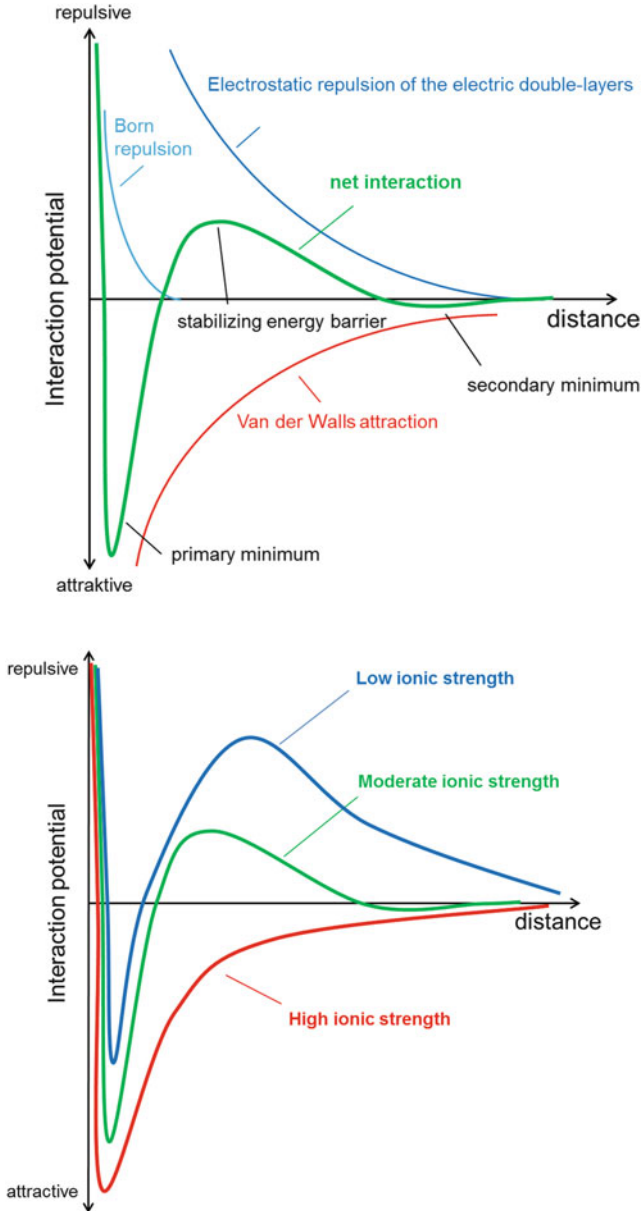
Fig. 1 Derjaguin–Landau–Verwey–Overbeek theory of electrostatic colloidal stability. *Upper panel*: The net interaction (*solid line*) is considered to result from the sum of attractive van der Waals forces and repulsive electrostatic double-layer forces. *Lower panel*: The effective interaction potential as a function of salinity. Effective stabilization takes place in low (*blue*) and moderate (*green*) ionic strength media, whereas the repulsive stabilizing barrier vanishes in high ionic strength media (*red*). Depending on the colloidal system, moderate salinity refers to an ionic strength between 1 mM ($\kappa^{-1} \approx 10$ nm) and 10 mM ($\kappa^{-1} \approx 3$ nm) in a monovalent 1:1 electrolyte. Under physiological conditions, a medium can be considered of high ionic strength with a Debye screening length around the Bjerrum length of the medium ($\kappa^{-1} \approx 0.8$ nm)

surfaces of two nanoparticles is larger than between the surfaces and surrounding water molecules, the so-called hydrophobic effect takes place, resulting in dehydration and aggregation of the particles [8].

3 Nanoparticles Under Physiological Conditions

3.1 Relevant Media

Generally, nanoparticle analysis in vitro and their use in cell culture experiments should be carried out under identical conditions [9]. The media have to be selected according to the individual needs of the various applications of NPs in physical chemistry, biophysics, biology, and medicine. In the following, these media are described in the order of complexity.

Here, the term "physiological salt conditions" describes an ionic strength of about 150 mM, in particular it denotes phosphate or bicarbonate buffer systems at a pH of 7.0–7.4. Phosphate buffered saline (PBS) is applicable in nanoparticle analysis when focusing only on physiological salinity. PBS consists of potassium phosphate monobasic, sodium phosphate dibasic, potassium chloride, and sodium chloride. RPMI1640 and DMEM basal media are widely used in cell and tissue cultures. In addition to phosphate and bicarbonate, nutrients such as glucose, amino acids, and vitamins are added to ensure cell viability.

Single proteins can be added to cell culture medium as model systems such as bovine serum albumin (BSA), human serum albumin (HSA), or fibronectin. This is mainly of interest to study the physicochemical effects of specific proteins on colloids because it provides a defined and reproducible composition of such test media.

Cell cultivation requires the addition of proteins and growth factors, which is commonly realized by addition of fetal bovine serum (FBS) to the cell culture medium. Usually 5–20% (v/v) of serum supplementation is applied.

However, in the fields of medicine, nanobiotechnology and also nanotoxicology experiments in blood serum, plasma, or full blood are of major interest because the in vivo situation should be mimicked as close as possible. Thus, characterization of NPs in such complex conditions should be the final step of in vitro experiments.

In general, NP analysis under physiological conditions becomes increasingly challenging with increasing complexity of the medium. Nevertheless, for a complete understanding of the nano-bio interface in humans and the environment, characterization of NPs under these highly complex conditions is mandatory. For preliminary studies, simplified models based on the first few media mentioned above may be useful for generating a first working hypothesis [10].

Fig. 2 Evolution of the hydrodynamic radius of silver NPs in pure RPMI as measured by DLS and indicated by the total scattering intensity. Agglomeration occurred after about 5 h. Adapted from (with permission from Kittler et al. [11])
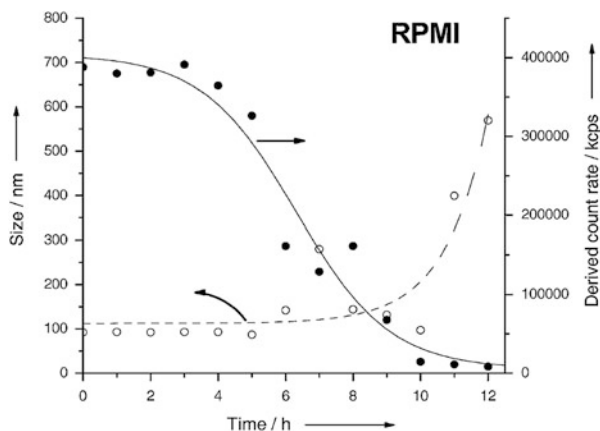
3.2 Effect of Physiological Salt Concentrations on Colloidal Properties

The high electrolyte content of physiological media has direct impact on the colloidal stability of NPs. High salinity results in the screening of surface charges, thus diminishing electrostatic repulsion between NPs. At this juncture, the Debye length scale becomes relevant, describing the range of electrostatic interactions between colloids. At a salinity of 150 mM, the Debye length is in the order of 0.8 nm only (for symmetric electrolytes like sodium chloride), leading to coagulation of exclusively electrostatically stabilized nanoparticles in physiological media (Fig. 2) [12–14].

According to DLVO theory, the nature of electrostatic stabilization is based on a kinetic barrier. By decreasing collision efficiency, the repulsive potential lowers the probability of coagulation of two colliding colloids. This leads to a second-order rate kinetics [15–17], where the electrostatic repulsion potential determines the timescale of coagulation.

The timescale for particle aggregation was found to be a few hours in the case of citrate-stabilized silver nanoparticles in RPMI1640 medium [11]. This is in contrast to electrostatically well-stabilized nanoparticles (with absolute values of $|\zeta| >$ 20 mV) in pure water, which are stable for months up to years.

3.3 The Nanomaterial Protein Corona

When nanomaterials enter any biological environment, they get covered by (bio) molecules, forming a corona, which influences the nanomaterials' physicochemical properties. Hence, the environment and humans are mostly not facing pristine ENPs but rather surface-coated ENPs. In particular, proteins bind to the surface of

nanoparticles forming a biological coating around the nanoparticle known as the protein corona [18]. This corona transforms the biological identity of the nanoparticle and, thus, may affect biomedical applications and/or modulate nanotoxicological effects and ecotoxicology [19, 20].

The formation process of a protein layer upon flat surfaces was firstly analyzed by Vroman in 1962 [21]. The corresponding Vroman effect describes the time-dependent composition of a protein adlayer, where the early state is dominated by abundant proteins, which adsorb unspecifically. Subsequently, adsorbed proteins are replaced by less abundant proteins, which bind with greater affinity, resulting in a complex series of adsorption and displacement steps [22]. Initially, this model was directly transferred to explain the evolution process of the protein corona around [23], which led to the concept of a "dynamic protein corona." In this model, a dynamic exchange of adsorbed and unbound proteins takes place. Hence, the composition of the corona is predominantly controlled by the association and dissociation constants of the proteins available in the particle suspension. Because certain protein groups display increased or reduced binding over time, a time-resolved knowledge of nanoparticle-specific protein adsorption is required to fully understand the interaction of nanoparticles with biological systems. In this context, it was recently shown for silica and polystyrene NPs of various sizes and surface functionalization that the formation of a protein corona is a very rapid process [24].

However, recent studies disclosed novel binding kinetics for individual protein groups, which cannot be explained solely by the Vroman effect. Present evolution models suggest to discriminate between a "hard" and a "soft" protein corona [25–28]. It is assumed that the soft corona forms by adsorption of weakly bound proteins. With respect to the analysis of the corona composition, the soft corona proteins desorb during the nanomaterial purification process. Thus, proteomics data of the corona refer to the hard corona, representing the proteins with high binding affinities only. Since the soft corona eludes subsequent detection, its existence remains to be confirmed.

The composition of the hard corona is clearly affected by nanoparticle properties, including size/surface curvature and zeta potential [29], surface functionalities [30], hydrophobicity [26], and topology [31]. Figure 3 displays the effect of NP size on the protein corona composition formed upon amorphous silica NPs. This composition was revealed by a proteome analysis, and proteins were classified according to their calculated molecular weight (MW) for illustration reasons.

However, none of the abovementioned physicochemical properties alone is exclusively able to control the formation, composition, and evolution of the protein corona. As protein exposure time was identified as an additional critical factor, a multiparameter classifier will most probably be required to generally model and predict nanoparticle–protein interaction profiles in biologically relevant environments [18, 24].

The protein coating does not only define the biological identity of NPs but can also drastically alter its colloidal stability. The protein corona can either have a stabilizing effect by inducing steric stabilization [32] or a destabilization effect,

Fig. 3 Comparison and characterization of silica NP-specific protein corona composition. Proteins are classified by their molecular weight. The hydrodynamic radii of SiNP-125, SiNP-20, and SiNP-8 are 71, 18, and 13 nm (by DLS), respectively (with permission from Tenzer et al. [29]). The composition of the protein corona is compared to the abundance in pure blood plasma
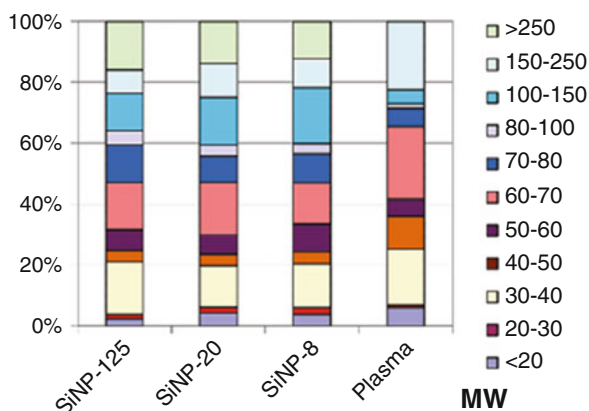
caused by a protein-mediated bridging, charge compensation, or introduction of charge inhomogeneity onto the NP surface [33]. The latter effect can result in aggregation of the nanomaterial, leading to an additional level of complexity in the description of NP systems. In a recent study, determination of the agglomeration state and the size of particles under physiological conditions by their surface properties is evidently demonstrated [34].

Nanoparticles with polymer chains attached to the surface are often referred to be highly "biocompatible," as unspecific interactions with biological components are minimized. The most common polymer affecting the biocompatibility of NPs is poly(ethylene oxide) (PEO), which is a water-soluble polymer that has a low affinity to proteins and is frequently combined with alternative functionalities [35–37]. Nanomaterials functionalized with PEO offer high colloidal stability even in liquids of physiological ionic strength caused by interparticle repulsion. Also protein adsorption is suppressed, which affects numerous cellular responses, including opsonization by cells of the reticuloendothelial system (RES). Thus, the circulation time in the blood system as well as the biodistribution of ENPs may be modulated via PEO functionalization [38, 39]. Hence, for certain biomedical and biotechnological applications, sterically stabilized nanoparticles may be of advantage [40].

4   Characterization Methods

In general, optical characterization of NPs is very challenging, since their size is below the refractive limit of visible light making direct optical detection via light microscopy impossible. Additionally, their individually different tendency to form aggregates depending on the surrounding medium disturbs appropriate characterization.

There are few methods which have been applied to characterize the size distribution of nanoparticle suspensions in biological environments. These can be classified into scattering and correlation methods, microscopy-based methods, and analytical methods based on hydrodynamic separation. One may distinguish between absolute methods like dynamic light scattering (DLS) and relative methods which necessitate calibration by a standard.

Another way to group the different characterization methods is the required sample preparation: some methods can be directly applied to diluted suspensions in the appropriate environment, such as DLS, small-angle X-ray scattering (SAXS), and cryogenic transmission electron microscopy (cryo-TEM). Other methods require special sample preparation like drying in transmission electron microscopy (TEM) or atomic force microscopy (AFM), thus affecting the state of dispersed species. Other methods like field-flow fractionation (FFF) are applied to the unmodified suspensions but typically do not operate appropriately in all kinds of physiological media.

4.1 Scattering and Correlation Methods

4.1.1 Light Scattering

Scattering of visible light by nanoparticle suspensions is a very frequently used and well-established principle for size characterization [41]. Photons interact with scattering centers of the analyzed particles by inducing oscillating dipoles. Relaxation of the dipole occurs by emitting light of the same frequency. The contrast factor K is given by the refractive index increment of the solute sample dn_D/dc to its concentration c and by the wavelength of incoming light, λ. The optical contrast factor is determined as

$$K = \frac{4\pi^2 n_D^2}{\lambda^4 N_A} \left(\frac{\partial n_D}{\partial c} \right)^2, \tag{1}$$

where n_D is the refractive index of the bulk solution and N_A is the Avogadro constant. The Rayleigh ratio, $R(\Theta)$, is the ratio of the measured scattering intensity to a standardized scattering intensity and it is independent of the experimental setup. The absolute scattering intensity for particles containing a single scattering center is given by

$$\frac{Kc}{R(\Theta)} = \frac{1}{M_w} + 2A_2 c. \tag{2}$$

Scattering intensity depends on the mass average molar mass of the analyte (M_w) and the second virial coefficient of osmotic pressure, A_2.

For larger particles whose size exceeds the limit of roughly $\lambda/20$, the Rayleigh ratio becomes dependent on the scattering angle, θ. The distance of different scattering centers within one particle results in interfering scattered light. For isotropic particles, angle dependency is a function of the scattering vector, q,

$$q = \left|\vec{q}\right| = \frac{4\pi n_D}{\lambda} \sin\left(\frac{\theta}{2}\right). \tag{3}$$

Angle-dependent scattering intensity is described by the Zimm equation:

$$\frac{Kc}{R(\theta)} = \frac{1}{M_w}\left(1 + \frac{1}{3}q^2\langle R_G^2\rangle_z\right) + 2A_2c. \tag{4}$$

The Zimm equation describes the major features of static light scattering (SLS). By measuring the angle-dependent time-averaged scattering intensity, one can determine the mass average molar mass, the second virial coefficient of osmotic pressure, and in the case of large particles the z-averaged square of the radius of gyration $\langle R_G^2\rangle_z$. These are basic properties in polymer analysis and thus relevant for the characterization of polymeric NPs. Additionally, the ratio of the radius of gyration obtained by SLS and the hydrodynamic radius, as determined by dynamic light scattering (see below), is known as ρ-ratio and provides useful information about the shape of the particles under study [41].

In dynamic light scattering (DLS), the intensity of the scattered light is recorded as a function of time as opposed to SLS which is time averaged. From DLS, the autocorrelation function $g_1(q, \tau)$ is established. The fluctuations in scattered light intensity arise from Brownian motion of the analyte species which alters the amount of scattering centers within the scattering volume. The autocorrelation function $g_1(q, \tau)$ describes the fluctuations of the scattering intensity as a function of momentary time intervals, τ. By making use of the Siegert relation, the exponential decay of the autocorrelation function provides information on the Stokes–Einstein diffusion coefficient D:

$$g_1(q, \tau) = \sqrt{\frac{\langle I(q,t)I(q,t+\tau)\rangle}{\langle I(q,t)\rangle^2} - 1} = \exp\left(-Dq^2\tau\right), \tag{5}$$

where $\langle I(q,t)\rangle$ is the averaged scattering intensity as a function of time. Extrapolation of $q \rightarrow 0$ yields the z-average of the diffusion coefficient $\langle D\rangle_z$ which can be used to calculate the corresponding hydrodynamic radius $\langle R_h^{-1}\rangle_z$ via the Stokes–Einstein relation:

$$R_h = \frac{k_B T}{6\pi\eta D}. \tag{6}$$

Therein, k_B is the Boltzmann constant, η is the solvent viscosity, and T is the absolute temperature. If the sample shows polydispersity, a monoexponential decay

of the autocorrelation function will not properly fit the experimental data; thus, a cumulant analysis may be applied. The only physically relevant information on sample polydispersity available in DLS is given by the μ_2 value, which is the deviation from monoexponential decay of the autocorrelation function. As convention, the μ_2 value is calculated at an angle of $90°$. Light scattering experiments must be performed with care as the scattering intensity of a single particle scales with the sixth power of its radius. To avoid superposition, micrometer-sized dust particles must be removed for an appropriate analysis by light scattering.

DLS of electrostatically stabilized nanoparticles under conditions of high ionic strength is very challenging due to destabilization of the particles and the formation of aggregates. Advanced experimental skills and experience are required to distinguish between scattering by single particles and aggregates as demonstrated in Fig. 4. Also proteins of various sizes, which are found in high concentration in biological environments, give rise to a significant scattering background. Consequently, DLS has rarely been applied for size (distribution) analysis in solutions containing serum proteins [42]. However, a sophisticated method based on DLS has recently been reported to measure particle size in blood plasma by separating the scattering intensities of different solute constituents [43].

These circumstances clearly indicate that careful instrumental calibration and adequate data examination must be applied to characterize nanoparticles in suspensions. Angle-dependent measurements provide additional information on the state of aggregation in contrast to backscattering methods. Particle studies using the popular automated devices operating at one scattering angle and with preassigned fitting procedures based on spherical shape models and Gaussian size distributions are qualitatively acceptable for low-salt conditions and monodisperse samples. Using these simplified experimental settings and assumptions, quantification of particle size within polydisperse samples must be considered inadequate, particularly under physiological conditions [44].

4.1.2 Zeta Potential Measurements

The surface charge of a given NP species determines colloidal stability, governs protein adsorption, and, thus, influences cellular uptake. Using the *Doppler* effect, electrophoretic light scattering of nanoparticle suspensions provides information on the effective charge of the particles [45]. This effective charge is quantified by measurements of the zeta potential, ς, which is the potential at the hydrodynamic slipping plane of the dynamic double layer (ddl). In electrophoretic light scattering, the electrophoretic mobility of the sample, μ, is observed and converted into its zeta potential by Eq. (7) [46, 47]

$$\varsigma = \mu \frac{4\pi\eta}{\varepsilon},$$

$$(7)$$

with $\varepsilon = \varepsilon_0\varepsilon_r$ the permittivity of the solvent as a product of absolute permittivity, ε_0, and relative dielectric constant of the solvent, ε_r. Similar to DLS, potentials derived
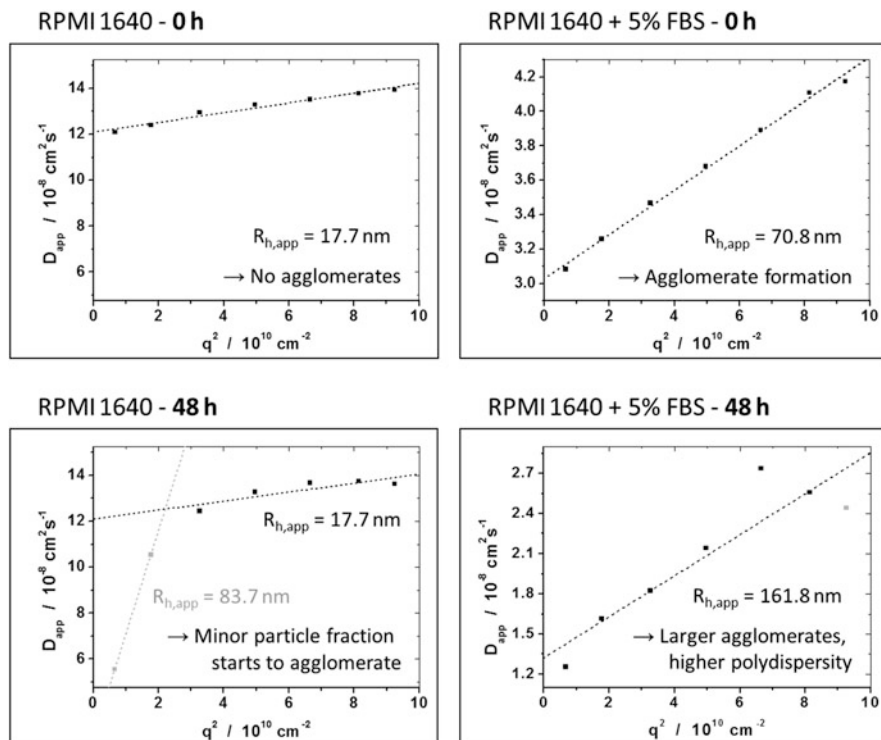
Fig. 4 Angle-dependent diffusion coefficients of 17-nm-sized silica particles in RPMI 1640 in the presence or absence of 5% FBS. Aggregation as a function of time is observed, and a bimodal size distribution is disclosed after 2 days due to the beginning of agglomeration in RPMI 1640

by automated devices for electrophoretic light scattering should be treated with care and used for qualitative rather than quantitative comparison of colloidal stability. Due to the primary electroviscous effect, caused by deformation of the electric double layer, the relationship between electrophoretic mobility and the corresponding zeta potential is not linear but undergoes a maximum, typically in the low ionic strength regime [48]. A simplified model used for zeta potential calculation becomes more and more adequate with increasing ionic strength and the resulting shrinkage of the electric double layer. To obtain a detailed description, electrokinetic phenomena may be described in terms of Mangelsdorf–O'Brien–White theory [49, 50].

The formation of a protein corona affects the zeta potentials as derived from electrophoretic light scattering in biological media. Measurements of electrophoretic light scattering after purification have clearly shown the formation of the protein corona on Au NPs to be dependent on time and protein concentration [28].

An alternative method to measure zeta potentials of nanoparticles in suspension is measuring the streaming potential [51, 52]. Shear forces cause the electric double layer of immobilized nanoparticles to be deformed. The potential resulting from the

ambition of the ions to diffuse back into their steady state can be measured and converted into a corresponding zeta potential. The main advantages of such techniques are the absence of complex electrokinetic phenomena. In addition, measurements are generally rather robust as no optics are required, and this method can be applied in biological media.

4.1.3 X-Ray and Neutron Scattering

In scattering experiments like SLS and DLS, the zoom factor is given by the scattering vector $\vec{q}$. One strategy to minimize q and, thus, to resolve more detailed structures is to reduce the wavelength of the incident light source. Accordingly, in small-angle X-ray and neutron scattering experiments (SAXS, SANS), de Broglie wavelengths are in the order of 0.1–10 nm. Generally speaking, the principles of scattering visible light, neutrons, and electrons are very similar while they do differ with respect to their individual contrast factors. Please note: in SLS, scattering occurs due to differences in refractive index, while different electron densities are observed in SAXS and scattering occurs at the level of atomic nuclei in SANS. Besides the radius of gyration, which is determined by angle-dependent intensity measurements, the particle form factor $P(q)$ can be observed for monodisperse samples by scattering methods [53, 54].

In polydisperse samples, averaged values are observed and no insight into the formation of a protein corona is available. As the form factor determines the applied fit model, a priori information on the particle shape is needed, as available from electron microscopy [55].

Further information can be obtained by scattering at high q-values, such as the surface-to-volume ratio (Porod regime) and the internal (fractal) structure of nanosized materials. SAXS and SANS are also frequently used to investigate structures of biomacromolecules [56], to characterize the structure of nanoemulsions (SANS) [57], or to observe the aggregation behavior of protein-bridged silica NPs (SAXS) [33]. By using high energy synchrotron radiation, improved SAXS resolution can be achieved and, for example, the formation of miscellaneous structures can be observed time resolved [58].

4.1.4 Fluorescence Correlation Spectroscopy

In fluorescence correlation spectroscopy (FCS), fluctuations of the fluorescent light are detected. This is a result of particle diffusion into or out of the observation volume resulting in temporal changes of the particle number concentration. The free diffusion of fluorescent particles is quantified by autocorrelation of the fluctuations of fluorescence intensity, analogous to DLS.

FCS has been used to quantify the amount of blood proteins on sulfonate and carboxylate-functionalized polystyrene NPs. Therein, discrimination between soft

and hard protein coronas was achieved by kinetic analysis [59]. Furthermore, FCS has been used to investigate the process of protein corona formation in situ. Research on interactions of FePt NPs with human serum albumin (HSA) [10] and transferrin [60] resulted in clear evidence that the time course of corona formation and its thickness are determined by the strength of the interaction between the protein and particle.

Measurements with higher precision can be achieved by dual-focus FCS (2fFCS) that includes an absolute calibration standard [61]. Based on knowledge about the molecular structure of proteins, the thickness of the protein corona was explained by the individual orientation of proteins on the particle surface by 2fFCS [62].

In comparison to dynamic light scattering, FCS has the inherent advantage to detect fluorescence-labeled particles in the presence of non-fluorescing proteins. Still, this correlation method is limited when it comes to measuring the size distribution of polydisperse samples. Moreover, FCS is only applicable to fluorescent nanoparticles. Non-fluorescent particles cannot be studied.

4.1.5   Particle Tracking Velocimetry

Particle tracking velocimetry (PTV) is a direct method to observe Brownian motion of nanoparticles and gain information on their size. The first automated systems tracking in 3D, based on multiple CCD cameras, were developed in the late 1980s [63]. Modern setups include two lasers with different wavelengths to illuminate the suspended particles which provide a sufficient amount of scattering light to track the motion of particles as individual scattering sources. The path length traveled by individual particles is converted into diffusion coefficients by the Einstein–Smoluchowski equation [11].

The impact of RPMI cell medium, supplemented with FBS or BSA, on NPs has been successfully investigated by Brownian motion tracking. It was found that agglomeration of Ag NPs occurs in pure RPMI and RPMI-BSA within a few hours, whereas particles remained well dispersed in RPMI-FBS. This finding was confirmed by DLS [11]. Interactions of BSA with citrate-stabilized Ag NPs and Au NPs were compared to the interactions of BSA with polystyrene NPs by means of PTV and circular dichroism (CD) spectroscopy. Much lower kinetic constants of BSA desorption were observed for citrate-coated metallic NPs than for polymer-coated NPs [64]. The combination of Brownian motion tracking and CD spectroscopy was shown to allow discrimination between the formation of protein mono- and multi-layers on NP surfaces [32].

As PTV is sensitive to brightness, the light scattered by larger particles dominates in polydisperse samples. Consequently, smaller particles will hardly be resolved in a multimodal mixture. Presenting PTV data as number averages results in an underestimation of rarely present particles. These drawbacks are overcome in DLS, so that both techniques complement one another.

4.2 Microscopy-Based Methods

4.2.1 Electron Microscopy

The size of nanoscale particles cannot be resolved with light microscopy because their size is smaller than the wavelength of visible light. One strategy to visualize NPs is to increase the frequency of the electromagnetic radiation used for imaging. In electron microscopy, the light source is an electron beam which interferes with the electron density of the sample. Artifacts induced by the sample preparation procedures prevent visualization of the particles as present in suspended state.

In transmission electron microscopy (TEM), highly resolved images of the NPs are obtained, and their size, polydispersity, and shape are determined from the transmitted electron density [65]. In contrast, scanning electron microscopy (SEM) provides a topographic view on the nanoparticles by collecting the backscattered electrons for imaging. Analysis of the scattered electron diffraction pattern offers information on the crystal structure of solid analytes [66].

To reduce the influence of artifacts and to receive a reasonable size distribution for the characterization of NP suspensions, a sufficient number of particles must be studied to enhance statistical significance. In TEM, the arrangement of the particles in the micrograph is mainly governed by artifacts resulting from drying of sample suspensions on carbon-coated copper grids. Additionally, in biological environment, proteins and other biomolecules denature and crystallize during the drying procedure giving rise to significant background intensities that reduce the contrast of the image.

To avoid secondary effects arising from the sample preparation and to study the state of dispersion as present in physiological media, cryogenic sample preparation can be applied (cryo-TEM) [67]. In this case, a droplet of suspension is placed onto a grid which consists of a porous carbon film. Thin films of solution occupy the holes and are shock-frozen in liquid propane to prevent water crystallization. Until use, the samples can be stored in liquid nitrogen. Analysis under external cooling provides a thin film of amorphously solidified water and media [68]. However, cryo-TEM is far away from becoming a standard characterization method because it is both time consuming and costly in addition to requiring a high degree of experimental experience [69].

Very fast mechanisms like structure formation of block copolymer micelles were elucidated by cryo-TEM [70], as well as the strength of weak interactions in carbon nanotube dispersions [71].

4.2.2 Atomic Force Microscopy

Atomic force microscopy (AFM) allows imaging beyond the resolution of conventional optical microscopes based on the interaction between a sharp tip and the sample surface. The tip with a radius of about 10 nm is attached to a cantilever

which is scanned over the sample surface. The cantilever bends and thus moves up and down according to its interaction with the surface. This movement is detected by a photodiode using the optical lever principle. The exact lateral and vertical movement of the cantilever is achieved with a piezo system, and the information obtained about probe position and lever deflection is combined into a topographic map of the sample [72]. In contrast to optical microscopy, AFM is not only capable of providing information about the sample topography but also about mechanical [73], viscoelastic, and thermal properties [74] as well as conductivity, surface potentials [75], and friction forces. This can be achieved by choice of the measurement mode. The most commonly used modes will be explained below.

AFM can be operated in air, vacuum, and liquid, allowing the investigation of samples under physiological conditions. The visualization of NPs is only possible, if these are fixed to a surface and accessible for the AFM tip. The resolution of the images is limited by the tip apex and, thus, by using tips with a single atom apex, atomic resolution can be achieved, which has been successfully demonstrated in ultrahigh vacuum [76] and in liquids [77].

One drawback of nanoparticle characterization by AFM is the limited number of observed particles. AFM is not a bulk method and thus always provides an excerpt from a limited number of particles included in a sample. Accordingly, it is essential to perform a considerable amount of measurements in order to do statistics on the results. As an alternative particle characterization, AFM is commonly used in combination with a bulk method which gives strong and reliable results.

As an example, Gurevich et al. [78] detected size changes of NPs upon exposure to a protein solution and compared the results from AFM with DLS experiments. Both methods found consistently that the average size of the nanoparticles increased due to the formation of a protein corona. A broader size distribution was found in DLS which was taken as a hint for particle aggregation. AFM images confirmed these results and visualized the formation of aggregates upon protein exposure. MacCuspie used a similar approach and investigated the effect of cell culture media on the colloidal stability of silver NPs by use of DLS, UV–Vis spectrometry, and AFM [79].

AFM can also be used to measure so-called force-versus-distance (F–D) curves. To record such F–D curves, either the sample or the tip (depending on the instrument) is moved up and down. The resulting deflection of the cantilever is measured and provides information about mechanical properties like the adhesion between the tip and sample or the elastic moduli of the surface [80]. This mode can also be operated in air or liquid, and Pyrgiotakis et al. recently reported about the development of a methodology to investigate NP–NP interactions based on force–distance curve measurements in biological media [81]. In their experiments, they were able to determine the thickness of a protein corona adsorbed onto Fe_2O_3 or CeO_2 NPs and the agglomeration potential of the protein-coated nanoparticles as a function of particle size. They found that NP–NP interactions and the thickness of the protein corona are highly specific for the particle material, primary particle size, and the physiological media. Schaefer et al. used a different approach and

investigated the interaction forces between NPs and proteins by measuring F–D curves [82].

4.3   Analytical Methods Based on Hydrodynamic Separation

4.3.1   Field-Flow Fractionation

Field-flow fractionation (FFF) denominates a family of separation techniques. In contrast to chromatographic methods, fractionation in FFF is not achieved by the interaction of the sample with a mobile and a stationary phase. Instead, the general principle refers to a physical field, which is acting perpendicular to a separation channel.

Interaction with the applied field drives the particles toward one channel boundary, the so-called accumulation wall. The mean distance of the sample to the accumulation wall is mainly influenced by the diffusion coefficients of the particles and the strength of the applied field. Larger particles are located next to the accumulation wall, whereas smaller particles stay farther apart due to their increased back diffusion. As the carrier flows in a parabolic shape through a thin channel, the elution velocity of the sample is determined by the velocity of the flow segment where it is located. Thus, in FFF, the separation occurs according to particle size, typically with smaller particles to elute first and larger to elute last.

Subtechniques differ in the kind of physical field which is applied. Examples are the thermal FFF (Th-FFF), sedimentation FFF (Sd-FFF), electrical FFF (E-FFF), and flow-FFF (Fl-FFF) [83–85].

4.3.2   Flow Field-Flow Fractionation

In Fl-FFF, a cross-sectional flow is established which acts as the separating field in addition to the laminar flow profile. This method includes two subtechniques, the symmetrical Fl-FFF (SF-FFF), where the top and the bottom wall of the channel are replaced by a frit and a membrane, and the asymmetrical Fl-FFF [86] (AF-FFF), where only the bottom wall of the fractionation channel is replaced by a membrane. This maintains a constant cross flow close to the accumulation wall.

In theoretical descriptions [87–89], the force induced by the field is replaced by a drift velocity, U, of the particles toward the accumulation wall. This mass transport leads to an increased concentration at the channel wall. Directed diffusion occurs along the concentration gradient $dc(x)/dx$ and is described by Fick's law. The overall mass flow, J, at the distance from the channel wall, x, is given by

$$J = -D\frac{dc(x)}{dx} - Uc(x). \tag{8}$$

In steady state, no mass flux is present and an exponential decay of the concentration profile is obtained.

$$c(x) = c_0\exp\left(-x\frac{|U|}{D}\right). \tag{9}$$

The effective layer thickness (l), which is a characteristic distance between the center of gravity of the sample and the accumulation wall, is described by the decay length $l = D/(x|U|)$. The smaller the particle, the more distant it is from the accumulation wall, resulting from large diffusion coefficients of small particles. Since flow velocity of the parabolic flow profile is a function of the distance to the accumulation wall, retention time becomes a function of particle size. A linear relation between the retention time and the hydrodynamic radius can be approximated.

$$t_{\mathrm{R}} = \frac{\pi\eta R_h \dot{V}_c w^2}{\dot{V} kT}, \tag{10}$$

where $\dot{V}$ is the detector flow rate, $\dot{V}_c$ the cross flow rate, and w the channel height.

Although hydrodynamic radii can be calculated directly by measuring the retention time, typical calibrations standards are applied to deduce the size of the sample. This is due to technical constraints, such as compressible membranes, which reduce the effective height of the channel, or programmed nonconstant flow conditions [86].

4.3.3   AF-FFF of Biomolecules

The operation of the Fl-FFF under physiological salt conditions is still challenging because high ionic strengths lead to increased particle–particle and particle–wall interactions [90]. As a result, the fractionation is dominated by hydrophobic interactions leading to a peak broadening [91] and asymmetry as well as a significant sample loss [92, 93].

AF-FFF is mostly used for analytical applications [94] and for a wide diversity of biomolecules, ranging from proteins [95], ribosomes [96], polysaccharides [97], or bioconjugated nanospheres [98].

The analytical fractionation of NPs incubated with serum reveals the dimensions of the adsorbed protein corona by a retarded retention time (RT) compared to NP in the absence of proteins. In Fig. 5, elugrams of superparamagnetic iron oxide NPs, coated with a monolayer of oleic acid and an amphiphilic block copolymer (AMP-SPIONS), are displayed [99].

Fig. 5 AF-FFF elugram of AMP-SPIONS before and after incubation with serum depleted of IgG and HSA (with permission from Ashby et al. [99])
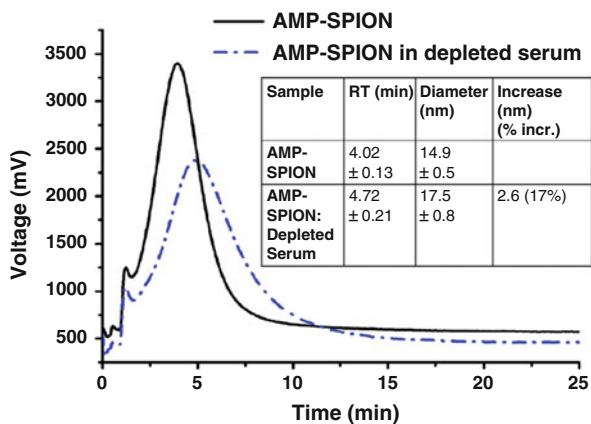
Evaluation of the retention time results in a relative size characterization of the sample, according to the calibration standard. This has been confirmed by investigations of size-dependent plasmon resonance of gold nanorods [100]. Additionally, the coupling of a variety of online detectors to the FFF instrument yields an extensive, multiparametric sample characterization, providing a comprehensive analysis emphasizing single fractions. Relevant online detectors are based on fluorescence detection and UV absorbance to determine retention times or refractive index detection for appropriate concentration determination. Also absolute size characterization detection by SLS (MALLS, multi-angle laser light scattering), DLS (QELS, quasi-elastic light scattering) [101, 102], or mass spectrometry (inductively coupled plasma mass spectrometry, ICPMS) [103] are applied. Combination of AF-FFF with offline DLS and TEM was recently shown to provide a complete characterization of the agglomeration state of NPs under physiological conditions [34].

The load capacity could provide a semi-preparative fractionation by an optimization of the flow conditions. Such an approach is the *slot outlet technique*, where the sample is enriched by removing a part of the carrier flow [104]. Using this technique leads to increased concentrations of specific NP-size fractions for toxicological studies [105] or to separation of NPs from present proteins [99]. An increased load capacity can also be obtained by optimizing the channel geometry. The circular asymmetrical flow field-flow eluator (CAFFFE) is an example of such an optimization with a circular array of focusing spots. This assignment provides preparative sample capacities [106].

4.3.4 Size Exclusion Chromatography

Size exclusion chromatography (SEC) is a separation method for molecules or particles dispersed in a liquid, commonly known as gel permeation chromatography or gel filtration, mostly in the case of polymers or proteins, respectively. The sample

flows through a column containing a packed bed of porous particles, called the stationary phase. Depending on the molecular or particle size of the analyte, individual species can diffuse into the pores of the stationary phase or will be excluded. Large analyte molecules or particles are excluded and will elute sooner, while smaller species enter the pores to a different extent and are found to elute later. By calibration with appropriate standards, the elution time can be related to size. For polymers or other molecular species, usually the molecular weight is of particular interest, which requires a new calibration for every material. In fact, the actual separation process is not determined by molecular weight but by the hydrodynamic volume of the analyte. This principle was eluded by Benoit [107] and is commonly known as universal calibration.

Traditionally, as to aqueous systems, SEC has been used for the purification and analysis of proteins and a number of water-soluble polymers such as dextrans, PEG, and others [108]. As to ENPs, a variety of different materials has been studied in both aqueous and organic solvent systems. A common problem is colloidal stability of the particles, which is generally provided by a coating or surfactant layer. Due to the intimate interaction of the particles with the stationary phase of the column, the surfactant layer is often prone to desorption which results in aggregation of the particles and/or adhesion to the stationary phase. To circumvent this problem, the mobile phase has been supplied with additional surfactant to keep the particles stable, in both aqueous and organic media [109, 110]. Particles modified with a polymeric coating or covalently attached molecules, such as PEG or proteins, have been shown to remain stable on the column, even under physiological salt conditions; by using globular proteins as calibration standards, their hydrodynamic diameter could be derived [111, 112]. Also, separation of NPs of different shapes has been demonstrated by SEC (Fig. 6) [113].

4.3.5 Gel Electrophoresis

Electrophoresis describes the migration of charged particles within an electric field. The motion velocity, v, is determined by the strength of the electric field, E, and the electrophoretic mobility, μ.

$$v = \mu \cdot E \tag{11}$$

Gel electrophoresis for molecular weight determinations of proteins is applied in an agarose or polyacrylamide gel with defined pore size matching the relevant range of sizes to be analyzed. Agarose gel electrophoresis was also established as proper size and shape characterization for colloidal particles [114], as well as bioconjugated gold NPs [115].

Gel electrophoresis has proven its particular usefulness in characterizing the protein corona on NPs in physiological environments. A well-established system in protein bioanalytics is polyacrylamide gel electrophoresis with the addition of sodium dodecyl sulfate (SDS-PAGE). Herein, SDS attaches to the protein sample
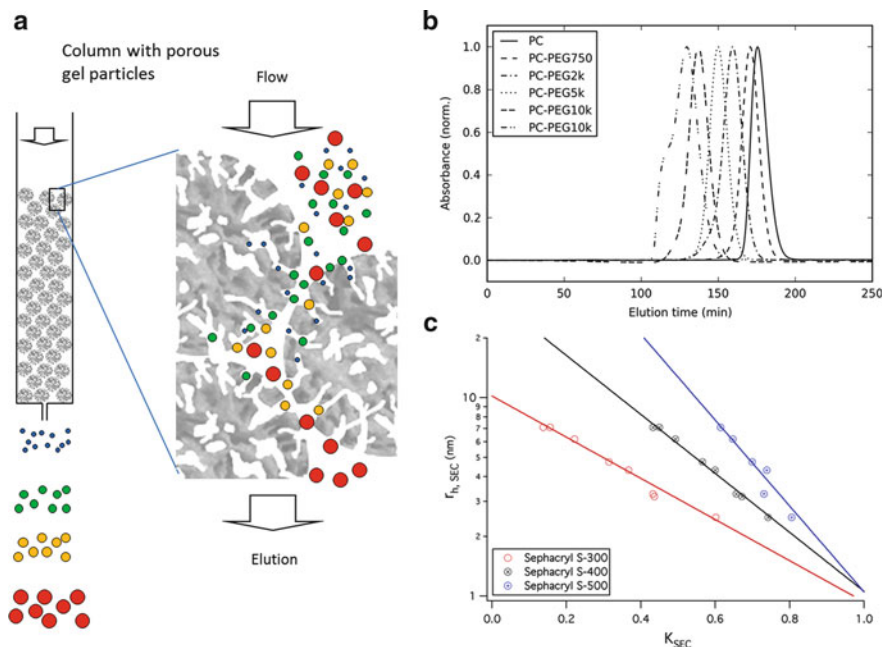
Fig. 6 Size exclusion chromatography. (**a**) Molecules or particles of different size are fractionated based on their hydrodynamic volume with respect to the pore size of the stationary phase. (**b**) Chromatogram of Au NPs with an amphiphilic polymer coating (PC) and PEG of different molecular weight (750–20 kDa), eluting at different times. (**c**) Size calibration of different Sephacryl media exhibiting different pore size, using globular proteins. K_{SEC} is the normalized partition coefficient, $r_{h,SEC}$ the hydrodynamic radius of the proteins (with permission from Sperling et al. [112])

to a constant amino acid-to-SDS ratio [116]. The highly negative charge of this surfactant is transferred to the protein, leading to a denaturation of the proteins into a rodlike shape, and a similar charge-to-mass ratio of all proteins is obtained. In an electric field, separation is achieved by sieving through the gel, where smaller proteins can pass through the pores faster than larger proteins. The relative mobilities in such gels are inversely proportional to the logarithm of the molecular weights. The molecular weight is determined relative to multiple protein markers with known molecular weight. The accuracy of this method for the molecular weight determination of proteins is approximately 5–10% [117]. An example of a SDS-PAGE gel is illustrated in Fig. 7. Proteins were stained with Coomassie blue. The first lane shows the molecular weight standard. Lanes 1 and 2 show proteins from cytosolic fluid forming the corona around plain and carboxyl-modified polystyrene NPs, respectively [27]. For a further investigation of proteins in the corona, selected bands can be excised from the SDS-PAGE gel and analyzed by mass spectrometry [24].

Fig. 7 SDS-PAGE gel stained with Coomassie blue. Lane from left to right: molecular weight standard, protein corona of plain polystyrene NPs, protein corona of carboxylated polystyrene NPs (with permission from Lundqvist et al. [27])
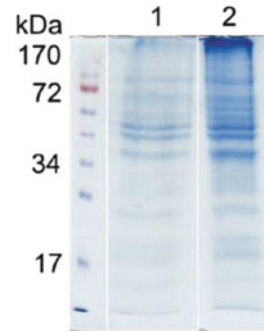
4.3.6 Analytical Ultracentrifugation

Classic centrifugation becomes analytical by applying detectors onto the rotor cell, measuring concentration distributions of the sedimenting sample. The common term for such experiments at rotation speeds of up to 80.000 rpm is called analytical ultracentrifugation (AUC) [118].

The process of sedimentation is expressed by the Lamm equation, which describes the local concentration c, at the radial position r in the ultracentrifugal field, as a function of time t with diffusion and sedimentation coefficients D and s, respectively.

$$\frac{\partial c}{\partial t} = \frac{1}{r}\frac{\partial}{\partial r}\left(rD\frac{\partial c}{\partial r} - s\omega^2 r^2 c\right) \tag{12}$$

Dependent on the rotor angular velocity ω, sedimentation coefficients or diffusion coefficients are obtained. Applying a density gradient yields the density of the sample, or at sedimentation–diffusion equilibrium conditions, the molecular weight and even stoichiometry of the interaction systems can be derived. Especially in aqueous multiphase systems, highly efficient separations of NP suspensions according to their size and shape were demonstrated [119].

The AUC is widely applied in biochemistry [120], biophysics, and pharmacy [121]. In these fields, interactions of proteins, DNA, and RNA as well as polysaccharides have been studied [122].

4.4 Comparison of Characterization Methods

All of the previously introduced methods provide a size characterization of a nanoscale material, whereas each technique comes along with advantages and limitations. The result of a single method will be influenced by particle size and its dispersity, the interaction forces, the weightings in case of averaging, and

inherently the fundamental principle of each characterization technique with its artifacts [123].

In the case of scattering and correlation methods, only average values are obtained which are influenced by sample polydispersity. One obtains the weight average of the molecular mass and the z-average of the squared radius of gyration in static light scattering, whereas dynamic light scattering yields an inverse z-average for the hydrodynamic radius. The advantage of scattering methods is the availability of absolute measurements, without calibration being necessary. Scattering methods also allow the measurement in solution under biologically relevant conditions. In FCS, the main advantage is that only fluorescent particles are correlated, and measurements in physiological media remain accurate. On the other side, the limitation to fluorescent samples requires some manipulation of non-fluorescent particles. Thus, non-fluorescent particles are not generally suitable to FCS. Another aspect to keep in mind is that light scattering is an ensemble method, whereas FCS, particle tracking, and electron microscopy are based on relatively few particles. Here, one has to assure representative sampling; hence, sample preparation may play a crucial role.

As microscopy directly provides an image of NPs, especially for the determination of the shape, TEM and SEM are reliable and necessary standards. While counting particles yields a size distribution, the accuracy will highly depend on the number of imaged particles. In cryo-TEM, the frozen state of NPs under physiological conditions can be imaged.

Fractionation methods are generally affected by interaction forces; thus, only a relative size characterization is obtained. Absolute measurements of size and size distribution can be accomplished by coupling the FFF to suitable online detectors, such as light and X-ray scattering or mass spectrometry. Also fractionation in a semi-preparative way can be archived with minor effort. The main limitation of Fl-FFF is fractionation at physiological salinities, where attractive forces dominate the elution process.

In conclusion, for characterization of NPs, especially in physiological conditions, no single method is complete. Detailed characterization results from combining different analytical methods with the awareness of the specific advantages and limitations of each method [34].

References

1. Linsinger T, Roebben G, Gilliland D, Calzolai L, Rossi F, Gibson P, Klein C (2012) Requirements on measurements for the implementation of the European Commission definition of the term 'nanomaterial'. Publications Office of the European Union JRC73260, ISBN: 978-92-79-25602-8
2. Williams D (2008) On the mechanisms of biocompatibility. Biomaterials 29(20):2941–2953
3. Nel A, Xia T, Madler L, Li N (2006) Toxic potential of materials at the nanolevel. Science 311(5761):622–627

4. Warheit D (2008) How meaningful are the results of nanotoxicity studies in the absence of adequate material characterization? Toxicol Sci 101(2):183–185

5. Israelachvili J (2011) Intermolecular and surface forces. Elsevier/Academic, Amsterdam

6. Landau L, Lifshitz E, Pitaevskij L (1998) Electrodynamics of continuous media. Butterworth-Heinemann, Oxford, 8

7. Russel W, Saville D, Schowalter W (1989) Colloidal dispersions. Cambridge University Press, Cambridge

8. Maskos M, Stauber R (2011) In: Ducheyne P (ed) Comprehensive biomaterials. Elsevier, Oxford

9. Kasper J, Hermanns M, Bantz C, Koshkina O, Lang T, Maskos M, Pohl C, Unger R, Kirkpatrick C (2013) Interactions of silica nanoparticles with lung epithelial cells and the association to flotillins. Arch Toxicol 87(6):1053–1065

10. Röcker C, Pötzl M, Zhang F, Parak W, Nienhaus G (2009) A quantitative fluorescence study of protein monolayer formation on colloidal nanoparticles. Nat Nanotechnol 4(9):577–580

11. Kittler S, Greulich C, Gebauer J, Diendorf J, Treuel L, Ruiz L, Gonzalez-Calbet J, Vallet-Regi M, Zellner R, Köller M, Epple M (2010) The influence of proteins on the dispersability and cell-biological activity of silver nanoparticles. J Mater Chem 20(3):512

12. Cho K, Lee Y, Lee C-H, Lee K, Kim Y, Choi H, Ryu P-D, Lee S, Joo S-W (2008) Selective aggregation mechanism of unmodified gold nanoparticles in detection of single nucleotide polymorphism. J Phys Chem C 112(23):8629–8633

13. Jiang J, Oberdörster G, Biswas P (2009) Characterization of size, surface charge, and agglomeration state of nanoparticle dispersions for toxicological studies. J Nanopart Res 11(1):77–89

14. Gebauer J, Treuel L (2011) Influence of individual ionic components on the agglomeration kinetics of silver nanoparticles. J Colloid Interface Sci 354(2):546–554

15. Derjaguin B, Storozhilova A, Rabinovich Y (1966) Experimental verification of the theory of thermophoresis of aerosol particles. J Colloid Interface Sci 21(1):35–58

16. Holmberg K (2002) Handbook of applied surface and colloid chemistry. Wiley, Chichester

17. Gregory J (2009) Monitoring particle aggregation processes. Colloids, polymers and surfactants. Special Issue in honour of Brian Vincent, vol 147–148, pp 109–123

18. Monopoli M, Åberg C, Salvati A, Dawson K (2012) Biomolecular coronas provide the biological identity of nanosized materials. Nat Nanotechnol 7(12):779–786

19. Oberdörster G (2010) Safety assessment for nanotechnology and nanomedicine: concepts of nanotoxicology. J Intern Med 267(1):89–105

20. Oberdörster G (2012) Nanotoxicology: in vitro-in vivo dosimetry. Environ Health Perspect 120(1):A13

21. Vroman L (1962) Effect of adsorbed proteins on the wettability of hydrophilic and hydrophobic solids. Nature 196(4853):476–477

22. Vroman L, Adams A (1969) Findings with the recording ellipsometer suggesting rapid exchange of specific plasma proteins at liquid/solid interfaces. Surf Sci 16:438–446

23. Lynch I, Dawson K (2008) Protein-nanoparticle interactions. Nano Today 3(1–2):40–47

24. Tenzer S, Docter D, Kuharev J, Musyanovych A, Fetz V, Hecht R, Schlenk F, Fischer D, Kiouptsi K, Reinhardt C, Landfester K, Schild H, Maskos M, Knauer S, Stauber R (2013) Rapid formation of plasma protein corona critically affects nanoparticle pathophysiology. Nat Nanotechnol 8(10):772–781

25. Cedervall T, Lynch I, Lindman S, Berggard T, Thulin E, Nilsson H, Dawson K, Linse S (2007) From the cover: understanding the nanoparticle-protein corona using methods to quantify exchange rates and affinities of proteins for nanoparticles. Proc Natl Acad Sci 104(7):2050–2055

26. Monopoli M, Walczyk D, Campbell A, Elia G, Lynch I, Baldelli Bombelli F, Dawson K (2011) Physical – chemical aspects of protein corona: relevance to in vitro and in vivo biological impacts of nanoparticles. J Am Chem Soc 133(8):2525–2534

27. Lundqvist M, Stigler J, Cedervall T, Berggård T, Flanagan M, Lynch I, Elia G, Dawson K (2011) The evolution of the protein corona around nanoparticles: a test study. ACS Nano 5 (9):7503–7509

28. Casals E, Pfaller T, Duschl A, Oostingh G, Puntes V (2010) Time evolution of the nanoparticle protein corona. ACS Nano 4(7):3623–3632

29. Tenzer S, Docter D, Rosfa S, Wlodarski A, Kuharev J, Rekik A, Knauer S, Bantz C, Nawroth T, Bier C, Sirirattanapan J, Mann W, Treuel L, Zellner R, Maskos M, Schild H, Stauber R (2011) Nanoparticle size is a critical physicochemical determinant of the human blood plasma corona: a comprehensive quantitative proteomic analysis. ACS Nano 5 (9):7155–7167

30. Lundqvist M, Stigler J, Elia G, Lynch I, Cedervall T, Dawson K (2008) Nanoparticle size and surface properties determine the protein corona with possible implications for biological impacts. Proc Natl Acad Sci 105(38):14265–14270

31. Mahmoudi M, Serpooshan V (2011) Large protein absorptions from small changes on the surface of nanoparticles. J Phys Chem C 115(37):18275–18283

32. Gebauer J, Malissek M, Simon S, Knauer S, Maskos M, Stauber R, Peukert W, Treuel L (2012) Impact of the nanoparticle–protein corona on colloidal stability and protein structure. Langmuir 28(25):9673–9679

33. Bharti B, Meissner J, Findenegg G (2011) Aggregation of silica nanoparticles directed by adsorption of lysozyme. Langmuir 27(16):9823–9833

34. Bantz C, Koshkina O, Lang T, Galla H-J, Kirkpatrick C, Stauber R, Maskos M (2014) The surface properties of nanoparticles determine the agglomeration state and the size of the particles under physiological conditions. Beilstein J Nanotechnol 5:1774–1786

35. Calvo P, Remuñán-López C, Vila-Jato J, Alonso M (1997) Novel hydrophilic chitosan-polyethylene oxide nanoparticles as protein carriers. J Appl Polym Sci 63(1):125–132

36. Nikolic M, Krack M, Aleksandrovic V, Kornowski A, Förster S, Weller H (2006) Tailor-made ligands for biocompatible nanoparticles. Angew Chem Int Ed 45(39):6577–6580

37. Chen H, Wu X, Duan H, Wang Y, Wang L, Zhang M, Mao H (2009) Biocompatible polysiloxane-containing diblock copolymer PEO- b -PγMPS for coating magnetic nanoparticles. ACS Appl Mater Interfaces 1(10):2134–2140

38. Aggarwal P, Hall J, McLeland C, Dobrovolskaia M, McNeil S (2009) Nanoparticle interaction with plasma proteins as it relates to particle biodistribution, biocompatibility and therapeutic efficacy. Adv Drug Deliv Rev 61(6):428–437

39. Dobrovolskaia M, Germolec D, Weaver J (2009) Evaluation of nanoparticle immunotoxicity. Nat Nanotechnol 4(7):411–414

40. Salvati A, Pitek A, Monopoli M, Prapainop K, Bombelli F, Hristov D, Kelly P, Aberg C, Mahon E, Dawson K (2013) Transferrin-functionalized nanoparticles lose their targeting capabilities when a biomolecule corona adsorbs on the surface. Nat Nanotechnol 8(2):137–143

41. Schärtl W (2007) Light scattering from polymer solutions and nanoparticle dispersions. Springer, Berlin

42. Lacerda S, Park J, Meuse C, Pristinski D, Becker M, Karim A, Douglas J (2010) Interaction of gold nanoparticles with common human blood proteins. ACS Nano 4(1):365–379

43. Rausch K, Reuter A, Fischer K, Schmidt M (2010) Evaluation of nanoparticle aggregation in human blood serum. Biomacromolecules 11(11):2836–2839

44. Jones C, Grainger D (2009) In vitro assessments of nanomaterial toxicity. Adv Drug Deliv Rev 61(6):438–456

45. Delgado A, González-Caballero F, Hunter R, Koopal L, Lyklema J (2007) Measurement and interpretation of electrokinetic phenomena. Elkin 06, International Electrokinetics Conference, June 25–29, Nancy, France 309(2):194–224

46. Hunter R (1993) Introduction to modern colloid science. Oxford University Press, Oxford

47. Lyklema J (1995) Fundamentals of interface and colloid science, Solid-liquid interfaces. Elsevier, Amsterdam, p s.1

48. Antonietti M, Vorwerg L (1997) Examination of the atypical electrophoretic mobility behavior of charged colloids in the low salt region using the O'Brian-White theory. Colloid Polym Sci 275(9):883–887

49. O'Brien R, White L (1978) Electrophoretic mobility of a spherical colloidal particle. J Chem Soc Faraday Trans 2 74:1607

50. Mangelsdorf C, White L (1990) Effects of stern-layer conductance on electrokinetic transport properties of colloidal particles. Faraday Trans 86(16):2859

51. van Wagenen R, Andrade J (1980) Flat plate streaming potential investigations: hydrodynamics and electrokinetic equivalency. J Colloid Interface Sci 76(2):305–314

52. Hayes R, Böhmer M, Fokkink L (1999) A study of silica nanoparticle adsorption using optical reflectometry and streaming potential techniques. Langmuir 15(8):2865–2870

53. Guinier A, Fournet G (1955) Small-angle scattering of X-rays. Wiley, New York

54. Glatter O (1977) A new method for the evaluation of small-angle scattering data. J Appl Crystallogr 10(5):415–421

55. McAlister B, Grady B (2002) The use of Monte-Carlo simulations to calculate small-angle scattering patterns. Macromol Symp 190(1):117–130

56. Blanchet C, Svergun D (2013) Small-angle X-Ray scattering on biological macromolecules and nanocomposites in solution. Annu Rev Phys Chem 64(1):37–54

57. Heunemann P, Prévost S, Grillo I, Marino C, Meyer J, Gradzielski M (2011) Formation and structure of slightly anionically charged nanoemulsions obtained by the phase inversion concentration (PIC) method. Soft Matter 7(12):5697

58. Jensen G, Lund R, Gummel J, Monkenbusch M, Narayanan T, Pedersen J (2013) Direct observation of the formation of surfactant micelles under nonisothermal conditions by synchrotron SAXS. J Am Chem Soc 135(19):7214–7222

59. Milani S, Baldelli Bombelli F, Pitek A, Dawson K, Rädler J (2012) Reversible versus irreversible binding of transferrin to polystyrene nanoparticles: soft and hard corona. ACS Nano 6(3):2532–2541

60. Jiang X, Weise S, Hafner M, Rocker C, Zhang F, Parak W, Nienhaus G (2009) Quantitative analysis of the protein corona on FePt nanoparticles formed by transferrin binding. J R Soc Interface 7(Suppl_1):S5

61. Dertinger T, Pacheco V, von der Hocht I, Hartmann R, Gregor I, Enderlein J (2007) Two-focus fluorescence correlation spectroscopy: a New tool for accurate and absolute diffusion measurements. Chemphyschem 8(3):433–443

62. Maffre P, Nienhaus K, Amin F, Parak W, Nienhaus G (2011) Characterization of protein adsorption onto FePt nanoparticles using dual-focus fluorescence correlation spectroscopy. Beilstein J Nanotechnol 2:374–383

63. Maas H, Gruen A, Papantoniou D (1993) Particle tracking velocimetry in three-dimensional flows. Exp Fluids 15(2):133–146

64. Treuel L, Malissek M, Gebauer J, Zellner R (2010) The influence of surface composition of nanoparticles on their interactions with serum albumin. Chemphyschem 11(14):3093–3099

65. Harris J, Roos C, Djalali R, Rheingans O, Maskos M, Schmidt M (1999) Application of the negative staining technique to both aqueous and organic solvent solutions of polymer particles. Micron 30(4):289–298

66. Feynman R, Leighton R, Sands M, Gottlieb M, Leighton R (2006) The Feynman lectures on physics. Pearson Addison-Wesley, San Francisco

67. Adrian M, Dubochet J, Lepault J, McDowall A (1984) Cryo-electron microscopy of viruses. Nature 308(5954):32–36

68. Mueller W, Koynov K, Fischer K, Hartmann S, Pierrat S, Basché T, Maskos M (2009) Hydrophobic shell loading of PB- b -PEO vesicles. Macromolecules 42(1):357–361

69. Milne J, Borgnia M, Bartesaghi A, Tran E, Earl L, Schauder D, Lengyel J, Pierson J, Patwardhan A, Subramaniam S (2013) Cryo-electron microscopy–a primer for the non-microscopist. FEBS J 280(1):28–45

70. Hamley I, Castelletto V, Fundin J, Yang Z, Crothers M, Attwood D, Talmon Y (2004) Cryo-TEM imaging of block copolymer micelles containing solubilized liquid crystal. Colloid Polym Sci 282(5):514–517
71. Shvartzman-Cohen R, Levi-Kalisman Y, Nativ-Roth E, Yerushalmi-Rozen R (2004) Generic approach for dispersing single-walled carbon nanotubes: the strength of a weak interaction. Langmuir 20(15):6085–6088
72. Binnig G, Quate C (1986) Atomic force microscope. Phys Rev Lett 56(9):930–933
73. Magonov S, Elings V, Whangbo M-H (1997) Phase imaging and stiffness in tapping-mode atomic force microscopy. Surf Sci 375(2–3):L385
74. Haeberle W, Pantea M, Hoerber J (2006) Nanometer-scale heat-conductivity measurements on biological samples. In: Proceedings of the seventh international conference on scanning probe microscopy, sensors and nanostructures 106(8–9):678–686
75. Berger R, Butt H-J, Retschke M, Weber S (2009) Electrical modes in scanning probe microscopy. Macromol Rapid Commun 30(14):1167–1178
76. Giessibl F (1995) Atomic resolution of the silicon (111)-(7x7) surface by atomic force microscopy. Science 267(5194):68–71
77. Jarvis S, Sader J, Fukuma T (2008) In: Bhushan B, Fuchs H, Tomitori M (eds) Applied scanning probe methods VIII. Springer, Berlin, Heidelberg
78. Gurevich L, Fojan P, Saxena R, Petersen S (2006) Mounting proteins on metal nanoparticles: statistical analysis of AFM images. 2006 NSTI Nanotechnology Conference and Trade Show, Boston, May 7–11, 2006. Nano Science and Technology Institute, Boston
79. MacCuspie R (2011) Colloidal stability of silver nanoparticles in biologically relevant conditions. J Nanopart Res 13(7):2893–2908
80. Butt H-J, Cappella B, Kappl M (2005) Force measurements with the atomic force microscope: technique, interpretation and applications. Surf Sci Rep 59(1–6):1–152
81. Pyrgiotakis G, Blattmann C, Pratsinis S, Demokritou P (2013) Nanoparticle–nanoparticle interactions in biological media by atomic force microscopy. Langmuir 29(36):11385–11395
82. Schaefer J, Schulze C, Marxer E, Schaefer U, Wohlleben W, Bakowsky U, Lehr C-M (2012) Atomic force microscopy and analytical ultracentrifugation for probing nanomaterial protein interactions. ACS Nano 6(6):4603–4614
83. Gildings J (1968) Nonequilibrium theory of field-flow fractionation. J Chem Phys 49(1):81–85
84. Giddings J (1993) Field-flow fractionation: analysis of macromolecular, colloidal, and particulate materials. Science 260(5113):1456–1465
85. Schimpf M, Caldwell K, Giddings J (2000) Field-flow fractionation handbook. Wiley-Interscience, New York, Chichester
86. Wahlund K, Giddings J (1987) Properties of an asymmetrical flow field-flow fractionation channel having one permeable wall. Anal Chem 59(9):1332–1339
87. Hovingh M, Thompson G, Giddings J (1970) Column parameters in thermal field-flow fractionation. Anal Chem 42(2):195–203
88. Giddings J (1973) The conceptual basis of field-flow fractionation. J Chem Educ 50(10):667
89. Davis J, Giddings J (1986) Feasibility study of dielectrical field-flow fractionation. Sep Sci Technol 21(9):969–989
90. Lang T, Eslahian K, Maskos M (2012) Ion effects in field-flow fractionation of aqueous colloidal polystyrene. Macromol Chem Phys 213(22):2353–2361
91. Andreev V, Stefanovich L (1993) Theory of field-flow fractionation with the reversible adsorption on channel walls. Chromatographia 37(5–6):325–328
92. Gigault J, Le Hécho I, Dubascoux S, Potin-Gautier M, Lespes G (2010) Single walled carbon nanotube length determination by asymmetrical-flow field-flow fractionation hyphenated to multi-angle laser-light scattering. J Chromatogr A 1217(50):7891–7897
93. Hagendorfer H, Kaegi R, Traber J, Mertens S, Scherrers R, Ludwig C, Ulrich A (2011) Application of an asymmetric flow field flow fractionation multi-detector approach for

metallic engineered nanoparticle characterization – prospects and limitations demonstrated on Au nanoparticles. Anal Chim Acta 706(2):367–378

94. Jungmann N, Schmidt M, Maskos M (2001) Characterization of polyorganosiloxane nanoparticles in aqueous dispersion by asymmetrical flow field-flow fractionation. Macromolecules 34(23):8347–8353

95. Rambaldi D, Reschiglian P, Zattoni A (2011) Flow field-flow fractionation: recent trends in protein analysis. Anal Bioanal Chem 399(4):1439–1447

96. Arfvidsson C, Wahlund K-G (2003) Time-minimized determination of ribosome and tRNA levels in bacterial cells using flow field–flow fractionation. Anal Biochem 313(1):76–85

97. Wittgren B, Wahlund K-G, Andersson M, Arfvidsson C (2002) Polysaccharide characterization by flow field-flow fractionation-multiangle light scattering: initial studies of modified starches. Int J Polym Anal Char 7(1–2):19–40

98. Li J, Zhong W (2008) A two-dimensional suspension array system by coupling field flow fractionation to flow cytometry. J Chromatogr A 1183(1–2):143–149

99. Ashby J, Schachermeyer S, Pan S, Zhong W (2013) Dissociation-based screening of nanoparticle–protein interaction via flow field-flow fractionation. Anal Chem 85(15):7494–7501

100. Runyon J, Goering A, Yong K-T, Williams S (2013) Preparation of narrow dispersity gold nanorods by asymmetrical flow field-flow fractionation and investigation of surface Plasmon resonance. Anal Chem 85(2):940–948

101. Rolland-Sabaté A, Mendez-Montealvo M, Colonna P, Planchot V (2008) Online determination of structural properties and observation of deviations from power law behavior. Biomacromolecules 9(7):1719–1730

102. Ehrhart J, Mingotaud A-F, Violleau F (2011) Asymmetrical flow field-flow fractionation with multi-angle light scattering and quasi elastic light scattering for characterization of poly (ethyleneglycol-b-ε-caprolactone) block copolymer self-assemblies used as drug carriers for photodynamic therapy. J Chromatogr A 1218(27):4249–4256

103. Schmidt B, Loeschner K, Hadrup N, Mortensen A, Sloth J, Bender Koch C, Larsen E (2011) Quantitative characterization of gold nanoparticles by field-flow fractionation coupled online with light scattering detection and inductively coupled plasma mass spectrometry. Anal Chem 83(7):2461–2468

104. Prestel H, Niessner R, Panne U (2006) Increasing the sensitivity of asymmetrical flow field-flow fractionation: slot outlet technique. Anal Chem 78(18):6664–6669

105. Knappe P, Boehmert L, Bienert R, Karmutzki S, Niemann B, Lampen A, Thünemann A (2011) Processing nanoparticles with A4F-SAXS for toxicological studies: iron oxide in cell-based assays. J Chromatogr A 1218(27):4160–4166

106. Maskos M, Schupp W (2003) Circular asymmetrical flow field-flow fractionation for the semipreparative separation of particles. Anal Chem 75(22):6105–6108

107. Grubisic Z, Rempp P, Benoit H (1967) A universal calibration for gel permeation chromatography. J Polym Sci B Polym Lett 5(9):753–759

108. Hagel L, Lundström H, Andersson T, Lindblom H (1989) Properties, in theory and practice, of novel gel filtration media for standard liquid chromatography. J Chromatogr A 476:329–344

109. Siebrands T, Giersig M, Mulvaney P, Fischer C (1993) Steric exclusion chromatography of nanometer-sized gold particles. Langmuir 9(9):2297–2300

110. Al-Somali A, Krueger K, Falkner J, Colvin V (2004) Recycling size exclusion chromatography for the analysis and separation of nanocrystalline gold. Anal Chem 76(19):5903–5910

111. Pinaud F, King D, Moore H-P, Weiss S (2004) Bioactivation and cell targeting of semiconductor CdSe/ZnS nanocrystals with phytochelatin-related peptides. J Am Chem Soc 126 (19):6115–6123

112. Sperling R, Liedl T, Duhr S, Kudera S, Zanella M, Lin C-A, Chang W, Braun D, Parak W (2007) Size determination of (Bio)conjugated water-soluble colloidal nanoparticles: a comparison of different techniques. J Phys Chem C 111(31):11552–11559

113. Wei G-T, Liu F-K, Wang C (1999) Shape separation of nanometer gold particles by size-exclusion chromatography. Anal Chem 71(11):2085–2091
114. Hanauer M, Pierrat S, Zins I, Lotz A, Sönnichsen C (2007) Separation of nanoparticles by gel electrophoresis according to size and shape. Nano Lett 7(9):2881–2885
115. Pellegrino T, Sperling R, Alivisatos A, Parak W (2007) Gel electrophoresis of gold-DNA nanoconjugates. J Biomed Biotech 2007
116. Shapiro A, Viñuela E, Maizel JV Jr (1967) Molecular weight estimation of polypeptide chains by electrophoresis in SDS-polyacrylamide gels. Biochem Biophys Res Commun 28 (5):815–820
117. Weber K, Osborn M (1969) The reliability of molecular weight determinations by dodecyl sulfate-polyacrylamide gel electrophoresis. J Bio Chem 244(16):4406–4412
118. Planken K, Cölfen H (2010) Analytical ultracentrifugation of colloids. Nanoscale 2(10):1849
119. Akbulut O, Mace C, Martinez R, Kumar A, Nie Z, Patton M, Whitesides G (2012) Separation of nanoparticles in aqueous multiphase systems through centrifugation. Nano Lett 12 (8):4060–4064
120. Schachman H (1959) Ultracentrifugation in biochemistry. Academic, New York
121. Liu J, Shire S (1999) Analytical ultracentrifugation in the pharmaceutical industry. J Pharm Sci 88(12):1237–1241
122. Scott D, Harding S, Rowe A (2005) Analytical ultracentrifugation. RSC, Cambridge
123. Domingos R, Baalousha M, Ju-Nam Y, Reid M, Tufenkji N, Lead J, Leppard G, Wilkinson K (2009) Characterizing manufactured nanoparticles in the environment: multimethod determination of particle sizes. Environ Sci Technol 43(19):7277–7284

Probing the Cytotoxicity of Nanoparticles: Experimental Pitfalls and Artifacts

**Jenny Domey, Lisa Haslauer, Ina Grau, Claudia Strobel,
Melanie Kettering, and Ingrid Hilger**

Abstract Throughout the last years, a huge variety of different nanoparticle formulations have been studied with the aim to assess their harmlessness in biological systems, to elucidate how the morphological features govern their impact on cells, and to develop cell labeling strategies for biomedical purposes. Most of such studies are based on the use of various cell viability assays. Interestingly, different results – even contradictory ones – have been observed between the groups, even though the respective nanoparticle formulations were more or less similar. One possible reason for such discrepancies is the occurrence of specific interactions between the nanoparticles and the ingredients of the respective cell viability assays. A similar situation can be encountered when researchers investigate the labeling of (stem) cells for biomedical purposes. Hereto, different labeling efficiencies were observed with the corresponding effects on cell viability and functionality. Therefore, the present review focuses on potential pitfalls and artifacts associated with the cytotoxicity evaluation of nanomaterials.

Keywords ATP · Cell viability assays · Iron oxide · MTS · MTT · Nanomaterials · Nanoparticles · Toxicity

J. Domey, L. Haslauer, I. Grau, C. Strobel and M. Kettering
Institut für Diagnostische und Interventionelle Radiologie I des Klinikums der Friederich-Schiller-Universität Jena, Bachstraße 18, D-07740 Jena, Germany

I. Hilger (✉)
Institut für Diagnostische und Interventionelle Radiologie I des Klinikums der Friederich-Schiller-Universität Jena, Bachstraße 18, D-07740 Jena, Germany

Institut für Diagnostische und Interventionelle Radiologie I des Klinikum der Friedrich-Schiller-Universität Jena, Forschungszentrum Lobeda, Erlanger Allee 101, D-07747 Jena, Germany
e-mail: ingrid.hilger@med.uni-jena.de

Contents

1   Introduction

Nanotechnology has emerged as a promising tool in different branches of science. Investigators are keen to understand the physicochemical properties of nanoscale materials (<100 nm) as a function of their size, shape, surface chemistry, and chemical composition. In the last years, extensive work has been done to elucidate the interactions between differently designed nanomaterials and biological systems. The main aim is to assess the impact of nanoparticle exposure or to identify potential applications in future medicine. In this context, different nanomaterial formulations have been exposed to different cell types, organisms (bacteria), tissues, and animals. As a result, scientists became aware of the complexity of these interactions. Particularly if injected into the blood stream, the adsorption of serum proteins on the nanoparticles' surface [1] is a determining factor governing their fate in the body and the uptake of nanoparticles by the respective target cells.

When analyzing the bio-pathological effects on cells, one of the first processes to consider is nanoparticle adsorption on the cell surface and internalization. Hereto, the nanoparticles' shape seems to be important. In this regard, rods were shown to induce maximum uptake, followed by spherical, cylindrical (more symmetrical than rods), and cubic nanoparticles; this is true for nanoparticles larger than 100 nm [2]. With decreasing size (smaller than 100 nm) spheres are better internalized than rods [3]. The aspect ratio and the composition of the nanoparticles [4] influence the degree of nanoparticle uptake as well. Besides uptake as well as electrostatic interactions, the intracellular degradation processes, which are largely dependent on the composition of the nanomaterial, influence their impact on cell viability. To test cell viability after nanoparticle exposure, different assay systems addressing specific metabolic pathways of the cell have been extensively used for screening purposes with more or less diverging results. The underlying reasons are rather complex and not well understood. A set of examples for the biological impact of specific nanomaterials and the problems associated with their experimental investigation will be detailed below.

Due to their good biocompatibility, iron oxide nanoparticles have been proposed in particular for a great variety of applications in medicine and biology. Examples are their use for cell separation procedures in life-science research or the labeling of stem cells in order to allow for an accurate monitoring of their migration via

magnetic resonance imaging (MRT). One important prerequisite for both applications is that the cells must retain their viability and functionality during these experimental manipulations.

This review focuses on the different aspects which are to be considered when cell viability assays are used to assess the cytotoxicity of nanoparticles and on the potential pitfalls which should be taken into account when cells are labeled with magnetic nanoparticles.

2 Validity of Cell Viability Assays

A huge variety of different cell viability assays have been developed to assess the impact of xenobiotics on cells. One very simple approach is the use of the dye trypan blue. It is a diazo dye which selectively stains dead cells. The dye is unable to pass the cell membrane of viable cells but enters the cytoplasm of dead cells with compromised membranes. The staining method has been described as "dye exclusion method," since it excludes live cells from staining. After staining, live cells are counted using a microscope. In a similar manner, the dye Evans blue has been used in cell viability assays.

Other assay systems address specific metabolic pathways in the cell. For example, the cellular membrane integrity can be assessed by determining the release of lactate dehydrogenase into the culture medium. The enzyme lactate dehydrogenase is normally localized in the cytosol and is consequently sequestered inside viable cells. A release occurs in damaged cells only. Advantages of this assay are fast performance and simple evaluation [5]. However, nanoparticle incubation is limited to low concentrations of serum proteins, since fetal serum contains distinct amounts of lactate dehydrogenase itself, which might lead to false-positive results. Low serum protein concentrations on the other hand might not mimic the in vivo situation appropriately, particularly when assessing the cytotoxic response of blood cells.

Another possibility is to determine the viability of a cell population via the so-called MTS assay. It is based on the reduction of a methyl tetrazolium salt (MTS: [3-(4,5-dimethylthiazol-2-yl)-5-(3-carboxy-methoxyphenyl)-2-(4-sulfophenyl)-2H-tetrazolium, inner salt]) to a water-soluble formazan product in presence of a corresponding amount of the redox coenzymes NADH/NADPH and endogenous dehydrogenases. The amount of converted tetrazolium salt is quantified photometrically (absorbance at 490 nm) and correlates with the number of living cells in the respective culture system [6]. Apart from the MTS, other tetrazolium salts have been proposed for cell viability studies, such as XTT (2,3-bis-(2-methoxy-4-nitro-5-sulfophenyl)-2H-tetrazolium-5-carboxanilide), WSTs (water-soluble tetrazolium salts, e.g., WST-1, WST-8), and MTT (3-(4,5-dimethylthiazol-2-yl)-2,5-diphenyl-tetrazolium bromide); MTT was the first compound that was introduced for dehydrogenase-based cell viability assessments and still required an additional solubilization step. Basically, all tetrazolium salt-based cell viability assays measure glycolytic activity. To exclude false-negative readouts particularly when testing viable but metabolically inactive cells, it is important to include untreated controls.

Alternatively, cell viability can be measured by the assessment of cellular ATP levels. This is accomplished by the so-called ATP assay, a luminescence assay system, which measures the metabolic activity of cells via the enzymatic transformation of D-luciferin and intracellular ATP to oxiluciferin and light.

A further endpoint assay to probe cell viability is the assessment of thymidine incorporation during DNA replication. This test system directly measures cell proliferation. When cell density allows for cell proliferation, it can also be used for viability assessments of cells with a short G1-phase as it is particularly the case for permanent cell lines. Experimentally, a specific thymidine analogue like EdU (5-ethinyl-2-deoxyuridine) is added to the culture medium and gets incorporated into newly synthesized DNA. Analysis is performed by a click labeling reaction of the incorporated EdU with a reagent containing copper and Oregon Green® 488 azide. For signal amplification, an anti-Oregon Green® antibody conjugated to the enzyme horseradish peroxidase (HRP) is used which then reacts with a specific substrate and produces a fluorescent product.

Recently, critical debates on the reliability of these testing systems especially for the MTS or MTT assay have been reported [7–10]. According to these reports, the in vitro cytotoxicity assays based on intracellular enzymatic conversions are prone to overestimate cell viability when they are incubated with certain nanoparticle formulations. One example is the exposure of rat gliosarcoma cells (9 L/lacZ) or murine macrophages (J774A.1) to carboxymethyl dextran-coated, clustered magnetic (iron oxide) nanoparticles as shown in Fig. 1. Even though care has been taken (e.g., by the incorporation of multiple washing steps or the separation of supernatant from cells) to prevent light absorbance due to the presence of nanoparticles in the sample, an overestimation of the cell viability using the MTS assay compared to the ATP assay is evident (Fig. 1). This overestimation of cell viability leads to erroneous EC_{50} values (Table 1) and is attributed to the interference of the nanoparticles with ingredients of the MTS assay resulting in artificially higher dehydrogenase activities. Interestingly, it has been shown that mesoporous silica nanoparticles can accelerate the exocytosis of formazan crystals after the particles have been taken up by HeLa cells and astrocytes. The authors attribute this effect to the perturbation of intracellular vesicle trafficking as a result of the nanoparticle uptake [11]. Similar relationships have already been observed for other chemicals as well: Hoskins et al. hypothesize that the false increase of cell viability as measured by MTS might be due to changes in redox metabolism as a response to the presence (uptake) of nanoparticles [8].

With respect to cell culture conditions, it is also well conceivable that the presence of aggregated magnetic nanoparticles on cells (Fig. 2) can bias the status of cell viability, particularly if colorimetric methods based on the light absorbance of enzymatic products are used (e.g., MTS test). It is rather challenging to control nanoparticle-mediated absorbance, since nanoparticles are mostly very prone to adhere to the cell culture ware or they get internalized in cells. Thus, subtraction of the "nanoparticle blank values" (in absence of cells) from those values recorded for cells incubated with nanoparticles would not entirely heal the effect of overestimation. Moreover, the overestimation of cell viability assessed via MTS
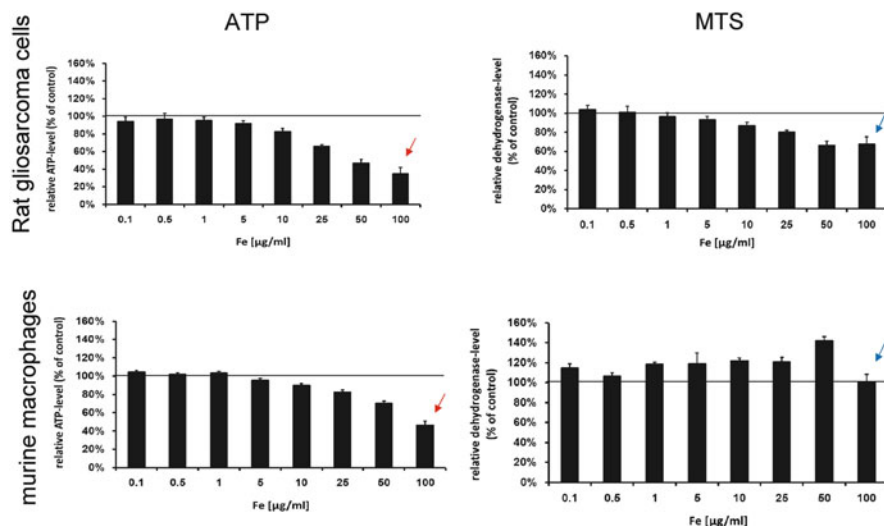
Fig. 1 Impact of nanoparticle exposure depends on the cell type and on the cell viability assay used. Relative ATP level (*left*) and dehydrogenase level (*right*) of rat gliosarcoma cells (9 L/lacZ, *top*) and murine macrophages (J774A.1, *bottom*) after exposure to carboxymethyl dextran-coated iron oxide nanoparticles for 24 h. The cellular ATP and dehydrogenase levels were normalized to the respective levels of untreated control cells (100%). According to DIN EN ISO 10993–5 a nanomaterial can be considered as toxic when cell viability drops below 70% (*dark line*). *Red arrows* indicate the loss of cell viability after nanoparticle incubation (100 µg/mL) which was determined by using a luminescent ATP assay for both cell lines. In contrast to that, *blue arrows* indicate only a slight loss in cell viability for rat gliosarcoma cells and constant cell viability for murine macrophages which is measured by the MTS assay

Table 1 MTS and ATP assays produce different values for the effective concentration EC_{50} of iron oxide nanoparticles in contact to murine macrophages and rat gliosarcoma cells

Incubation time	Murine macrophages		Rat gliosarcoma cells	
	MTS	ATP	MTS	ATP
24 h	>100*	86	>100*	>100*
48 h	>100*	92	>100*	58

Rat glioblastoma cells (9 L/lacZ) and murine macrophages (J774A.1) were incubated with nanoparticles for 24 and 48 h. EC-50 concentrations as given in the table (in µg/mL) were calculated from data of both assays. >100* = the effective dose is higher than the highest nanoparticle concentration under test (100 µg/mL)

can differ in dependence on the cell line under study. For example, as shown in Fig. 1, overestimation was more pronounced for macrophages than for glioblastoma cells. This observation can be attributed to the fact that the first provide much more intercellular spaces for nanoparticles to hide than the latter. Hence, this would mean that the confluency status of the respective cell population at the time of nanoparticle exposure might also influence the outcome of cell viability assays.
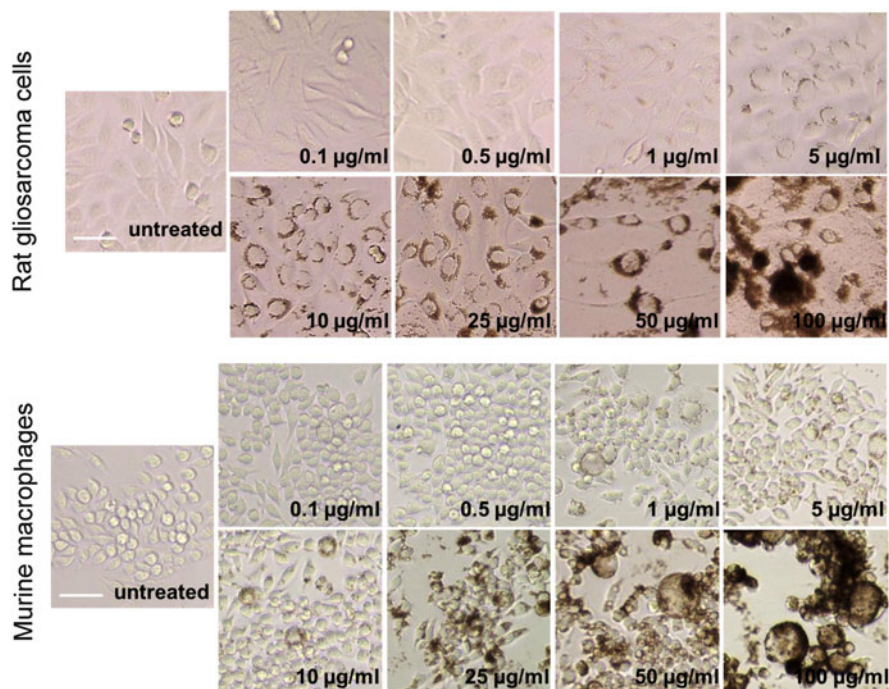
Fig. 2 Aggregation of iron oxide nanoparticles on the cell surface leads to opaque areas which are usually not removed by washing. Rat gliosarcoma (9 L/lacZ) cells and murine macrophages (J7747A.1) were incubated with carboxymethyl dextran iron oxide nanoparticles and examined via light microscopy (scale bar 50 µm)

In contrast, when using the ATP assay after exposure of the cells to iron oxide nanoparticles, a consistent decrease of viability can be observed with increasing particle concentrations. This effect applies for the two cell lines under investigation (glioblastoma cells and murine macrophages, Fig. 1), demonstrating that the cyto-toxic effect is not cell line dependent. This finding does not corroborate with the data gained with the MTS assay under identical experimental conditions (cell lines, nanoparticle concentrations, incubation times; Fig. 1) for the reasons described above. The observations are in agreement with the findings of other authors when data derived from assays based on cellular ATP are closest to the data that were gathered by counting viable cells (Fig. 3) or trypan blue exclusion [2, 3]. Since the ATP assay system measures luminescence, there is no interference with the parti-cles' intrinsic light absorbance, which is particularly influential in the case of iron oxide nanoparticles. If the nanoparticles to be tested emit light by themselves (e.g., due to functionalization with fluorescent dyes for microscopy studies), potential interferences with luminescence from the assay system should be assessed using appropriate controls.
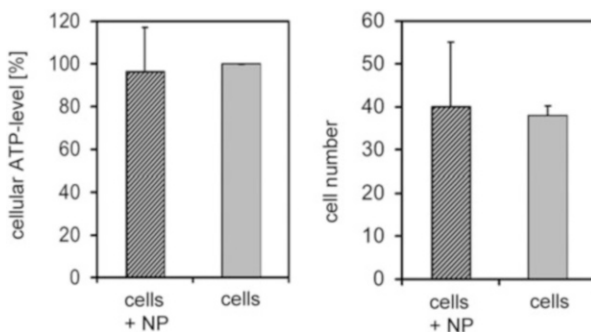
Fig. 3 Comparison of Au@Fe$_3$O$_4$ nanoparticle impact on cellular ATP levels and the number of viable cells after exposure. Human microvascular endothelial cells (HMEC-1) were incubated with ("cells+NP") or without ("cells") Au@Fe$_3$O$_4$ nanoparticles (50 µg/mL Fe (II)/(III)) for 24 h. Cellular ATP values were normalized to control values (no particle exposure, native cells), which were set as 100%. Number of viable cells per section is determined via microscopy (nonviable cells were removed by washing). *NP*, nanoparticles

Interestingly, it was found that certain carbon nanotube formulations are able to convert MTT into its MTT-formazan-insoluble form in the absence of any living organism. For example, polyoxyethylene sorbitan mono oleate-suspended carbon nanotubes (SWCNTs) interfere less with an MTT assay than sodium dodecyl sulfate-suspended ones [12]. Therefore, it is imperative to carefully validate cytotoxicity assays to ensure correct experimental data.

Specific interactions between nanoparticles and certain ingredients of cell viability assays are more likely to occur for some nanoparticle formulations than for others. In this context, SWCNTs appear to interact with some tetrazolium salts such as MTT but not with WST-1 or XTT. These effects are related to the insoluble nature of the MTT-formazan rather than the enzymatic reaction [13]. Particularly multi-walled carbon nanotubes may bind to the insoluble formazan product and prevent its re-solubilization [14]. Conflicting results were observed with several different assays such as neutral red, MTT, or cytokine IL-8 release when assessing carbon nanomaterial cytotoxicity in epidermal cell culture systems [15]. Up to now, there are only hypotheses about the reasons for these different interactions which merit further studies.

Another example of conflicting results is the outcome of the ATP assay reading cellular ATP levels when it is compared to the so-called EdU-incorporation assay after exposure of cells to Au@Fe$_2$O$_3$ Janus particles (Fig. 4). Specific reactions between the assay components and the nanoparticles are easily controlled by exposing the nanoparticles alone (without the presence of cells) to the reagents of the assay system. As shown in Fig. 4, no interactions of the nanoparticles with the components of the ATP assay can be detected, indicating that the decrease of cell viability in the presence of particles is reliable. In contrast, when applying the EdU-incorporation assay, distinct fluorescence signals can be detected in the presence of nanoparticles without cells. The explanation is as follows: EdU
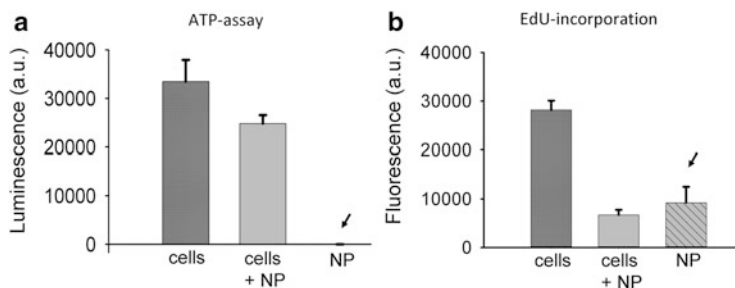
Fig. 4 Outcome of ATP and a thymidine incorporation assays on human endothelial cells after incubation with Au@Fe$_3$O$_4$ nanoparticles. Assay ingredients were incubated with HMEC-1 cells only ("cells"), or with cells and magnetic nanoparticles ("cells+NP", 50 μg/mL Fe(II)/(III)), or nanoparticles only (NP). (**a**) Luminescence-based ATP assay. (**b**) Thymidine incorporation assay using the analogue EdU. For analysis, a fluorescent substrate is attached to the incorporated uridine. Luminescence and fluorescence are given in arbitrary units. *NP*, nanoparticles

detection (EdU incorporated into DNA) is based on a click reaction, which is a copper-catalyzed covalent reaction between an azide and an alkyne (see also above). Copper is likely to undergo redox reactions with iron from the iron oxide based nanoparticles, particularly if the shielding of the metallic core by the particle shell is not appropriate [16]. From this observation one can conclude that cell viability assays based on redox reactions can only be performed with (metallic) nanoparticles as long as they are covered by an intact surface shielding.

A similar effect can be found when analyzing the effects of CeO$_2$ nanoparticles on cells. The differences of the readouts "cellular ATP" and "cellular dehydrogenase activity" as shown in Fig. 5 can be attributed, at least partially, to the adsorption of insoluble formazan products on the CeO$_2$ nanoparticles with increasing time of incubation. Consequently the cell viability will rather be underestimated. This is in agreement with the observations on carbon nanotubes described above.

Irrespective of the readout used in cell viability assessment, one has to keep in mind that validity of such assays is confined to the in vitro situation only. Direct toxicity extrapolations to the in vivo situation should be undertaken with great care, since (1) nanomaterials are mostly applied in nonphysiologically high concentrations in in vitro experiments; (2) the outcome represents mostly the response of one cell system (exception: co-culture systems), whereas a complex interaction between different cell types takes place in an in vivo environment; (3) the absence of an immune system in vitro; (4) numerous investigators use serum-free media to prevent nanoparticle agglomeration in vitro, a situation which is never encountered in vivo; and (5) in the case of complete culture medium, opsonization processes in presence of fetal calf serum do not necessarily represent the situation in humans.

Those studies that report on interferences of nanoparticles with cell viability assays clearly implicate the necessity of standardizing these assays and of including the correct controls. There is also a strong need for reference materials. Additionally, the experience and knowledge gained so far strongly indicates that more than one readout parameter should be considered when the biological response to
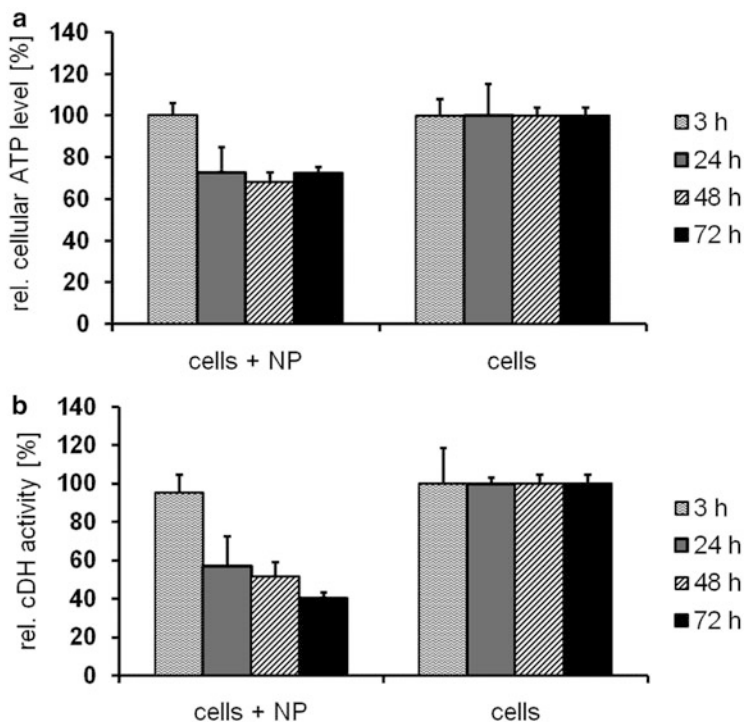
Fig. 5 Outcome ATP and MTS assay for human endothelial cells after incubation with CeO_2 nanoparticles. HMEC-1 were incubated with 100 µg/mL (size: 40 nm) CeO_2 nanoparticles for 3–72 h. (**a**) ATP assay, (**b**) MTS assay. NP, nanoparticles

nanomaterials is studied. Particularly helpful and informative are viability assays in combination with assays probing other biological markers of cellular physiology, such as cytoskeleton integrity or the occurrence of reactive oxygen species (ROS) in order to be able to draw adequate conclusions and exclude potential methodological biases. In this context, a very detailed particle characterization including hydrodynamic diameter, polydispersity index, zeta potential, and serum protein opsonization properties is extremely valuable and necessary for accurate data analysis.

3 Effects of Nanoparticle Labeling Processes on Cells

One of the most prominent manipulations of cells using nanoparticles is cell labeling for various biomedical purposes. In biomedical research, specific labeling of cells has been applied frequently to select distinct subpopulations with defined surface expression patterns. For instance, cells are incubated with target-affine and selectively functionalized magnetic particles based on iron oxide.

Labeled cells can be separated selectively from a mixed population by applying magnetic columns which retain labeled cells in the presence of a magnetic field. Elution can easily be performed by removal of the column from the magnetic field.

Another concept is the labeling of stem cells with the aim of monitoring their delivery and migration to target organs that are affected by a specific disease via MR imaging. It is a prerequisite for this approach that those cells retain their normal viability, functionality, and capability of migration during labeling. The labeling of stem cells is mainly based on the cellular mechanisms of endocytosis [17], depending in a complex manner on size, shape, surface charge, and chemistry of the nanoparticles, as well as on the cell type. Additionally, several strategies have been proposed to enhance cellular uptake, such as the use of commercial transfection reagents and nanoparticle functionalization with cell membrane translocating peptides. These strategies have been nicely summarized by Neoh and Kang [18] and Berman et al. [19] among others.

In the literature, different labeling efficiencies have been reported so far. For example, mesenchymal and hematopoietic stem cells are labeled with carboxyldextran-coated nanoparticles up to 8.3pg Fe(II)/(III)/cell [20] or just up to 2.6pg Fe(II)/(III)/cell [21], respectively. In contrast epithelial liver carcinoma cells incubated with carboxymethyl dextran nanoparticles have internalized 110pg Fe/cell [22], while lung carcinoma cells took up 202pg Fe(II)/(III)/cell after exposure to aminosilane nanoparticles [23].

These differences in labeling efficiency might be due to the individual uptake activities of cells but also, at least partially, due to methodological artifacts. One challenge is the fact that discrimination between NPs on the surface of the cell and those which have been already internalized is experimentally hard to achieve. We have observed that after incubation of cells with starch-coated iron oxide nanoparticles and subsequent separation of labeled cells from non-labeled ones with the help of a magnetic column, the amount of iron per cell distinctly drops after magnetic separation (Fig. 6). Interestingly, the effect did not depend on whether the cells were labeled by nanoparticle sedimentation compared to magnetic field (83 mT)-mediated nanoparticle encounter. The effect is more striking when cells are exposed to particularly high iron oxide nanoparticle concentrations. The underlying reason for this observation is the presence of nanoparticle aggregates on the cell surface which obviously can be removed during magnetic separation using a magnetic column but not via the regular washing steps with buffer during the labeling procedure per se. Therefore, in vitro labeling of cells should be performed with reasonable nanoparticle concentrations in order to avoid excess of nanoparticle association on the cell surface which affects the labeling efficiency.

We could show that the use of magnetic delivery of NPs and magnetic separation of cells do not alter the intracellular compartmentalization of magnetic nanoparticles. In this context, iron oxide nanoparticles were found to be localized in the endosomes and secondary lysosomes in accordance to other reported studies [24–26].
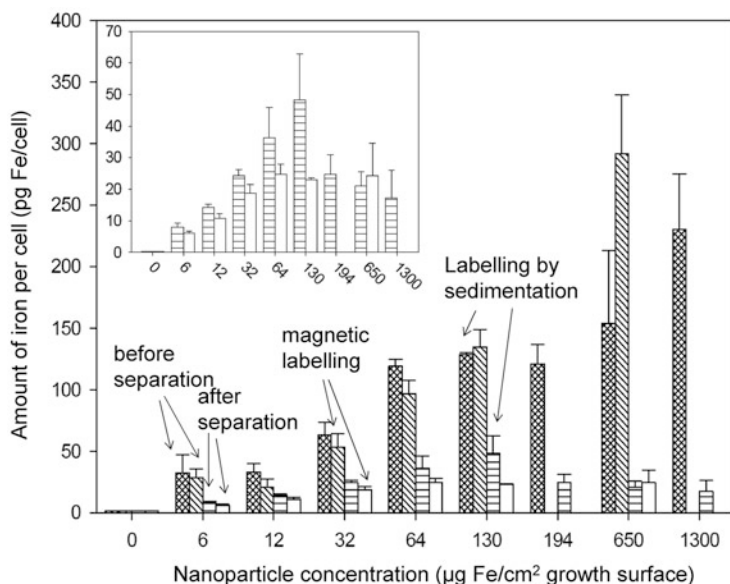
Fig. 6 The labeling efficiency of human adenocarcinoma cells decreases distinctly after separation using magnetic columns. BT-474 cells were exposed for 24 h to iron oxide nanoparticles (up to 1300 μg Fe(II)/(III)/cm^2 growth surface) without (labeling by sedimentation) or in the presence of a 83 mT magnet (magnetic labeling). After washing off unbound nanoparticles, cells were harvested. Labeled cells were separated from non-labeled ones using a magnetic column. Inset: magnified presentation of data obtained after magnetic separation of labeled cells

Extensive studies have already proven a good biocompatibility of iron nanoparticles. The viability of epithelial liver carcinoma cells (110pg Fe(II)/(III)/cell) or human colon carcinoma cells (7pg Fe(II)/(III)/cell) was 95% of non-treated controls [22, 27] after intracellular NP delivery. Similar results were found for mesenchymal (8.3pg Fe(II)/(III)/cell) or hematopoietic stem cells (2.6pg Fe(II)/(III)/cell) [21]. Nevertheless, labeled cell populations exposed to magnetic separation can experience a drop of their viability as shown in Fig. 7. The drop in viability is particularly visible for labeled cells but independent on the strategy of cell labeling (magnetic delivery compared to sedimentation). Such effects could arise from specific interactions of the cell membrane with the filling material of the columns or the applied shear stress [28].

Even though iron oxide nanoparticles are considered to be of no harm in terms of viability and functionality of stem cells, in several cases an inhibition of chondrogenesis [29, 30], a decrease in migration capacity, colony formation ability [31], and inhibition of osteogenic differentiation [32] were observed. Accordingly, specific manipulation procedures necessary for cell labeling require an adequate postlabeling analysis to ensure cell viability and functionality after the nanoparticles are attached to their target.
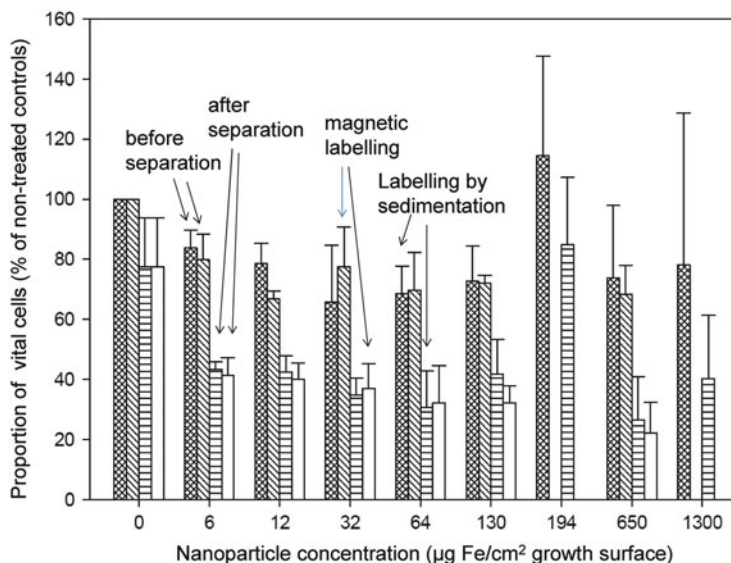
Fig. 7 Impact of cell labeling on the viability of human adenocarcinoma cells. BT-474 cells were exposed for 24 h to iron oxide nanoparticles (up to 1300 μg Fe(II)/(III)/cm^2 growth surface) without ("labeling by sedimentation") or in the presence of an 83 mT magnet ("magnetic labeling"). After removing unbound nanoparticle cells were harvested. Labeled cells were separated from non-labeled ones using a magnetic column. After elution from the column, labeled cells were seeded again on a cell culture plastic matrix and were assessed for cell viability

4 Conclusion

In conclusion, experimental data from different research groups have shown that specific interactions between nanomaterials and ingredients of cell viability assays can lead to distinct over- or underestimations of cytotoxicity. This data suggests that there is a need to undertake multiple different assays in parallel with appropriate controls and the respective nanomaterials should be adequately characterized in terms of their morphology and chemical composition. Additionally, the limitations of extrapolations to the in vivo situation should be taken into account. With respect to labeling of cells for biomedical applications, reasonable nanoparticle concentrations should avoid overestimation of labeling efficiency due to the formation of large nanoparticle aggregates on the cell surface. The retention and elution of labeled cells from magnetic columns is prone to affect viability of cells. These artifacts exemplify potential pitfalls which could hinder the progress of biomedical applications of nanomaterials in the future.

References

1. Tenzer S et al (2011) Nanoparticle size is a critical physicochemical determinant of the human blood plasma corona: a comprehensive quantitative proteomic analysis. ACS Nano 5 (9):7155–7167
2. Gratton SEA et al (2008) The effect of particle design on cellular internalization pathways. Proc Natl Acad Sci U S A 105(33):11613–11618
3. Chithrani BD, Ghazani AA, Chan WCW (2006) Determining the size and shape dependence of gold nanoparticle uptake into mammalian cells. Nano Lett 6(4):662–668
4. Wang J et al (2010) The complex role of multivalency in nanoparticles targeting the transferrin receptor for cancer therapies. J Am Chem Soc 132(32):11306–11313
5. Decker T, Lohmann-Matthes ML (1988) A quick and simple method for the quantitation of lactate dehydrogenase release in measurements of cellular cytotoxicity and tumor necrosis factor (TNF) activity. J Immunol Methods 115(1):61–69
6. Buttke TM, McCubrey JA, Owen TC (1993) Use of an aqueous soluble tetrazolium formazan assay to measure viability and proliferation of lymphokine-dependent cell-lines. J Immunol Methods 157(1–2):233–240
7. Hong SC et al (2011) Subtle cytotoxicity and genotoxicity differences in superparamagnetic iron oxide nanoparticles coated with various functional groups. Int J Nanomedicine 6:3219–3231
8. Hoskins C et al (2012) Dilemmas in the reliable estimation of the in-vitro cell viability in magnetic nanoparticle engineering: which tests and what protocols? Nanoscale Res Lett 7:1–12
9. Wang PW, Henning SM, Heber D (2010) Limitations of MTT and MTS-based assays for measurement of antiproliferative activity of green tea polyphenols. PLoS One 5(4)
10. Monteiro-Riviere NA, Inman AO, Zhang LW (2009) Limitations and relative utility of screening assays to assess engineered nanoparticle toxicity in a human cell line. Toxicol Appl Pharmacol 234(2):222–235
11. Fisichella M et al (2009) Mesoporous silica nanoparticles enhance MTT formazan exocytosis in HeLa cells and astrocytes. Toxicol In Vitro 23(4):697–703
12. Belyanskaya L et al (2007) The reliability and limits of the MTT reduction assay for carbon nanotubes-cell interaction. Carbon 45(13):2643–2648
13. Worle-Knirsch JM, Pulskamp K, Krug HF (2006) Oops they did it again! Carbon nanotubes hoax scientists in viability assays. Nano Lett 6(6):1261–1268
14. Cheng C et al (2009) Toxicity and imaging of multi-walled carbon nanotubes in human macrophage cells. Biomaterials 30(25):4152–4160
15. Monteiro-Riviere NA, Inman AO (2006) Challenges for assessing carbon nanomaterial toxicity to the skin. Carbon 44(6):1070–1078
16. Gao LZ et al (2007) Intrinsic peroxidase-like activity of ferromagnetic nanoparticles. Nat Nanotechnol 2(9):577–583
17. Conner S, Schmid S (2003) Regulated portals of entry into the cell. Nature 422:37–44
18. Neoh KG, Kang ET (2012) Surface modification of magnetic nanoparticles for stem cell labeling. Roy Soc Chem 8:2057–2069
19. Berman SM, Walczak P, Bulte JWM (2011) Tracking stem cells using magnetic nanoparticles. Wiley Interdiscip Rev Nanomed Nanobiotechnol 3(4):343–355

20. Ittrich H et al (2007) In vivo magnetic resonance imaging of iron oxide-labeled, arterially injected mesenchymal stem cells in kidneys of rats with acute ischemic kidney injury: detection and monitoring at 3T. J Magn Reson Imaging 25(6):1179–1191
21. Daldrup-Link HE et al (2005) Hematopoietic progenitor cells from umbilical cord blood and from peripheral blood for subsequent in vivo tracking in a xenotransplant mouse model XXX. Acad Radiol 12(4):502–510
22. Sun R et al (2005) Physical and biological characterization of superparamagnetic iron oxide- and ultrasmall superparamagnetic iron oxide-labeled cells – a comparison. Invest Radiol 40 (8):504–513
23. Ma YJ, Gu HC (2007) Study on the endocytosis and the internalization mechanism of aminosilane-coated Fe_3O_4 nanoparticles in vitro. J Mater Sci Mater Med 18(11):2145–2149
24. Kettering M et al (2007) Magnetic nanoparticles as bimodal tools in magnetically induced labelling and magnetic heating of tumour cells: an in vitro study. Nanotechnology 18:175101
25. Jordan A et al (1999) Endocytosis of dextran and silan-coated magnetite nanoparticles and the effect of intracellular hyperthermia on human mammary carcinoma cells in vitro. J Magn Magn Mater 194(1–3):185–196
26. Daldrup-Link HE et al (2003) Targeting of hematopoietic progenitor cells with MR contrast agents. Radiology 228(3):760–767
27. Pinkernelle J et al (2005) Imaging of single human carcinoma cells in vitro using a clinical whole-body magnetic resonance scanner at 3.0T. Magn Reson Med 53(5):1187–1192
28. Seidl J, Knuechel R, Kunz-Schughart LA (1999) Evaluation of membrane physiology following fluorescence activated or magnetic cell separation. Cytometry 36(2):102–111
29. Kostura L et al (2004) Feridex labeling of mesenchymal stem cells inhibits chondrogenesis but not adipogenesis or osteogenesis. NMR Biomed 17(7):513–517
30. Bult JWM et al (2004) Chondrogenic differentiation of mesenchymal stem cells is inhibited after magnetic labeling with ferumoxides. Blood 104(10):3410–3412
31. Schafer R et al (2009) Labeling of human mesenchymal stromal cells with superparamagnetic iron oxide leads to a decrease in migration capacity and colony formation ability. Cytotherapy 11(1):68–78
32. Chen YC et al (2010) The inhibitory effect of superparamagnetic iron oxide nanoparticle (Ferucarbotran) on osteogenic differentiation and its signaling mechanism in human mesenchymal stem cells. Toxicol Appl Pharmacol 245(2):272–279

Monitoring the Impact of Nanomaterials on Animal Cells by Impedance Analysis: A Noninvasive, Label-Free, and Multimodal Approach

Michaela Sperber, Christina Hupf, Michael-M. Lemberger, Barbara Goricnik, Nadja Hinterreiter, Sonja Lukic, Maximilian Oberleitner, Judith A. Stolwijk, and Joachim Wegener

Abstract Experimental assays based on living cells have emerged to an indispensable tool in the life sciences as a compromise between animal experiments and purely molecular interactions analysis. Label-free monitoring of such assays is rather new and its technical progress has been driven by the accumulating evidence that the molecular constituents of label-based approaches might manipulate the assay cells or their readout might be affected by the compound being tested in the assay. This has been particularly evident in the field of nanotoxicology as many nanomaterials are luminescent or redox active or they inhibit the activity of enzymes that are used to analyze the cell response. Among the established label-free techniques to monitor cell-based assays, impedance analysis is the farthest developed with respect to the available assay formats, throughput, and information content of the raw data. This chapter will summarize the general principles of impedimetric cell monitoring, introduce the available assay formats, and show how these have been applied to unravel the biological response of nanoscale particles on different levels of cell physiology. The description and interpretation of impedimetric assays will be embedded in a thorough discussion on the pros and cons of label-free versus label-based monitoring of animal cells in biomedical assays.

M. Sperber, C. Hupf, M.-M. Lemberger, B. Goricnik, N. Hinterreiter, S. Lukic, M. Oberleitner, J.A. Stolwijk, and J. Wegener (✉)
Institut fuer Analytische Chemie, Chemo- and Biosensorik, Universitaet Regensburg, Regensburg, Germany
e-mail: Joachim.Wegener@ur.de

Contents

1   Cell-Based Assays in Bioanalysis: Relevance, Requirements, and Restrictions

Throughout the last decades elaborate experimental techniques to isolate and culture mammalian cells in vitro have been developed and continuously improved so that cell cultures from almost any mammalian tissue are available today for experiments ex vivo (i.e., in vitro). This development has been originally motivated by the perspective to study one particular cell type apart from the complexity of an entire organism under well-defined laboratory conditions [1, 2]. Understanding fundamental cellular physiology on a molecular level often requires this in vitro environment as an unconditional prerequisite to apply the powerful approaches of molecular bioanalysis [3]. But cultured cells are not just simplified study objects to understand the molecular mechanisms of life, they also serve as valuable tools in bioanalysis when used as sensory elements in cell-based assays (CBAs). In CBAs the cells are exposed to a chemical, biological, or physical challenge along a well-defined protocol, and the response of the cells to this challenge is used as a *biomarker*. When the cell type, the assay protocol, and the readout approach, which is used to quantify the cell response, are properly selected, CBAs provide a first and valuable estimate for the corresponding tissue response within the living organism. In this sense, CBAs are considered to be an intermediate between complex testing in living animals and simple, binary, or ternary molecular assay systems. Compared to animal testing, cell-based assays (CBAs) provide a

significantly improved reproducibility and much more control over the experimental conditions. But CBAs will never be capable of replacing in vivo experiments entirely as they cannot mimic the systemic interplay between the various organs and tissues of a multicellular organism including organ-specific metabolization. However, the latter may contribute significantly to a compound cytotoxic profile, bioactivity, or bioavailability.

Besides the scientific arguments for cells as useful model systems with reduced complexity, the sheer number of tests required by legislature or professional compound screening campaigns makes an alternative to animal testing mandatory for ethical, economic, and practical reasons. Compound libraries, which are regularly screened in pharmaceutical research for biological activity, easily contain more than 10^6 different drug candidates that need to be tested. Here, living cells derived from the target organ have become indispensable test objects to scan these huge libraries with sufficient throughput and at acceptable cost [4, 5]. Nowadays CBAs are not only applied in initial screening, they also contribute increasingly to the subsequent compound profiling (lead optimization) and the establishment of structure-activity relationships. They are an accepted strategy to reduce animal experiments in drug development to a minimum and confine them to later stages within this process.

Monitoring the specific activities of drug candidates is one major application of cell-based assays. Moreover, they are enormously valuable to identify unspecific impacts or unintended side effects on living organisms – independent of whether these are of chemical, biological, or physical origin [1]. Studies addressing the general *cytotoxicity* aim to quantify the dose or formulation of a given compound or treatment that living organisms can tolerate without any significant impairment of viability or functionality [6, 7]. A mechanistic understanding of the harmful reaction is often neglected in these studies that are solely focused on identifying biological impact or response to chemicals or treatments. Among others, these kinds of biosafety tests have been enforced by the REACH regulation within the European Union for an enormous amount of existing chemicals so that cell-based testing is without alternative. CBAs are also applied to test physical challenges for their potential influence on cell physiology. The impact of weak electromagnetic fields on living cells, for instance, has received considerable attention in the current era of ubiquitous wireless communication [8, 9]. There is also a strong demand to screen for *bio-* or *cyto-compatibility* of man-made materials that are converted to active or passive implants for the human body [10]. The surfaces of these materials have to be compatible with cell settling and cell anchorage in order to be fully integrated into the organism [11].

This tremendous need for biological testing has been further increased in recent years by the amazing scientific progress in nanotechnology. Over the last two decades, nanotechnology produced a myriad of different nanosized structures with enormously interesting material and functional properties. Quantum dots (QDs), carbon nanotubes (CNTs), carbon dots (CDs), gold nanoparticles, and soot and pigment particles are among the most well-known representatives. But also less "famous" nanomaterials made from polymers, noble metals, or inorganic materials

have raised considerable interest for applications in the biomedical field and other areas of our daily life. Despite of their undisputed usefulness in certain areas, there is a constant and justified concern that these nanomaterials may have unwanted biological effects on cells and organisms that have not yet been discovered and understood entirely. Research into the toxicological impact of nanoparticles on human health and possible hazards for the environment is still in its infancy [12]. Among other indicators, the importance and relevance of understanding the biological effects of nanomaterials is expressed by the fact that the entire journals have been founded and dedicated to this particular aspect of nanosized objects. So there is obviously a strong need for assays and devices that are capable of reporting quantitatively on the response of living systems to nanomaterials [12]. In this new field of *nanotoxicology*, cell-based assays have been and will be performed heavily. They have contributed significantly to the current state of our knowledge [13–15]. The majority of studies has applied those well-established assay formats that read cell viability, activation of signal transduction pathways, or other enzymatic cascades with the help of colorimetric or fluorescence-based staining protocols. Over the years evidence accumulated that these label-based assays have a somewhat limited applicability in nanotoxicology as most nanomaterials scatter or absorb light, show an inherent luminescence, or interfere otherwise with the assay reagents. Thus, techniques and approaches to read out cell-based assays without using labels or additives became more and more relevant and accepted – in particular as they provide continuous monitoring of the cells instead of a sole endpoint analysis. The following chapters provide a thorough discussion on label-based versus label-free readout approaches for cell-based assays with special emphasis on nanotoxicology before impedance analysis is introduced as powerful and multi-model technique to measure the response of living cells exposed to nanomaterials. A short survey about the core component of any cell-based assay, the sensor cells, is placed upfront.

2 Cells as Sensors

The cells that are used as sensors in cell-based assays are the most critical and delicate component that determines the performance of any CBA. They have to be uncompromised by the experimental procedure so that the observed biological impact is unambiguously attributable to the test compound and not a consequence of improper assay conditions. This statement may look trivial, but it requires that the entire experiment fulfills the rather stringent conditions of cell culture: 37°C, physiological pH, isotonic solutions, sufficient oxygenation, and aseptic environment. Moreover, routine propagation of the sensor cells has to be standardized on all levels to ensure reproducible performance, sensitivity, and composition of the cell population. It has to be emphasized that cultured cells continuously adapt to the external conditions by clonal selection such that inappropriate cell culture

techniques or cell handling sooner or later result in irreversible changes of the cell population.

The cell types that are used as sensors in CBAs strongly depend on the question to be answered and the technical requirements of a given assay format. Several classes of cultured cells are used as test objects that differ with respect to their life span in vitro, the ease of their maintenance in a laboratory environment, and most importantly their differentiation, i.e., the expression of a highly functional and specialized phenotype. *Primary cultured cells* are used immediately after their isolation from the donor organism. Accordingly, they are very similar to the cells in the original tissue in vivo [16]. They most closely mimic the enzymatic activities and overall physiology of their correspondents in the body. However, using primary cells in CBAs is commonly avoided as they have to be isolated from donor animals for every experiment which is time consuming, tedious, and expensive. Moreover, these cells are very sensitive to the in vitro environment and dedifferentiate easily. *Finite cell lines* result from primary cultured cells upon extensive and long-term propagation in the laboratory and they are often derived from tumor tissue. They are easy to grow in the lab, metabolically active, and usually undergo cell senescence after approximately 65 doublings. After that this cell lineage loses its ability to proliferate and dies out. When genetic transformation occurs along their life span in the lab, these cells lose their growth limitation and they become immortal. Such *immortalized cell lines* can be propagated infinitely so that they are available for assays and experiments in unlimited quantities. The most famous example of such a cell line is the human cell line HeLa. It is the most widely used cell line in biomedical research worldwide and the first human cell ever grown in vitro in the 1950s [17]. Pharmaceutical assays often rely on *genetically engineered cell lines* that express a cell surface receptor or an enzyme of interest with much higher copy number than their wild-type correspondents. This overexpression of the target protein turns these cells into very sensitive indicators for the interaction of the target protein with its ligand. Accordingly, engineered cell lines are heavily used in pharmaceutical screening campaigns. In other cases the cells are additionally engineered to express an easy-to-detect reporter gene product (e.g., EGFP, luciferase, or galactosidase) as a response to the presence of a compound with a given bioactivity. For instance, cells have been described that express a fluorescent protein whenever they experience genotoxic stress [18]. The reporter gene is placed under the control of a stress-sensitive promoter so that gene expression is switched on when genotoxic stress arises. These cells do not provide information with respect to the molecular origin of the genotoxicity, but they reliably indicate this very specific biological response independent of the stressor. It has been demonstrated that certain nanomaterials are capable of activating this kind of response in selected cell types [18]. *Stem cells* have a very important and valuable role as sensing elements in cell-based assays [19]. These cells can be experimentally stimulated to differentiate into highly specialized phenotypes like neuronal cells or cardiomyocytes. When a test compound (chemical, nanoparticle, etc.) is present during this differentiation process, it is possible to identify any deviation from the regular, unperturbed differentiation path and thereby unravel any impact on

developmental processes. Embryonic stem cell lines derived from animals are commercially available, whereas human stem cells are only accessible in the form of *induced pluripotent stem cells* (iPS) that are derived from somatic tissues.

3 Label-Free Versus Label-Based Assay Strategies

The number of applications for cell-based assays (CBAs) is huge and steadily increasing. For a successful assay format, it is indispensable but not sufficient to have an appropriate cell culture model available. It is equally important to have sensitive experimental strategies to *monitor* the behavior of these cells upon exposure to drugs, toxins, nanomaterials, or other stressors. Moreover, the response of the cells to a given stimulus needs to be measured quantitatively in order to determine threshold concentrations, to establish structure-activity relationships, or to compare different classes of compounds within one assay. Two different strategies have evolved to monitor and analyze cell-based assays. They are classified as *label-based* or *label-free* readout approaches dependent on whether they rely on auxiliary compounds (fluorescent probes, antibodies, chromophores, etc.) to make the cell response measurable or not. Label-free approaches do not rely on chemical detection principles but measure physical quantities (impedance, refractive index, viscoelasticity, etc.) to quantify the cell response. Both approaches differ significantly with respect to the characteristics of their analytical performance and are, thus, discussed and compared briefly in this chapter.

3.1 Label-Based Analysis of Cell-Based Assays

Many different biochemical and cytological assays have been developed over the years to measure the cells' viability, metabolic status, or proliferative activity quantitatively. Most of them rely on chromophores, fluorescent, or otherwise luminescent probes that recognize a given molecular biomarker (ATP, NADH, etc.) that is unequivocally associated with the biological function to be studied. The probes (labels) change their optical properties (absorbance, luminescence) upon biomarker binding and allow for a quantitative determination. Hence, these assays are dependent on exogenous additives to be incubated with the cells. However, using probes or labels that are either (1) consumed along the analytical assay, (2) bioactive [20], or (3) (photo)toxic [21] is problematic and restricts the application of these label-based assays to so-called *endpoint* readings. In endpoint assays the exposure time with the test compound is predefined by the experimenter, and the cells are commonly sacrificed for subsequent analysis at the end of exposure. Dependent on the details of the assay, it is often necessary to lyse or permeabilize the cells in order to release the endogenous biomarker (e.g., ATP, NADH), which is indicative for the current status of cell viability or metabolic

activity, from the cytoplasm, and to determine its concentration extracellularly. Continuous observation of one cell population is impossible for these assays. Time-dependent information requires running multiple replicates for any exposure time to be analyzed in parallel. These assays typically report with very high molecular specificity on the concentration of the preselected *biomarker* like ATP, NADH, or products of enzymatic conversion. They show typically very low cross-reactivity. But they miss any other unforeseen response of the cells. In a sense these assays must be considered as being *biased* as they only read what has been planned to read before starting the experiment. If the response of the cells is different than expected, the assay may be blind or provides false-negative results. Nevertheless, these easy-to-perform low-tech assays have proven their usefulness in uncounted studies around the world and contributed considerably to our current understanding of basic physiological and pathophysiological processes.

Table 1 summarizes the most widespread label-based, biochemical assays to measure cell viability. They are categorized in two classes: (1) assays addressing membrane integrity and (2) assays addressing the metabolic activity of the cells. Whereas the first category refers to the fact that dying cells loose the integrity of their plasma membranes, the latter reads the decrease of the cells' metabolic activity as an indicator for cell death.

1. Membrane integrity assays either measure the uptake of a membrane-impermeable probe from the extracellular fluid into the cytoplasm of the cells or the efflux of intracellular molecules into the supernatant. Typical probes for membrane integrity that are applied to the extracellular fluid are *trypan blue* or *naphthalene black*. The characteristic staining of cells that have lost the integrity of their membrane and accumulated either one of the two dyes is easily visible in bright-field light microscopy. The microscopic identification of dead cells is more sensitively achieved using fluorescent probes like propidium iodide (PI) or ethidium homodimer (EHD). If membrane integrity is compromised, these dyes get access to the nucleus, intercalate into the DNA, and mark dead cells with a bright nuclear fluorescence which can be easily detected microscopically or by cytometry. In contrast, the LDH assay is based on measuring the activity of the cytoplasmic enzyme *lactate dehydrogenase* in the extracellular supernatant. LDH can only be present in the extracellular buffer, if the membrane diffusion barrier has been compromised and efflux of enzyme molecules has occurred. The readout requires adding the enzyme's substrates to the supernatant and coupling the enzymatic reaction to the formation of a colorimetric or fluorescent dye so that quantification is accessible by optical means. Monitoring the leakage of a cytosolic enzyme as an indicator for a loss of membrane integrity is significantly more sensitive than following the influx of a stoichiometric color-imetric probe given the inherent amplification that is associated with enzyme detection.

2. The so-called MTT assay – with the MTS and WTT variants being closely related – is the most widely applied assay to measure cell viability via their metabolic activity [22]. The assay reads the cells' pool of the redox coenzymes,

Table 1 Label-based assays to monitor cell viability of cultured cells in vitro

Indicator	Reagent(s)	Mechanism	Detection
Increase in biomass			
Total protein	Coomassie brilliant blue G Sulforhodamine B Naphthol blue-black Crystal violet	Dyes bind to cellular proteins; the amount of bound dye is proportional to the biomass of cells	Absorbance of cell extract or fixed cell layer
Total DNA	DAPI Hoechst 33258 Hoechst 33342	Dyes bind to DNA; the amount of bound dye is proportional to the DNA content of cells	Fluorescence of cell homogenate or fixed cell layer
Proliferation activity			
DNA synthesis	^{3}H-Tymidine ^{125}I-Deoxyuridine	Incorporation of (radio) labeled nucleotide analogue during DNA replication in dividing cells	Scintillation
	Br-dU (5-bromo-2′-deoxyuridine)		Anti-Br-dU antibody, ELISA, microscopy
	EdU (5-ethynyl-2′deoxyuridine)		Click reaction with fluorescent dyes
Protein synthesis	^{3}H-Leucine, ^{35}S-methionine	Incorporation of radiolabeled amino acid in proliferating cells	Scintillation
Markers for cell proliferation	Antibodies to Ki-67, PCNA, cyclins, and others	Immunological detection of characteristic proteins in proliferating cells	Immunocytochemistry, ELISA
Metabolic activity			
Reducing coenzymes (NADH, NADPH; FADH, FMNH)	Tetrazolium salts MTT; XTT; MTS; WST-1;INT	Reduction of tetrazolium salts in the presence of reducing coenzymes forms colored water-soluble or insoluble formazan dyes	Absorbance of solubilized formazan
	Resazurin	The blue, nonfluorescent resazurin is reduced by living cells to give the pink fluorescent dye resorufin	Absorbance of educt or fluorescence of product in the extracellular medium
Enzyme activity, e.g., cellular esterase activity	E.g., calcein AM, fluorescein diacetate	Intracellular hydrolysis of fluorogenic probe precursor by cellular esterases	Fluorescence of stained cells
ATP level	Luciferase, luciferin	ATP-dependent conversion of luciferin to luminescent oxyluciferin	Luminescence in cell hydrolysate
pH gradients (ATP level)	Neutral red	Neutral red accumulates in lysosomes due to ATP-driven pH gradients in living cells	Absorbance of cell extract

NADH and FADH$_2$. It is chemically based on the reduction of colorless tetrazolium salts to deep red formazan by NADH/FADH$_2$ which is easily quantified by photometry. Variants of this assay like alamarBlue™ or PrestoBlue™ follow the same strategy but use fluorogenic detection of the redox reactions. Another class of metabolic assays is based on membrane-permeable but nonfluorescent reagents like calcein AM that get hydrolyzed by esterases inside metabolically active cells. The resulting calcein is green fluorescent but no longer membrane permeable so that it accumulates in the cytoplasm. Dead cells are unable to catalyze the conversion of calcein AM and thereby do not accumulate green cytoplasmic fluorescence as an indicator for cell viability. A variant of this assay is based on the same principles but uses fluorescein diacetate instead of calcein AM [22]. But please note that Knight et al. recently reported a strong phototoxicity in the test cells after excitation of intracellular calcein [21]. Hence, continuous observation of the cells along the time course of exposure to a given stressor may be paralleled by the phototoxicity of the calcein probe itself and may lead to false-positive readouts. Other metabolic assays read the ATP levels inside the cells as an indicator for viability. A direct quantification of ATP is achieved by measuring the chemiluminescence associated with ATP-dependent conversion of luciferin to oxyluciferin. More indirect is the neutral red (NR) uptake assay. NR accumulates in the lysosomes as long as the pH inside the lysosomes is lower than in the rest of the cell due to the activities of ATP-driven proton pumps. Thus, the more ATP is available, the more pronounced is the pH gradient across the lysosomal membrane and the stronger is the NR uptake. Thus, a colorimetric measurement of NR uptake quantifies the amount of ATP indirectly as the concentrations of both compounds are correlated [14].

Although toxicologists have traditionally associated cell death with *necrosis*, emerging evidence suggests that different types of environmental contaminants exert their toxicity, at least in part, by triggering *apoptosis* [23]. Whereas *necrosis* is defined as cell death in response to unfavorable external conditions (heat, pH, toxins), *apoptosis* is the genetically encoded cell suicide. Once a cell triggers for internal or external reasons the apoptosis pathway, a sequence of well-defined and orchestrated steps of self-digestion occur that can be monitored by specific assays that are not included in Table 1. The assays in Table 1 are general viability assays, but they are not capable of distinguishing between apoptosis and necrosis. A concise review about bioanalytical assays to distinguish between apoptosis and necrosis has been recently given by Vanden Berghe and colleagues [24].

Table 2 provides a survey of the most widely accepted label-based assays to measure cell proliferation, i.e., the ability of a cell to divide and to multiply. Obviously cell proliferation and its up- or downregulation by exogenous chemicals or nonchemical stressors are important parameters to decide on their biological impact. The assays in Table 2 are grouped in three categories: (1) assays reading an increase in biomass as the ultimate biomarker for proliferation, (2) assays addressing more specific molecular hallmarks of cell proliferation, and (3) assays

Table 2 Label-based assays to quantify the proliferative activity of cultured cells in vitro

Indicator	Reagent(s)	Mechanism	Detection
Membrane integrity			
Dye exclusion assays	Naphthalene black	Cytoplasm of dead cells with permeable membranes is stained by the dye which is not membrane permeable	Bright-field microscopy of blue-black stained dead cells
	Trypan blue		
	Propidium iodide	Dead cells with permeable membranes are stained by the membrane-impermeable dye. If cell membranes are damaged, dye stains nucleic acids by intercalation in double-stranded DNA	Red fluorescence from nuclei of dead cells
	Ethidium homodimer-1		
Enzyme leakage assay, e.g., lactate dehydrogenase (LDH)	Lactate, NAD^+, diaphorase, resazurin	Cytosolic housekeeping enzyme LDH is released from cells with damaged membranes and catalyzes oxidation of lactate to pyruvate in extracellular buffer producing NADH; NADH then reduces resazurin to fluorophore resorufin catalyzed by diaphorase	Fluorescence or absorbance in extracellular medium
Metabolic activity			
Reducing coenzymes (NADH, NADPH; FADH, FMNH)	Tetrazolium salts MTT (is) MTS (s)	Reduction of yellow water-soluble tetrazolium salts by reducing coenzymes to colored water-insoluble (is) or water-soluble (s) formazan dyes	Absorbance of solubilized formazan
	Resazurin (e.g., alamarBlue ©, PrestoBlue ©)	Reduction of nonfluorescent membrane-permeable resazurin (blue) by reducing coenzymes to membrane-permeable red-fluorescent resorufin	Fluorescence or absorbance in extracellular medium
Enzyme activity (e.g., intracellular esterase activity)	Fluorescein diacetate	Intracellular hydrolysis of membrane-permeable precursor (fluorescein diacetate, calcein AM) by cellular esterases to membrane-impermeable fluorophore (fluorescein, calcein) which is trapped in the cell	Green cytoplasmic fluorescence of stained viable cells
	Calcein AM		
ATP level	Luciferase, luciferin	ATP-dependent conversion of luciferin to luminescent oxyluciferin	Luminescence in cell hydrolysate
pH gradients (ATP level)	Neutral red	Neutral red accumulates in lysosomes due to ATP-driven pH gradients in living cells	Absorbance of solubilized stain

reading metabolic activity. The assays in group (3) are essentially the same as they are used to measure cell viability. The experimental protocols are just slightly different with respect to the cell culture. Please note: viability assays are recorded at the end of an exposure time relative to an untreated control in order to quantify

the fraction of living cells in a given population. Proliferation assays based on measuring metabolic activity rely on the fact that total metabolic turnover is directly proportional to the number of contributing cells so that readings do no longer report on viability but cell number. When the assay is repeated in well-defined time intervals, it reports on the change in cell number with time. Obviously these assays run into problems when cell proliferation is supposed to be studied in the presence of a stressor that also affects the individual cell's metabolic turnover. This ambiguity between cell number and cell-specific metabolic activity is difficult to sort out. The underlying chemical principles of the assays grouped in category (3) are the same as described above.

Those assays grouped together in category (1) measure the total amount of protein or DNA within a given cell population. Both quantities are directly proportional to cell number and therefore report on population dynamics. The probes that are used to quantify total protein or DNA have been selected because of their ability to bind to protein or DNA stoichiometrically. Absorbance or fluorescence readout then reports on the probe concentration and, thus, on cell number.

Group (2) summarizes those assays that more specifically probe proliferative activity by measuring the amount of newly synthesized DNA or protein. In these assays the cells are incubated with radiolabeled nucleotides or amino acids, respectively. The amount of radioactivity introduced into the cells' protein or DNA pool after a well-defined exposure time reports on DNA or protein biosynthesis. These assays, however, require the handling of isotopes in specialized laboratories and a disposal system for radioactive waste. Due to these extra efforts and requirements, fluorescence-based assays are preferred. The Br-dU assay is such a fluorescence-based analogue. It relies on incubating the cells of interest with the thymine analogue Br-dU which becomes incorporated into newly synthesized DNA. The nonnatural Br-dU is later recognized by fluorophore-labeled antibodies so that the total amount of newly synthesized DNA can be estimated from readings of fluorescence intensity.

Both types of assays addressing either viability or proliferation have been applied heavily to report on the biological response of cultured cells to nanomaterials and they have proven to be valuable. However, it requires caution and the proper controls to ensure that the nanomaterials themselves do not interact with the ingredients of the assays and thereby cause false-positive or false-negative readings. Recently Holder et al. [25] reported that carbon-based nanomaterials like soot or diesel soot reduce MTT to formazan under cell-free incubation conditions and produce significant artifacts in MTT-based viability assessment. The same particles showed absorbance of LDH on their surface so that membrane rupture of cells was heavily underestimated. Similar effects have been reported for other nanomaterials like Ag nanoparticles [26] or TiO_2 nanoparticles [27]. Moreover, the readout for most assays summarized in Tables 1 and 2 are based on absorbance or fluorescence intensity measurements. Optical detection is, however, often disturbed by light scattering imposed by nanosized objects in the test solution. Absorbance measurements may read too high, whereas fluorescence intensity measurements may read too low in the presence of scatter centers. This phenomenon is often

overlooked when optical probes are used to quantify cell behavior in the presence of nanomaterials.

3.2 Label-Free Analysis of Cell-Based Assays

Label-free readout approaches monitor the cell response without colorimetric, fluorogenic, or radiolabeled additives. These techniques are based on physical rather than on chemical transduction principles. They integrate to various degrees over the entire cell body and report on holistic parameters like cell shape, the average refractive index, or the integral electrical resistance of the cells in the assay. These optical or electrochemical measurements are performed with low amplitude physical signals and they have proven to be noninvasive in nature. Thus, label-free cell observation approaches allow for continuous cell monitoring for hours, days, or even weeks without sacrificing the cells at any point. Accordingly, a single experiment provides additional information on the dynamics of the cell response to a given compound or stressor. Moreover, the readout is entirely unbiased as it reports on the cell response in a holistic, integrative manner without making any a priori assumptions about the molecules involved downstream to the primary event. Independent of the exact molecular mechanism of action, the cell response will be recorded unspecifically by the integrative physical measurements. In return the experiment does not provide any molecular information on a possible mechanism of action by itself. Figure 1 sketches the most prominent label-free readout technologies that are used to monitor cell-based assays. In all but one approach, the cells are grown on surfaces that are part of the physical transducer system, like the gate of a transistor or a planar gold-film electrode. The detection principles are optical, electrochemical, or piezoelectric. Other approaches that are not included in Fig. 1 have also been published occasionally, but they have not yet evolved beyond the proof-of-concept status and are not yet considered a routine technology.

The most obvious and straightforward label-free approach to study cells during their exposure to drugs, toxins, or nanomaterials is transmission light microscopy which is noninvasive and reports on changes in cell morphology and optical thickness [28]. As cells do not absorb visible light to an analytically useful degree, it requires phase contrast, digital interference contrast, or digital holography to visualize the cells on appropriate supports without using chromophores or fluorophores. In all these microscopic techniques, cell morphology/cell shape is the integral, holistic bioanalytical indicator for any impact on cell physiology but without molecular specificity or any detailed indication about the mechanisms involved [29]. Among the microscopic techniques, one approach has attracted considerable attention throughout recent years: digital holographic microscopy (DHM, cp. Fig. 1a) [30, 31]. DHM provides 3D images of transparent objects like living cells and is, thus, ideally suited for time-resolved phenotypic screening based on cell morphology [32]. Holographic imaging is diffraction limited in the xy-plane (perpendicular to optical axis), but it provides a much better resolution in
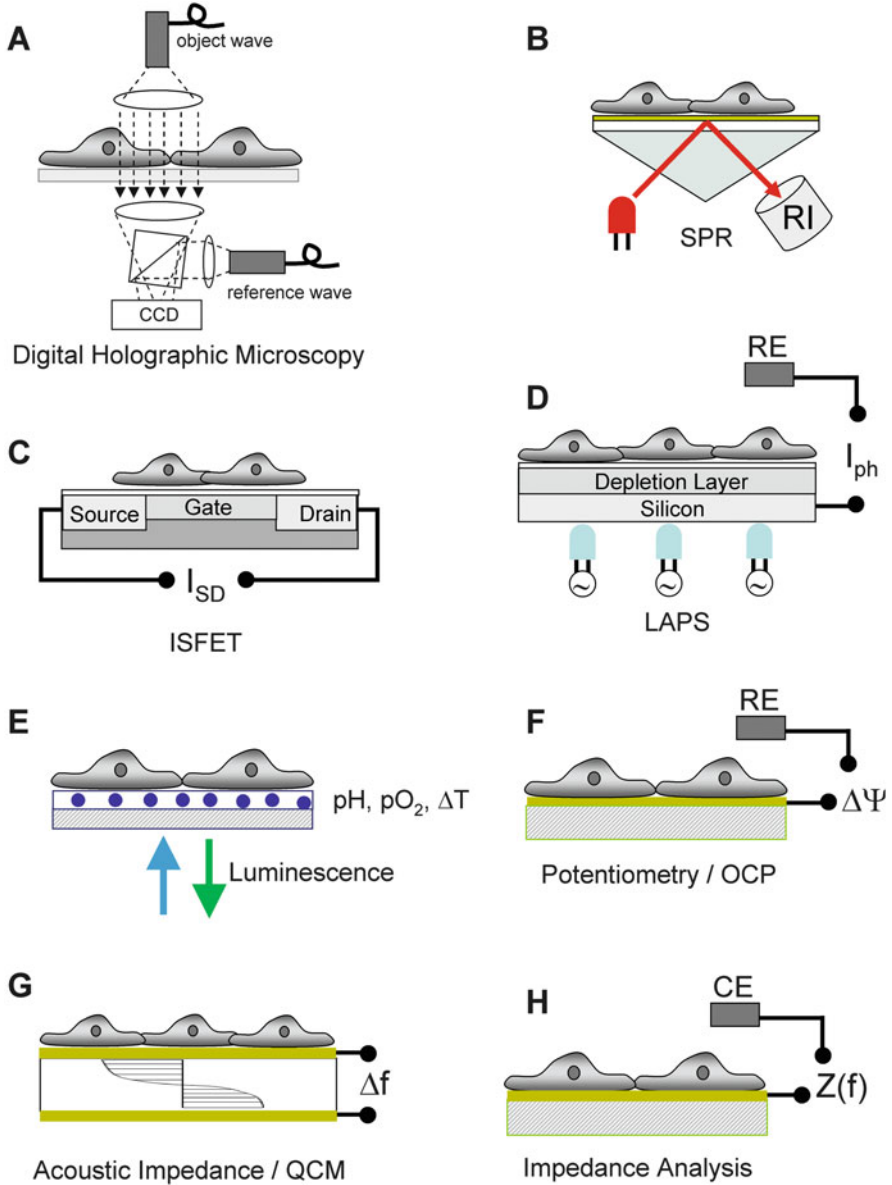
Fig. 1 Label-free transducer techniques to monitor cell-based assays. *SPR* surface plasmon resonance, *RI* reflected intensity, *RE* reference electrode, I_{ph} photocurrent, *LAPS* light addressable potentiometric sensor, I_{SD} source–drain current, *ISFET* ion selective field effect transistor, *OCP* open circuit potential, *QCM* quartz crystal microbalance, *CE* counter electrode

z-direction (parallel to optical axis) on the order of just a few nanometers so that very accurate, 3D cell shape information is available for analysis.

Please note, traditional phase contrast or bright-field images of living, unstained animal cells are sometimes difficult to analyze and interpret with respect to cell morphology as (1) these micrographs do not provide 3D information of the cell bodies and (2) cell borders are often blurred by complex optical effects. The only limitation of DHM is the need for sophisticated image analysis software and expertise to extract quantitative parameters from the recorded micrographs. However, quantitative analysis is the indispensable basis to evaluate the biological impact of chemicals, nanomaterials, or other stressors and to compare the tolerable doses. DHM has been described just recently for 96 well formats [31], a development that paves the way for high-throughput applications.

Even though it is commonly not considered as a classical light microscopy technique, surface plasmon resonance imaging (SPRi, cp. Fig. 1b) has also demonstrated its potential to image cell-based assays noninvasively [33]. Published examples comprise successful monitoring of the cell response to the stimulation of cell surface receptors [34, 35] or allergen encounter [36]. SPRi in the most commonly applied setup reads changes in refractive index (RI) within 100–200 nm from the growth surface. Changes in RI during cell-based assays are generally attributed to a "dynamic mass redistribution" (DMR) that is most often caused by a rearrangement of the cytoskeleton and the accompanying changes in cell morphology [37]. Thus, the information content of SPRi is similar to light microscopy-based readouts but more sensitive and confined to changes close to the growth surface. Conventional, non-imaging SPR [38–40] or devices based on resonant waveguide grating [41, 42] have proven their outstanding performance in monitoring cell-based assays just recently [41, 43]. Waveguide devices have been brought into 384-well format and contributed significantly to pharmacology as a transducer for the activation of intracellular signaling pathways. It is noteworthy that the cells have to adhere tightly to the culture surface as the method is blind for any change in refractive index that originates farther away from the surface than 100 nm (evanescent field technique). The analysis of 3D cell aggregates will, thus, be impossible.

Very different label-free transducer concepts have been proposed to measure the physiological response of living cells to any kind of external challenge via the associated changes in energy metabolism [44]. Since (1) energy metabolism is ubiquitous in all cells and (2) the rate of energy metabolism has proven to be very sensitive to a broad range of physiological modulations [45], holistic devices reading metabolic activity are applicable to a huge number of bioanalytical problems and screenings. Since enhanced metabolic activity commonly goes hand in hand with the production and secretion of acids, it can be readily monitored by pH-sensitive devices that measure extracellular acidification rates after proton efflux from the cytoplasm, e.g., based on ISFETs (ion selective field effect transistors, cp. Fig. 1c) [46, 47] or LAPS (light addressable potentiometric sensors, cp. Fig. 1d) [48–51]. In pH-sensitive ISFETs, the proton concentration at the gate surface controls the gate potential and, thus, the source-to-drain current which is the

readout quantity. In contrast, the working principle behind LAPS devices requires backside illumination with a laser diode to locally create charge carriers in the semiconductor layer. The resulting photocurrent (I_{ph}) depends on the potential in the pH-sensitive depletion layer facing the solution which often consists of Ta_2O_5. It is a unique feature of LAPS devices that readings can be taken with lateral resolution just dependent on the position of the illuminating LED. Thus, the technique allows for visualizing the lateral distribution of extracellular acidification, whereas ISFET readings integrate over the entire cell population adhered to the gate. In a comparative study, ISFETs and LAPS showed very similar analytical characteristics like sensitivity, drift, and response to pH shifts [52]. Both techniques have in common that the system needs to get flushed with fresh assay buffer in regular cycles to reconstitute original pH conditions. It is the *rate* of pH shift after every flushing cycle that is sequentially recorded and used for quantitative metabolic analysis. Thus, phases of pH measurement alternate regularly with phases of buffer exchange along the entire assay. Accordingly, the experimental setup requires pumps and tubing that may cause experimental problems due to leakage, plugging, or contamination. On the other hand, the repeated flush with assay buffer allows for a very simple and well-defined administration of the test compound. In contrast to measurements of the oxygen consumption rate (OCR) – determined, for example, by classical Clark oxygen electrodes or optical readings based on luminescence quenching – extracellular acidification is sensitive to both glycolytic metabolism and respiration. The most recent devices combine oxygen partial pressure pO_2 measurements and pH readings within one setup based on ISFET technology [47]. Optical readouts of pH and pO_2 are technically much simpler and make use of luminescent probes that either change their spectral properties upon proton binding or get quenched in the presence of oxygen, respectively (Fig. 1e). Sensor spots impregnated or decorated with the pH- or pO_2-sensitive probes have been deposited in the culture dish, and the analytical readout is performed by optical fibers from the outside [53].

Besides reading extracellular acidification of adherent cells, ISFETs are also used to monitor the functional activity of electrically excitable cells, most notably neurons [54–56]. Compared to patch clamping, which is the golden standard for recording action potentials, the cells are not mechanically stressed by adhering to the flat and passivated gate of an ISFET. In this sense, ISFET-based recordings are clearly less invasive and capable of reading the impact of almost all kinds of stressors on neuronal activity. Extracellular recording of action potentials with planar metal electrodes has been known for decades as another noninvasive technical option to study excitable cells [57]. When several of these electrodes were grouped to form *multielectrode arrays*, a spatially resolved analysis of neuronal networks became possible. More recently, Wooley et al. [58] have introduced a related technology by growing adherent but electrically non-excitable cells on the surface of gold-film electrodes. When the potential of these cell-covered electrodes is measured relative to a reference electrode (e.g., Ag/AgCl) in the bath (Fig. 1f), cell-type-specific voltage readings have been reported and these voltages vanish when the cells die and retract from the electrode surface. Apparently, living cells

produce a cell-type-specific ionic environment between the lower plasma membrane and the electrode surface that influences the electrode potential. These so-called *open circuit potential* (OCP) measurements were robust enough to monitor the time course of cell death when the sensor cells were exposed to drugs that are in routine clinical use for chemotherapy [58].

Another class of label-free approaches to monitor CBAs uses piezoelectric resonators and the associated acoustic waves. The *quartz crystal microbalance* (QCM) is by far the most widely known and most often applied device from this category [59]. The QCM has a long track record as a mass-sensitive tool to study adsorption reactions at the solid–liquid interface. It operates noninvasively and with a superb time resolution that is much better than necessary for most cell-related studies. The core component of this technique is a thin, disk-shaped piezoelectric (AT-cut) quartz crystal sandwiched between two gold-film electrodes (Fig. 1g). When an oscillating potential difference is applied between the surface electrodes, the piezoelectric resonator performs mechanical shear oscillations parallel to the crystal faces at the resonator's fundamental resonance frequency. This mechanical oscillation is highly sensitive for any changes at the resonator surface, so that adsorption or desorption processes are measurable as decrease or increase of the resonance frequency [59]. More detailed information about the material in contact to the crystal surface is provided by analyzing the shear oscillation of the resonator using principles of impedance analysis [60, 61]. The amplitude of the mechanical shear oscillation depends on the driving voltage and the resonance frequency. When the device is operated in physiological fluids, it is commonly below 1 nm in the center of the resonator and falls off toward the periphery. This low mechanical displacement together with an oscillating frequency in the MHz regime renders the QCM a truly noninvasive transducer for cell-based assays. Within the 1990s it was first recognized that the QCM signal is sensitive to cell attachment and spreading [62, 63]. Accordingly, the device was used to record the time profiles of cell adhesion under various experimental conditions in order to test surface compositions for their biocompatibility or to analyze the molecular details of cell surface interactions [64]. Later it has been recognized that QCM readings of confluent cell layers report on cellular micromechanics which is dominated by the intracellular cytoskeleton [65]. Recognizing this connection has led to many applications of QCM devices in cell-based bioanalytics [66]. For instance, the QCM has been used as a transducer in cell-based cytotoxicity assays [67, 68] as well as to analyze the cellular response to nanomaterials [69, 70]. However, the results are sometimes difficult to interpret and leave considerable ambiguities – in particular when the resonance frequency is the only parameter being measured.

Figure 1h sketches the principle of a very special label-free device to monitor cell-based assays that is in the focus of this contribution: impedance analysis of cell-covered gold electrodes. The technique has been referred to as ECIS for *electric cell-substrate impedance sensing* [71, 72]. In ECIS cells are grown on planar gold-film electrodes that are deposited on the bottom of a regular cell culture dish or a multiwell plate. The electrical impedance of such an electrode increases when mammalian cells attach and spread on its surface as the current is forced to

flow around the insulating cell bodies. With the current bypassing the cell bodies on extracellular ionic pathways, impedance arises in the narrow cleft underneath the cells and in the intercellular cleft between adjacent cells before it escapes into the bulk. In a nutshell, the recorded impedance signal is predominantly sensitive to two distinct contributions: (1) coverage of the electrode with cells and (2) changes in cell morphology. It is obvious that the impedance increases when the electrode is gradually filled with cells since the surface area available for unrestricted current flow is decreasing accordingly. This correlation is the physical basis for using ECIS as a device to monitor cell attachment [73], cell proliferation [74], and also cell migration [75] noninvasively and time resolved. Sensitivity of ECIS to cell morphology relies on the fact that any change in cell shape alters the extracellular ionic current pathways and it thereby alters the impedance of the cell-covered electrodes [72]. It has been estimated by model calculations that cell shape changes far below the resolution of an optical microscope are measurable and detectable using the ECIS technique. This capability of monitoring cell shape changes with a time resolution from milliseconds to hours makes ECIS a very versatile and multimodal tool to monitor adherent cells while they are exposed to drugs, toxins, or xenobiotics in general [76–79] including nanomaterials. State-of-the-art commercial devices allow for impedance-based assays in 96-well or even 384-well format. The details of the ECIS technology and a review about its application to monitor the biological impact of nanomaterials are in the focus of this chapter.

3.3   Comparison of the Different Assay Strategies

Figure 2 illustrates the difference between both assay philosophies – label-based versus label-free – on the example of a compound that binds to its cell surface receptor and releases an intracellular signaling cascade.
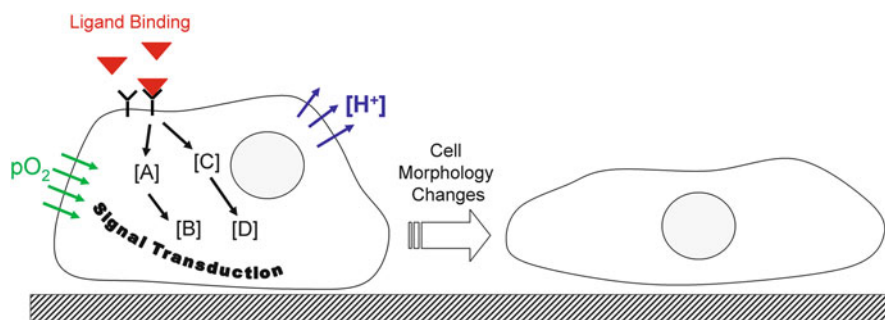
Fig. 2 Hypothetical cell-based assay during which cell surface receptors are stimulated with a corresponding agonist that induces receptor activation coupled to intracellular signaling cascades. Eventually the cell will respond by distinct morphology changes

Please consider the following thought experiment: two different competing signaling cascades (1) and (2) are coupled to a given cell surface receptor. Cascade (1) leads to the formation of intracellular messengers A and then B after receptor activation. In contrast, cascade (2) first generates the messenger C and then D. Alternative coupling of one receptor to two competing signaling cascades is a physiological scenario well known from G-protein-coupled receptors (GPCRs). At the end of either signaling cascade, the activation of the receptor leads to a distinct change in cell morphology.

A specific *label-based* assay is tailored to read the concentration of the signaling molecule A, B, C, or D ideally without any cross talk. The experimenter has to decide before the experiment which signaling molecule to choose as a biomarker for receptor activation. Alternatively, four individual assays for A, B, C, and D have to be performed in parallel. To determine the concentration of any of these signaling molecules, the cells have to be permeabilized to ensure that the specific assay reagents and additives reach the analyte in the cytoplasm. If an assay for biomarker A is selected but the test compound (ligand) triggers the alternative signaling cascade via C/D or another yet unknown pathway, the assay will return a false-negative result for the given exposure time. So the experiment is specific, but biased and invasive, and it only provides information for a single time point.

In contrast, a label-free assay that is sensitive for changes in cell morphology monitors the cells continuously. As these readout technologies rely on noninvasive physical measurements (see below), cell physiology is not affected by the measurement itself. Independent of the signaling cascade involved, the cells will change their morphology when the test compound activates the receptor since animal cells respond to any intra- or extracellular stimulus or stressor by subtle cell shape changes. So the assay correctly reports on receptor activation and the time profile of the associated integral, holistic cell response independent on the signaling cascade involved. However, the assay does not specify the signaling pathway – not even whether a yet unknown pathway has been activated. It is important to note and to recognize that coupling of receptor activation to a yet unknown pathway is only observable by such holistic label-free approaches that do not require a priori knowledge about the nature of the signaling molecules involved. Recently, several strategies have been developed to overcome the inherent lack of specificity of label-free readout approaches and their inability to identify a signaling pathway. For instance, direct and receptor-independent experimental modulation of the intracellular concentrations of either A, B, C, or D is used to specifically trigger one particular pathway. When these well-defined signaling experiments are monitored by label-free transducers, the system can be trained in the sense that the time profiles of cell shape changes indicate the underlying signaling pathway without any specific molecular assay [37, 80, 81]. Moreover, engineered cell lines that carry a genetically encoded suppression of one or more signaling pathways are used for training label-free readout technologies. Ideally, pattern recognition of the dynamic response profile will later indicate the signal transduction cascade without any specific probes involved.

With the individual advantages and limitations of both label-based and label-free readout techniques in mind, it is straightforward that they should be thought as complementing but not as competing techniques. Whereas label-free detection is strong in reporting a yet ill-defined biological response with broadest specificity but very high sensitivity, only label-based approaches are capable of identifying unequivocally a molecular mechanism of action for a given perturbation of cell status. Whereas label-free analysis of cell-based assays provides the time course of the cell response and thus the system's dynamics, label-based assays offer a significantly higher throughput. So when both approaches are used in parallel with their individual advantages and strengths, they can provide a rather comprehensive and efficient analysis of a cellular response to any kind of stress or stimulus.

4 Basics and Concepts of Electric Cell-Substrate Impedance Sensing (ECIS)

The idea of *electric cell-substrate impedance sensing* (ECIS) has been introduced by Giaever and Keese, who were the first to grow mammalian cells directly on the surface of gold-film electrodes and to record the concomitant changes of the electrode's complex electrical impedance [71, 72, 82, 83]. The first paper was published in 1984 so that the technique is nowadays in its thirties. In the meantime the original approach has been modified and adapted in many ways by other researchers who defined new names or acronyms for the different variants. But as they all go back to the pioneering work of Giaever and Keese, this article will use the name ECIS in general for impedance-based monitoring of adherent cells. As already outlined in a preceding chapter, ECIS readings are sensitive to (1) the coverage of the electrodes with cells and (2) the 3D shape of the cells on the electrode. These rather generic sensitivities are used for a broad range of different assays addressing several key features of cell physiology. Thus, ECIS is considered a multimodal cell monitoring platform.

4.1 Basic Concept of the Measurement

Figure 3 sketches the basic concept of the ECIS technique in more detail than provided by Fig. 1. In ECIS the cells of interest are grown on the surface of planar gold-film electrodes that are deposited on the bottom of a regular cell culture dish. The electrochemical impedance Z of the two-electrode arrangement is the readout parameter to monitor the cells and to describe their potential response to any kind of external stimulus.

Originally the electrodes were prepared on the bottom of individual Petri dishes of several-milliliter volume. Nowadays, the electrode pairs are produced as arrays
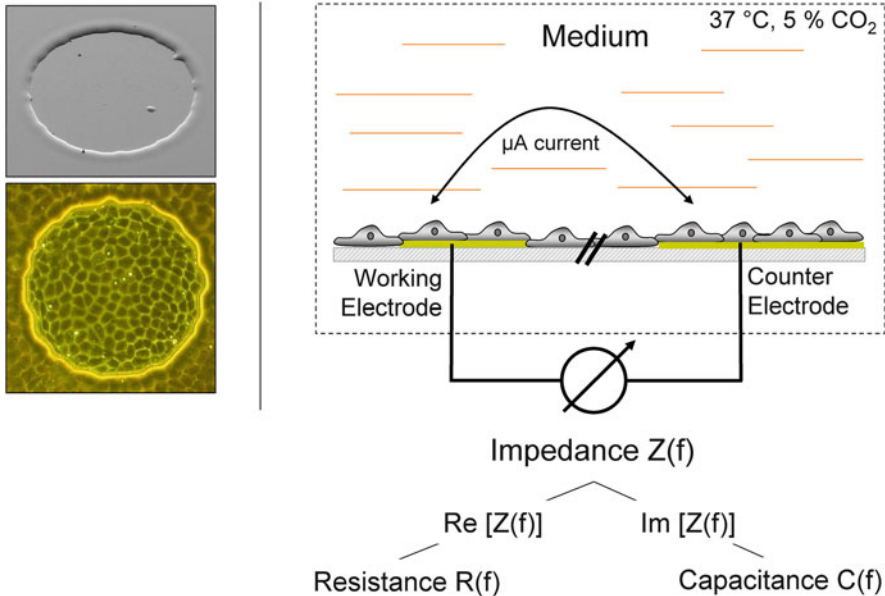
Fig. 3 Schematic representation of the ECIS principal. The cells are grown on planar gold-film electrodes deposited on the bottom of a cell culture dish. They are bathed in ordinary cell culture medium. The working electrode is made significantly smaller than the counter electrode so that the total impedance of the entire system is dominated by the impedance of the cell-covered working electrode. The insert to the left shows an electron micrograph of the cell-free, circular working electrode (*top*) of 250 μm diameter together with a phase contrast micrograph of a cell-covered electrode (*bottom*). The electrodes are produced by cutting a corresponding hole in a photoresist overlayer that insulates the rest of the gold film from the electrolyte

in 8-, 16-, 96-, or even 384-well formats to allow for sufficient parallelization and throughput. When cells are inoculated in these wells, they attach and spread on the electrode surfaces and grow to a confluent monolayer with time under regular cell culture conditions (37 °C, 5–10 % CO_2). The electrical connection between the two coplanar cell-covered electrodes is provided by regular cell culture medium that contains all nutrients and growth factors the cells require. The original approach by Giaever and Keese makes use of two electrodes that differ with respect to their surface area. By making the "counter electrode" at least 100 times larger than the "working electrode," the impedance of the latter dominates the readout of the entire system (cp. Fig. 3) as the impedance scales with the inverse of the electrode area. Thus, the observed changes in electrical impedance arise predominantly from changes that occur at the surface of the working electrode in the original layout [72].

To achieve sufficient sensitivity even for cells providing weak signals, the working electrode should be kept small [72]. Most data available in the literature has been recorded with circular working electrodes of 250 μm diameter in combination with a 500–1,000 times larger counter electrode as indicated in Fig. 4a.
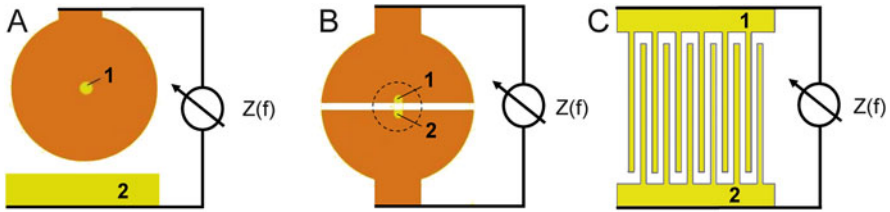
Fig. 4 Different electrode layouts as they are used in impedance-based cellular assays. (**A**) Small working (*1*) and big counter electrode (*2*); (**B**) small working (*1*) and small counter electrode (*2*) with the option to be integrated in micro-wells (*dashed line*); (**C**) interdigitated finger electrodes (*1* and *2*)

Instead of using a coplanar counter electrode, it is also possible to work with a dipping electrode reaching into the culture medium from above. As long as the surface of the dipping electrode is large and the associated interface impedance low, the readout of the system is not affected by this change in electrode geometry [84], but the coplanar arrangement holds significant practical advantages [85].

Other electrode layouts have been established over the years that are tailored for assays with a focus on specific aspects of cell physiology. Figure 4b sketches an electrode arrangement with two electrodes of the same size. Here the impedance readout reflects the averaged response of the cells on both electrodes. As both of them are still small, this arrangement provides a similar sensitivity than the classical arrangement shown in Fig. 4a. With the distance between the electrodes 1 and 2 being on the order of the electrode diameter, the electrodes can be integrated into a micro-well (dashed line) to allow for experiments in volumes of less than 20 μL. Both electrode layouts (Fig. 4a, b) provide the response of a rather small cell population which is just a fraction of all the cells in the entire well. This may create problems whenever the cell population is not distributed homogeneously across the well but shows a position-dependent difference with respect to cell size, cell density, or the cells' responsiveness to a given stimulus. Moreover, assays reporting on cell attachment or cell proliferation are affected by the initial density of cells on the electrode which might be stochastic for small electrodes. Thus, in both cases interdigitated electrode arrangements like the one shown in Fig. 4c provide significant improvement. They integrate over a much bigger fraction of the entire well such that local differences are averaged out and the signal originates from a much bigger fraction of the entire cell population. In return, the increase in total electrode area is disadvantageous for certain assays that require high sensitivity or the use of invasive electric fields for electroporation or cell wounding as will be discussed below.

The *complex* electrical impedance Z of the cell-covered electrodes is the physical parameter reporting on cell behavior (cp. Fig. 3). Its measurement relies on currents (~ μA) and voltages (~ mV) that have proven not to be invasive or harmful to the cells on the electrode [86]. In the literature the time course of the *magnitude* of the complex impedance |Z| is the most widely used descriptor for cell behavior.

Some commercial devices only provide |Z| as a readout parameter. When the *complex* impedance Z is available from more advanced instrumentation, it can be broken down into its real[1] and imaginary[2] components which are expressed as the resistance R (real) and capacitance C (imaginary)[3] of the system, respectively. It depends on the type of assay which quantity is the most well suited and the most sensitive parameter to monitor cell behavior. For instance, it has been shown that the total capacitance of the system is linearly dependent on the fractional surface coverage of the electrode so that capacitance readings are the most direct parameter reporting on cell spreading or cell proliferation [73, 74]. In this article we will only use the *magnitude* of the impedance |Z| as a quantitative descriptor of cell behavior. When time course data is reported, the impedance magnitude is commonly normalized. One common way of normalization is to set the first data point as 1 (100%) and the dimensionless physical observable is then called "normalized impedance":

$$\text{Norm. } |Z| \; = \; |Z|(t)/|Z|(0). \tag{1}$$

One manufacturer of impedance devices for cell analysis has introduced the term "cell index" to describe cell behavior. The "cell index" is calculated by subtracting the impedance of the cell-free electrode from the actual reading before normalization to the value of the cell-free electrode:

$$\text{Cell Index} = \big(|Z|(t) - |Z|(0)_{\text{cell-free}}\big)/\, |Z|(0)_{\text{cell-free}}. \tag{2}$$

As a consequence all experiments have to start with a cell-free electrode in this system to get the reference values $|Z|(0)_{\text{cell-free}}$. Please note that the "cell index" commonly starts at 0, but it may go negative dependent on the equilibration of the electrodes before the experiment.

Another very important and often underestimated parameter in ECIS-type recordings is the AC frequency used for the experiment. The AC frequency controls the current pathway across the cells that are adherently grown on the electrode surface, and thus, it significantly influences the outcome of the experiment as sketched in Fig. 5.

At low frequencies ($f < 1$ kHz) the cells behave essentially like insulating particles forcing the current to flow around the cell bodies on paracellular pathways (solid line in Fig. 5). Current leaving the electrode has to flow through the confined and narrow channels between the lower plasma membrane and the electrode surface before it can escape through the paracellular shunt between adjacent cells into the bulk medium. With the current bypassing the cell bodies, it picks up impedance contributions in the cell–electrode junction as well as in the contact area between neighboring cells. Whenever the cell changes its shape, the geometry of these

---

[1] Impedance for the fraction of the total current that is in phase with the voltage

[2] Impedance for the fraction of the total current that is 90° out of phase with the voltage

[3] $C = 1/[2\cdot\pi\cdot f\cdot\text{Im}(Z)]$ with f as the AC frequency.
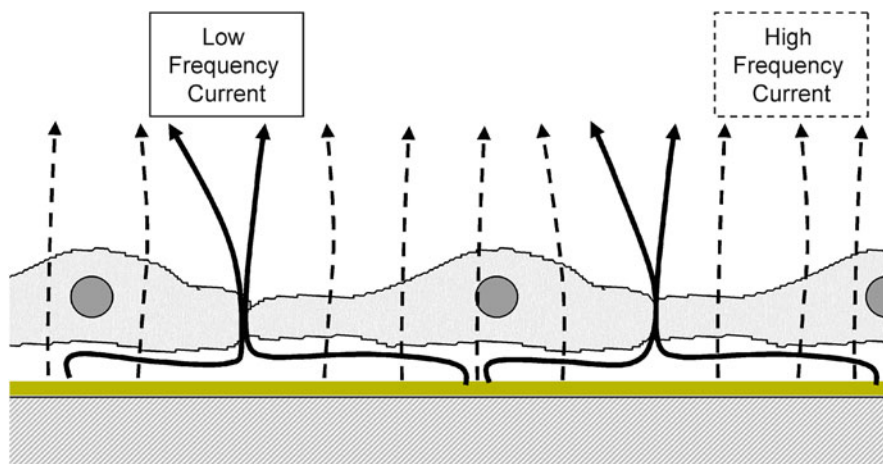
Fig. 5 Frequency-dependent current pathways across a patch of cells adherently grown on the electrode surface. *Solid lines* indicate paracellular current flow underneath and between adjacent cells at low AC frequencies ($f < 1$ kHz for the systems described here), whereas dashed lines describe transcellular currents across the plasma membranes at high AC frequencies (f > 10 kHz)

current pathways and the associated impedance will change accordingly. At high frequencies ($f > 10$ kHz), the current can capacitively couple through the cell membranes (dashed lines in Fig. 5) passing the lower and the upper membrane in the form of a displacement current. Accordingly, high-frequency impedance readings can be used to measure the membrane capacitance. Please note: the specific capacitance of the unfolded plasma membrane is app. 1 μF/cm^2 independent of the cell type. Deviations from this value are solely caused by membrane protrusions like microvilli or invaginations which may increase the true surface area of the membrane significantly over the projected area. Thus, measurements of the membrane capacitance report on membrane topography. Moreover, as (1) the impedance of the cell-covered electrodes is dominated by the capacitance of the cell membranes at high frequencies and (2) the total membrane capacitance scales with the number of cells on the electrode, high-frequency impedance (or capacitance) readings are favorably used to monitor changes in electrode coverage as, for instance, during cell spreading or cell proliferation. At intermediate frequencies (1 kHz $< f <$ 10 kHz), the total current leaving the electrode is split up and it uses both pathways trans- and paracellular. In a sense the AC frequency plays a similar role in ECIS as the focus level in microscopic imaging. The focus level determines which part of the cells is predominantly visible in a microscopic image (top, center, bottom) just like the AC frequency determines in ECIS which cell functionality is mirrored in the datasets (cell shape changes, membrane topography, or electrode coverage).

Recognizing the importance of the AC frequency for the information content of impedance-based cellular assays suggests to measure the impedance along a range of frequencies in order to collect a maximum of information about the cells under
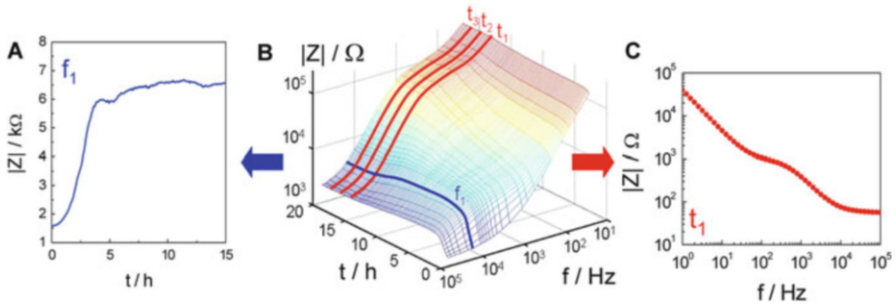
Fig. 6 Evolution of the frequency-dependent impedance magnitude (**b**) of a planar gold-film electrode of 250 μm diameter when initially suspended MDCK-II cells are seeded to confluence on the electrode surface at time zero. *Red lines* indicate frequency spectra of the impedance at individual time points along the experiment (**c**). The *blue line* highlights the time course of the impedance at one frequency (**a**) [87].

test. In a sense repeated frequency scans are similar to scanning a biological specimen microscopically at different focus levels for later 3D image reconstruction. Thus, monitoring time-dependent cell responses in this measurement mode requires recording of repeated frequency scans of the cell-covered electrodes for the time of the experiment. The meaningful frequency range for ECIS-like experiments stretches from 1 Hz to 1 MHz. Dependent on the cell type, this frequency range can get adjusted and confined – in particular as the poorer the time resolution of the repeated measurements, the broader the frequency range to scan. Figure 6 shows the impedance raw data for a typical experiment in which the time course of cell spreading to an initially cell-free ECIS electrode is monitored by repeated frequency scans.

The center graph (Fig. 6b) shows a waterfall plot of the measured impedance magnitude |Z| as a function of AC frequency and experimental time. At $t = 0$ h the impedance spectrum $|Z|(f)$ corresponds to the impedance spectrum of the cell-free electrode. At the end of the experiment, the recorded impedance spectrum represents a fully cell-covered electrode. The red lines indicate individual spectra at any given time point t (t_1, t_2, t_3, ...). The blue line indicates the change in impedance magnitude |Z| for one fixed frequency f_1 along the experiment. Figure 6a, c provides a 2D perspective on the time-dependent impedance at frequency f_1 (Fig. 6a) or the frequency-dependent impedance at time point t_1. The latter is like a snapshot of the cell status with a maximum of information, whereas the former describes the change of one cell functionality that is mirrored in the impedance magnitude |Z| at f_1. Once the complete information (Fig. 6b) is recorded, any type of 2D presentation can be created after the experiment.

Most literature studies on impedance-based cellular assays present time course data of the impedance magnitude |Z| at one particular frequency as shown in Fig. 6a. The AC frequency of the experiment is often predefined by the manufacturer of the device to some average value. Optimization of the AC frequency to the assay and the cell type is only rarely described even though this could potentially pave the

way to many more experimental options and improved data quality. In the current example, the impedance magnitude |Z| at f_1 mirrors the time course of spreading of initially suspended cells to the electrode surface (Fig. 6a). The frequency-dependent impedance data (Fig. 6c) cannot be interpreted directly. A detailed analysis of the data requires modeling and least-square optimization of the model parameters. This particular mode of the measurement will be briefly discussed in Sect. 4.3 even though only a very limited number of researchers have yet made use of this powerful tool.

4.2 Impedance-Based Cell Monitoring: A Multimodal Platform Technology with Broad Applicability

With its generic sensitivity to electrode coverage and morphology changes of the cells on the electrode, ECIS can be applied as a monitoring tool in many different assays that are routinely performed in biomedical research. This chapter introduces the various modes of impedance-based assays and illustrates their individual performance with the help of sample data. Figure 7 sketches the different assays
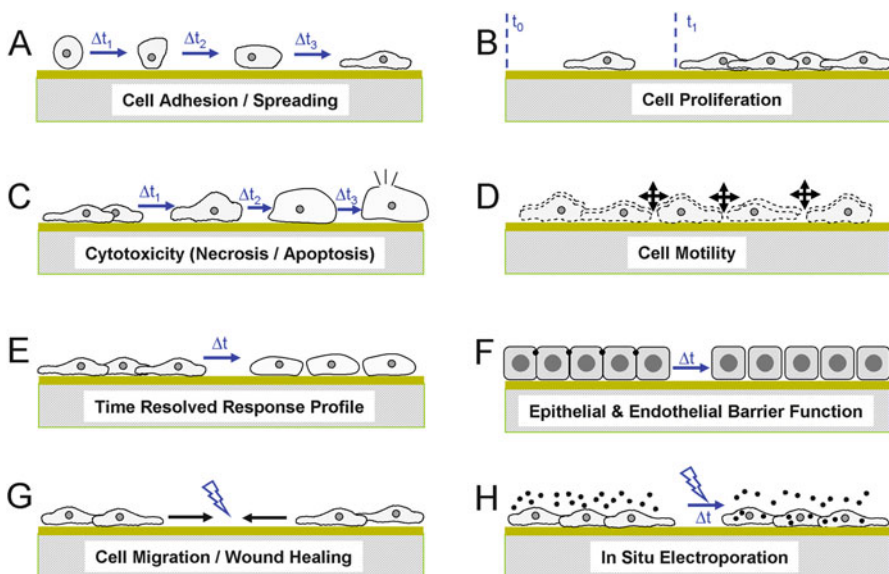
Fig. 7 A collection of different impedance-based cellular assays has been developed capable of monitoring (**a**) the rate of cell spreading; (**b**) the rate of cell proliferation; (**c**) the cytotoxicity profile for a given drug or toxin; (**d**) the micromotility of the cells; (**e**) the time-dependent response of the cells to any kind of stressor (e.g., ligand for cell surface receptor, magnetic field, virus load); (**f**) the barrier function of epithelial and endothelial cell monolayers; (**g**) the rate of cell migration; and (**h**) the loading of adherent cells by in situ electroporation (ISE). The blue flashes indicate the application of invasive electric fields as part of the assay

for adherent cells that are all monitored by noninvasive readings of the electrode impedance. The assays illustrated in Fig. 7g–h are special in the technical sense that they represent a combination of noninvasive cell monitoring and invasive cell manipulation by invasive electric fields (indicated by blue flashes). The cell migration assay (Fig. 7g) is based on killing those cells of a confluent monolayer that reside on the electrode surface with the help of a lethal electrical field [75]. The field irreversibly destroys the plasma membranes. Once the cells on the electrode are dead, cells from the periphery of the electrode, which were not exposed to the electric field, start to migrate into the open space (electrode) within the culture vessel. Repopulation of the electrode by cells that migrate in from the periphery is then again monitored by noninvasive impedance readings. Thus, the elevated electric field is used to create a well-defined lesion within the cell layer similar to the well-known *scratch assay* in which the wound is created mechanically. When strength and duration of the elevated electric field are carefully adjusted, it is possible to reversibly open the plasma membranes of the cells on the electrode (instead of irreversible wounding) to inject membrane-impermeable molecules or nanomaterials into the cytoplasm (Fig. 7h). This in situ electroporation (ISE) is typically sandwiched between two phases of impedance monitoring before and after the ISE pulse so that the response of the cells to the introduction of extracellular material is monitored in real time [88, 89].

The implementation of (invasive) electric field-assisted cell manipulation expands the range of accessible cell-based assays. These extra modes are tailored to study different hallmarks of cell physiology. Please note that the ECIS assays shown in Fig. 7 can also be applied as sequences instead of just a single assay. For instance, an assay reading the time course of cell spreading (Fig. 7a) can be followed by an assay reading cell motility (Fig. 7b) before cell migration is studied in a wound healing assay (Fig. 7g). These or similar sequences of assays can be applied to one and the same cell population since the impedance-based readout is noninvasive (except for the cell killing) and does not require any labels.

Figure 8 shows typical datasets for the various assays illustrated in Fig. 7. The data will be individually discussed in subsequent paragraphs. All of these assay types have also been applied to unravel the biological impact of nanomaterials, as will be detailed below. Considering the enormously wide applicability of ECIS-based assays to such diverse aspects of cell physiology suggests that in the long run ECIS might play a similar role for the analysis of adherent cells as flow cytometry does for the analysis of suspended cells.

4.2.1   Kinetics of Cell Spreading

Recording the kinetics of cell spreading is often used as a quantitative descriptor of cell matrix interactions. ECIS is ideally suited to monitor the time course of cell attachment and spreading with a time resolution down to seconds. To run the assay, monodisperse suspensions of cells are inoculated into the wells of an ECIS
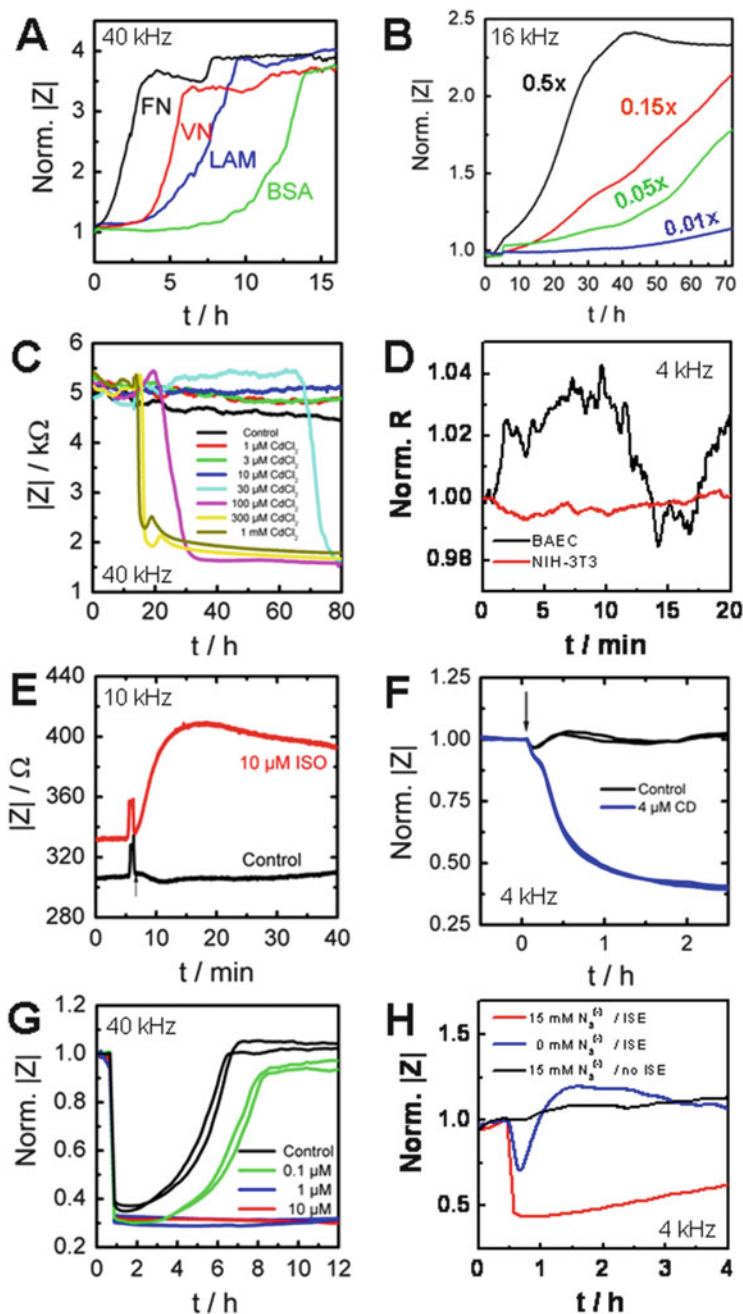
Fig. 8 Typical time courses for selected impedance-based cellular assays addressing (**a**) the kinetics of cell spreading to different extracellular matrix proteins (MDCK cells; *FN* fibronectin, *VN* vitronectin, *LAM* laminin, *BSA* bovine serum albumin); (**b**) the time course of cell proliferation for different seeding densities (NRK cells); (**c**) cytotoxicity assessment for exposure of NRK cells to cadmium chloride; (**d**) cell form fluctuations (micromotion) of two different cell lines; (**e**) time-resolved response profiles of bovine aortic endothelial cells to stimulation with the adrenaline-

electrode array. Attachment and subsequent spreading of the cells on the electrode surface is mirrored by a concomitant increase of the measured impedance with time. This time course data is then used for a quantitative analysis of the spreading process [73]. Figure 8a shows the typical time course of the normalized impedance (every value is normalized to the first data point) when suspended MDCK cells (*M*adin-*D*arby *c*anine *k*idney) attach and spread on electrodes that have been pre-coated with different proteins like fibronectin (FN), vitronectin (VN), laminin (LAM), or bovine serum albumin (BSA). The data reveals a preferred and accelerated spreading of MDCK cells on FN-coated electrodes completed within 4 h, whereas it takes more than 10 h before the cells even start spreading on BSA-coated electrodes [73]. Cell spreading is preferably recorded at a frequency >10 kHz when the signal is dominated by the gradual increase of electrode coverage. Please note that the impedance magnitude |Z| does not scale linearly with the gradual surface coverage. If the geometrical spreading rate of the cell body is required for further analysis, the capacitance should be used as a readout parameter instead as it provides the fractional surface coverage at any time point of the measurement directly. It has been described recently that this rate of cell spreading s is proportional to the ratio of cell-to-substrate adhesion energy W_E and the cortical membrane tension τ ($s \propto W_E/\tau$) that counteracts the flattening of the cell body [91].

4.2.2 Cell Proliferation

Figure 8b shows the typical time course of the normalized impedance over a total of 80 h when proliferation of NRK cells (*n*ormal *r*at *k*idney) is monitored with a continuous increase of the cell number on the electrode surface. Four different cell densities have been inoculated in this example in individual wells to demonstrate the different population dynamics. "0.5x" cell density means that the inoculum was adjusted such that the number of cells is sufficient to cover app. 50% of the electrode surface without the necessity for any further cell division. The initial cell number is then titrated down to 1/50 of the highest cell inoculum. Cell spreading of the initially seeded cells is completed within the first 5 to 10 h. The subsequent time course mirrors cell proliferation. The continuous and time-resolved observation of electrode coverage provides access to the cells' doubling times and how this might change upon exposure to toxins or other experimental stimuli. It is noteworthy that all curves in Fig. 8b show a change in slope approximately 35 h after inoculation. These dips in the impedance time traces indicate a synchronized cytokinesis of the cells on the electrode as the cells were grown to contact inhibition before they were collected for the proliferation experiment.

Fig. 8 (continued) derivative isoprenaline (ISO); (**f**) impact of cytochalasin D on epithelial barrier function (MDCK); (**g**) the impact of daunomycin on the rate of cell migration in an ECIS-based wound healing assays; and (**h**) influence of sodium azide on viability of NRK cells after delivery to the cytoplasm via ISE. Adapted from [90]

Similar observations have been made for synchronized HeLa cells in the literature [92].

4.2.3   Cytotoxicity (Apoptosis, Necrosis)

Monitoring the cytotoxicity of drugs, toxin, and pollutants in contact to adherent cells is one of the most important and widely applied impedance-based cellular assays [76, 93, 94]. The spectrum of stressors comprises chemical, biological, and physical challenges to the cells. The biggest asset of noninvasive and label-free devices in this respect is the opportunity for continuous and automated observation over extended time periods so that there is no need to predefine the exposure time a priori. When the cells are followed continuously for a prolonged time, dose–response relationships can be established for different exposure times from a single experiment providing significant extra information. Upon exposure to eventually lethal challenges, the cells will undergo either apoptosis or necrosis. During necrosis the bodies swell and eventually rupture. Apoptotic cells disassemble themselves, shrink, and retract. In either case the electrode impedance will decrease from the values of cell-covered electrodes to values of cell-free electrodes as soon as the toxic response is complete. Figure 8c shows typical time traces of the impedance magnitude |Z| for confluent NRK cells that were exposed to increasing concentrations of cadmium chloride after an initial 12 h of baseline recording. The cytotoxic impact of the cadmium ions is clearly dose dependent, and for the highest concentrations, the cells round up from the electrode surface immediately. For 30 µM $CdCl_2$ the NRK cells seem initially unaffected for more than 60 h of exposure before even these cells die presumably due to an accumulation of harmful impact. Cadmium concentrations equal or lower than 10 µM do not induce any cell response within the observation time. From datasets like this, EC_{50} values can be extracted for any exposure time from a few minutes to almost 72 h.

4.2.4   Cell Motility (Micromotion)

Even in confluent monolayers with no open spaces for lateral cell migration, the individual cells are constantly in motion. Intracellular organelles are changing positions and the cell bodies perform stochastic shape fluctuations that are metabolically driven and mediated by the cytoskeleton. These fluctuations become visible in time-lapse video microscopy with single cell resolution. They are also mirrored in subtle fluctuations of time-resolved impedance readings of cell-covered ECIS electrodes. When they were first discovered, the term *micromotion* was invented for this kind of cell body dynamics. Micromotion is most sensitively detected by the associated impedance fluctuations at intermediate AC frequencies when the signal is sensitive for both changes in extracellular current pathways and membrane topography. The impedance fluctuations scale with the amplitude of cell body dynamics. Thus, ECIS provides a quantitative and automated experimental

access to such cell shape fluctuations as a bioanalytical descriptor of cell behavior that has proven to be very sensitive to nutrient supply, cytoskeleton-active drugs, and the inherent and individual motility of different cell types [95–97]. Figure 8d shows micromotion time traces of two different cell lines with a distinctly different inherent motility: bovine aortic endothelial cells and NIH-3T3 fibroblasts. Whereas the latter show a rather smooth resistance profile, the former create a very noisy time series which is like an imprint of their cell body dynamics. Please note that micromotion datasets are typically recorded for only a few minutes. Thus, they must be considered as being a "snapshot" of cell motility.

4.2.5 Time-Resolved Response Profiles

The term "time-resolved response profile" (TRRP) refers to an assay type that provides an unbiased observation of the cells' response to any kind of stimulus inducing a cell shape change. In a sense the cytotoxicity assay described above is a special case of a TRRP along which the cells eventually die. But the general term TRRP also comprises assays that record non-harmful changes in cell physiology like the onset of intracellular signal transduction cascades [37], cell volume changes [98], or changes in cell differentiation [99]. Recording a TRRP to a yet unknown challenge or stimulus is most meaningful performed by recording repeated frequency scans in order to gather a maximum of information about the cell response. Later on, during analysis, an appropriate frequency can be selected to create and analyze the time course data. As an example, Fig. 8e shows the response of confluent layers of bovine aortic endothelial cells when exposed to a 10 μM bolus of isoprenaline (ISO) relative to a vehicle control. ISO is a derivative of adrenalin that binds to the β-adrenergic cell surface receptors stimulating the associated intracellular signal transduction cascade. The time profile of intracellular signal transduction after receptor activation is mirrored in the time course of the impedance magnitude |Z|. Repeated performance of this assay with other doses of ISO provides the database to establish dose–response relationships that characterize the ligand–receptor interaction [100]. Similar assays can be performed to study entirely different cell physiological phenomena, but they always return a time-resolved response profile for the experimental stimulus.

4.2.6 Monitoring Epithelial and Endothelial Barrier Function

Time-resolved response profiles as introduced in the preceding paragraph are typically recorded at an intermediate AC frequency providing the highest sensitivity of the measurement. It is the rationale of this strategy to detect even the smallest cell response to a given stimulus regardless of which part of the cell body is responsible for the observed signal change. For assays addressing a more specific question, it may be advantageous or even necessary to "zoom in" on certain parts of the cell body and make the overall signal being dominated by this particular cell

structure. The AC frequency at which a TRRP is recorded provides control over the current pathway across the cell layer, as will be detailed in Sect. 4.3. Thus, selecting a tailored frequency provides the experimental option to prefocus the impedance readout to the point of interest within the cell layer. Monitoring epithelial or endothelial barrier function is one example for such a scenario. These interfacial tissues line all inner and outer surface of the body. By virtue of their location, they serve as a diffusion barrier between the two compartments that they are separating and restrict the diffusion of solutes along the paracellular shunt between adjacent cells. The structural basis of this barrier function is provided by the so-called tight junctions, a special type of cell junction occluding the paracellular shunt at the most apical pole. When ECIS readings are performed below a threshold frequency that depends on electrode size and cell type, the measurement predominantly mirrors the tightness of these junctions [101]. Figure 8f shows the time course of the normalized impedance |Z| when a layer of kidney epithelial cells (MDCK) is exposed to the fungal toxin cytochalasin D (CD). CD is known to inhibit actin polymerization but to leave depolymerization unaffected such that a net contraction of the filaments occurs. The shortening and disassembly of the filaments is accompanied by an opening of the tight junctions and a corresponding loss of barrier integrity. The time course of the impedance shown in Fig. 8f reports on the breakdown of the epithelial barrier completed within 2 h. Cells under control conditions remain largely unaffected by a corresponding dose of the solvent only. As nanomaterials enter the human body by permeating across epithelial and/or endothelial tissues depending on their site of entry and their final destination, this special type of TRRP is an important ECIS-based assay to evaluate the interaction of nanomaterials with the inner and outer surfaces of the body. It is noteworthy that even with a perfect frequency selection, ECIS readings will only be dominated but not exclusively determined by the tight junctions. A clear and unambiguous analysis of barrier function in response to some experimental stimulus requires multifrequency impedance recordings followed by quantitative data analysis using a physical model [85, 102]. This aspect of ECIS data recording and analysis is addressed in the subsequent section (Sect. 4.3.)

4.2.7 Cell Migration/Wound Healing

Cell migration is commonly studied with the help of so-called wound healing assays. Several variants have been developed that all have in common that a geometrically well-defined lesion or cell-free area is introduced (scratch assays) or maintained (barrier assay) within a confluent cell monolayer, respectively. When the assay is started by introducing the lesion or removing the barrier to the cell-free area, the cells start to migrate into the open space such that a confluent cell layer is formed at the site of the initial lesion. Closing of the lesion is followed and analyzed by video microscopy to determine the speed of migration. Compared to the well-established *scratch assay*, the ECIS-based wound healing assay replaces (1) mechanical by electrical wounding of the cell layer and (2) microscopic

observation of wound closure by noninvasive impedance measurements. Electrical wounding is performed by applying a voltage of several volts (4–5 V) for several seconds (20–30 s) to the cell-covered electrode which leads to irreversible membrane electroporation and cell lysis. Figure 8g shows the time course of the normalized impedance of confluent NRK cell layers before and after the cells on the electrode are killed by an electrical voltage pulse. After pulse application the impedance decreases immediately to values of a cell-free electrode as the cells on the electrode have been irreversibly permeabilized. Within the next hours, the impedance slowly recovers to pre-pulse values as the cells from the periphery of the wound start to migrate into the open space under control conditions (black) [75]. The experiment in Fig. 8g compares the time course of wound healing for NRK cells that were exposed to increasing concentrations of daunomycin, a compound used in chemotherapy. Small doses of just 0.1 μM slow down the healing process; at higher concentrations of 1 and 10 μM, wound healing is completely inhibited. Obviously cell migration is efficiently compromised by daunomycin concentrations higher or equal to 1 μM. Time course data like the one shown in Fig. 8g can be analyzed for characteristic parameters describing the healing process in quantitative terms (e.g., time necessary for 50% impedance recovery $t_{50\%}$) such that dose–response relationships are accessible.

4.2.8 In Situ Electroporation

Section 4.2.7 describes the use of elevated electric fields to kill the cells on the electrode and introduce a well-defined lesion into the cell layer to initiate cell migration and wound healing. In this assay the cells are killed by an irreversible dielectric breakdown of their plasma membranes that get permeabilized and lose their function as a diffusion barrier. When the voltage pulse is carefully adjusted – in particular with respect to pulse duration – it can be used to *reversibly* permeabilize the membrane for a short time. This phenomenon is called *electroporation* as the membrane is thought to be porated during field application. Reversible permeabilization or electroporation can be used to introduce membrane impermeable compounds from the extracellular fluid into the cytoplasm by facilitated diffusion through the electropermeabilized membrane. Whereas cell wounding works best and very efficient with pulses of 20–30 s duration, electroporation pulses are only applied for 100–200 ms to ensure reversibility of membrane permeabilization. The voltage or field strength is similar in both assays as wounding and electroporation require the membrane potential to exceed approximately 1 V for dielectric breakdown. Under these conditions, the pores created in the membrane are thought to have diameters in the nanometer range that are small enough to heal as soon as the field is switched off. Electroporation is commonly applied to suspended cells in cuvette-like chambers with electrodes on opposing sides. When the electric field is applied to adherent cells with the help of planar electrodes that the cells grow on, the technique is referred to as *in situ electroporation* (ISE). ISE has been integrated in ECIS experiments such that the impedance of a cell-covered

electrode is measured before and after the ISE pulse [88, 89]. With this integration of ISE in ECIS-based cell monitoring, the cell response to the ISE pulse and the concomitant introduction of membrane impermeable compounds from the extra-cellular fluid is directly measurable. There is an unavoidable overlay of the cell response to the ISE itself and the compound injection. But the cells recover from the ISE alone within less than an hour so that any cell response later than this is caused by the compound that has reached the cytoplasm by diffusion through the electropores. Figure 8h illustrates the outcome of combined ECIS-ISE assays. Normal rat kidney (NRK) cells were grown to confluence on ECIS electrodes, before they were exposed to 15 mM NaN_3 in the extracellular fluid. Without ISE the cells do not show any significant response to the presence of NaN_3 (black curve) even though it is a well-known inhibitor of the electron transport chain (ETC). However, NaN_3 is not membrane permeable and is therefore excluded from the cytoplasm. Upon ISE (40 kHz, 4.0 V, 200 ms), the azide is introduced into the cytoplasm and it gets access to the ETC (red curve). Accordingly, the cells respond immediately by a significant drop of the measured impedance that just poorly recovers along the time course of the experiment. ISE alone (blue curve) does also lead to an impedance drop as the homeostasis of the cells has been disturbed by the electroporation pulse. The impedance recovers, however, to pre-pulse values within less than an hour. This assay can be used to introduce nanomaterials into the cytoplasm on membrane-independent mechanism and study their impact on cell physiology.

4.3   Modeling the Impedance of Cell-Covered Electrodes

Recording time course data of the impedance at one particular frequency is one experimental option to monitor, analyze, and interpret the cell response within the various impedance-based assays described above. By careful selection of the monitoring frequency, the measurement can be tailored to report predominantly on a given cell structure (e.g., barrier forming tight junctions, membrane topography). Even though ECIS readings are dominated by the electrical properties of this particular cell structure under these conditions, there will always be contributions from other sources included in the signal. Exclusive information is only available from multifrequency impedance readings and subsequent analysis of the recorded impedance spectra by physical modeling. The modeling breaks down the overall, holistic impedance of the cell layer into contributions of the different cell structures. When impedance spectra have been recorded repeatedly along the time course of the experiment (cp. Fig. 6), each single spectrum may get analyzed by this model yielding the time courses of the individual impedance contributions or cell-related parameters derived from these. An analogy to optical microscopy might again be helpful in this context: when the AC frequency in ECIS experiments is considered as an equivalent to the focus level in microscopy, then time course data at a single frequency corresponds to time-lapse video microscopy at a constant focus level.
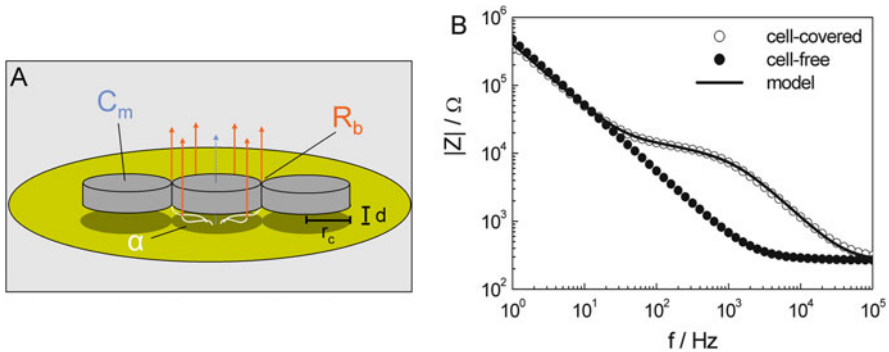
Fig. 9 (**a**) Schematic to visualize the electrochemical model that is used to analyze the frequency-dependent impedance of cell-covered gold-film electrodes. (**b**) Frequency-dependent impedance of a cell-free gold-film electrode (*filled circles*) compared to the frequency-dependent impedance of a cell-covered gold-film electrode (*open circles*). The solid line represents the transfer function of the model after parameter optimization

Within this context repeated frequency scans resemble a time-resolved 3D reconstruction of the cells. Physical modeling of the data is similar to a deconvolution algorithm in this comparison that provides the observation of individual cell structures with improved resolution.

The analysis of the overall frequency-dependent impedance is preferentially performed by fitting a physical model that was originally derived by Giaever and Keese [72] to the experimental data using least-square optimization. The transfer function of the model is derived by considering the cells as circular disks with radius r_c hovering in a distance d above the electrode surface (Fig. 9a). It is assumed that the extracellular current flows radially along the electrolyte-filled space formed between the lower membrane of the cell and the electrode surface (cell–electrode junction) before escaping into the bulk solution through the paracellular shunt. The impedance arising in the cell–electrode junction underneath the cells is represented in the model by a parameter α which is defined as follows:

$$\alpha = r_c \cdot (\rho/d)^{\frac{1}{2}}. \tag{3}$$

Herein, ρ denotes the specific electrolyte resistivity within the cleft between membrane and electrode, and d represents the height of the cleft. The unit of α is $\Omega^{\frac{1}{2}}$ cm. With respect to units, it might be more intuitive to use α^2 as a measure for the resistance of the cell–electrode junction as the latter is measured in units of Ω cm^2. Further up in the paracellular shunt between adjacent cells, impedance arises at the level of the cell-cell junctions which is accounted for in the model by a resistance R_b (resistance between cells).

As indicated in Fig. 9a and also Fig. 5, there is a fraction of the current flowing across the plasma membranes through the cells on transcellular pathways. This current has to overcome the impedance imposed by the plasma membranes Z_m. Plasma membranes are typically characterized with respect to their dielectric

behavior by resistive and capacitive properties. As the membrane resistance is typically several orders of magnitude higher than the capacitive impedance, the model simplifies the membrane impedance by a simple capacitor. Thus, the third parameter of the model C_m accounts for the specific capacitance of the plasma membrane. Comparing the specific capacitance of the *unfolded* plasma membranes of very different cell types returns a rather constant value of 1 µF/cm^2 for all of them indicating that the specific dielectric properties are rather similar independent of the cell type. If the measured value for C_m deviates significantly from 1 µF/cm^2, this is a strong indication that the plasma membrane is folded by microvilli or membrane invaginations. Membrane folding produces a significant increase of the true plasma membrane surface area compared to the projected area of the cell body. This is an important mechanism of cell types involved in active solute transport, like transporting epithelia, to increase solute transfer rates. Accordingly, the numerical value of C_m reports on membrane topography and its changes along the time course of an experiment.

Bringing all contributions together, the total impedance of the cell-covered electrode is described by the equation

$$Z_{total} = \left(\frac{1}{Z_n} \left(\frac{Z_n}{Z_n + Z_m} + \frac{\frac{Z_m}{Z_n + Z_m}}{\frac{\gamma r_c}{2} \frac{I_0(\gamma r_c)}{I_1(\gamma r_c)} + R_b \left(\frac{1}{Z_n} + \frac{1}{Z_m} \right)} \right) \right)^{-1} \tag{4}$$

with $\gamma \cdot r_c$ abbreviating

$$\gamma r_c = r_c \sqrt{\frac{\rho}{h} \left(\frac{1}{Z_n} + \frac{1}{Z_m} \right)} = \alpha \sqrt{\frac{1}{Z_n} + \frac{1}{Z_m}}. \tag{5}$$

In these equations Z_n is the impedance of the naked (cell-free) electrode, Z_m is the total impedance of the apical and basolateral plasma membranes with $Z_m = 2/(i \cdot \omega \cdot C_m)$, and I_0 and I_1 are modified Bessel functions of the first kind of order 0 and 1, respectively. The impedance of the cell-free electrode is available from corresponding measurements or by analysis of the low-frequency end of the spectrum assuming a constant phase element behavior (CPE), so that $Z_n = Z_{CPE}$ [85, 102]. More details about the derivation of this model are given elsewhere [72].

Figure 9b compares the frequency-dependent impedance magnitude of a cell-covered electrode (open circles) with the impedance of the same electrode but without cells (filled circles). The solid black line in Fig. 9b represents the calculated values of Eq. (4) after the parameters of the model were adjusted to the experimental data by least-square optimization. Good agreement between experimental and model data is apparent and underlines that the three-parameter model derived by Giaever and Keese describes the impedance of the cell-covered electrode completely using a minimum number of parameters. Accordingly, *time-resolved* impedance readings are not only suitable to track changes in cell morphology, a detailed analysis of the *frequency-dependent* impedance also provides information

which part of the cell body responds to the stimulus. Up to now time-lapse video microscopy is the only experimental alternative to disclose similar information [103]. However, ECIS is significantly more sensitive than optical microscopy [72], and it is capable of reporting on subtle morphology changes in the nanometer range.

A note of caution is added here with respect to the modeling of ECIS-like impedance data: in the literature models with a higher number of parameters have been described which supposedly derive more cell-related parameters from the same type of raw data. But closer inspection of the fitting results always confirms that those models are more or less overparameterized and some parameters are redundant. The ECIS model described above does not suffer from these shortcomings and is the best, nonredundant model available till now [76].

To underline this statement, Fig. 10 shows a set of numerical simulations based on the transfer function given in Eq. (4). These curves illustrate the response of the frequency-dependent impedance to changes in any one of the three cell-related parameters R_b, α, or C_m. The black curve in all three figures (Fig. 10a–c) represents a somewhat arbitrary reference cell layer attached to a gold-film electrode of 0.03 cm^2 surface area. The reference cell layer is characterized by the following triple of ECIS parameters: $R_b = 50$ Ω cm^2; $\alpha = 10$ $\Omega^{0.5}$ cm; $C_m = 1$ μF/cm^2. In this calculation the impedance of the cell-free electrode (Z_n) including the bulk electrolyte was set to typical values that we know from the pool of our data. In Fig. 10a the resistance between cells R_b representing the cell–cell junctions is sequentially increased from 50 Ω cm^2 to 200 Ω cm^2, whereas all other parameters were kept constant. The figure shows that the almost frequency-independent, horizontal part of the spectrum that separates the two dispersions is shifted to higher |Z| values with no changes to the internal structure of the spectrum. However, when the parameter α is sequentially increased (Fig. 10b) from 10 to 40 $\Omega^{0.5} \cdot$cm, while all other parameters are kept constant, it is the slope in this center region of the spectrum that increases and makes this part more and more frequency dependent. As R_b determines the height of the central "step" in the impedance spectrum, whereas α dictates the slope in that regime, both parameters are distinguishable and can be quantified independently. Figure 10c finally demonstrates that the impedance spectrum changes in the region of the high-frequency dispersion when the
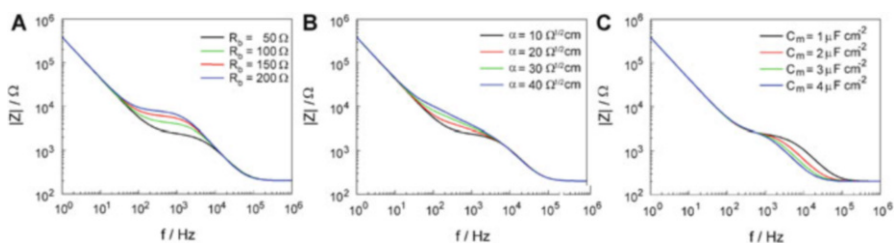
Fig. 10 Numerical simulations of the frequency-dependent impedance for cell-covered electrodes assuming different cell-related parameters. (**a**) Variation of the parameter R_b: $\alpha = 10$ $\Omega^{0.5}$ cm, $C_m = 1$ μF/cm^2. (**b**) Variation of the parameter α: $R_b = 50$ Ω cm^2, $C_m = 1$ μF/cm^2. (**c**) Variation of the parameter C_m: $R_b = 50$ Ω cm^2, $\alpha = 10$ $\Omega^{0.5}$ cm

membrane capacitance C_m is sequentially altered from 1 to 4 $\mu F/cm^2$, while the parameters R_b and α were kept constant.

These simulations illustrate that the ECIS model fully describes all spectral features for the frequency-dependent impedance of a cell-covered electrode in the frequency regime that is affected by the presence of cells on the electrode. The high- and low-frequency regime of the spectra shown in Fig. 10 is determined by the impedance of the electrode–electrolyte interface or the resistance of the culture medium, respectively. Both are not affected by morphology changes of the cells on the electrode. In order to extract more than three cell-related parameters from the frequency-dependent impedance of cell-covered electrodes, other electrode layouts, frequency regimes, or well-defined chemical manipulations of the cells on the electrode are required.

It is important to recognize that the acquisition of repeated frequency scans requires time and is only applicable to assays and cell responses that do not occur on timescales of seconds or a few minutes. This ECIS mode provides a maximum of information about the cells under study but at the cost of a rather poor time resolution. As a compromise the frequency range, the number of frequencies per sweep, or the number of wells followed in parallel can be reduced and adapted to meet the time resolution that is needed for later analysis.

5   Measuring the Biological Impact of Nanomaterials by Impedance Analysis: A Multimodal Approach

Analyzing the biological impact of nanomaterials by label-free approaches is still in its infancy. Researchers all over the globe have just started to recognize the advantages of label-free cellular assays for the assessment of nanomaterials' biological effects in vitro. This development will persist as it has been shown that some of the most established label-based assays suffer from interferences of the nanoparticles with the reagents of the assay. The subsequent paragraph summarizes some of the results that have been obtained from impedance-based assays when adherent cells encounter nanomaterials in different situations along their life span. This overview is, however, not meant to provide a complete survey about all the literature to the subject but much more a cursory collection to highlight their potential. It is important to recognize that to the best of our knowledge, all the impedance-based assays described above have been only applied individually. Another level of understanding might become available when sequences of these assays are applied to one given cell population exposed to a nanomaterial of interest, yielding a complex response profile with information from different aspects of cell physiology (e.g., adhesion, micromotion, migration).

5.1 Nanoparticle Impact on Cell Adhesion

When anchorage-dependent mammalian cells are suspended as single cells in solution, the natural tissue architecture including the extracellular matrix materials, cell-to-matrix junctions, and cell-to-cell junctions and the organization of the intracellular cytoskeleton are changed dramatically – to mention just a few structural features. Nanoparticle encounter in this situation may have a significant impact on their normal attachment and spreading to a protein-decorated surface and their later maturation into a polarized and differentiated phenotype. When the particles are severely harmful, the cells might not even be able to spread but die close after their interaction with the nanomaterial. Hondroulis et al. studied the impact of six different nanomaterials on the physiology of such a diverse pair of cell types as human lung fibroblasts and rainbow trout gill epithelial cells [104] that were exposed to the nanomaterials in suspension prior to inoculation. The rationale for this selection of test cells has been the notion that nanomaterials are likely to be absorbed by the human body via the airways when they are released into the atmosphere. Under these conditions, lung cells are the first to encounter these materials. Moreover, when nanoparticles get access to the ecosystem, they may end up in ground water and eventually in the aquatic system. This latter scenario is modeled by using rainbow trout cells. The homemade electrode arrays were produced according to the specifications of the commercial arrays bearing a small circular electrode of 250 μm and a much bigger counter electrode. Instead of reporting the impedance magnitude |Z|, the authors monitor cell behavior by the real part of the complex impedance, the resistance, at an unspecified frequency. The cells were seeded in a rather high inoculum so that a complete monolayer was formed within 20 h under control conditions. The nanoparticles were mixed into the cell suspension prior to inoculation. Thus, this assay reports on the nanomaterial impact on cell adhesion and spreading upon the extracellular matrix proteins as well as subsequent cell maturation. The raw data is therefore rather similar to a *cell spreading* assay, as it is depicted in Fig. 8a. Both cell types did not attach and spread on the electrodes at all when CdO nanoparticles were present in the seeding solution indicating their very toxic potential. In contrast, neither 10 nm nor 100 nm Au particles showed any impact on the time course of cell spreading and maturation. The toxicity of silver nanoparticles and single wall carbon nanotubes was in between these two extremes. The smaller silver nanoparticles with 10 nm diameter were found to be significantly more toxic than the bigger ones (100 nm). Please note that this impedance-based assay reports on the response of the cells to nanomaterials when their cytoskeleton fibers are largely disassembled and the cell body is in an entirely unpolarized state. A comparison to the response of mature cell monolayers is therefore quite difficult.

   This general assay scheme of monitoring changes in the time course of attachment, spreading, and maturation of adherent cells in the presence or absence of test compounds has been applied to other pairs of nanomaterial/cell type as well. For instance, Male et al. [105] studied the time course of cell spreading and maturation

by resistance readings at 4 kHz when Chinese hamster lung fibroblasts V79 cells were exposed to different types of quantum dots (CdTe, CdSe, InGaP). Whereas CdTe- and CdSe-based quantum dots affected V79 cells significantly in this assay, the InGaP-based QDs did not induce any cell response. The latter did not show any indication for toxicity at all. Surprisingly the initial rate of resistance increase during cell spreading within the first hour of the experiment was not affected in any case. But the impact of the toxic particles changed the time course drastically after that. Compared to the control population, the CdTe-QDs induced a transient maximum in the resistance exceeding the control curve and a subsequent dose-dependent decrease toward resistance values of a cell-free electrode by the end of the 20 h observation time [105]. In contrast the CdSe-QDs did not induce such an overshooting of the resistance and the subsequent decrease was less pronounced and almost linear in time. InGaP-QDs did not affect the shape of the time-dependent resistance curves at all. Thus, the different time course patterns may reflect different mechanisms of action of the different types of QDs. Moreover, the raw data allowed the calculation of a time-dependent EC_{50} which decreased with increasing exposure time as observed for other materials as well.

The same protocol was applied by the same group to study the cytotoxicity of TiO_2 particles of different shape and different crystal structure (rutile versus anatase). V79 cells were again used as test system together with the very popular insect cell line Sf9 [106]. The V79 cells showed a dose-dependent sensitivity to rutile-type TiO_2 nanoparticles ($EC_{50} \approx 300$ ppm), but they were entirely insensitive to anatase-type particles indicating that the crystal structure of the material might be decisive for its biological response. It is very likely the surface of the particle that changes with the crystal lattice so that the cells respond differently to particle encounter. Comparing the resistance time courses of these experiments to the ones reported for quantum dots above [105] reveals that the TiO_2 particles produce an individual time course pattern that is strikingly different from the one recorded for QDs even though the same cell line was used in the very same experimental setting. Thus, the shape of time course data in ECIS-like experiments may contain extra information about the mechanism of cell-nanoparticle encounter. When insect cells Sf9 were used in this assay, the cell response was also individually different for the different TiO_2 forms, anatase and rutile. Similar to the mammalian test system, the insect cells responded more sensitively to the rutile-type TiO_2 particles ($EC_{50} \approx 158$ ppm) but were also affected by anatase-type particles with EC_{50} values between 200 and 400 ppm dependent on the anatase content of the test material [106].

Another type of assay [107] seeds the test cells at rather high inoculum such that there is only very little room for further cell proliferation. The cells are allowed to settle on the electrode for 16–20 h before the nanomaterials are added to the system. The control curves show that the cells have not reached an equilibrium impedance value after this preincubation indicating that a mature cell monolayer has not yet formed. When the nanomaterials are added to the system, the final impedance increase compared to control conditions and its subsequent time course are affected dependent on the dose and the material under test. Severe interference of the

nanoparticles with cell physiology brings back the impedance to values of a cell-free electrode. Otero-Gonzales et al. performed this assay using human bronchial epithelial cells (cell line 16HBE14o) as test cells and screened eleven different inorganic nanoparticles for their impact on cell maturation. The observation time in the presence of the particles was 60 h. Particles made from Fe^0, CeO_2, Fe_2O_3, HfO_2, TiO_2, and ZrO_2 were found to have no significant bioresponse below 1,000 mg/mL. In contrast, particles produced from $Al_2O_3 < SiO_2 < Ag^0 \approx Mn_2O_3 \approx ZnO$ were increasingly invasive to the human lung epithelial cells. The analysis of the time course data after 48 h of exposure was in close agreement with MTT assays performed in parallel except for the Al_2O_3 particles. This material showed a strikingly decreased invasiveness in the MTT assay which might be due to an interaction between the particles and the assay reagents [107]. It is noteworthy that none of the nanomaterials produced any change in the measured impedance in the absence of cells indicating that there is no interference with the electrodes or any other part of the experimental setup.

5.2 Nanoparticle Impact on Cell Proliferation

Studying cell proliferation is among the most widely applied cell-based assays as it addresses the most relevant hallmark of tumor progression. Drugs that have a potential to be used as cytostatic in chemotherapy are often tested in such assays to substantiate their biological activity and unravel their potency. Moreover, chemicals that are suspected of interfering with cell proliferation are screened for their cytostatic activity to define threshold concentration below which these compounds are safe to use. Figure 7b sketches the ECIS-based proliferation assay which is easy to perform and simply relies on the sensitivity of the measured impedance on electrode coverage. Since the impedance mirrors the coverage of the electrode, its change with time is an indicator for the proliferation rate of the cells under test. Thus, the cells are commonly seeded in low density at the beginning of the experiment to produce an initially sparse coverage of the electrode. As soon as the initially seeded cells start to proliferate, the overall impedance increases with time due to the increasing number of cells on the electrode. Figure 8b provides sample data for the outcome for such an impedance-based proliferation assay for different seeding densities and a total experiment time of 72 h. When the experiment is repeated for a given dose of a test compound, the slope of the impedance curve reveals a potential change in cell proliferation. Cell proliferation assays are heavily performed when the biological activity of nanomaterials is tested and considered. Most studies prefer the more classical label-based approaches, but as the evidence accumulates that many nanomaterials interact with the different constituents of such assays [108], label-based approaches are catching up.

In one of the earliest studies in this respect, Huang et al. [109] used impedance-based proliferation assays to study the impact of commercially available silica particle mixtures that had a wide distribution of diameters (0.35–3.5 μm). Two

different human lung carcinoma cell lines (A549 and SK-MES-1) were used as test systems. The authors carefully optimized the experimental protocol to ensure that particle exposure was timed such that the cells were in exponential growth phase and particle impact on cell proliferation was studied. These preexperiments to establish the proper assay conditions were of the same type as shown in Fig. 8b. The individual seeding densities for both cell lines were adjusted to yield exponentially growing cells on the electrode surface after 24 h. At this point in time, the particles were added in increasing concentrations. The experimental data nicely shows that particle impact is cell type dependent with the SK-MES-1 cells being more sensitive to nanoparticle encounter. Whereas the data shows just a slowdown of cell growth with an EC_{50} value of 0.21 mg/mL for A549 cells, the impedance fell below the starting values for SK-MES-1 cells indicating that they were not just slowed down in their proliferation, but a fraction of the cells must have retracted or even rounded up which is indicative for the onset of cytotoxicity. Accordingly, the EC_{50} values for particle impact were found to be 0.04 mg/mL after an exposure time of 36 h [109].

Chuang et al. studied the impact of gold nanoparticles on the proliferative capacity of six different cell lines derived from different tissues (the colon, lung, connective tissue, kidney) applying impedance-based assays [108]. They used three types of gold nanoparticles as model compounds which differed only slightly with respect to their sizes: (a) 10×39 nm, (b) 10×41 nm, and (c) 10×45 nm. The cells were seeded in low inoculum, allowed to attach and spread on the electrode surface before they were exposed to the different nanoparticles for 72 h, while the proliferation-based increase in cell number on the electrode surface was monitored by impedance readings. The six different cell lines were differently affected in their growth. The lowest dose that was tested in these experiments was 72 ng/mL, and some cell types were slowed down in their growth rate significantly by this particle concentration, as, for instance, A549 cells derived from the lung (10×45 nm). Other cell types responded to the nanoparticle encounter when concentrations were equal or higher than 180 ng/mL as, for instance, AGS cells derived from the colon (10×39 nm). NIH-3T3 fibroblasts were found to be the least sensitive as they could take 360 ng/mL before a slowdown of their growth rate was observed (size not specified). One conclusion of these experiments has been highly anticipated: the impact of gold nanoparticles on cell proliferation is dependent on cell type and tissue origin.

Much less anticipated is when one cell type was exposed to the same doses of gold nanoparticles that differ by just 2–4 nm in size (e.g., 10×41 nm versus 10×45 nm), the particles' impact on cell proliferation was found to be strikingly different. For instance, the proliferation rates of A549 cells (lung) were heavily affected by 72 ng/mL of 10×45 nm particles, whereas they showed just a very moderate response when exposed to 360 ng/mL of 10×41 nm particles [108]. The other cell types in this study were also able to differentiate between particles of such a slightly different diameter. In all cases gold particles with an intermediate size of 10×41 nm were the least invasive. This astonishing result was confirmed by classical MTS assay that provided EC_{50} values for the different particle types.

Similar to the impedance-based readings, the MTS assays returned that the particles with the intermediate size of 10×41 nm are the ones with the smallest biological impact and their EC_{50} value was almost two orders of magnitude higher than the corresponding value for the other two particle sizes. Thus, a difference of 2–4 nm in size supposedly changes the toxicity of gold rods drastically. According to this study, the impact of the particles on cell proliferation does not correlate with their intracellular accumulation, but an alternative mechanism of action explaining the extreme size sensitivity of the different cell types has not been described. A side note is worth mentioning: MRC-5 cells (human lung) were reliably tested for their sensitivity toward gold nanoparticles by impedance-based assays. For reasons that were not specified, the same cells could neither be tested in MTS, trypan blue, nor colony formation assays [108]. This finding underlines the broad and generic applicability of impedance-based assays to almost all cell types as long as they grow adherently.

With a similar experimental strategy, Moe et al. [110] studied the impact of TiO_2 and Ag nanoparticles on the proliferation of the two human lung carcinoma cell lines, A549 and SK-MES-1, mentioned before as well as the widespread Chinese hamster ovary cell line (CHO-K1). Cell proliferation in the presence and absence of the particles was monitored by impedance readings. In addition, the viability of the three cell lines was tested by the well-known *neutral red uptake* (NRU) assay in the absence and presence of the particles after 24 or 48 h of exposure, respectively. The NRU assay quantifies the intracellular ATP stores and thereby reports quantitatively on cell viability. However, the TiO_2 particles interfered significantly with the NRU readout such that the cell response to the presence of the particles was not accessible. Accordingly, the NRU assay was only helpful as a reference assay when silver nanoparticles were studied.

To study the impact of the two types of nanoparticles on cell proliferation, suspended cells of either type were first seeded into the electrode containing wells such that the coverage of the well was close to 50% after an overnight incubation. Once this situation was established, the cells were exposed to the different nanoparticle loads and monitored continuously for a total of 60 h. Similar to the previously discussed report by Chuang et al. [108], the impedance of the individual electrodes was increasing due to cell proliferation at the time point when the particles were added. Dependent on the particles' impact on the cells, the time course of the measured impedance was not affected relative to an untreated control, retarded, stalled, or inverted. The threshold concentration EC_{50} for the Ag nanoparticles ranged between 5 and 70 μg/mL for all three cell lines (A549 > CHO-K1 > SK-MES-1), whereas EC_{50} values for TiO_2 particles range between 15 and 200 μg/mL (A549 > CHO-K1 > SK-MES-1). The NRU assay correlated favorably with the impedance data for the Ag nanoparticles. However, please note: EC_{50} values reported here are considerably higher than the ones reported by Chuang et al. [108] for the same cell lines.

It is one of the strengths of time-resolved cell monitoring to be able to create a dose–response relationship for any exposure time along the experiment. The authors made use of this option and produced dose–response relationships at any

hour of the experiment such that an EC_{50} value was accessible for each exposure time. Plotting these EC_{50} values as a function of time visualized the change of EC_{50} with increasing contact time between cell and nanomaterial. The following conclusions were drawn from the time course of the EC_{50}s: (1) For all combinations of cell types and particles that were studied in this report, the EC_{50} value decreased by one to two orders of magnitude as the exposure time increased. (2) In all cell lines Ag nanoparticles were found to be more toxic to the cells than TiO_2 nanoparticles. (3) The EC_{50} values for Ag or TiO_2 nanoparticles were found to be cell type dependent. (4) Impedance-based assays provided approximately the same EC_{50} values compared to the NRU assay when both assays could be applied in parallel. (5) According to the authors, the shape of the EC_{50} time course data may contain information on the mechanism of action by which the nanoparticles affect cell physiology. Thus, impedance-based proliferation assays as described by Moe et al. including several cell lines and particle types provide the concentration-, time-, cell-, and material-dependent response of cell proliferation to nanomaterial encounter [110].

Due to their omnipresence in our daily lives (e.g., coating of food containers and refrigerators) and their use for nutritional purposes in particular, Boehmert et al. addressed the impact of Ag nanoparticles on cells of the digestive system [111]. The colon carcinoma cell line $CaCo_2$ was used as a physiological model. Similar to the experimental studies described above, the cells were seeded in low inoculum to provide cells in logarithmic growth phase on the electrode surface. After a 24 h preincubation, two types of peptide-coated nanoparticles with a diameter of 20 or 40 nm, respectively, were added to the wells in increasing concentrations ranging between 5 and 100 µg/mL. Even for the lowest concentration of particles of either size, the impedance decreased down to the cell-free electrode values within 45 h of total exposure. The higher the concentration of the particles, the faster the observed impedance decrease. For the highest concentration applied, the impedance returned to cell-free values within 5 h indicating the severe toxicity of the peptide-decorated Ag nanoparticles [111]. Control experiments showed that the peptides alone in soluble form were not bioactive at all. No significant difference for the different particle diameters was observed. Interestingly, soon after nanoparticle addition to the maturing cells, the impedance increased, reached a transient maximum, and decreased below the starting values. The transient maximum in impedance was a constant, dose-dependent feature in all these studies but has not been fully understood yet.

5.3   Time-Resolved Response Profiles: Cytotoxicity

Assays addressing the time-resolved response profiles, as defined here, are performed on mature monolayers of cells that have been grown to confluence on the electrode surface. The stationary monolayer was then exposed to a well-defined dose of nanomaterials and followed with time by noninvasive, single-frequency
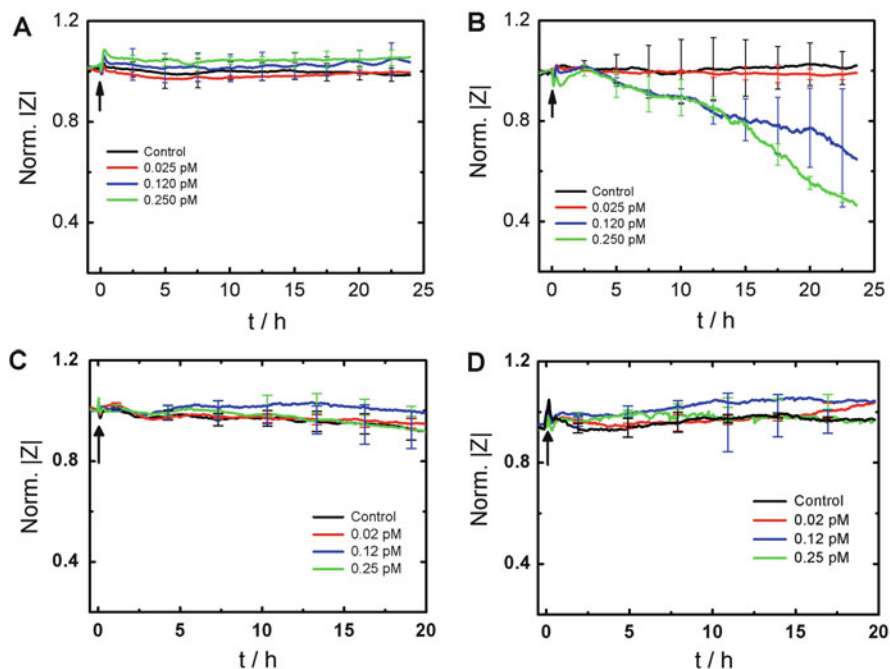
Fig. 11 Time course of the normalized impedance (4 kHz) when confluent MCF-7 cells (**a**, **b**) or confluent NRK cells (**c**, **d**) were exposed to increasing concentrations of silica particles with a diameter of 150 nm (**a**, **c**) or 2 μm (**b/d**). Addition of the particles is indicated by the arrows at time zero. All experiments have been performed at least twice (average ± SD)

impedance readings. Figure 11a, b summarizes the interaction of the human breast cancer cell line MCF-7 exposed to increasing concentrations of commercial silica nanoparticles with different diameters (Fig. 11a, 150 nm; Fig 11b, 2 μm) as monitored by impedance readings at a sampling frequency of 4 kHz.

The cell response was found to depend on the diameter of the particles. Whereas the cells do not show any measurable response along the exposure to 150 nm silica particles up to a concentration of 0.25 pM (Fig. 11a), they undergo a significant morphological change in the presence of 2 μm particles when concentrations are higher than 0.12 pM (Fig. 11b). The cell response starts within 2–3 h after particle addition. Within the observation time of 24 h, impedance readings for the highest particle load approached values known for cell-free electrodes indicating a severe response of the cells to the silica microparticles. Similar experiments were performed with normal rat kidney (NRK) cells using the same particles at the same concentrations (Fig. 11c, d). These cells were neither affected by the nanoparticles nor by the microparticles indicating that the bioresponse to nano-/micromaterials is very much dependent on the cell type as has been documented in the preceding chapters as well. This is part of the reason why it has been so tremendously difficult throughout the last decade to define generic rules for the

impact of nanomaterials on living cells and to derive design rules for nanomaterials based on such in vitro studies. From a more technical viewpoint, the data shown in Fig. 11 highlights again that impedance readings provide continuous information about the cell response for 24 h with no measurable impact of the measurement on the cells themselves as proven by the stationary time course under control conditions. The observation time is easily expanded to several days and only limited by the cell culture.

Among the organic nanomaterials, polystyrene-based nanoparticles have been used frequently as model systems to study the impact of nanoparticles of different diameter or different surface charge on diverse bio-systems. The surface charges are controlled by chemical modification with amine groups on the one hand and carboxylate or sulfate groups on the other. Figure 12 shows the response of
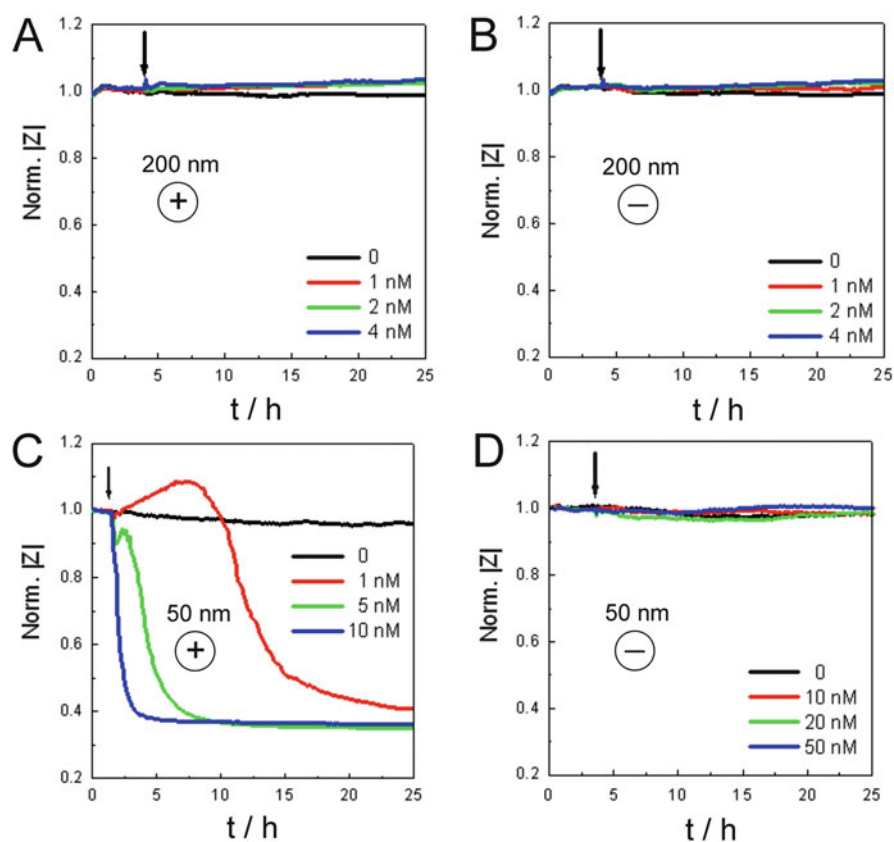
Fig. 12 Time course of the normalized impedance when confluent NRK cell layers are exposed to increasing concentrations of polystyrene beads with 200 nm (A/B) or 50 nm (C/D) diameter. NPs were either decorated with positively charged amino groups (A/C) or negatively charged carboxylic groups (B/D). The impedance was recorded at an AC frequency of 40 kHz and normalized to the first data point

confluent layers of normal rat kidney (NRK) cells when they were exposed to commercial polystyrene (PS) beads of two different diameters (Fig. 12A, B, 200 nm; C, D, 50 nm) that were decorated either with amino (Fig. 12A, C) or carboxy (Fig. 12B, D) functionalities, respectively, to test for size and charge effects. Impedance measurements were conducted at an AC frequency of 40 kHz such that any retraction or permeabilization of the cell bodies was sensitively reported. Polystyrene particles of 200 nm diameter (Fig. 12A, B) do not show any impact on the adherent NRK cells independent of their surface charge (Fig. 12A positive; Fig. 12B negative) up to a particle concentration of 4 nM. Along the entire exposure time of 20 h, there is no significant change in the normalized impedance indicating no morphological response of the cells to the presence of the particles. At first glance one may conclude that the missing cell response may be explained by a negligible particle uptake. But even though there was no measurable change in cell morphology, the fluorophore-labeled particles had been internalized by the cells during the experiment as demonstrated in Fig. 13 for the lowest concentration of 1 nM. The positive surface charge led to a much more pronounced particle uptake compared to their negatively charged correspondents. But even the rather high concentrations of polystyrene beads inside the cytoplasm did not cause any measureable reaction of the NRK cells studied here.

In contrast, when the same cells were exposed to polystyrene beads of 50 nm diameter (Fig. 12C, D), positively charged particles (Fig. 12C) induced an immediate and dose-dependent response within 12 h of exposure even for the lowest concentration applied. Please note that the impedance increases for a 1 nM exposure before it decreases to values of a cell-free electrode. Negatively charged polystyrene beads of the same size do not induce a toxic response for the same or significantly higher concentrations (Fig. 12D) suggesting that the positive charge density on the particle surface might be responsible for the severe interaction with cell viability shown in Fig. 12C. In particular, the immediate response of the cells to 5 and 10 nM of positively charged polystyrene beads suggests that a direct membrane interaction is likely to be responsible for the observed effects rather than any intracellular effects after particle ingestion. Increasing the concentration of negatively charged NPs ($d = 50$ nm) up to a final concentration of 50 nM (Fig. 12D) did still not provide any measurable cell reaction. Accordingly, the particles are biologically inactive in this assay for the concentration range under test. The interested reader is referred to the analysis of NRK cell migration upon exposure to the same particles described in the next paragraph. Under conditions of the migration assay, the particles do affect the cells in a measurable way.

Section 6 of this book describes the synthesis, characterization, and some bioanalytical applications of so-called carbon dots (CDs). CDs are carbon nanomaterials prepared by hydrothermal synthesis from starch and amino acids. The particles have an amorphous core structure and a small amount of sp^2-hybridized carbon atoms along the particle surface that renders these materials luminescent. CDs prepared from starch are extremely small with a diameter of just 2–3 nm and a slightly negative surface potential. When these particles were tested for
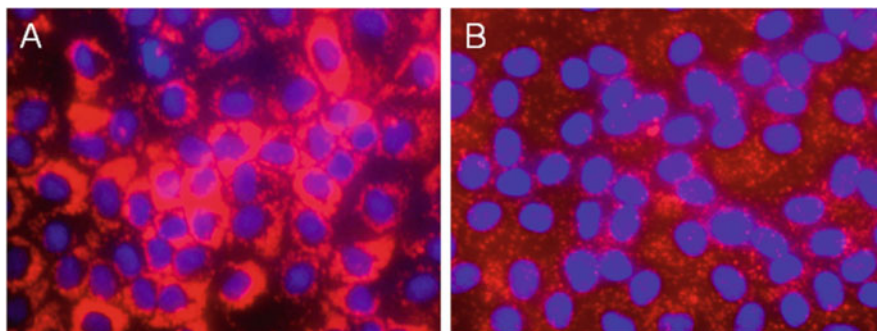
Fig. 13 Fluorescence mircrographs of confluent NRK cells after incubation with positively (**a**) or negatively (**b**) charged polystyrene NPs ($d = 200$ nm) for 24 h at 1 nM concentration. Beads were labeled with a red emitting fluorophore. Nuclei are counterstained by the intercalating dye DAPI
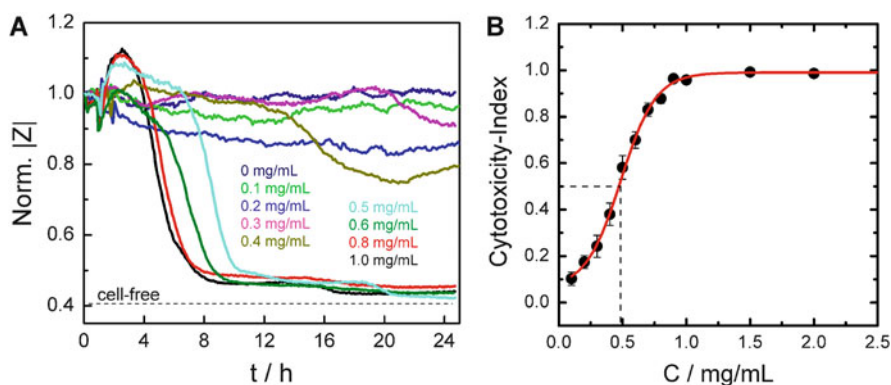
Fig. 14 (**a**) Time course of the normalized impedance at a sampling frequency of 4 kHz when confluent NRK cells are treated with increasing concentrations of carbon nanodots (CD). The normalized impedance of a cell-free electrode is indicated by a dashed line. (**b**) Cytotoxicity index for confluent NRK cell monolayers that were exposed to increasing concentrations of CDs. The cytotoxicity was assessed using the commercial PrestoBlue™ assay. Quantitative analysis provides an EC_{50} value of (0.48 ± 0.02) mg/mL

cytotoxicity, the corresponding ECIS readings returned the data summarized in Fig. 14a.

Concentrations of 0.4 mg/mL and below the normalized impedance ($f = 4$ kHz) behaved rather stationary along the entire 24 h of exposure. Thus, concentrations up to 0.4 mg/mL do not induce any acute cytotoxicity. The situation changes for slightly increased concentrations of CDs that led to a severe response within the time-resolved response profile. 0.5 mg/mL are already sufficient to induce a severe decrease of the normalized impedance starting app. 8 h after the cells encountered CDs. Amazingly, the impedance increased by roughly 10% within these first hours of the experiment before it started to descend. Higher concentrations of CDs produced a similar time course characterized by a transient increase of the

impedance before it decreased to values of a cell-free electrode. Accordingly, concentrations of 0.5 mg/mL of CDs and higher killed confluent NRK cells within 24 h of exposure providing an estimated EC_{50} value between 0.4 and 0.5 mg/mL.

In order to confirm the dose–response function obtained from label-free impedance monitoring, the assay was repeated with respect to particle concentration, incubation time, and cell type under test but with a biochemical readout (PrestoBlue™ assay which is a variant of the MTT assay) that measures the metabolic activity of the cells (cp. Table 1). For a 24 h exposure time, the biochemical analysis provided an EC_{50} value of (0.48 ± 0.02) mg/mL which compares favorably with the outcome of the ECIS-based assay. Repeating these experiments with a different, large-scale production batch of C-Dots revealed that there is some batch-to-batch variation in toxicity. This might be caused by slight changes introduced into the production parameters or the subsequent purification steps by the scale-up. This new batch showed an EC_{50} value of (1.1 ± 0.1) mg/mL in both toxicity assays, the biochemical PrestoBlue and the label-free ECIS profiles. Thus, this data confirms what has been hypothesized and found before: nanoparticle functional properties may be slightly affected when synthesis and purification steps are scaled up and they need to be reconfirmed for every little change in the preparation scheme.

A similar time-resolved response profile as the one shown in Fig. 14a for NRK cells exposed to CDs has been observed for A549 cells (pulmonary epithelium) during exposure to CuO or ZnO nanoparticles using a very different electrode layout and instrumentation [112]. Thus, the initial increase in the time course of the impedance shortly after nanoparticle encounter, as observed in both studies, seems to be a more general phenomenon associated with cell stress. We have observed this prelude to the cytotoxicity-induced impedance decrease also for other chemical stressors that were capable of killing cells within the next 20 h. At this point we can only speculate about the mechanistical basis for this observation. But it seems straightforward to conclude that exposure to the various nanoparticles leads to necrotic cell death which is characterized by an initial cell swelling before the membrane ruptures. Cell swelling would transiently reduce the width of all paracellular current pathways before the membrane is permeabilized. Thus, a transient increase in impedance may indicate transient cell swelling as a hallmark of necrotic instead of apoptotic cell death. It is noteworthy that these mechanistical details are only available from time-resolved cell monitoring; they would have been overlooked by traditional endpoint assays.

The study of Seiffert et al. [112] is particularly interesting in this context from a quantitative and a mechanistic perspective. As mentioned above, the study reports on the biological impact of CuO, ZnO, and TiO_2 nanoparticles on A549 cells. Whereas CuO and ZnO were found to be toxic, TiO_2 was not at all harmful to the cells within 24 h. The EC_{50} values for the toxic metal oxide particles were found to be 28 µg/mL for CuO and 55 µg/mL for ZnO. It is noteworthy that both values are at least one order of magnitude smaller than the EC_{50} value found for CDs. Moreover, the authors addressed the transient increase in impedance magnitude starting within 2 h after nanoparticle addition in more detail. By established label-based assays,

they found no nanoparticle impact on membrane integrity within the time of the transient impedance increase, a slight upregulation of apoptosis, morphological changes of the nucleus, production of reactive oxygen species (ROS), and eventually an increased efflux of glutathione from the cytoplasm into the extracellular space mediated by ATP-dependent multidrug resistance efflux pumps (MRP-1). Since glutathione is involved in several cellular detoxification strategies, its involvement is not surprising. However, it remains to be elucidated why the cells pump glutathione out of the cytoplasm as a response to the presence of intracellular stressors [112]. A reasonable explanation considers glutathione as a second messenger of apoptosis. Once it has left the cytoplasm, there is a stronger increase in reactive oxygen species pushing the cell along the apoptotic pathway. It is, however, unclear how these molecular processes inside the cell lead to an increase in impedance – in particular as apoptosis is known to shrink cells and reduce their volumes.

5.4 Nanoparticle Impact on Cell Migration

The capacity of cells to close an experimental wound is commonly used to quantify their ability to migrate. In the so-called scratch assay, cells are grown to confluence before a scratch of a few hundred microns (equal to several cell diameters) is introduced into the cell layer. The cells from the periphery migrate into the open space and wound closure is commonly followed by time-lapse video microscopy. This technique is labor intense and suffers from problems of creating reproducible wounds. Alternatively, instead of scratching a wound into a confluent cell monolayer, the initially suspended cells are seeded in special cell culture dishes that contain a removable barrier. Once the cell layer has reached confluency, the barrier is removed and the cells start migrating into the open space. The wound size is much better controlled and reproduced by the barrier assay, but it still requires tedious time-lapse video microscopy for analysis with its limited throughput. The ECIS-based migration assay as described above avoids many of these problems. The wounds match always exactly the size of the electrodes and the experiment can be performed entirely automated in 96-well format without opening the incubator door providing a time resolution in the order of a few minutes. Thus, the assay is very well suited to study the impact of nanomaterials on cell migration in quantitative terms.

From the data in the previous paragraph, we have learned that negatively charged polystyrene nanoparticles of 50 nm diameter did not show any measurable effect on cell viability. The time-resolved response profile did not reveal any morphological reaction of the cells to nanoparticle encounter even though microscopic inspection clearly indicated that even negatively charged nanoparticles were taken up by the cells. So the hypothesis was pursued that the nanoparticles may not have any harmful impact on resting cells that neither proliferate nor migrate but may affect more active cells. Thus, confluent layers of NRK cells were incubated

Fig. 15 Time course of the normalized impedance (32 kHz) during an automated wound healing/ migration assay in the presence of increasing concentrations of negatively charged polystyrene nanoparticles with 50 nm diameter
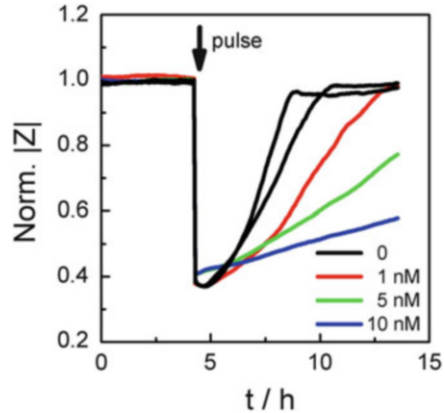
with the negatively charged polystyrene nanoparticles in the same concentration range that has been applied in the viability studies. The cells were allowed to internalize the particles for a total of 24 h before the wound healing assay was applied. Figure 15 summarizes the outcome of this experiment. After 4 h of baseline recording, the cell layers were wounded by an elevated electric field pulse (arrow in Fig. 15). The parameters of the field (4.0 V, 30 s, 40 kHz) had been optimized for quantitative killing of the cells on the electrode before. The impedance magnitude at a sampling frequency of 40 kHz was used for monitoring. After pulse application the normalized impedance dropped to values of a cell-free electrode immediately but started to recover after a short lag phase due to the repopulation of the electrode by cells from the periphery.

The black curve shows the time course of the normalized impedance under control conditions, whereas the colored curves show the results of experiments with increasing concentrations of the negatively charged polystyrene nanoparticles. It is obvious from the data that negatively charged NPs, which had no measurable effect on the viability of resting cells, retard wound closure and, thus, the migration of cells from the periphery into the center of the wound in a dose-dependent manner. Accordingly, these experiments indicate that it might not be sufficient to look only for the (integral) toxicity of NPs but to study also their impact on more specific, supposedly more vulnerable key events of cell physiology like cell migration.

Studying the time-resolved response profiles of confluent NRK cells exposed to increasing concentrations of C-Dots revealed that concentrations equal or higher than 1.1 mg/mL (scale-up batch, please compare Sect. 5.1) induced a severe toxicity. When the cells were treated with lower concentrations, no significant changes of the normalized impedance occurred indicating no impact on cell morphology or physiology. Based on the experience with the polystyrene nanoparticles described in the preceding paragraph, subtoxic concentrations of CDs were tested for their impact on cell migration using the ECIS-based migration assay. Figure 16 shows the time course of the normalized impedance, when confluent layers of NRK
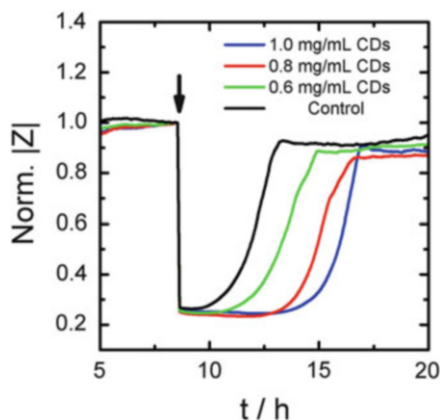
Fig. 16 Time course of the normalized impedance at a sampling frequency of 32 kHz when confluent NRK cells were first exposed to increasing but sublethal concentrations of carbon dots (CDs) before the elevated AC electric field (2.4 mA, 32 kHz, 30 s) was applied (*arrow*) to wound the cells. Cell migration was found to be highly sensitive to the preincubation with CDs 4 h prior to pulse application even though these concentrations were shown not to induce an acute toxicity within 48 h

cells were first exposed to increasing concentrations of CDs for 4 h before the wounding pulse (2.4 mA, 32 kHz, 30 s) was applied.

Immediately after pulse application, the impedance dropped to values of a cell-free electrode before it recovered to pre-pulse values with time. However, recovery times were found to be strongly dependent on a preincubation of the cells with CDs. The higher the concentration of the nanoparticles that was added to the cells, the slower is the healing process and the more affected is cell migration relative to control conditions. Please note that CD concentrations were adjusted to be below the threshold concentration of 1.1 mg/mL that induced cytotoxicity directly. Thus, the same conclusion applies for the C-Dots that has been described for the polystyrene nanoparticles above: the impact of nanoparticles strongly depends on the status of the test cells. Different cell functions or different cell states are obviously individually sensitive to nanoparticle encounter.

Figure 11c of the previous chapter has shown the tolerance of confluent NRK cells with respect to silica particles of 150 nm diameter. Concentrations were increased up to 0.25 pM, and no significant morphological response of the cells was observed by ECIS readings. Similar to the scenarios described above for polystyrene particles and CDs, we were interested to find out whether the rather inert silica particles might be capable of affecting cell migration. Accordingly, NRK cells were grown to confluence on the ECIS electrodes. The cells were then exposed to silica particles in three concentrations (same as in Fig. 11c) and studied by the automated, ECIS-based migration assay. The results are summarized in Fig. 17. In contrast to polystyrene particles and CDs, we could not observe any impact of the silica particles on the migration of NRK cells. The observed differences in the time traces shown in Fig. 17a are just due to the unavoidable data
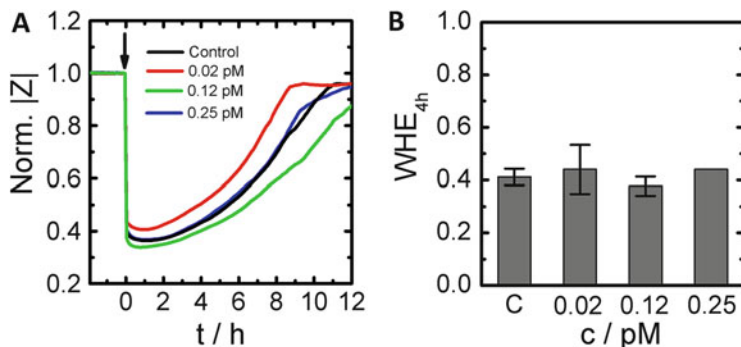
Fig. 17 (**a**) Time course of the normalized impedance at a sampling frequency of 32 kHz when confluent NRK cells, preloaded with silica nanoparticles of 0.15 μm diameter in increasing concentrations, were studied in the ECIS-based migration assay. The wounding pulse (4.0 V, 32 kHz, 30 sec) was applied as indicated by the *arrow*. (**b**) Synopsis of all migration assays performed under replicate conditions. The wound healing efficiency is defined as the normalized impedance 4 h after pulse application ($n = 2$; average $\pm$ SD)

scattering but are averaged out for the pool of our data summarized in Fig. 17b. The wound healing efficiency (WHE) plotted in Fig. 17b is defined as the value of the normalized impedance 4 h after the wounding pulse was applied. It therefore mirrors the recovery of the impedance and, thus, the number of cells that have migrated into the wound from the periphery.

Taken together, the experiments described above clearly indicate that nanoparticle doses that are not causing an immediate toxicity may still affect the migration of the same cells significantly. This observation underlines that it is not sufficient to study just cytotoxicity measured as membrane leakage or metabolic activity for a comprehensive judgment on the biological impact of nanoscale particles. Highly specialized cellular functions like cell migration might still be compromised. On the other hand, the example of silica particles in contact to NRK cells (Fig. 17) indicates that even this is not a general rule but must be individually addressed for every nanoparticle–cell combination. With the number of physiological key events like migration, the number of different tissues and cell types, plus the number of different nanomaterials in mind, it is obvious that there is an enormous demand for high-throughput testing and screening.

5.5 Nanoparticle Impact on Cell Motility (Micromotion)

In contrast to cell *migration*, the term cell *motility* does not denote a net lateral movement of the cells but simply the dynamics of the cell bodies. As described in Sect. 4.2.4, the cell body is constantly undergoing metabolically driven shape fluctuations that are caused by corresponding activities of the cytoskeleton, by the intracellular movement of organelles, and by thermal motion of different cell

constituents. Since these cell shape fluctuations change the extracellular current pathways correspondingly, cell motility or "micromotion" can be recorded by single frequency ECIS readings. When data acquisition is limited to 15–20 min, the observed impedance fluctuations provide a snapshot of the actual cell body dynamics that can be analyzed quantitatively. Figure 8d shows a typical dataset recorded in *micromotion mode* for two different cell lines. The question has been pursued whether or not micromotion experiments might be useful and sensitive enough to report on a potential impact of nanoparticles on cell physiology. This idea was driven by a more recent literature report indicating that micromotion reads the onset of cytotoxicity to molecular toxins significantly more sensitive than regular ECIS readings [78, 97].

ECIS data acquisition in *micromotion* mode is straightforward. The instrument is set to a designated frequency and the complex impedance is recorded with a time resolution of one second or even faster for a time period between 10 and 20 min. The observed impedance fluctuations mirror the dynamic rearrangements of the cell body and are not due to poor electronic equipment. Figure 18a compares the time course of the normalized resistance (real part of complex impedance) at a frequency of 4 kHz for vital cells and cells that were killed by formalin fixation prior to micromotion readings. Whereas the vital cells show a seemingly chaotic fluctuation pattern with time, the dead cells only provide a drift in the impedance signal which might be due to a slight evaporation of water. Obviously the fixation of all cell protein has ceased the ability of the cells to be motile and dynamic. Electronic noise would be persistently visible even in the data for the dead cells, but it can be hardly observed.
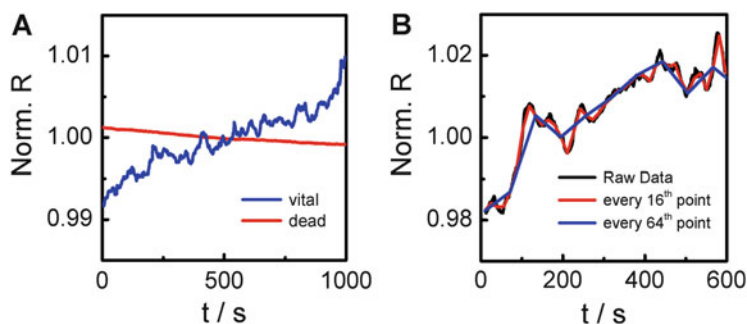
Fig. 18 (**a**) Micromotion data recorded for vital and dead MDCK cells at a sampling frequency of 4 kHz. The fluctuations in cell shape are most sensitively mirrored in the real part of the complex impedance (R) which is here normalized to the time average value. Whereas vital cells show chaotic resistance fluctuations which are associated with their cell body dynamics, the signal for the dead cells is just a slight drift. (**b**) The graph illustrates the calculation of the standard deviation of increments (SDI) for different "time resolutions." The *black curve* shows the original data. The *red curve* just connects every 16th data point, and the blue curve connects just every 64th data point. The standard deviation of the associated increments (SDI) mirrors the fluctuation amplitude at the different timescales (16 s => SDI-16; 64 s => SDI-64)

The tricky part about micromotion is data analysis and data reduction. It is the goal to process the raw data such that the intensity of the fluctuations is represented by a single number. Several algorithms have been tested and described that all have their individual advantages and disadvantages. The interested reader is referred to the publications by Lo and co-workers for a thorough over- and review [96, 113, 114]. Here we will only describe experiments that made use of the two most straightforward analysis procedures returning (1) the standard deviation of increments SDI or (2) the slope of the power spectrum computed for the micromotion raw data. Both methods are only described briefly below:

1. To calculate the SDI value, the raw data is first normalized to the time average of the dataset and detrended – if necessary – by subtracting a linear regression line. Then the increments between two subsequent data points i and $(i + 1)$ are calculated along the entire dataset (Fig. 18b). Finally all increments are averaged and the standard deviation of the average is computed. When the fluctuation within the time trace is big, the standard deviation of the increments (SDI) is big. It scales with the intensity of the fluctuations in the raw data. Thus, the numerical value of the SDI is a direct measure for cell micromotion. Since fluctuations should be considered on different timescales for later analysis and interpretation, the procedure is repeated with every data point i and $(i + 3)$ omitting the data points in between (cp. Fig. 18b). The calculation now returns a measure for impedance noise on a timescale of 4 s, whereas the first calculation expresses the noise on a timescale of 2 s. These two quantities are then defined as SDI-2 or SDI-4. Performing the calculation with data point i and $(i + 63)$ returns the SDI-64 which quantifies the noise in the impedance time course on a timescale of 64 s. We have arbitrarily chosen the SDI-64 to describe the outcome of micromotion experiments as SDI-64 had shown the best sensitivity for changes in cell motility in our hands. Please note that we could have also measured the impedance only every 64 s to calculate the SDI-64. By reading the impedance at every second, however, it is possible to calculate SDI-2, SDI-4, SDI-8, and so on for every experiment later on – without any a priori selection of the time resolution. The most suitable parameter can then be selected after the experiment for best possible interpretation or highest sensitivity.

   Using this mode of micromotion analysis, we studied the impact of silica nanoparticles on MCF-7 and NRK cells that were also examined in the other ECIS assays described above. Thus, confluent layers of MCF-7 and NRK cells were exposed to different concentrations of silica nanoparticles ($d = 150$ nm) for 24 h before data acquisition in "micromotion mode" was started. The preincubation allows for particle uptake and intracellular processing. After this preincubation cell motility was monitored by micromotion recordings with a time resolution of 1 s. After sequential data acquisition for every electrode, the data was evaluated by computing the SDI-64 for every condition. Figure 19 summarizes the impact of silica nanoparticles on MCF-7 and NRK micromotion. Neither for MCF-7 (Fig. 19a) nor for NRK cells (Fig. 19b), we observed a significant impact of the particles on cellular micromotion. Obviously the cells
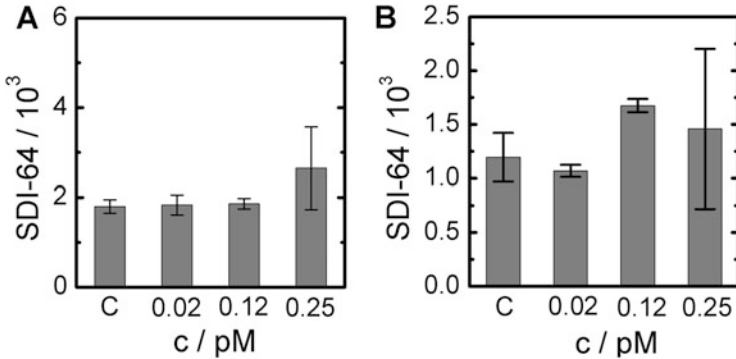
Fig. 19 Synopsis of micromotion experiments with confluent layers of (**a**) MCF-7 or (**b**) NRK cells in the presence of silica particles of 150 nm diameter. The cells were incubated with the particles for 24 h before micromotion readings were taken. The raw data (resistance normalized to the time average) was analyzed as described in the text to extract the standard deviation of increments for a timescale of 64 s (SDI-64). The sampling frequency was set to 4 kHz

are indeed not affected in their cell body dynamics by the presence of the particles when they are in some kind of a resting state within a cell monolayer. The observed changes were not significant.

2. Another approach of data evaluation detrends the impedance raw data and then calculates the power spectral density function of the time series by fast Fourier transformation (FFT), i.e., FFT transforms the time-dependent information of the impedance fluctuations into a frequency-dependent information. In other words, micromotion time course data is broken up into a series of individual periodic contributions (sine, cosine) that would add up to the original time course data upon superposition. The amplitudes of the individual periodic contributions are provided by the value of the power spectral density function at the corresponding frequency. Thus, the power spectrum identifies dominating periodic recurrences within the time traces quite easily by peaks. However, no such dominating periodicities in the impedance time course have ever been observed during nanoparticle encounter in our hands. With no dominating periodicities in the power spectrum, we extracted the slope of the peak-free power spectrum m as a quantitative parameter to describe the pattern of micromotion data. The slope m reports on how periodic contributions to the experimental micromotion time series are on average smeared over a given frequency range. When *white noise* is subjected to FFT, for instance, the corresponding power spectrum shows that all individual periodic contributions independent of frequency have the same amplitude. Thus, it provides a power spectrum with a slope of zero. In contrast, signal fluctuations caused by Brownian motion are characterized by a slope of $m = (-2)$ in the power spectrum indicating that higher-frequency contributions have a smaller amplitude. In a more recent study, we found that cellular micromotion is characterized by a slope of $m = (-2.5)$ in the power spectrum – quite heavily dependent on cell type

Table 3 Comparison of EC_{50} values for confluent layers of MDCK cells (strain II) that were exposed to different types of nanoparticles as indicated in the table

	ECIS EC_{50}/24 h	MTT EC_{50}/24 h	ECIS EC_{50}/48 h	MTT EC_{50}/48 h
CTAB-Au-rods	0.2 nM	nr	0.1 nM	0.1 nM
HOOC-PEG-Au-rods	nr	nr	nr	nr
H_2N-PEG-Au-rods	nr	nr	nr	nr
Multi-shell QDs	0.3 µM	nr	0.15 µM	32 µM

The analytical readout was performed by ECIS-based micromotion analysis or the classical MTT assay after exposure times of 24 or 48 h, respectively [70]. The gold rods had a long axis of 39 nm and a short axis of 17 nm. The diameter of the multi-shell quantum dots was 5–6 nm

CTAB cetyltrimethylammonium bromide, *PEG* polyethylene glycol, *QDs* quantum dots, *nr* no measurable response of cells for all concentrations studied

and culture conditions [115]. This led to the idea to use the slope *m* as a descriptor for micromotion when the cells are exposed to different kinds of nanoparticles in different concentrations. Based on the calculated slope values for every nanoparticle dose, EC_{50} values were extracted for the concentration-dependent impact of the particles on cell motility. Table 3 compares the EC_{50} values derived from micromotion experiments with the outcome of biochemical MTT assays that were performed in parallel [70]. The comparison includes multi-shell quantum dots (QDs; 5–6 nm) and gold nano-rods (17×39 nm) with different surface decorations: cetyltrimethylammonium bromide (CTAB), carboxy-terminated PEG, or amino-terminated PEG.

Based on Table 3, the MTT assay did not report any response of the cells to any of the particles under test for an exposure time of 24 h. Accordingly, redox metabolism was not affected to any measurable extent. Micromotion analysis, however, did show a measurable impact for two out of four particle types with EC_{50} values of 0.2 nM for CTAB-coated Au-rods or 0.3 µM for multi-shell quantum dots. The two PEGylated particle types did not induce any measurable change in cell physiology according to both assays. For the 48 h exposure experiment, both assays returned again no effect for the PEG-coated particles independent on whether they were decorated by amino- or carboxy-groups. CTAB-coated rods and the multi-shell quantum dots were found to be biologically active with individual EC_{50} values. Whereas both assays returned an EC_{50} value of 0.1 nM for the CTAB-coated particles, there was a striking difference in EC_{50} for the multi-shell QDs. ECIS-based micromotion analysis returned an EC_{50} of 0.15 µM which is in the same range as the outcome of the 24 h experiment. The MTT assay surprisingly provided an EC_{50} value which was $200\times$ higher than the one from micromotion analysis in the order of 30 µM. The reasons for this discrepancy are unclear in particular as both assays returned similar results for the CTAB-coated rods. Whether or not the multi-shell QDs might have any interference with the MTT reagents is unclear but does not seem to be very likely. An alternative yet speculative explanation for the observed differences might be that the QDs interfere with another cellular structure or function other than redox metabolism that is crucial for

micromotion and very sensitive for any interference by particles. If this hypothesis holds true, the MTT assay is blind for this primary interaction of the QDs with cellular structures or functions and only reports on the less sensitive impact on redox metabolism. The integrative nature of the ECIS signal might have detected even this high sensitive interaction as it reads any disturbance of cell physiology that eventually changes cell body dynamics. Technically it is noteworthy that the 24 h and 48 h exposure experiments were performed sequentially with one and the same cell population using the ECIS readout, whereas MTT assays had to be performed separately for either exposure time. The most striking differences between label-based (MTT) and label-free readouts (ECIS micromotion) become very obvious from the micromotion experiments.

6   Conclusion and Outlook

The present contribution was meant to highlight the specific merits and limitations of impedance-based cell monitoring for the analysis of cell-nanoparticle interactions in vitro. The noninvasive and quantitative nature of the measurement together with the outstanding time resolution provides a very special and differential perspective on the cellular response to nanomaterial encounter with several insights that are not accessible from other assay formats. The examples discussed in the preceding paragraphs also showed that there are no simple rules describing the cell-nanomaterial interactions as there are so many variables that contribute to the final outcome. Cell types, culture conditions, extracellular environment, buffer composition, and presence of serum proteins are just a few experimental parameters affecting this complex molecular interplay. From the nanomaterial side, we have to consider size, surface decoration, stability, adhesiveness for proteins or other biomolecules, and the long-term chemical stability, to mention just a few. The inclusion of all aspects from the biological and material side creates a multidimensional parameter matrix that is hard to oversee and to handle. Any attempt of getting closer to more generic rules describing the cell-nanomaterial interactions requires an enormous amount of additional in vitro testing. Thus, throughput of bioanalytical assays is becoming a more and more serious issue on the way to a better understanding of the potential harm of nanomaterials for the biosphere. But throughput is not enough. It also takes multiparameter experiments to tackle this complex problem from different sides providing different descriptors. Thus, we need a combination of *high-content* and *high-throughput* approaches for the analysis of in vitro assays. This chapter showed that impedance-based cell monitoring is indeed multimodal with the capacity to provide a multiparameter description of cell-nanomaterial encounter.

A huge variety of different impedance-based assays can be performed that are neither invasive to the cells nor do they rely on additives or reagents. Instead of running these assays individually, they can be pursued in sequences on one and the same cell population such that different perspectives on cell-nanomaterial

Fig. 20 Scheme for an
interactions score card that
summarizes the interactions
between different
nanomaterials and one
selected model cell line as
derived from different
impedance-based assays
that are performed
individually or sequentially.
The descriptors of every
assay are ranked relative to
the particle-free control
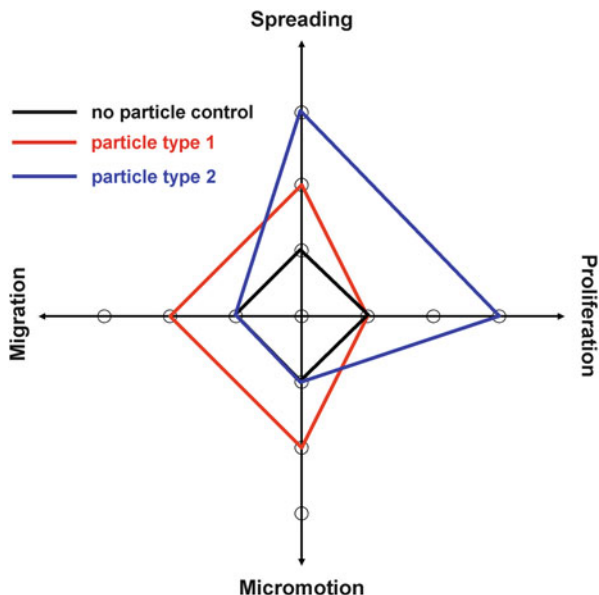
interactions become accessible – all for the same cells. The analysis of sequentially performed, time-resolved assays on one cell population will yield a collection of descriptors and their dynamics, thus a significantly improved information content which is badly needed regarding the complexity of the system under test. As an example, it seems straightforward to (1) study the adhesion of cells to pre-coated electrodes in the presence of nanomaterials, (2) follow their proliferation to a confluent monolayer, and (3) measure their micromotion as a measure for cell body fluctuations before (4) the cells are exposed to an ECIS-based migration assay to probe the impact of the particles on cellular migration. Dependent on the invasiveness of the particle under study, this sequence may end before all assays have been performed due to the extended exposure time, but this would make an information by itself. Since assay sequences run entirely automated and preprogrammed without any input by the user, sequential assays seem very valuable in particular for those materials that are considered less aggressive and that might be of use in the biomedical field.

Independent of whether different assays are performed sequentially on one and the same cell population or individually on different batches of the same cell line, meaningful data reduction seems to be another possible target to reduce the complexity of the problem. Therefore, we suggest establishing *interaction score cards* or *interaction profiles* that provide an overview over the outcome of all assays for one particular cell type in contact to different nanomaterials. Figure 20 illustrates this idea of such an *interaction profile* for the above-given sequence of four assays that are performed in the presence or absence of different nanomaterials. The interaction profile has four dimensions, one for every assay. The outcome of the

assay is scored for every material on a relative scale with the no particle control serving as the internal reference. The descriptors of the individual assays (e.g., EC_{50} values) are ranked relative to the internal control and the ranking is denoted in the 4D profile line as shown in Fig. 20.

This formalism will compare the bioresponse of different materials not just assay by assay but will provide an overview at a glance and highlight the interaction points of the different nanomaterials with cell physiology. This formalism can be scaled up or down dependent on the number of assays belonging to the pool of experiments, and it may open our eyes for yet unidentified correlations or dependencies. Every piece of understanding will help along the long and winding road toward sustainable design rules for nanomaterials that can guide process development and provide a first line of defense against the potential threats of nanomaterials – simply by avoiding the generation of harmful species up front.

References

1. Bradlaw JA (1986) Evaluation of drug and chemical toxicity with cell culture systems. Fundam Appl Toxicol 6(4):598–606
2. Horrocks C, Halse R, Suzuki R, Shepherd PR (2003) Human cell systems for drug discovery. Curr Opin Drug Discov Devel 6(4):570–575
3. Conway BR, Demarest KT (2002) The use of biosensors to study GPCR function: applications for high-content screening. Receptors Channels 8(5-6):331–341
4. Beske OE, Goldbard S (2002) High-throughput cell analysis using multiplexed array technologies. Drug Discov Today 7(18 Suppl):S131–S135
5. Johnston PA (2002) Cellular platforms for HTS: three case studies. Drug Discov Today 7 (6):353–363
6. Horakova K (1999) The use of cell culture systems for the assessment of general cellular toxicity and to detect the nature and location of free radical damage. Gen Physiol Biophys 18 Spec No:63–69
7. Zucco F, De Angelis I, Testai E, Stammati A (2004) Toxicology investigations with cell culture systems: 20 years after. Toxicol In Vitro 18(2):153–163
8. Carlo GL, Jenrow RS (2000) Scientific progress – wireless phones and brain cancer: current state of the science. MedGenMed 2(3), E40
9. Valberg PA (1997) Radio frequency radiation (RFR): the nature of exposure and carcinogenic potential. Cancer Causes Control 8(3):323–332
10. Pizzoferrato A, Ciapetti G, Stea S, Cenni E, Arciola CR, Granchi D, Savarino L (1994) Cell culture methods for testing biocompatibility. Clin Mater 15(3):173–190
11. Wintermantel E, Shah-Derler B, Bruinink A, Petitmermet M, Blum J, Ha SW (2002) Biokompatibilität. In: Wintermantel E, Suk-Woo H (eds) Medizintechnik mit biokompatiblen Werkstoffen und Verfahren. Springer, Berlin, pp 5–44
12. Elsaesser A, Howard CV (2012) Toxicology of nanoparticles. Adv Drug Deliv Rev 64 (2):129–137

13. Love SA, Maurer-Jones MA, Thompson JW, Lin YS, Haynes CL (2012) Assessing nanoparticle toxicity. Annu Rev Anal Chem (Palo Alto Calif) 5:181–205
14. Marquis BJ, Love SA, Braun KL, Haynes CL (2009) Analytical methods to assess nanoparticle toxicity. Analyst 134(3):425–439
15. Maurer-Jones MA, Bantz KC, Love SA, Marquis BJ, Haynes CL (2009) Toxicity of therapeutic nanoparticles. Nanomedicine (Lond) 4(2):219–241
16. Freshney IR (2010) The culture of animal cells: a manual of basic technique. Wiley, Hoboken
17. Scherer WF, Syverton JT, Gey GO (1953) Studies on the propagation in vitro of poliomyelitis viruses. IV. Viral multiplication in a stable strain of human malignant epithelial cells (strain HeLa) derived from an epidermoid carcinoma of the cervix. J Exp Med 97(5):695–710
18. Fendyur A, Varma S, Lo CT, Voldman J (2014) Cell-based biosensor to report DNA damage in micro- and nanosystems. Anal Chem 86(15):7598–7605
19. Davila JC, Cezar GG, Thiede M, Strom S, Miki T, Trosko J (2004) Use and application of stem cells in toxicology. Toxicol Sci 79(2):214–223
20. Hu H, Deng H, Fang Y (2012) Label-free phenotypic profiling identified D-luciferin as a GPR35 agonist. PLoS One 7(4), e34934
21. Knight MM, Roberts SR, Lee DA, Bader DL (2003) Live cell imaging using confocal microscopy induces intracellular calcium transients and cell death. Am J Physiol Cell Physiol 284(4):C1083–C1089
22. Sumantran VN (2011) Cellular chemosensitivity assays: an overview. Methods Mol Biol 731:219–236
23. Robertson JD, Orrenius S (2000) Molecular mechanisms of apoptosis induced by cytotoxic chemicals. Crit Rev Toxicol 30(5):609–627
24. Vanden Berghe T, Grootjans S, Goossens V, Dondelinger Y, Krysko DV, Takahashi N, Vandenabeele P (2013) Determination of apoptotic and necrotic cell death in vitro and in vivo. Methods 61(2):117–129
25. Holder AL, Goth-Goldstein R, Lucas D, Koshland CP (2012) Particle-induced artifacts in the MTT and LDH viability assays. Chem Res Toxicol 25(9):1885–1892
26. Oh SJ, Kim H, Liu Y, Han HK, Kwon K, Chang KH, Park K, Kim Y, Shim K, An SS, Lee MY (2014) Incompatibility of silver nanoparticles with lactate dehydrogenase leakage assay for cellular viability test is attributed to protein binding and reactive oxygen species generation. Toxicol Lett 225(3):422–432
27. Lupu AR, Popescu T (2013) The noncellular reduction of MTT tetrazolium salt by TiO$_2$ nanoparticles and its implications for cytotoxicity assays. Toxicol In Vitro 27 (5):1445–1450
28. Weiss DG (1987) Videomicroscopic measurements in living cells: dynamic determination of multiple end points for in vitro toxicology. Mol Toxicol 1(4):465–488
29. Bayyoud T, Hofmann J, Spitzer M, Bartz-Schmidt KU, Yoeruek E (2014) Cytotoxic properties of sunitinib and sorafenib on human corneal epithelial cells. Curr Eye Res 39 (2):149–154
30. Bettenworth D, Lenz P, Krausewitz P, Bruckner M, Ketelhut S, Domagk D, Kemper B (2014) Quantitative stain-free and continuous multimodal monitoring of wound healing in vitro with digital holographic microscopy. PLoS One 9(9), e107317
31. Rappaz B, Breton B, Shaffer E, Turcatti G (2014) Digital holographic microscopy: a quantitative label-free microscopy technique for phenotypic screening. Comb Chem High Throughput Screen 17(1):80–88
32. Kuhn J, Shaffer E, Mena J, Breton B, Parent J, Rappaz B, Chambon M, Emery Y, Magistretti P, Depeursinge C, Marquet P, Turcatti G (2013) Label-free cytotoxicity screening assay by digital holographic microscopy. Assay Drug Dev Technol 11(2):101–107
33. Mir TA, Shinohara H (2012) Label-free observation of three-dimensional morphology change of a single PC12 cell by digital holographic microscopy. Anal Biochem 429(1):53–57

34. Shinohara H, Sakai Y, Mir TA (2013) Real-time monitoring of intracellular signal transduction in PC12 cells by two-dimensional surface plasmon resonance imager. Anal Biochem 441 (2):185–189

35. Yanase Y, Hiragun T, Ishii K, Kawaguchi T, Yanase T, Kawai M, Sakamoto K, Hide M (2014) Surface plasmon resonance for cell-based clinical diagnosis. Sensors (Basel) 14 (3):4948–4959

36. Horii M, Shinohara H, Iribe Y, Suzuki M (2011) Living cell-based allergen sensing using a high resolution two-dimensional surface plasmon resonance imager. Analyst 136 (13):2706–2711

37. Scott CW, Peters MF (2010) Label-free whole-cell assays: expanding the scope of GPCR screening. Drug Discov Today 15(17-18):704–716

38. Peterson AW, Halter M, Tona A, Bhadriraju K, Plant AL (2009) Surface plasmon resonance imaging of cells and surface-associated fibronectin. BMC Cell Biol 10:16–33

39. Peterson AW, Halter M, Tona A, Bhadriraju K, Plant AL (2010) Using surface plasmon resonance imaging to probe dynamic interactions between cells and extracellular matrix. Cytometry A 77A(9):895–903

40. Robelek R (2009) Surface plasmon resonance sensors in cell biology: basics & application. Bioanal Rev 1(1):57–72

41. Fang Y (2010) Live cell optical sensing for high throughput applications. Adv Biochem Eng Biotechnol 118:153–163

42. Fang Y, Ferrie AM, Fontaine NH, Mauro J, Balakrishnan J (2006) Resonant waveguide grating biosensor for living cell sensing. Biophys J 91(5):1925–1940

43. Deng H, Wang C, Su M, Fang Y (2012) Probing biochemical mechanisms of action of muscarinic M3 receptor antagonists with label-free whole cell assays. Anal Chem 84 (19):8232–8239

44. Wolf B, Brischwein M, Baumann W, Ehret R, Kraus M (1998) Monitoring of cellular signalling and metabolism with modular sensor- technique: the PhysioControl-Microsystem (PCM). Biosens Bioelectron 13(5):501–509

45. Owicki JC, Parce JW (1990) Bioassays with a microphysiometer. Nature 344(6263):271

46. Lehmann M, Baumann W, Brischwein M, Ehret R, Kraus M, Schwinde A, Bitzenhofer M, Freund I, Wolf B (2000) Non-invasive measurement of cell membrane associated proton gradients by ion-sensitive field effect transistor arrays for microphysiological and bioelectronical applications. Biosens Bioelectron 15(3-4):117–124

47. Lehmann M, Baumann W, Brischwein M, Gahle H, Freund I, Ehret R, Drechsler S, Palzer H, Kleintges M, Sieben U, Wolf B (2001) Simultaneous measurement of cellular respiration and acidification with a single CMOS ISFET. Biosens Bioelectron 16(3):195–203

48. Hafner F (2000) Cytosensor Microphysiometer: technology and recent applications. Biosens Bioelectron 15(3-4):149–158

49. McConnell HM, Owicki JC, Parce JW, Miller DL, Baxter GT, Wada HG, Pitchford S (1992) The cytosensor microphysiometer: biological applications of silicon technology. Science 257 (5078):1906–1912

50. Owicki JC, Bousse LJ, Hafeman DG, Kirk GL, Olson JD, Wada HG, Parce JW (1994) The light-addressable potentiometric sensor: principles and biological applications. Annu Rev Biophys Biomol Struct 23:87–113

51. Parce JW, Owicki JC, Kercso KM, Sigal GB, Wada HG, Muir VC, Bousse LJ, Ross KL, Sikic BI, McConnell HM (1989) Detection of cell-affecting agents with a silicon biosensor. Science 246(4927):243–247

52. Fanigliulo A, Accossato P, Adami M, Lanzi M, Martinoia S, Paddeu S, Parodi MT, Rossi M, Sartore M, Grattarola M, Nicolini C (1996) Comparison between a LAPS and an FET-based sensor for cell-metabolism detection. Sens Actuators B 32(1):41–48

53. Ungerbock B, Charwat V, Ertl P, Mayr T (2013) Microfluidic oxygen imaging using integrated optical sensor layers and a color camera. Lab Chip 13(8):1593–1601

54. Fromherz P (1999) Extracellular recording with transistors and the distribution of ionic conductances in a cell membrane. Eur Biophys J 28(3):254–258

55. Fromherz P, Offenhausser A, Vetter T, Weis J (1991) A neuron-silicon junction: a Retzius cell of the leech on an insulated- gate field-effect transistor. Science 252(5010):1290–1293

56. Fromherz P, Stett A (1995) Silicon-neuron junction: capacitive stimulation of an individual neuron on a silicon chip. Phys Rev Lett 75(8):1670–1673

57. Gross GW, Rhoades BK, Azzazy HM, Wu MC (1995) The use of neuronal networks on multielectrode arrays as biosensors. Biosens Bioelectron 10(6-7):553–567

58. Woolley DE, Tetlow LC, Adlam DJ, Gearey D, Eden RD (2002) Electrochemical monitoring of cell behaviour in vitro: a new technology. Biotechnol Bioeng 77(7):725–733

59. Janshoff A, Galla HJ, Steinem C (2000) Piezoelectric mass-sensing devices as biosensors-an alternative to optical biosensors? Angew Chem Int Ed Engl 39(22):4004–4032

60. Kipling AL, Thompson M (1990) Network analysis method applied to liquid-phase acoustic-wave sensors. Anal Chem 62(14):1514–1519

61. Yang MS, Thompson M (1993) Multiple chemical information from the thickness shear mode acoustic-wave sensor in the liquid-phase. Anal Chem 65(9):1158–1168

62. Gryte DM, Ward MD, Hu WS (1993) Real-time measurement of anchorage-dependent cell-adhesion using a quartz crystal microbalance. Biotechnol Prog 9(1):105–108

63. Wegener J, Janshoff A, Galla HJ (1998) Cell adhesion monitoring using a quartz crystal microbalance: comparative analysis of different mammalian cell lines. Eur Biophys J Biophys Lett 28(1):26–37

64. Saitakis M, Gizeli E (2012) Acoustic sensors as a biophysical tool for probing cell attachment and cell/surface interactions. Cell Mol Life Sci 69(3):357–371

65. Wegener J, Seebach J, Janshoff A, Galla HJ (2000) Analysis of the composite response of shear wave resonators to the attachment of mammalian cells. Biophys J 78(6):2821–2833

66. Heitmann V, Wegener J (2007) Monitoring cell adhesion by piezoresonators: impact of increasing oscillation amplitudes. Anal Chem 79(9):3392–3400

67. Marx KA, Zhou T, Montrone A, McIntosh D, Braunhut SJ (2007) A comparative study of the cytoskeleton binding drugs nocodazole and taxol with a mammalian cell quartz crystal microbalance biosensor: different dynamic responses and energy dissipation effects. Anal Biochem 361(1):77–92

68. Marx KA, Zhou T, Montrone A, Schulze H, Braunhut SJ (2001) A quartz crystal microbalance cell biosensor: detection of microtubule alterations in living cells at nM nocodazole concentrations. Biosens Bioelectron 16(9-12):773–782

69. Pietuch A, Bruckner BR, Schneider D, Tarantola M, Rosman C, Sonnichsen C, Janshoff A (2015) Mechanical properties of MDCK II cells exposed to gold nanorods. Beilstein J Nanotechnol 6:223–231

70. Tarantola M, Schneider D, Sunnick E, Adam H, Pierrat S, Rosman C, Breus V, Sonnichsen C, Basche T, Wegener J, Janshoff A (2009) Cytotoxicity of metal and semiconductor nanoparticles indicated by cellular micromotility. ACS Nano 3(1):213–222

71. Giaever I, Keese CR (1984) Monitoring fibroblast behavior in tissue culture with an applied electric field. Proc Natl Acad Sci U S A 81(12):3761–3764

72. Giaever I, Keese CR (1991) Micromotion of mammalian cells measured electrically. Proc Natl Acad Sci U S A 88(17):7896–7900

73. Wegener J, Keese CR, Giaever I (2000) Electric cell-substrate impedance sensing (ECIS) as a noninvasive means to monitor the kinetics of cell spreading to artificial surfaces. Exp Cell Res 259(1):158–166

74. Stolwijk JA, Michaelis S, Wegener J (2012) Cell growth and cell death studied by electric cell-substrate impedance sensing. In: Jiang WG (ed) Electric cell-substrate impedance sensing and cancer metastasis, vol 17, Cancer metastasis – biology and treatment. Springer, Heidelberg, pp 85–117

75. Keese CR, Wegener J, Walker SR, Giaever I (2004) Electrical wound-healing assay for cells in vitro. Proc Natl Acad Sci U S A 101(6):1554–1559

76. Arndt S, Seebach J, Psathaki K, Galla HJ, Wegener J (2004) Bioelectrical impedance assay to monitor changes in cell shape during apoptosis. Biosens Bioelectron 19(6):583–594

77. Curtis TM, Widder MW, Brennan LM, Schwager SJ, van der Schalie WH, Fey J, Salazar N (2009) A portable cell-based impedance sensor for toxicity testing of drinking water. Lab Chip 9(15):2176–2183

78. Opp D, Wafula B, Lim J, Huang E, Lo JC, Lo CM (2009) Use of electric cell-substrate impedance sensing to assess in vitro cytotoxicity. Biosens Bioelectron 24(8):2625–2629

79. Tran TB, Nguyen PD, Um SH, Son SJ, Min J (2013) Real-time monitoring in vitro cellular cytotoxicity of silica nanotubes using electric cell-substrate impedance sensing (ECIS). J Biomed Nanotechnol 9(2):286–290

80. Fang Y (2011) Label-free receptor assays. Drug Discov Today Technol 7(1):e5–e11

81. Schroder R, Janssen N, Schmidt J, Kebig A, Merten N, Hennen S, Muller A, Blattermann S, Mohr-Andra M, Zahn S, Wenzel J, Smith NJ, Gomeza J, Drewke C, Milligan G, Mohr K, Kostenis E (2010) Deconvolution of complex G protein-coupled receptor signaling in live cells using dynamic mass redistribution measurements. Nat Biotechnol 28(9):943–949

82. Giaever I, Keese CR (1986) Use of electric fields to monitor the dynamical aspect of cell behavior in tissue culture. IEEE Trans Biomed Eng 33(2):242–247

83. Giaever I, Keese CR (1993) A morphological biosensor for mammalian cells. Nature 366 (6455):591–592

84. Janshoff A, Wegener J, Sieber M, Galla HJ (1996) Double-mode impedance analysis of epithelial cell monolayers cultured on shear wave resonators. Eur Biophys J 25(2):93–103

85. Wegener J (2009) Impedance analysis of cell junctions. In: Fuchs H (ed) Nanoprobes, vol 6, Nanoprobes. Wiley VCH, Weinheim, pp 325–357

86. Wegener J, Sieber M, Galla HJ (1996) Impedance analysis of epithelial and endothelial cell monolayers cultured on gold surfaces. J Biochem Biophys Methods 32(3):151–170

87. Wegener J, Seebach J (2014) Experimental tools to monitor the dynamics of endothelial barrier function: a survey of in vitro approaches. Cell Tissue Res 355(3):485–514

88. Stolwijk JA, Hartmann C, Balani P, Albermann S, Keese CR, Giaever I, Wegener J (2011) Impedance analysis of adherent cells after in situ electroporation: non-invasive monitoring during intracellular manipulations. Biosens Bioelectron 26(12):4720–4727

89. Wegener J, Keese CR, Giaever I (2002) Recovery of adherent cells after in situ electroporation monitored electrically. Biotechniques 33 (2):348, 350, 352 passim

90. Lukic S, Wegener J (2015) Impedimetric monitoring of cell-based assays. In: eLS. Wiley, Chichester

91. Frisch T, Thoumine O (2002) Predicting the kinetics of cell spreading. J Biomech 35 (8):1137–1141

92. Wang L, Wang L, Yin H, Xing W, Yu Z, Guo M, Cheng J (2010) Real-time, label-free monitoring of the cell cycle with a cellular impedance sensing chip. Biosens Bioelectron 25 (5):990–995

93. Hong J, Kandasamy K, Marimuthu M, Choi CS, Kim S (2011) Electrical cell-substrate impedance sensing as a non-invasive tool for cancer cell study. Analyst 136(2):237–245

94. Xie F, Xu Y, Wang L, Mitchelson K, Xing W, Cheng J (2012) Use of cellular electrical impedance sensing to assess in vitro cytotoxicity of anticancer drugs in a human kidney cell nephrotoxicity model. Analyst 137(6):1343–1350

95. Lo CM, Keese CR, Giaever I (1994) pH changes in pulsed CO_2 incubators cause periodic changes in cell morphology. Exp Cell Res 213(2):391–397

96. Lo C-M, Keese CR, Giaever I (1993) Monitoring motion of confluent cells in tissue culture. Exp Cell Res 204:102–109

97. Lovelady DC, Friedman J, Patel S, Rabson DA, Lo CM (2009) Detecting effects of low levels of cytochalasin B in 3T3 fibroblast cultures by analysis of electrical noise obtained from cellular micromotion. Biosens Bioelectron 24(7):2250–2254

98. Lo CM, Linton M, Keese CR, Giaever I (2001) Correlated motion and oscillation of neighboring cells in vitro. Cell Commun Adhes 8(3):139–145

99. Bagnaninchi PO, Drummond N (2011) Real-time label-free monitoring of adipose-derived stem cell differentiation with electric cell-substrate impedance sensing. Proc Natl Acad Sci U S A 108(16):6462–6467
100. Wegener J, Zink S, Rosen P, Galla H (1999) Use of electrochemical impedance measurements to monitor beta-adrenergic stimulation of bovine aortic endothelial cells. Pflugers Arch 437(6):925–934
101. Hartmann C, Zozulya A, Wegener J, Galla HJ (2007) The impact of glia-derived extracellular matrices on the barrier function of cerebral endothelial cells: an in vitro study. Exp Cell Res 313(7):1318–1325
102. Wegener J, Hakvoort A, Galla HJ (2000) Barrier function of porcine choroid plexus epithelial cells is modulated by cAMP-dependent pathways in vitro. Brain Res 853(1):115–124
103. Dieterich P, Odenthal-Schnittler M, Mrowietz C, Kramer M, Sasse L, Oberleithner H, Schnittler HJ (2000) Quantitative morphodynamics of endothelial cells within confluent cultures in response to fluid shear stress. Biophys J 79(3):1285–1297
104. Hondroulis E, Liu C, Li CZ (2010) Whole cell based electrical impedance sensing approach for a rapid nanotoxicity assay. Nanotechnology 21(31):315103
105. Male KB, Lachance B, Hrapovic S, Sunahara G, Luong JH (2008) Assessment of cytotoxicity of quantum dots and gold nanoparticles using cell-based impedance spectroscopy. Anal Chem 80(14):5487–5493
106. Male KB, Hamzeh M, Montes J, Leung AC, Luong JH (2013) Monitoring of potential cytotoxic and inhibitory effects of titanium dioxide using on-line and non-invasive cell-based impedance spectroscopy. Anal Chim Acta 777:78–85
107. Otero-Gonzalez L, Sierra-Alvarez R, Boitano S, Field JA (2012) Application and validation of an impedance-based real time cell analyzer to measure the toxicity of nanoparticles impacting human bronchial epithelial cells. Environ Sci Technol 46(18):10271–10278
108. Chuang SM, Lee YH, Liang RY, Roam GD, Zeng ZM, Tu HF, Wang SK, Chueh PJ (2013) Extensive evaluations of the cytotoxic effects of gold nanoparticles. Biochim Biophys Acta 1830(10):4960–4973
109. Huang L, Xie L, Boyd JM, Li XF (2008) Cell-electronic sensing of particle-induced cellular responses. Analyst 133(5):643–648
110. Moe B, Gabos S, Li XF (2013) Real-time cell-microelectronic sensing of nanoparticle-induced cytotoxic effects. Anal Chim Acta 789:83–90
111. Bohmert L, Niemann B, Thunemann AF, Lampen A (2012) Cytotoxicity of peptide-coated silver nanoparticles on the human intestinal cell line Caco-2. Arch Toxicol 86(7):1107–1115
112. Seiffert JM, Baradez MO, Nischwitz V, Lekishvili T, Goenaga-Infante H, Marshall D (2012) Dynamic monitoring of metal oxide nanoparticle toxicity by label free impedance sensing. Chem Res Toxicol 25(1):140–152
113. Lovelady DC, Richmond TC, Maggi AN, Lo CM, Rabson DA (2007) Distinguishing cancerous from noncancerous cells through analysis of electrical noise. Phys Rev E Stat Nonlin Soft Matter Phys 76(4 Pt 1):041908
114. Lai YT, Lo CM (2014) Assessing in vitro cytotoxicity of cell micromotion by Hilbert-Huang transform. Conf Proc IEEE Eng Med Biol Soc 2014:3200–3203
115. Sapper A, Reiss B, Janshoff A, Wegener J (2006) Adsorption and fluctuations of giant liposomes studied by electrochemical impedance measurements. Langmuir 22(2):676–680

Interaction of Nanoparticles with Lipid Monolayers and Lung Surfactant Films

Mridula Dwivedi, Amit Kumar Sachan, and Hans-Joachim Galla

Abstract It has been shown that the interactions of nanoparticles with lipid and lipid–peptide monolayers mimicking the lung surfactant strongly depend on the physical properties of the nanoparticles, their size, and on the physical properties of the surface film. Hydrophobic nanoparticles have been found inserting into fluid phases of lipid monolayers. They have an adverse effect on the functional properties of the pulmonary surfactant, which strongly depends on the nanoparticle size. But how NPs disturb or inhibit this surfactant function still remains unclear. Experimental evidences gathered under physiologically relevant conditions or from in vivo studies are still lacking. The present review summarizes systematic investigations on simplified model systems of the lung surfactant using high-resolution bioanalytical techniques that have provided valuable hints and indications about the interactions of NPs with the surfactant layer at the molecular level. Further studies are needed in particular for a more detailed understanding of the mechanism by which NPs are capable of crossing the surfactant barrier even though they experience a very different and individual free energy barrier at the interface.

Contents

M. Dwivedi, A.K. Sachan, and H.-J. Galla (✉)
Institute for Biochemistry, University of Münster, Wilhelm Klemm Str. 2, 48149 Münster, Germany
e-mail: gallah@uni-muenster.de

Abbreviation

AFM	Atomic force microscopy
BODIPY-PC	2-(4, 4-difluoro-5-methyl-4-bora-3a, 4a-diaza-s-indacene-3-dodecanoyl)-1-hexadecanoyl-sn-glycero-3-phosphocholine
CL	Cholesterol
CTAB	Cetyltrimethylammonium bromide
DMAB	Didodecyldimethylammonium bromide
DPPC	Dipalmitoyl phosphatidylcholine
DPPE	Dipalmitoyl phosphatidylethanolamine
DPPG	Dipalmitoyl phosphatidylglycerols
DPPS	Dipalmitoyl phosphatidyl serine
DTAB	Dodecyltrimethylammonium bromide
EMM	Endothelial model cell membranes
Hepes	2-[4-(2-hydroxyethyl)piperazin-1-yl]ethanesulfonic acid
LC	Liquid-condensed phase
LE	Liquid-expanded phase
LS	Lung surfactant
NPs	Nanoparticles
PBS	Phosphate-buffered saline
PI	Phosphatidylinositol
POPG	Palmitoyl oleoyl phosphatidylglycerol
PVA	Polyvinyl alcohol
SM	Sphingomyelin
SP-B	Surfactant-specific protein B
SP-C	Surfactant-specific protein C

1 Introduction

Due to the rapid development of nanotechnology, nanoparticles are nowadays widely used in different areas of normal life as, for instance, in food, as surface coatings, in packing materials and household tools like refrigerators or medical instruments, in skin lotions to protect against sun, or in clothing to avoid bad smell [1–7]. Moreover, nanoparticles are used as carriers for drugs or as diagnostic tools in medicine as well as in research. For example, functionalized quantum dots are used as fluorescent markers to label specific structures in living cells [8–12]. Thus, humans come in contact continuously with nanoparticles that might enter the body via the skin, the intestine, or the lung. Independent of the route of entry, those nanoparticles have to cross biological interfaces and cellular barriers and thus come into contact with the lipids and proteins of the cellular membranes. Due to these interactions the nanoparticles may be coated by different membrane components that may alter their physicochemical surface properties. This, in turn, may modify their biocompatibility or cytotoxic potential. Therefore an understanding of the

interactions of nanoparticles with lipid membranes is crucial for a better assignment of their effects on biological systems. Lipid monolayers are the most simplified model membranes to investigate such interactions. Compared to bilayer membranes these systems are much more sensitive to the modification of fluidity and nanoscopic lateral organization. Moreover, tools like fluorescence microscopy [13, 14], atomic force microscopy [15, 16], or even spatially resolved secondary ion mass Spectrometry [17] could be used to analyze the topology, the structural organization, and the chemical composition, even within domain structures. Thus, lipid monolayers are excellent tools to study the biophysical aspects of membranes under the influence of nanoparticles.

One of the main entry routes to the human body, the lung, contains a lipid–protein monolayer at the air-alveolar interface, which is called the lung surfactant. This is the first barrier/line of defense that nanoparticles encounter before entering the alveolar subphase and reaching the lung epithelium. Thus, protein-doped lipid monolayers are not only a suitable model system to study the interactions of nanoparticles with lipid membranes, but their behavior upon nanoparticle encounter is also of physiological relevance. Since the major task of the lung surfactant is the maintenance of a low surface tension preventing the collapse of the lung, nanoparticles may cause functional disturbances that could lead to a reduced ability to breathe when they interfere with the structural organization of the surfactant.

2 Interaction of Hydrophobic Nanoparticles with Lipid Monolayers

Numerous studies have been performed to elucidate the effect of nanoparticles on the lipid monolayer films at the air–water interface. The different Physico-chemical properties of the nanoparticles, like size, shape, and surface characteristics including charge and functional groups, influence their interactions with the lipid monolayers. Harishchandra et al. investigated the effect of 24 nm hydrophobic polymeric nanoparticles (AmorSil20) on DPPC (dipalmitoylphosphatidylcholine) and DPPG (dipalmitoylphosphatidylglycerol) lipid films [18]. These hydrophobic nanoparticles were dissolved in a chloroform/methanol solution along with the model lipids and spread onto the aqueous subphase using a microsyringe. The influence of nanoparticles on the interfacial properties of the lipid monolayer was studied using a *surface pressure* versus *area-per-molecule* isotherm which provides information regarding the molecular organization at the air–water interface (Fig. 1).

The typical DPPC isotherm shows a liftoff pressure at around 85 Å^2 (area-per-molecule) value followed by a characteristic coexistence region of the *liquid-expanded* (LE) and the *liquid-condensed* (LC) phase which is indicated by a plateau in the surface pressure–area isotherm. The phase behavior of the lipid monolayer is significantly influenced by the nanoparticles in the lipid film. The DPPC isotherm is consistently shifted towards higher area-per-molecule values at low surface
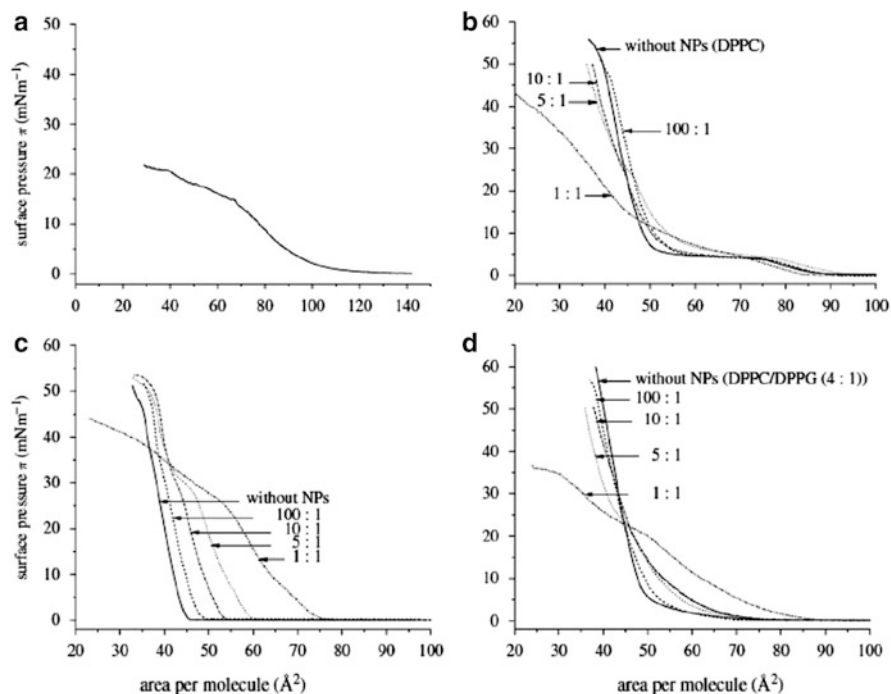
Fig. 1 Surface pressure–area (π–A) isotherms for (**a**) pure AmorSil20 NPs (*solid line*) and mixtures of (**b**) DPPC, (**c**) DPPG, (**d**) DPPC/DPPG (4:1 mol ratio), and AmorSil20 NPs (with permission from Harishchandra et al. [18])

pressure values (<25 mNm^{-1}) with increasing concentration of nanoparticles in the film. Also, the area per molecule along which phase coexistence occurs is diminished with increasing nanoparticle concentration (Fig. 1b). The surface pressure–area isotherm of pure nanoparticles shows retention of the nanoparticles at the air–water interface until it reaches a maximum surface pressure of 21 mNm^{-1} and collapses into the subphase (Fig. 1a). This indicates that hydrophobic nanoparticles are surface active and can form a monolayer at the air–water interface, probably due to the high free energy barrier preventing the nanoparticles from entering into the subphase. The DPPC isotherm in the presence of a very high concentration of nanoparticles exhibits a "kink" at the 25 mNm^{-1} surface pressure implying squeeze out of material into the subphase. This *squeeze out* is thought to indicate the migration of the nanoparticles along with the lipids into the subphase. The presence of nanoparticles in DPPG films showed similar effects compared to DPPC films (Fig. 1c). However, the impact of the nanoparticles on the isotherm was much larger in the case of DPPG. Also, a kink due to the *squeeze out* of material was observed in the presence of high concentrations of nanoparticles similar to DPPC films. In a binary mixture of DPPC/DPPG, the isotherm was again observed to be shifted towards higher area-per-molecule values along with the presence of the kink

implying escape of the material into the subphase (Fig. 1d). Another interesting observation in the lipid–nanoparticle isotherm was the decreased slope of the curve in the region representing the liquid-condensed phase. This implies an increased compressibility of the lipid film and hence a decreased cooperativity between the lipid molecules due to the presence of nanoparticles. The nanoparticles are thought to possibly disrupt the molecular organization of the lipid molecules, thus making the interaction between the lipid molecules weaker.

A lipid monolayer phase separates depending on the surface pressure forming different phase domains. The domain morphology can be studied using epifluorescence microscopy when the lipid monolayer is doped with a fluorescent probe. This probe cannot enter the tightly packed liquid-condensed phase and, hence, preferentially partitions into the liquid-expanded phase allowing visualization of the phase domains. DPPC monolayers have been shown previously to form differently shaped domains at different surface pressures. The most interesting region is the LE–LC coexistence region with the multilobed liquid-condensed domains forming islands in the liquid-expanded phase. In the presence of nanoparticles, these LC domains display a rounder rather than a multilobed morphology and a reduction of the domain size in the phase coexistence region (Fig. 2). This observation is in accordance with the surface pressure isotherms where the molecular area of the phase coexistence region is diminished or disappeared in the presence of nanoparticles. A similar effect of nanoparticles is observed in the phase
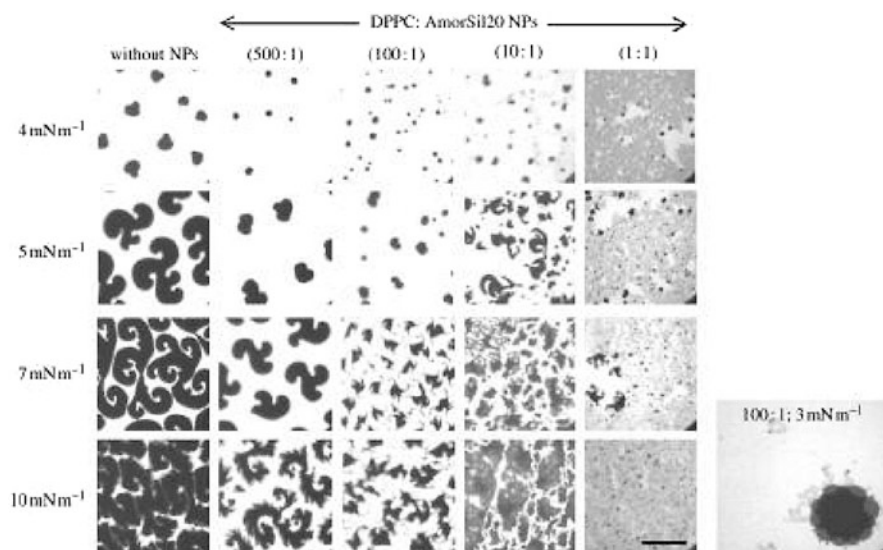
Fig. 2 Fluorescence micrographs of DPPC monolayers containing different concentrations of AmorSil20 NPs spread on pure water at 20 °C. Images taken at different surface pressures are shown. An additional image shows the aggregates of NPs surrounding the rigid domains at the interface of the two phases. All samples were doped with 0.5 mol% fluorescent dye BODIPY-PC. *Scale bar*, 50 μm (with permission from Harishchandra et al. [18])

behavior of DPPC/DPPG binary mixtures where a domain size reduction is observed along with reduced nucleation and formation of domains. Nanoparticle aggregates are also observed to be localized at the phase domain boundaries.

The equilibrium shapes and sizes of the isotropic coexisting liquid phases in a monolayer have been rationalized using mainly two competing factors: (1) the line tension present between the adjacent domains (λ) and (2) the difference in the dipole densities in these phases (μ) [18–21]. Line tension arises due to the hydrophobic mismatch between the coexisting phases; hence, it favors the formation of large circular domains. The dipole density difference or the long-range dipolar forces favor the formation of small noncircular domains. These forces compete with each other to determine the shape and size of the domains based on the ratio λ/μ^2 which is proportional to R_{eq}, the equilibrium radius. If the actual radius of the domain is smaller than R_{eq}, the domains formed are circular, and in the case where it is greater than R_{eq}, the domains formed are noncircular and extended. With increasing surface pressure this ratio decreases so that the equilibrium radius decreases such that R becomes $>R_{eq}$ and large noncircular and multilobed domains are formed. In the presence of the nanoparticles, the domain size decreases with R becoming $<R_{eq}$ implying a decreased dipole density difference or an increased line tension. The dipole density difference is also a function of packing order of the lipid molecules. Hence, the nanoparticles most probably disrupt the molecular packing order of the lipid monolayer, thus causing altered phase behavior of the lipid film.

Another study performed by our group illustrated the influence of nanoparticle diameter on their effect on DPPC monolayers [22]. Polymeric hydrophobic nanoparticles with a diameter of 136 nm are able to cause a change of slope of the DPPC isotherm within the liquid-condensed region, and they diminished the LE–LC coexistence plateau region (Fig. 3). The compressibility of the monolayer
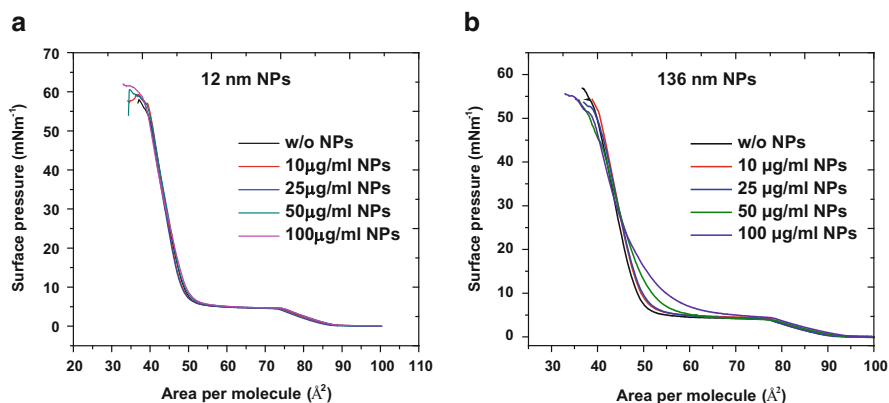
Fig. 3 Surface pressure–area isotherm for (**a**) DPPC exposed to increasing concentrations of small nanoparticles (~12 nm) and (**b**) DPPC exposed to increasing concentrations of large nanoparticles (~136 nm) with 25 mM Hepes + 3 mM CaCl2 as the subphase (with permission from Dwivedi et al. [22])
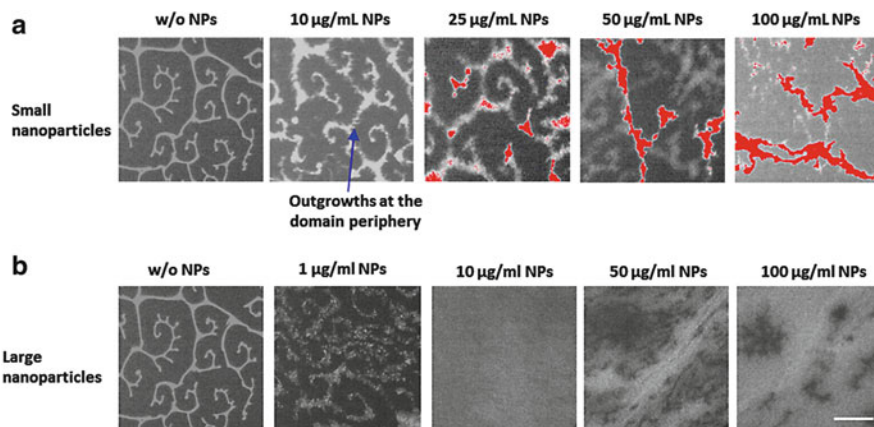
Fig. 4 Epifluorescence micrographs for DPPC films in the presence of increasing concentrations of (**a**) small nanoparticles (~12 nm) and (**b**) large nanoparticles (~136 nm) on water as the subphase at 20 °C. The DPPC monolayer is doped with 0.5 mol% BODIPY-PC which preferentially partitions into the liquid-expanded phase. The *red region* indicates the 12 nm nanoparticles. The images are taken at 10 mNm^{-1} surface pressure. *Scale bar* is 50 μm (with permission from Dwivedi et al. [22])

film is apparently increased, and hence, the cooperativity between lipid molecules is decreased in the presence of 136 nm nanoparticles. The presence of 12 nm nanoparticles, however, does not have any significant effect on the phase behavior of the DPPC film.

Furthermore, the morphology of the phase domains formed during the compression of DPPC monolayers was studied by epifluorescence microscopy. In the presence of large nanoparticles (136 nm), the LC phase domains were highly branched and formed network-like structures for the lowest concentration of NPs. While in the presence of the small nanoparticles (12 nm), the LC domain size decreased (Fig. 4). The presence of large nanoparticles mainly decreased the line tension between the phase domains, thus leading to the formation of highly branched domains. However, small nanoparticles, most probably, affected the packing of the lipid molecules, thus, causing formation of smaller domains with localized outgrowth at the domain periphery.

Peetla et al. [23] studied the interaction of 60 nm hydrophobic polystyrene nanoparticles of different surface chemistry with endothelial model cell membranes (EMM). The model membrane consisted of dipalmitoyl phosphatidylcholine (DPPC), dipalmitoyl phosphatidylethanolamine (DPPE), phosphatidylinositol (PI), dipalmitoyl phosphatidyl serine (DPPS), sphingomyelin (SM), and cholesterol (CL) lipid mixture spread onto a phosphate-buffered saline (PBS) subphase forming a monolayer at the air–water interface. The interaction of the differently functionalized nanoparticles with the monolayer was studied at a constant surface pressure of 30 mNm^{-1}, which is around the surface pressure in a bilayer lipid
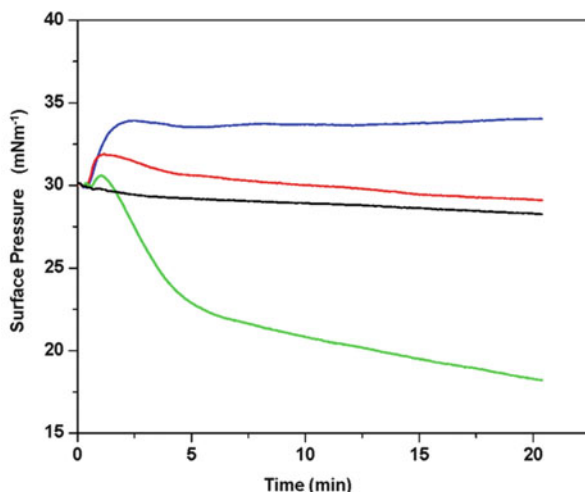
Fig. 5 Effects of NP surface groups on surface pressure of endothelial cell model membrane. A 50 μL portion of a diluted suspension of NPs was injected below the EMM through the injection port using a Hamilton digital microsyringe without causing disturbance to the membrane. Change in surface pressure π was recorded continuously with time. NP size = 60 nm. Concentration = 10 μg/mL. Key: *blue*, aminated; *red*, carboxylated; *green*, plain; *black*, water control without NPs (with permission from Peetla et al. [23])

membrane. The amino-modified nanoparticles were shown to increase the surface pressure of the EMM lipid film much more over time than the carboxylated or the plain nanoparticles (Fig. 5). The increase in surface pressure was smaller in the case of the carboxylated compared to aminated nanoparticles. In the case of plain nanoparticles, the surface pressure values decreased significantly. The authors stipulate the electrostatic interactions between the anionic lipids in the film and the positively charged amino groups to be responsible for the higher level of interaction between the aminated nanoparticles and the EMM. The carboxylated nanoparticles are speculated to have minimum interaction with the EMM, whereas the plain nanoparticles, which are hydrophobic in nature, are thought to cause a loss of phospholipids from the interface into the bulk, thus decreasing the surface pressure values. The hydrophobic nanoparticles are believed to interact with the hydrophobic acyl chains of the lipid molecules thus mobilizing them from the interface into the bulk. Moreover, surface pressure–area isotherms of EMM in the presence of these differently functionalized nanoparticles were recorded to study the penetration of the nanoparticles into the EMM film. The presence of aminated nanoparticles shows a significant shift of the isotherm towards higher area-per-molecule values, whereas it remained unaffected by the presence of carboxylated nanoparticles (data not shown). In the presence of plain nanoparticles, the isotherms shifted to lower area-per-molecule values at higher surface pressures. AFM analysis supported the presence of higher numbers of aminated nanoparticles in the EMM monolayer film as compared to the carboxylated and plain nanoparticles. The

observed increase in surface pressure for positively charged particles is, however, rationalized by electrostatic interaction between the nanoparticles and the negatively charged headgroups of the monolayer rather than their penetration into the monolayer. This interaction was assumed to lead to the condensation of the monolayer film causing an increase in the surface pressure. Therefore, the interaction of the nanoparticles with the partly anionic monolayer film was shown to be dependent on the functional group and the cationic charge on the surface of the nanoparticles. The plain hydrophobic nanoparticles were shown to destabilize the lipid monolayer by causing loss of the material into the bulk phase.

In another study using the same model system, it was consistently shown that the functional groups covering the surface of the nanoparticles are critical and determine their interaction with the lipid monolayer films [24]. The surface of the 130 nm polystyrene nanoparticles was coated with cationic surfactants like di-chained didodecyldimethylammonium bromide (DMAB); single-chained cetyltrimethylammonium bromide (CTAB), or dodecyltrimethylammonium bromide (DTAB). Also, polyvinyl alcohol was used as a nonionic polymeric surfactant to cover the surface of the nanoparticles. The surface pressure of the EMM monolayer increased significantly over time with the addition of the DMAB-covered nanoparticles. Whereas the surface pressure of the EMM monolayer increased only slightly and then decreased back to the baseline level in the presence of CTAB-, DTAB-, and PVA-covered nanoparticles (Fig. 6). With the addition of plain hydrophobic nanoparticles, the surface pressure decreased rapidly.
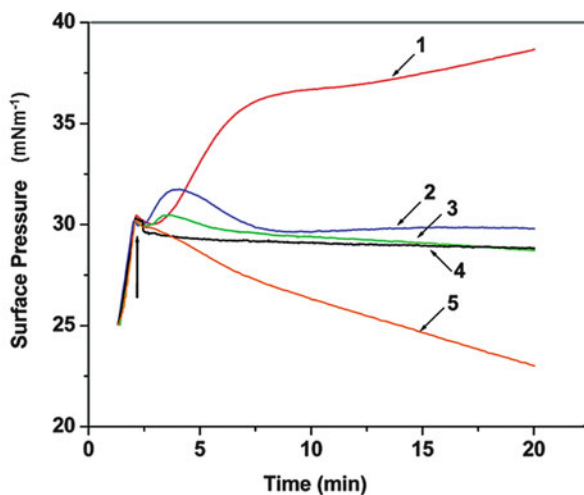
Fig. 6 Changes in surface pressure of the EMM with time caused by interaction of the membrane with different surfactant-modified NPs. Fifty microliters of a 1 % NP suspension were injected into the subphase below the EMM without causing a disturbance to the membrane itself. Any change in surface pressure over time was immediately recorded. Final nanoparticle concentration in subphase was 10 μg/mL. Key: *1*, DMAB-modified NPs; *2*, CTAB-modified NPs; *3*, DTAB-modified NPs; *4*, PVA-modified NPs; *5*, unmodified NPs. Representative data from at least three repeats are shown (with permission from Peetla and Labhasetwar [24])

The higher level of hydrophobicity of the DMAB-covered nanoparticles was thought to facilitate an increased interaction with the EMM monolayer. The surface pressure–area isotherm of the EMM was recorded to more deeply understand the penetration of the nanoparticles into the membrane. The study showed that all the cationic surfactant-covered nanoparticles penetrated the monolayer at low lipid densities. However, at higher lipid densities only DMAB-covered nanoparticles were retained. This was concluded from the observation that the surface pressure–area isotherm got shifted towards higher area-per-molecule values in the presence of DMAB-covered nanoparticles, whereas CTAB-, DTAB-, and PVA-covered nanoparticles caused a shift of the isotherm towards a higher area only at low surface pressures. AFM scans showed the presence of DMAB-covered nanoparticles homogeneously distributed across the EMM monolayer without any preferential partitioning to lipid phases. The number of CTAB-covered nanoparticles was smaller compared to DMAB, and these NPs were mainly anchored to the *liquid-condensed* domains. This led to the conclusion that the DMAB-covered nanoparticles were able to enter the monolayer film, and since they interact hydrophobically with the lipid film, they are dispersed throughout the monolayer. CTAB-covered nanoparticles were thought to interact electrostatically with the condensed phase and hence are found to be localized in that area. Thus, the authors could show that the more hydrophobic cationic surfactants provided stronger interaction of the nanoparticles with the EMM monolayer and increased their penetration into the lipid film. The higher interaction of DMAB as compared to CTAB is rationalized as follows: one of the acyl chains of DMAB is thought to anchor to the surface of the hydrophobic nanoparticles, whereas the other acyl chain is free to anchor to the monolayer film. This interaction is not possible for the single-chained CTAB- and DTAB-covered nanoparticles. Hence, in these cases, electrostatic interactions are dominant. It is important to note that the plain nanoparticles, which are hydrophobic in nature but do not have a hydrophobic acyl chain to anchor, cause a loss of lipid material from the interface into the bulk. A schematic representation illustrating the individual effects of different nanoparticles on EMM monolayers is shown in Fig. 7. Thus, not only the surface charge but also the structure of the molecule at the surface of the nanoparticle affects its interaction with the monolayer.

Likewise, a number of studies have been performed to investigate the effects of hydrophilic nanoparticles on lipid monolayers. Stuart et al. [25] investigated the effect of hydrophilic gelatin nanoparticles on DPPC monolayers. The surface pressure–area isotherm is shifted towards higher area-per-molecule values in the presence of gelatin nanoparticles in the subphase. The collapse pressure of the lipid monolayers did not decrease in the presence of nanoparticles indicating that the film is not destabilized by the nanoparticles.

Another study performed by the same group addressed the effect of gelatin nanoparticle size on their interactions with the DPPC monolayers. It turned out that particles with a diameter of 236 nm have the strongest interactions with the lipid film [26]. The surface pressure–area isotherms displayed a shift towards higher area-per-molecule values in the presence of all nanoparticles. However,
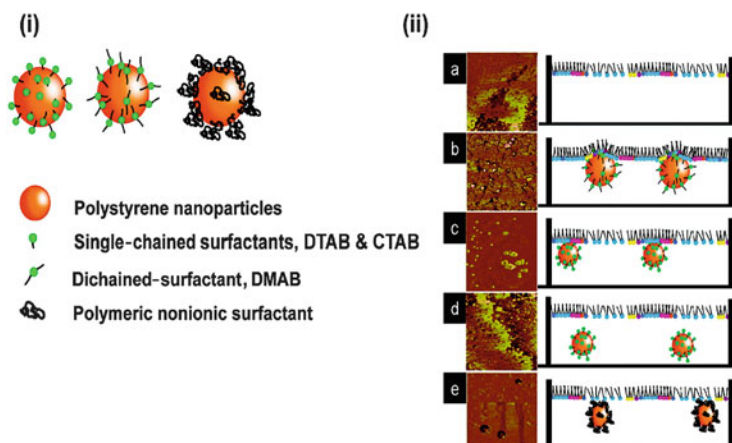
Fig. 7 (**i**) Schematic representation describing the interaction of NPs decorated with different surfactants endothelial model membranes (EMM). (**ii**) (*a*) EMM alone and schematic representation of the individual interactions of (*b*) DMAB-, (*c*) CTAB-, (*d*) DTAB-, and (*e*) PVA-modified NPs with the model membrane. DMAB-modified NPs penetrate the EMM, whereas CTAB-modified NPs interact with phospholipid liquid-condensed domains through electrostatic interactions. DTAB- and PVA-modified NPs did not interact. Corresponding AFM phase images of Langmuir–Schaefer (LS) films show that DMAB-modified NPs become embedded in between phospholipids, whereas CTAB-modified NPs attach to the condensed phospholipid domains (with permission from Peetla and Labhasetwar [24])

the alteration in the phase behavior of the DPPC monolayer was different for differently sized nanoparticles.

Kelvin probe microscopy had been employed to observe the surface potential changes due to the presence of nanoparticles in the subphase. The orientation of the lipid headgroups in contact to the aqueous subphase and the oriented water molecules just beneath the lipid headgroups cause the generation of dipole potentials. Kelvin probe microscopy can be used to measure these dipole potentials. The surface potential curve increases sharply for DPPC monolayers when phase transition occurs, possibly due to a rearrangement of the acyl chains of the lipid molecules and the reorientation of water surrounding the DPPC molecules. In the presence of gelatin nanoparticles, the surface potential curve is quite different from that of pure DPPC. The steep increase observed for pure DPPC monolayers during phase transition is diminished in the presence of nanoparticles, and a rather gradual increase of the surface potential is observed. Also, the maximum surface potential achieved by the DPPC film is significantly reduced in the presence of nanoparticles, and this effect is independent of the particle size. Hence, it was inferred that the reorientation of the acyl chains of the lipid molecules during phase transition is delayed significantly in the presence of gelatin nanoparticles. Owing to the size of individual nanoparticles, a large number of lipid molecules are affected simultaneously. Also, gelatin nanoparticles are hydrophilic in nature and hence can reorient the dipole of water molecules themselves, thus, causing the dipole potential

of the monolayer film to change. With this study, the authors could conclusively prove that the nanoparticles could interact with the lipid molecules and alter their orientation with respect to the water molecules and consequently alter the phase behavior of the lipids, irrespective of their size.

Degen et al. [27] showed the influence of charges within the monolayer film on the absorption of positively charged Υ-Fe$_2$O$_3$ nanoparticles. The surface pressure–area isotherm of stearylamine monolayers showed a much more pronounced shift of the isotherm towards higher area-per-molecule values compared to stearyl alcohol monolayers and in particular compared to stearic acid monolayers. This behavior was thought to be due to the repulsion between the amino group and the positively charged nanoparticles leading to an expansion of the isotherm. X-ray reflectivity measurements were employed to investigate the adsorbance of the nanoparticles to the monolayer film. The diffraction pattern remained unchanged over time for stearylamine and stearyl alcohol. However, it showed formation of an adsorbed layer of nanoparticles beneath the stearic acid monolayer film with time. This was again explained by electrostatic interaction which provide attractive forces between the Fe$_2$O$_3$ nanoparticles and the stearic acid monolayer, but repulsive forces between the stearylamine monolayers and the particles. This was also supported by surface potential measurements which increased significantly over time for stearic acid monolayers rather than stearylamine and stearyl alcohol monolayers (Fig. 8).

The afore mentioned and many more studies have been carried out independently with the common goal to understand the interactions between a lipid monolayers and nanoparticles. The degree to which lipid monolayers are affected by dispersed nanoparticles depends on the physicochemical properties of the nanoparticles and, to some extent, of the lipid monolayer. The presence of plain hydrophobic nanoparticles mixed with an uncharged lipid monolayer seems to affect the phase behavior of the monolayer in a size-dependent manner. The large

Fig. 8 Surface potential isotherms of stearic acid (**a**), stearyl alcohol (**b**), and stearylamine (**c**) spread on a subphase containing γ-Fe$_2$O$_3$ nanoparticles (W% $= 0.7$ g/L) at 30 mNm^{-1} surface pressure (with permission from Degen et al. [27])
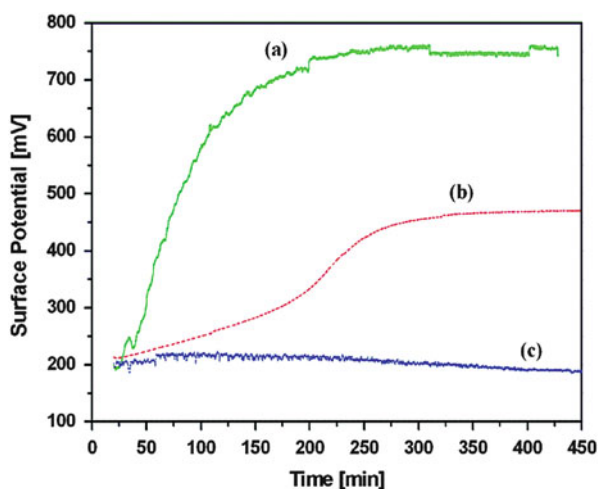
nanoparticles with diameter of around 150 nm tend to severely disrupt the phase behavior of the lipid film as compared to the smaller 12 nm nanoparticles. However, both hydrophobic nanoparticles are consistently retained in the lipid film irrespective of their size. The presence of charged nanoparticles in the subphase below a slightly anionic lipid film shows predominantly electrostatic interactions governing the observed changes in the phase behavior of the lipid film. The electrostatic attractive force of the anionic lipid film with cationic nanoparticles has been assumed to cause condensation of the lipid film, whereas nanoparticles with repulsive electrostatic force do not cause significant change in the phase behavior. Likewise, it has also been proposed that the presence of positively charged nanoparticles in the subphase below a positively charged monolayer affects the phase behavior owing to the repulsive interaction. The presence of plain hydrophobic nanoparticles causes destabilization of the ionic lipid film due to the interaction of the nanoparticles with the acyl chains of the lipids. Hence, electrostatic interactions have been shown to be much more dominant than the hydrophobic interactions. Functionalization of the nanoparticle surface also significantly affects the interaction of the nanoparticles with the lipid films. Presence of a free acyl chain provides an anchoring group to the lipid film thus facilitating insertion into the lipid membrane and alteration in the phase behavior. Adsorption or insertion of nanoparticles to the lipid film can also be facilitated by electrostatic attraction between the lipid film and the nanoparticles. Hence, it is essential for the appropriate and efficient usage of nanotechnology in the different medical and commercial applications that the major physicochemical properties of nanoparticles (size) and their surface decoration (hydrophobicity, charge, structure of surface-immobilized molecules) are considered and expected to have an individual impact on biological membranes. The available data do not allow deriving general and broadly applicable interaction rules yet, but the tendencies described above provide a first line of evidence.

3 The Pulmonary Surfactant Film at the Air–Alveolar Interface

Lungs are the essential respiratory organ in mammals. It is the principal function of the lungs to transport oxygen from the atmosphere into the blood circulation and to release carbon dioxide from the blood circulation to the atmosphere. The lungs of mammals consist of highly branched structures that terminate into the millions of tiny membranous sacs called alveoli, the functional units of mammalian lungs (Fig. 9).

Each *alveolus* needs to cyclically inflate and deflate for a mechanically efficient breathing process. At the air-side surface of each alveolus, there exists an air–aqueous interface. The existence of surface tension at the air–aqueous interface can render the inflation process of alveoli energetically as well as mechanically
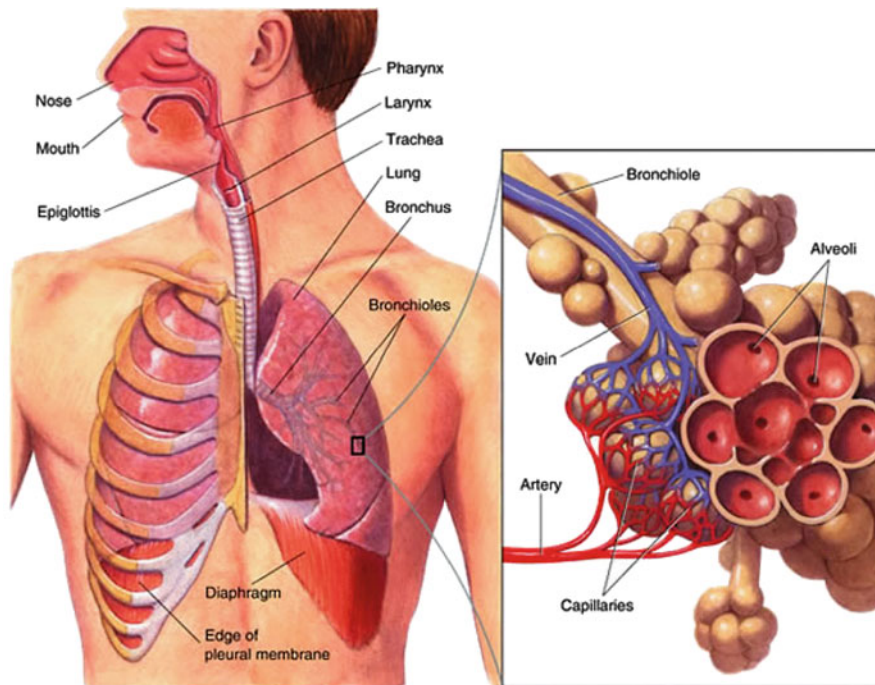
Fig. 9 Schematic of the human lungs, showing its highly branched substructure containing numerous terminal alveolar sacs to maximize the surface area for gas exchange (http://www.goldiesroom.org)

unfavorable and consequently can cause alveolar collapse, i.e., *atelectasis*. This, however, does not occur in a healthy lung respiratory system, since the surface tension is minimized by the presence of a thin film at the air–aqueous interface of each alveolus. This thin film consists of a complex and highly surface-active mixture of lipids and proteins and is referred to as "lung surfactant" or "pulmonary surfactant" [28–30].

The pulmonary surfactant film at the air–alveolar interface is considered to be a monomolecular film of surfactants. However, various studies involving in vivo, in vitro, in situ, and ex situ experimental approaches and employing different biophysical techniques, such as electron microscopy, atomic force microscopy, fluorescence microscopy, captive bubble tensiometry, X-ray reflectivity, and neutron reflectivity measurements, have accumulated strong evidence that at least some parts of the pulmonary surfactant film are more than just a monolayer [31–37]. The interfacial surfactant monolayer contains closely associated discrete patches of surfactants in multilamellar/multilayer form, with a minimum of one extra bilayer (Fig. 10). These multilayered patches have been named as the surface-associated reservoirs (SARs) of surfactants, which have been proposed to be functionally vital for the continuous integrity and functioning of the film.
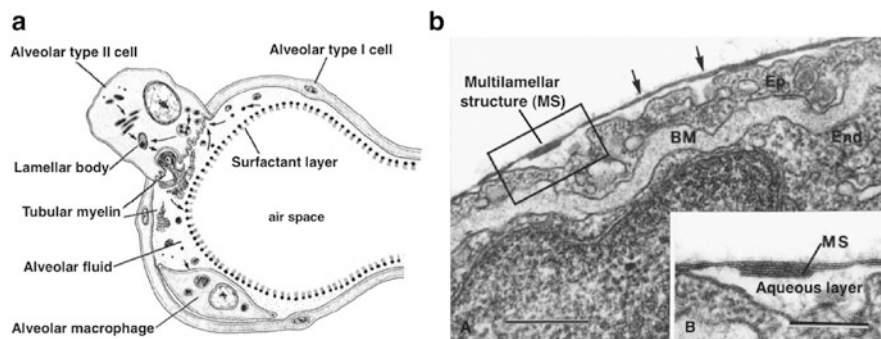
Fig. 10 (**a**) Schematic of a cross-sectional view of an alveolus. (**b**) An electron micrograph showing the multilamellar structures in the pulmonary surfactant film of guinea pig lungs (with permission from Schurch et al. [31] and Scarpelli and Mautone[38])

The main physiological function of pulmonary surfactant is the reduction of surface tension at the air–aqueous interface of each alveolus. The presence of the pulmonary surfactant film limits the surface tension to ~0–25 mNm^{-1} during dynamic compression and expansion cycles of the interface and avoids the alveolar collapse. In general, three crucial physicochemical phenomena are required at the air–aqueous interface for an efficient functioning of the pulmonary surfactant film during a regular breathing process: (1) rapid adsorption of the surfactant materials from the aqueous subphase to the interface, (2) reduction of the surface tension close to 0 mNm^{-1} upon respiratory surface area compression at expiration, and (3) rapid re-spreading of the compressed film without much elevation of the surface tension during surface area expansion at inspiration [30, 39, 40].

Besides helping the lungs to maintain patency, the pulmonary surfactant film possesses a number of other important functions. Due to the continuous exposure of the lungs to the environmental air, this film serves as a first barrier and line of defense against invading pathogens, particles, and/or allergens reaching the inner alveolar space, thus providing a specific as well as nonspecific host defense [41, 42]. It also inhibits the leakage of serum or alveolar fluid into the airways, which otherwise would cause pulmonary edema [43, 44].

As mentioned above, pulmonary surfactant is an unconditional prerequisite for lung function and a smooth breathing process. Therefore, deficiency, dysfunction, and/or absence of an operative pulmonary surfactant system at the air–alveolar interface can cause multiple respiratory dysfunctions, such as respiratory distress syndrome (RDS) in infants [45–47] and acute respiratory distress syndrome (ARDS) in adults [48–50].

4   Deposition of Nanomaterials Along the Pulmonary Route and Their Interaction with the Pulmonary Surfactant Film

Human lungs inhale and exhale around 10,000 L of air from the environment per day [51]. Due to the continuous contact with the environment, exposure of the lungs to the airborne particles and microorganisms is inevitable. With the advent and constant expansion of nanotechnology in diverse aspects of life, such as food, cosmetics and pharmacology to medicines, (bio)chemical and mechanical engineering, optics to electronic engineering, and space science, nanosized as well as microsized particles/materials are omnipresent in society [8–10, 12, 52].

After inhalation, deposition of these particles can take place at different units of the respiratory tree, i.e., the large conducting airways, the small conducting airways, and the alveoli. The mechanism and the deposition rate of differently sized particles vary in different parts of the lung and depend largely on the thermodynamic and/or aerodynamic diameter of the inhaled particles.

There are three main mechanisms by which particle deposition can occur in the pulmonary system: sedimentation, inertial impaction, and diffusion [53]. Unlike impaction and sedimentation, diffusion deposition is inversely related to the particle size. Therefore, drag forces, such as gravity, inertial force, and resistant force of the inhaling air, are negligible in case of nanosized entities (NSE, particles below 0.1 μm in diameter); the diffusion process for NSEs predominates in the lung airways and carries them to the inner parts of the lungs (Fig. 10) [54]. Despite the differences in the breathing characteristics and the structure of the respiratory tract in humans and animals (rodents, monkeys, dogs, and minipigs), similar particle deposition patterns in the lungs have been observed with the smaller particles being preferably deposited in the internal regions of the lungs [55, 56]. This higher tendency of the NSEs to reach alveolar regions begets their interaction with the vitally important pulmonary surfactant film.

But there is also a positive and useful aspect of pulmonary deposition. The respiratory system, especially the alveolar region, provides an enormous surface area of around 140 m^2 in humans [57, 58]. Thus, the pulmonary route for drug administration is of great interest not only for the local treatment of lung diseases (e.g., lung cancer or asthma) but also for the fast and efficient systemic delivery of drugs. The bioavailability of peptides and proteins targeted through the pulmonary route has been shown to be 10–200 times more efficient compared to other noninvasive routes [59]. Nanocarriers may be used to deliver drugs to the lungs. Hence, a detailed investigation of the interactions between the pulmonary surfactant film and the NSEs/NPs is essential to understand their impact on the structural and functional characteristics of this lipid–peptide layer. However, the highly dynamic, thin, and vulnerable nature of this film makes it cumbersome and complicated to perform any real-time study of the pulmonary surfactant in vivo. Therefore, the major research on pulmonary surfactant films has been conducted in vitro, by spreading of natural surfactants, modified natural surfactants, or synthetic

(model) pulmonary surfactants on the aqueous subphases to study the air–aqueous interface [60–64]. Similarly, investigations of the impact of different types of NSEs/NPs on the functional and structural organization of the pulmonary surfactant film have been performed primarily in vitro. It has been found that the interaction of NPs with the model pulmonary surfactant film as well as its individual components can compromise the biophysical characteristics of the film, including its molecular nature, its vital impact on surface tension, and its lateral compressibility and re-spreadability. Besides, these interactions can also have indirect effects causing lung surfactant film dysfunction.

5 Impact of Nanoparticles on the Adsorption of Surfactant to the Air–Water Interface and Surface Activity of the Film

The surface activity of the film is, as mentioned before, very often analyzed by recording the surface pressure versus area per lipid molecule isotherm of the film at the air–aqueous interface. As previously discussed, exposure of various-sized gelatin-based nanoparticles (136, 197, 221, 236, and 287 nm diameters) has shown a shift of the isotherm along the x-axis towards higher values of the area per molecule compared to the pure DPPC monolayer film with no destabilization effect; however, the surface potential of the film was found to be dramatically affected [25, 26]. Similarly, polyorganosiloxane NPs (~20 nm diameter) do not alter the surface activity of a DPPC/DPPG/SP-C (80:20:0.4 mol %) containing model pulmonary surfactant film up to a certain dose of exposure [16]. Another study examined the influence of polymeric nanoparticles, including poly(styrene), poly(D,L-lactide-co-glycolide), and the cationic polymer poly(butylmethacrylate-co-(2-dimethyl-aminoethyl)methacrylate-co-methyl methacrylate) (Eudragit E100) with distinct physicochemical properties (zeta potential and surface hydrophobicity) on the adsorption to the air–water interface and the resulting surface tension of bovine surfactant (Alveofact). Reduction of surface tension was observed to be dose dependent: Eudragit E100 ≪ poly(D,L-lactide-co-glycolide) ≪ poly(styrene). Positively charged Eudragit E100 nanoparticles showed almost no effect [65]. Gold NPs (~15 nm core diameter) have shown a dramatic destabilization effect on a DPPC/POPG/SP-B (70:30:1; wt/wt/wt) containing semisynthetic pulmonary surfactant film even at low concentration. These NPs have also been shown to impair the adsorption of surfactants to the air–aqueous interface and subsequent formation of a surface-active film [66]. However, the hydrophobic hexadecanethiolate-capped gold ($C_{16}SAu$) NPs at concentrations of 0.2 mol % in DPPC and 16 wt% in Survanta, a naturally derived clinical pulmonary surfactant film, have no influence on their surface pressure–area isotherms [67]. Moreover, nanosized titanium dioxide (TiO_2) particles, but not microsized TiO_2 particles, as well as nanosized polystyrene particles reduce surface activity of Curosurf, a natural porcine

pulmonary surfactant preparation [68]. Nanoparticles (~90 nm diameter) made of hydrophilic hydroxyapatite, a biocompatible and biodegradable material, have also shown a significant time-dependent inhibition of Infasurf, a natural pulmonary surfactant preparation [69] in vitro.

A major point of investigation is the impact of nanoparticles on the structural organization of the film at low and high surface tensions. Pulmonary surfactant films at and below equilibrium surface pressures form phase-separated domains, referred to as the *liquid-condensed* (LC) and the *liquid-expanded* (LE) domains. At higher compression, i.e., higher surface pressures or lower surface tensions, the pulmonary surfactant film undergoes a transition from its two-dimensional nature into the third dimension and forms uniformly distributed areas with multilayer structures of surfactant in the LE phase, associated with a densely packed mono-layer of LC domains. In vitro studies on clinical and synthetic pulmonary surfactant preparations have reported that metal NPs (e.g., Au and TiO_2) significantly disturb the ultrastructure of the surfactant film. Bakshi et al. have shown by captive bubble tensiometry that Au NPs reduce the adsorption of surfactants to the air–aqueous interface and, thus, forming a surface-active film that could otherwise provide a low surface tension during compression of the film [66]. Recently, hydrophobic hexadecanethiolate-capped Au ($C_{16}SAu$) NPs were exposed to Langmuir mono-layers of pure DPPC lipid and Survanta, a naturally derived clinical pulmonary surfactant. Addition of $C_{16}SAu$ NPs shows almost no discernible impact on the domain structures of Survanta monolayers; however, monolayer structures of DPPC are affected [16]. Moreover, Schleh and coworkers studied the influence of particle size by using micro- and nanosized TiO_2 particles. These authors reported using pulsating bubble surfactometer measurements that TiO_2 NPs can induce surfactant dysfunction, but not TiO_2 microparticles [25, 26]. They have concluded that the particles' size and their surface area can play an important role with respect to the biophysical response of the surfactant in the lung even though the underlying mechanism of surfactant inhibition still remains elusive. Kanno et al. used pure DPPC and surfactant isolated from mouse lung lavage as pulmonary surfactant model systems and reported that interaction of eicosane NPs also causes dysfunc-tion of the surfactant [70]. Recently, the interactions of hydrophilic hydroxyapatite NPs (biocompatible and biodegradable) with a natural pulmonary surfactant (Infasurf) were investigated. Fan and coworkers observed a reduction of surfactant activity upon NP encounter. They investigated the cause of surfactant inhibition and found that the adsorption of surfactant proteins on the surface of the hydroxyapatite NPs is primarily responsible for the inhibitory mechanism rather than the particles' direct interference with the film at the interface [69]. It is important to note that the surfactant proteins play a pivotal role in accelerating the adsorption and re-spreading of the phospholipids at the air–aqueous interface. Moreover they facilitate the surfactant film's compression to avail surface tension to near-zero values, which is a prerequisite for a normal breathing process [30, 71].

Sachan et al. [16] studied the impact of 24 nm hydrophobic polyorganosiloxane nanoparticles on the integrity and structural organization of a model pulmonary surfactant film. By using scanning force as well as electron microscopy, it was
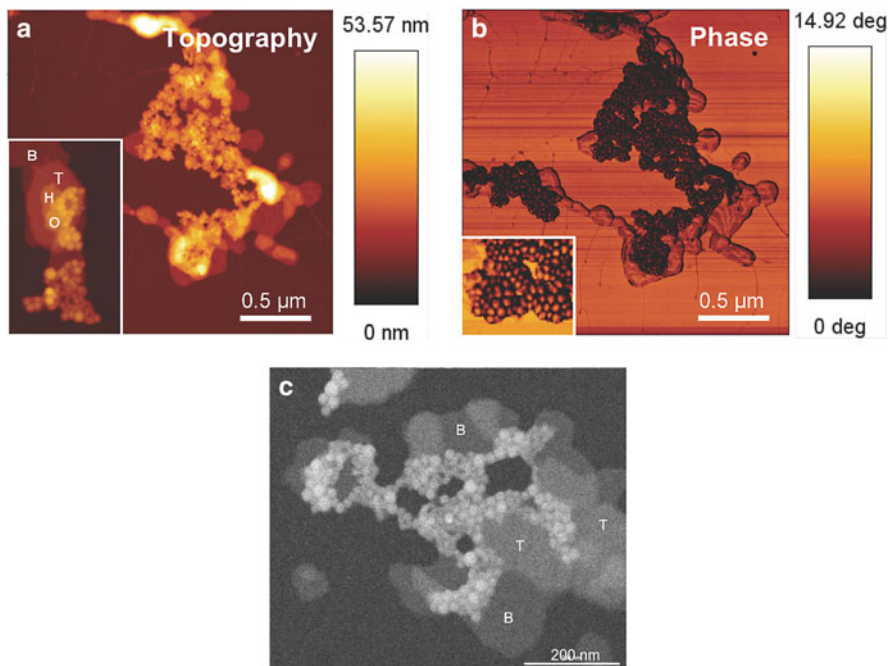
Fig. 11 (**a**) High-resolution intermittent contact mode topography images of pulmonary surfactant films containing 50 μg/mL hydrophobic polyorganosiloxane NPs transferred at 52.5 mNm^{-1}. *Inset* shows evident close interactions of NPs with the surfactant bilayer "b," tetralayer "t," hexalayer "h," and octalayer "o" structures. (**b**) High-resolution phase images of pulmonary surfactant film containing 50 μg/mL NPs. The *inset* shows a magnified view (phase shift contrast) on the top of NPs present within the pulmonary surfactant film. (**c**) Dark-field electron microscopy image of (unstained) pulmonary surfactant film containing 50 μg/mL NPs transferred at 52.5 mNm^{-1} from pure water subphase. In the image, B and T represent bilayer and tetralayer protrusion structures, respectively (with permission from Sachan et al. [16])

shown that these nanoparticles are localized primarily in the fluid phase at low surface pressure, similar to pure lipid films. At high surface pressure, when three-dimensional protrusions form, these nanoparticles are embedded within the surface-associated structures (Fig. 11). Moreover, the authors showed that the majority of the nanoparticles remained at the interphase and are not released into the aqueous subphase even under repeated compression and re-expansion cycles. In another paper Sachan and Galla [72] showed that this strong retention is due to an intense coating of the nanoparticles with lipids. This causes a rearrangement of the lateral organization of the surfactant surrounding the nanoparticles whereby the lipid molecules around nanoparticles prefer a more upright orientation due to hydrophobic–hydrophobic interaction, whereas the tilted tails are preferred by the background monolayer. Such a shift in lipid arrangement has also been proposed by MD simulations [73].
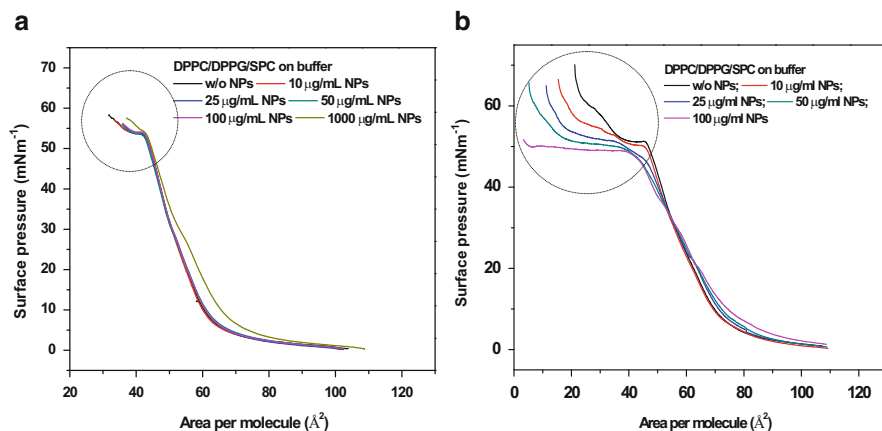
Fig. 12 (**a**) Surface pressure–area isotherm for a DPPC/DPPG/SP-C (80:20:0.4 mol%) monolayer + 12 nm nanoparticles. (**b**) Pressure area isotherm for a DPPC/DPPG/SP-C (80:20:0.4 mol%) monolayer + 136 nm nanoparticles. All measurements were done on 25 mM Hepes + 3 mM CaCl2 as the subphase at 20 °C (with permission from Dwivedi et al. [22])

Moreover, a molecular simulation study has shown that carbonaceous NPs (hydrophobic, carbon rich) alter the structure and packing of the individual components of a surfactant film composed of DPPC lipids and the protein SP-B reducing its functionality. Interestingly, they also observed that these hydrophobic carbonaceous NPs exhibit a high free energy barrier at the interface in the presence of a surfactant film [74]. In conclusion, a number of studies using organic NPs, inorganic NPs, metal NPs, and NPs engineered otherwise have shown mild to drastic impacts on the different model systems for the pulmonary surfactant film.

Based on the finding that the 24 nm AmorSil20 particles did not substantially affect the structural organization of the lung surfactant up to a given threshold concentration, Dwivedi et al. [22] investigated whether the same hydrophobic nanoparticles, just bigger in diameter, would have an impact. As described above, they were able to show that 136 nm nanoparticles induce a drastic decrease in the line tension between phases of pure DPPC monolayers leading to reduced phase separation (Fig. 4). Added to an artificial lung surfactant film, the 136 nm nanoparticles cause a drastic change in the surface activity of the lipid film. In the presence of these bigger NPs, the surface pressure–area isotherm showed an extended plateau region. Apparently an increase in the surface pressure as seen under particle-free conditions was effectively inhibited which is equivalent to a potential lung surfactant dysfunction (Fig. 12).

To further investigate the structural reorganization of the multilayer protrusion structures in the presence of 136 nm NPs, atomic force microscopy was applied. The topology of the film was studied at a surface pressure value where the plateau region is formed. At the low-pressure side of the plateau region, the molecular arrangement of the multilayer protrusion structures is intact. However, at the high-pressure side of the plateau region, the network structure is completely disrupted,
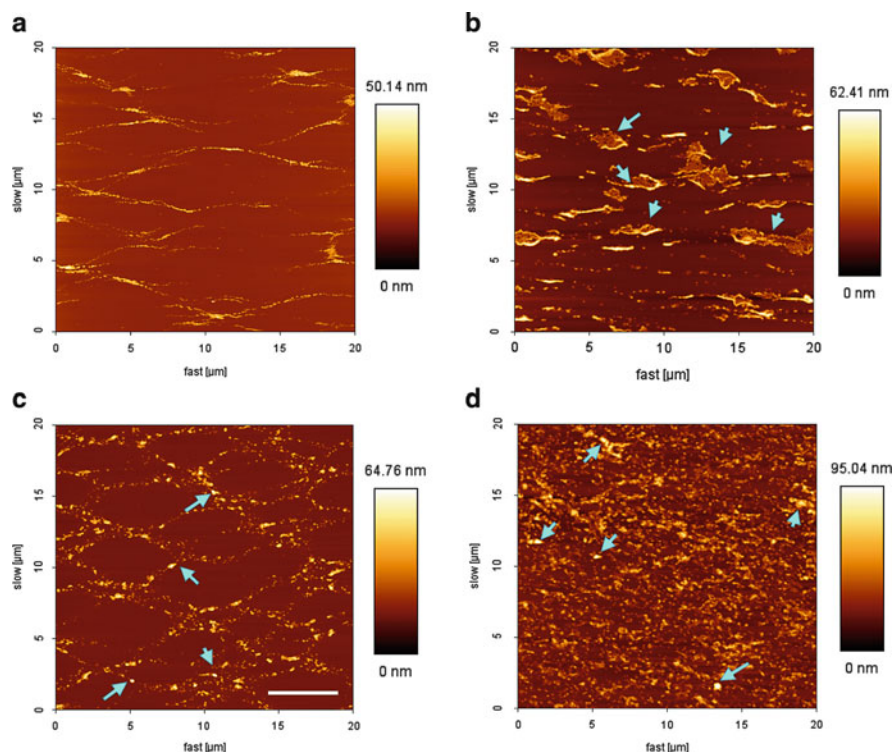
Fig. 13 AFM topography images of (**a**) pure DPPC/DPPG/SP-C (80:20:0.4 mol %) monolayer lipid film; (**b**) with 100 µg/mL 12 nm nanoparticles at surface pressures within the plateau region; (**c**) with 100 µg/mL 136 nm nanoparticles transferred to a solid support at the low-pressure end of the plateau region; (**d**) with 100 µg/mL 136 nm nanoparticles transferred to a solid support at the high-pressure side of the plateau region. The film was compressed on 25 mM Hepes + 3 mM CaCl2 as the subphase at 20 °C. The clusters of nanoparticles around the protrusion structures are marked by arrows. *Scale bar* 5 µm (with permission from Dwivedi et al. [22])

and formation of multilayer protrusions is enhanced (Fig. 13). Hence, the constant surface pressure during compression is attributed to the enhanced formation of multilayer protrusion structures.

Since DPPC is the major component of this artificial lung surfactant film, the reduced phase separation effect of 136 nm nanoparticles on the DPPC film has been reproduced by this artificial lung surfactant film. The enhanced multilayer protrusion formation and the disruption of the network structure are attributed to the decreased phase separation between the fluid and the rigid phases of the film. The 12 nm nanoparticles showed similar effects compared to 20 nm nanoparticles; in both cases surface activity and structural organization of the artificial lung surfactant film were preserved. Furthermore, 136 nm and 12 nm nanoparticles were found to form clusters associated with the multilayer protrusions, and they were retained in the film even after repeated compression/re-expansion cycles. Additionally,

vesicle insertion kinetic studies showed that 136 nm nanoparticles severely inhibited the vesicle insertion process and caused a drastic effect even at low concentrations compared to 12 nm nanoparticles of the same type. Hence, the size of the nanoparticles does indeed have a large impact on the functionality of an artificial lung surfactant.

This interaction study of NPs with the pulmonary surfactant film is important not only to provide insight into the harmful effects of NPs on the pulmonary surfactant film, but also to understand their potential toxicity for the underlying cells and their clearance from the cellular and circulatory system. During interaction, the adsorption of pulmonary surfactant components on Au, TiO_2, and polystyrene NPs as well as on quartz, diesel soot, and kaolin has been demonstrated [66, 68, 75]. This adsorption process leads to a change in surface decoration and modified physico-chemical properties of the NPs providing an altered behavior in vitro or in vivo. The surface chemistry change is represented as change of "molecular signature" or "biological identity," which defines cellular toxicity, activity, and clearance rate. Therefore, these interaction studies are equally important as safety and efficacy considerations of drugs delivered to the pulmonary system by nanoparticles, nanocarriers, or nanoprobes.

References

1. Sanguansri P, Augustin MA (2006) Nanoscale materials development – a food industry perspective. Trends Food Sci Technol 17(10):547–556
2. Weir A et al (2012) Titanium dioxide nanoparticles in food and personal care products. Environ Sci Technol 46(4):2242–2250
3. Dubas ST, Kumlangdudsana P, Potiyaraj P (2006) Layer-by-layer deposition of antimicrobial silver nanoparticles on textile fibers. Colloids Surf A Physicochem Eng Asp 289(1–3):105–109
4. Hoet PH, Bruske-Hohlfeld I, Salata OV (2004) Nanoparticles - known and unknown health risks. J Nanobiotechnology 2(1):12
5. Villalobos-Hernández JR, Müller-Goymann CC (2006) Sun protection enhancement of titanium dioxide crystals by the use of carnauba wax nano-particles: the synergistic interaction between organic and inorganic sunscreens at nanoscale. Int J Pharm 322(1–2):161–170
6. Villalobos-Hernández JR, Müller-Goymann CC (2007) In vitro erythemal UV-A protection factors of inorganic sunscreens distributed in aqueous media using carnauba wax–decyl oleate nanoparticles. Eur J Pharm Biopharm 65(1):122–125
7. Nesseem D (2001) Formulation of sunscreens with enhancement sun protection factor response based on solid lipid nanoparticles. Int J Cosmet Sci 33(1):70–79
8. Mazzola L (2003) Commercializing nanotechnology. Nat Biotechnol 21(10):1137–1143
9. Nel A et al (2006) Toxic potential of materials at the nanolevel. Science 311(5761):622–627
10. Sung JC, Pulliam BL, Edwards DA (2007) Nanoparticles for drug delivery to the lungs. Trends Biotechnol 25(12):563–570
11. De Jong WH, Borm PJA (2008) Drug delivery and nanoparticles: applications and hazards. Int J Nanomedicine 3(2):133–149
12. Mansour HM, Rhee YS, Wu XA (2009) Nanomedicine in pulmonary delivery. Int J Nanomedicine 4:299–319
13. von Nahmen A et al (1997) The phase behavior of lipid monolayers containing pulmonary surfactant protein C studied by fluorescence light microscopy. Eur Biophys J 26(5):359–369

14. Krol S et al (2000) Formation of three-dimensional protein-lipid aggregates in monolayer films induced by surfactant protein B. Biophys J 79(2):904–918

15. Wang L et al (2005) Monolayer–multilayer transitions in a lung surfactant model: IR reflection–absorption spectroscopy and atomic force microscopy. Eur Biophys J 34 (3):243–254

16. Sachan AK et al (2012) High-resolution investigation of nanoparticle inter-action with a model pulmonary surfactant monolayer. ACS Nano 6(2):1677–1687

17. Leufgen KM et al (1996) Imaging time-of-flight secondary Ion mass spectrometry allows visualization and analysis of coexisting phases in langmuir – blodgett films. Langmuir 12 (7):1708–1711

18. Harishchandra RK, Saleem M, Galla HJ (2010) Nanoparticle interaction with model lung surfactant monolayers. J R Soc Interface 7:S15–S26

19. Benvegnu DJ, McConnelll HM (1992) Line tension between liquid domains in lipid mono-layers. J Phys Chem 96(16):6820–6824

20. McConnell HM (1991) Structures and transitions in lipid monolayers at the air-water-inter-face. Annu Rev Phys Chem 42:171–195

21. Benvegnu DJ, McConnell HM (1993) Surface dipole densities in lipid monolayers. J Phys Chem 97(25):6686–6691

22. Dwivedi MV et al (2014) Size influences the effect of hydrophobic nano-particles on lung surfactant model systems. Biophys J 106(1):289–298

23. Peetla C, Labhasetwar V (2008) Biophysical characterization of nanoparticle-endothelial model cell membrane interactions. Mol Pharm 5(3):418–429

24. Peetla C, Labhasetwar V (2009) Effect of molecular structure of cationic surfactants on biophysical interactions of surfactant-modified nanoparticles with a model membrane and cellular uptake. Langmuir 25(4):2369–2377

25. Stuart D et al (2006) Biophysical investigation of nanoparticle interactions with lung surfactant model systems. J Biomed Nanotechnol 2(3–4):245–252

26. Ku T et al (2008) Size dependent interactions of nanoparticles with lung surfactant model systems and the significant impact on surface potential. J Nanosci Nanotechnol 8(6):2971–2978

27. Degen P et al (2008) In situ observation of gamma-Fe_2O_3 nanoparticle adsorption under different monolayers at the air/water interface. Langmuir 24(22):12958–12962

28. Goerke J (1974) Lung surfactant. Biochim Biophys Acta 344(3–4):241–261

29. Veldhuizen R et al (1998) The role of lipids in pulmonary surfactant. Biochim Biophys Acta 1408(2–3):90–108

30. Goerke J (1998) Pulmonary surfactant: functions and molecular composition. Biochim Biophys Acta 1408(2–3):79–89

31. Schurch S, Green FHY, Bachofen H (1998) Formation and structure of surface films: captive bubble surfactometry. Biochim Biophys Acta 1408(2–3):180–202

32. Bachofen H et al (2005) Structures of pulmonary surfactant films adsorbed to an air-liquid interface in vitro. 1720(1–2):59–72

33. Amrein M, vonNahmen A, Sieber M (1997) A scanning force and fluorescence light micros-copy study of the structure and function of a model pulmonary surfactant. Eur Biophys J 26 (5):349–357

34. Diemel RV et al (2002) Multilayer formation upon compression of surfactant monolayers depends on protein concentration as well as lipid composition - an atomic force microscopy study. J Biol Chem 277(24):21179–21188

35. Knebel D et al (2002) Scanning force microscopy at the air-water interface of an air bubble coated with pulmonary surfactant. Biophys J 82(1):474–480

36. Follows D et al (2007) Multilayers at the surface of solutions of exogenous lung surfactant: direct observation by neutron reflection. Biochim Biophys Acta 1768(2):228–235

37. Bourdos N et al (2000) Analysis of lung surfactant model systems with time-of-flight second-ary ion mass spectrometry. Biophys J 79(1):357–369

38. Scarpelli EM, Mautone AJ (1994) Surface biophysics of the surface monolayer theory is incompatible with regional lung function. Biophys J 67(3):1080–1089
39. Serrano AG, Perez-Gil J (2006) Protein-lipid interactions and surface activity in the pulmonary surfactant system. Chem Phys Lipids 141(1–2):105–118
40. Zuo YY et al (2008) Current perspectives in pulmonary surfactant - inhibition, enhancement and evaluation. Biochim Biophys Acta 1778(10):1947–1977
41. Crouch E, Wright JR (2001) Surfactant proteins A and D and pulmonary host defense. Annu Rev Physiol 63:521–554
42. Ledford JG, Pastva AM, Wright JR (2010) Collectins link innate and adaptive immunity in allergic airway disease. Innate Immun 16(3):183–190
43. Maina JN et al (2010) Recent advances into understanding some aspects of the structure and function of mammalian and avian lungs. Physiol Biochem Zool 83(5):792–807
44. Blanco O, Perez-Gil J (2007) Biochemical and pharmacological differences between preparations of exogenous natural surfactant used to treat respiratory distress syndrome: role of the different components in an efficient pulmonary surfactant. Eur J Pharmacol 568(1–3):1–15
45. Nkadi PO, Merritt TA, Pillers DAM (2009) An overview of pulmonary surfactant in the neonate: genetics, metabolism, and the role of surfactant in health and disease. Mol Genet Metab 97(2):95–101
46. Merrill JD, Ballard RA (2003) Pulmonary surfactant for neonatal respiratory disorders. Curr Opin Pediatr 15(2):149–154
47. Clements JA, Avery ME (1998) Lung surfactant and neonatal respiratory distress syndrome. Am J Respir Crit Care Med 157(4):S59–S66
48. Wegner DJ et al (2007) A major deletion in the surfactant protein-B gene causing lethal respiratory distress. Acta Paediat 96(4):516–520
49. Lawson WE et al (2005) Increased and prolonged pulmonary fibrosis in surfactant protein C-deficient mice following intratracheal bleomycin. Am J Pathol 167(5):1267–1277
50. Nogee LM et al (1994) A mutation in the surfactant protein-B gene responsible for fatal neonatal respiratory-disease in multiple kindreds. J Clin Invest 93(4):1860–1863
51. Gehr P, Bachofen M, Weibel ER (1978) The normal human lung: ultra-structure and morphometric estimation of diffusion capacity. Respir Physiol 32(2):121–140
52. de Jong D et al (2008) No effect of one-year treatment with indomethacin on Alzheimer's disease progression: a randomized controlled trial. PLoS One 3(1)
53. Igor G (2003) Targeting by deposition. In: Hickey AJ (ed) Pharmaceutical inhalation aerosol technology, 2nd edn. CRC Press, Boca Raton
54. de Boer AH et al (2002) Characterization of inhalation aerosols: a critical evaluation of cascade impactor analysis and laser diffraction technique. Int J Pharm 249(1–2):219–231
55. Cheng YS et al (2008) Lung deposition of droplet aerosols in monkeys. Inhal Toxicol 20 (11):1029–1036
56. Windt H et al (2010) Particle deposition in the lung of the Gottingen minipig. Inhal Toxicol 22 (10):828–834
57. Byron P (1985) Respiratory pharmacology and toxicology. J Pharm Sci 75(1):108 (By Mannfred A, Hollinger WB (1986) Saunders Company, Philadelphia, PA. p 207. 23 × 15 cm. ISBN 0-7216-1617-8. $19.95)
58. Stone KC et al (1992) Allometric relationships of cell numbers and size in the mammalian lung. Am J Respir Cell Mol Biol 6(2):235–243
59. Patton JS (1996) Mechanisms of macromolecule absorption by the lungs. Adv Drug Deliv Rev 19(1):3–36
60. Perez-Gil J (2001) Lipid-protein interactions of hydrophobic proteins SP-B and SP-C in lung surfactant assembly and dynamics. Pediatr Pathol Mol Med 20(6):445–469
61. Nakorn PN et al (2007) Surfactant protein C and lung function: new insights into the role of alpha-helical length and palmitoylation. Eur Biophys J 36(4–5):477–489
62. Klenz U et al (2008) Influence of lipid saturation grade and headgroup charge: a refined lung surfactant adsorption model. Biophys J 95(2):699–709

63. Seifert M et al (2007) Solubility versus electrostatics: what determines lipid/protein interaction in lung surfactant. Biophys J 93(4):1192–1203
64. Saleem M et al (2009) Calcium ions as "miscibility switch": colocalization of surfactant protein B with anionic lipids under absolute calcium free conditions. Biophys J 97(2):500–508
65. Beck-Broichsitter M et al (2011) Biophysical investigation of pulmonary surfactant surface properties upon contact with polymeric nanoparticles in vitro. Nanomedicine 7(3):341–350
66. Bakshi MS et al (2008) Metal nanoparticle pollutants interfere with pulmonary surfactant function in vitro. Biophys J 94(3):855–868
67. Tatur S, Badia A (2012) Influence of hydrophobic alkylated gold nanoparticles on the phase behavior of monolayers of DPPC and clinical lung surfactant. Langmuir 28(1):628–639
68. Schleh C et al (2009) The effect of titanium dioxide nanoparticles on pulmonary surfactant function and ultrastructure. Respir Res 10
69. Fan QH et al (2011) Adverse biophysical effects of hydroxyapatite nanoparticles on natural pulmonary surfactant. ACS Nano 5(8):6410–6416
70. Kanno S, Furuyama A, Hirano S (2008) Effects of eicosane, a component of nanoparticles in diesel exhaust, on surface activity of pulmonary surfactant monolayers. Arch Toxicol 82(11):841–850
71. Possmayer F et al (2001) Surface activity in vitro: role of surfactant proteins. Comp Biochem Physiol A Mol Integr Physiol 129(1):209–220
72. Sachan AK, Galla HJ (2013) Understanding the mutual impact of interaction between hydrophobic nanoparticles and pulmonary surfactant monolayer. Small 12(10):201300315
73. Schneemilch M, Quirke N (2010) Molecular dynamics of nanoparticle translocation at lipid interfaces. Mol Simul 36(11):831–835
74. Choe S et al (2008) Molecular dynamics simulation study of a pulmonary surfactant film interacting with a carbonaceous nanoparticle. Biophys J 95(9):4102–4114
75. Wallace WE et al (2007) Phospholipid lung surfactant and nanoparticle surface toxicity: lessons from diesel soots and silicate dusts. J Nanopart Res 9(1):23–38

Carbon Nanodots: Synthesis, Characterization, and Bioanalytical Applications

Michael-M. Lemberger, Thomas Hirsch, and Joachim Wegener

Abstract Carbon dots (CDs) are a new class of carbon-rich nanoparticles with exciting physicochemical properties that make them an interesting material for bioanalytical applications. Since their first description in 2004, several preparation techniques have been developed and described in literature, either starting from carbon raw materials (e.g., soot, graphite) or molecular precursors (e.g., carbohydrates, citric acid). The resulting particles are typically only a few nanometers in size, and their surfaces are decorated with functional groups that are rich in oxygen. The presence of oxygenated functionalities on the surface renders the particles dispersible in water. Carbon dots contain a fraction of carbon atoms that are sp^2 hybridized with delocalized electrons on the surface – the basis for the particles' characteristic photoluminescence. The wavelength of the emitted light is dependent on the wavelength of the excitation source and shows remarkable photostability. Carbon dots are also readily excited in the NIR but still emit visible light (upconverted photoluminescence) which provides significant advantages for in vivo imaging. Nowadays CDs are considered as emerging tools in luminescence-based bioanalytics with their full potential yet to be discovered.

Keywords Bioanalytics • Carbon dots • Live-cell imaging • Nanoparticles • Nanoprobes • Photoluminescence

Contents

M.-M. Lemberger (✉), T. Hirsch, and J. Wegener
Institute of Analytical Chemistry, Chemo- and Biosensors, University of Regensburg, Universitätsstraße 31, 93053 Regensburg
e-mail: michael.lemberger@ur.de

1 Introduction

Nanobiotechnology has emerged as a major area of fundamental and applied research due to the enormous potential and unprecedented performance of nanoscale tools in analytics, diagnostics, and therapy [1]. Nanostructures are by definition between 1 and 100 nm in size, which is one of the reasons for their ability to manipulate and study biological objects on-site as well as to measure compounds with biomedical relevance in situ [2]. Nanoscale particles have been modified in many different ways so that they can accommodate multiple functionalities needed for their site-specific targeting within a biological system, e.g., by binding to cell-surface receptors and local operation like measuring the concentration of an analyte of interest or releasing a cargo compound. In contrast to organic molecules, nanoparticles are commonly very stable, and they are rather resistant to oxidation or degradation processes in living organisms. Accordingly, targeted interactions between the nanoparticles with their inherent functionalities and biological structures open up a new avenue of applications in biomedical research. Throughout the last decade several types of nanoparticles have been developed and studied in detail. Their most important classes are metal oxide particles (such as TiO_2 or Fe_3O_4), polymer particles like latex beads, silica particles, colloidal gold, and *quantum dots* (Q-dots) [3].

Among them, Q-dots are particularly interesting, since they exhibit intrinsic fluorescence which makes them attractive candidates for imaging applications. The particles themselves are nanocrystals of semiconducting material, such as ZnSe, CdSe, or CdTe, typically in a size range between 1 and 10 nm [4]. A special feature of Q-dots is that their optical properties can be tuned by varying the particle diameter [5]. Furthermore, they show high brilliancy, photostability, and rather broad excitation spectra that allow for simultaneous excitation of several different Q-dots and thus multicolor fluorescence colors with a single excitation source [6]. However, these particles also have certain disadvantages such as their hydrophobicity, making it impossible to use them without further surface modification in a physiological environment. Therefore, Q-dots have to be encapsulated in silica or in polymers, such as polyethylene glycol (PEG), rendering them water dispersible

[7]. This, in turn, leads to increasing particle sizes and limits their application in vitro and in vivo. Additionally, it was found that certain Q-dots exhibit a significant cytotoxicity, which can be caused by very different mechanisms [8]: (i) Q-dots often contain toxic elements (e.g., with the exception of ZnSe), such as cadmium or other heavy metals, which may leach out of the particle and enter the cells during particle degradation [9]; (ii) Q-dots can catalyze the formation of harmful free radicals, particularly reactive oxygen species, upon incubation with living cells [10].

Dealing with those disadvantages drives the search for alternative nanomaterials with similar luminescence properties but lower toxicity and better stability in aqueous dispersions. The search for new materials brought carbon nanoallotropes into the focus of researchers. After the discovery of fullerenes [11], other carbon-based materials like nanodiamonds [12], carbon nanotubes [13], carbon nanofibers [14], and graphene [15] have been described and characterized. Most recently, a new allotrope with strong intrinsic luminescence has been named *carbon nanodots* or *carbon dots* (CDs). CDs were first described in the year 2004 as "fluorescent carbon" in a fraction of electrophoretically purified carbon nanotubes derived from arc discharge soot [16]. Nomenclature of these new particles was not uniform in the very first years of their discovery, calling them "fluorescent carbon nanoparticles" or "carbon nanocrystals." In the meantime the term *carbon (nano)dots* became most common, emphasizing their similarity to Q-dots.

Since CDs were first mentioned in the literature, several different preparation methods have been developed, and the full characterization of the resulting material has made considerable progress. Typically, CDs are in a size range of just a few nanometers. They are mostly described to have a graphitic sometimes amorphous core with a surface passivated by oxidation processes or by a polymer layer [17]. Figure 1 shows high-resolution *transmission electron microscopy* (TEM) images of CDs, prepared from natural gas soot [18].

The particles show an amorphous structure with only small areas of regular lattice-like order. They can even contain other elements such as hydrogen, oxygen, or nitrogen [19]. The presence of these elements, especially oxygen, leads to very good water dispersibility and is the chemical basis for the particles' luminescence properties. CDs show high photostability and do not contain toxic elements, such as heavy metals, and they can be synthesized at low cost [20]. These unique properties make CDs interesting for various scientific applications in (bio)analytics or opto-electronics to mention just two [21]. Figure 2 supports this notion strongly by presenting the number of publications per year that deal with carbon dots and their use in various fields of science.

Among all possible applications it has been predicted that CDs have their highest potential as a contrast agent in fluorescence imaging of biological systems, like cells or even living organisms [22].

Fig. 1 Typical transmission electron micrographs of CDs recorded at (**a**) low and (**b**) high resolution. The insert in (**a**) shows the particle size distribution. Crystalline lattices are identified in (**b**). With permission from [18]
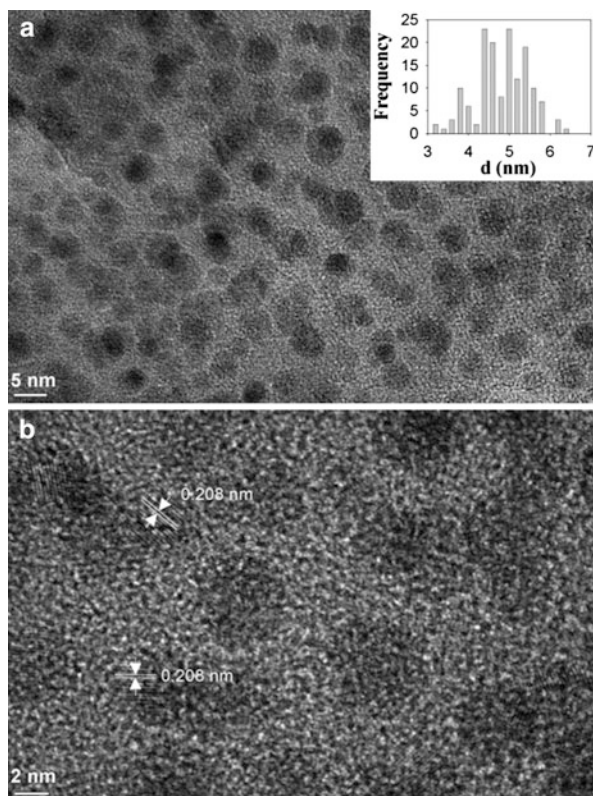
Fig. 2 The number of publications per year according to SciFinder® when the terms "carbon dots" or "carbon nanodots" are used for searching the database from 2004 to Oct. 2014
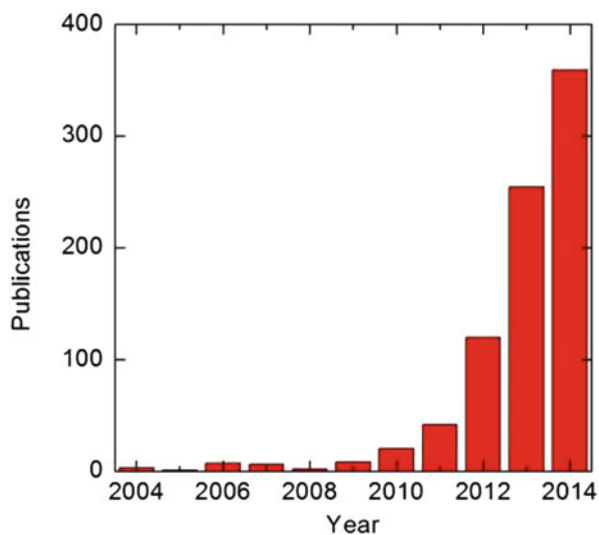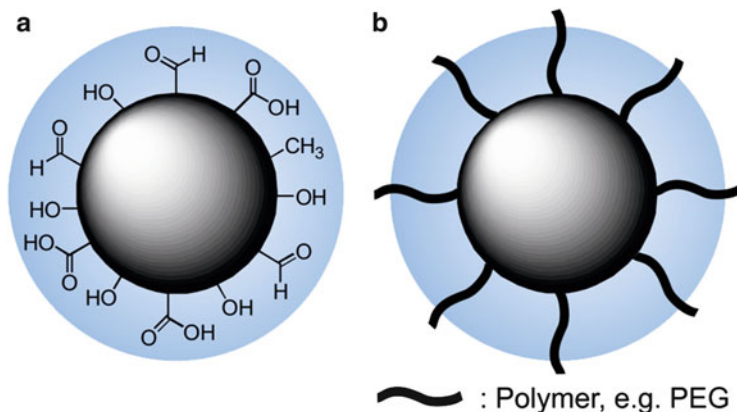
Fig. 3 Passivation of CDs (**a**) by surface oxidation or (**b**) or by decoration with polymers

2   Synthesis and Particle Preparation

Starting from the first identification of CDs [16] in the year 2004 as luminescent fraction ("fluorescent carbon") in an electrophoretic purification of carbon nanotube fragments that had been exposed to arc discharge, a lot of methods were developed to produce this material. In the first publication describing the preparation of CDs only two years later, Sun et al. used laser ablation of carbon targets, which is similar to the fabrication of carbon nanotubes [23]. The resulting nanometer-sized carbon particles, characterized by electron microscopy, had to be passivated by a polymer layer (such as PEG) to obtain stable aqueous suspensions of CDs with bright luminescence. Polymer coating is one out of several techniques for the preparation of CDs from raw carbon nanoparticles through passivation (Fig. 3). CDs are also obtained by oxidative passivation of raw carbon nanoparticles. As such, ordinary (candle) soot oxidized with nitric acid or hydrogen peroxide yields luminescent CDs that are stable in aqueous suspensions [24]. According to these studies surface passivation is a major requirement for photoluminescence (PL) of CDs as it provides emissive surface states, described in detail in the luminescence properties chapter.

A lot of other, very different techniques to prepare CDs have been described. The reason for this great variety of preparation techniques is the lack of a precise definition of the CDs' molecular composition and structure. In general, CDs can be prepared like many other nanomaterials in *top-down* or *bottom-up* approaches (Fig. 4). The *top-down* approaches apply methods like arc discharge, laser ablation, and electrochemical exfoliation to break down macroscopic carbon materials and obtain nanometer-sized CDs. In contrast, the *bottom-up* approaches make use of molecular precursors or complex mixtures of precursors that are exposed to microwave radiation, heat, ultrasound, or harsh chemicals to form CDs [17]. The various methods are discussed in detail below.
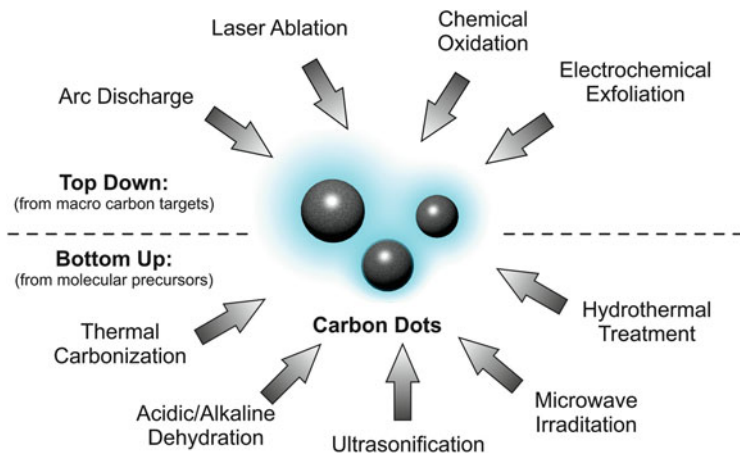
Fig. 4 Top-down and bottom-up reparation methods for CDs

2.1 Top-Down Preparation of CDs

Top-down approaches apply physical methods to prepare CDs from carbon macro material. Laser ablation has been the first technique applied for CD preparation as mentioned before. Sun et al. used a Nd:YAG laser (1,064 nm) for the ablation of a carbon target under a flow of argon and water vapor at 900°C [23]. These raw carbon nanoparticles showed no photoluminescence (PL) and had to be oxidized with nitric acid under reflux in a second preparation step. Afterwards they were passivated with PEG or poly propionylethylene-imine-co-ethyleneimine (PPEI-EI), respectively, before they showed PL in aqueous suspensions. The estimated size of the CDs obtained from this protocol was about 5 nm with a quantum yield in the range of 4%. A similar approach was described by Li et al. [25]. Here commercially available carbon nanoparticles were dispersed in solvent and irradiated by an unfocussed Nd:YAG laser (532 nm) under stirring. The laser irradiation passivated the surface of the carbon nanoparticles and decorated it with oxygen-containing groups which renders the CDs photoluminescent. This method was a simplification to the one of Sun et al., since CDs could be prepared in liquid medium by laser irradiation without an additional complex setup.

Another top-down technique is the electrochemical exfoliation from graphite [26]. Here CDs are released into aqueous solution from a graphite rod as a working electrode during cyclovoltammetry (−3.0–+3.0 V vs. Ag/AgCl). On such high potentials water is decomposed under formation of radicals which attack the electrode. These CDs have an average size of 2.0 nm, emit blue luminescence under UV excitation, and also show electrochemiluminescence (ECL). With a similar strategy carbon paste electrodes have been used as starting material for electrochemical preparation of CDs by oxidation at +9 V vs. standard calomel electrode potential (SCE) in 0.1 M NaH_2PO_4 aqueous solution [27]. The formation

of CDs is also possible through the electrochemical oxidation of water which leads to the formation of hydroxyl and oxygen radicals that attack the anode and generate water-soluble CDs. These electrochemically formed CDs darken the initially colorless solution gradually from yellow to brown [28]. The particles show a high surface density of oxygen-containing functional groups which explains their good water dispersibility. Electrochemical preparation methods provide another interesting synthetic option: tuning of the luminescence properties of CDs [29]. In one strategy bundles of carbon fibers were used as working electrodes, and different potentials were applied relative to a reference electrode. It was found that the applied voltage had significant influence on the release time of the particles (darkening of the suspension), on their size and – most interestingly – on their PL properties. It turned out that higher potentials lead to an increased oxidation of the CDs' surfaces and, thus, influence the nature of the emissive sites on their surface which significantly alter their photophysical properties (see below).

2.2 Bottom-Up Preparation of CDs

While the top-down approaches deal with the preparation of CDs from carbon macro materials, the bottom-up approaches start from molecular precursors. One of the simplest ways to do so is *thermal carbonization* of the starting material. Bourlinos et al. reported "surface functionalized carbogenic dots" through thermal decomposition of different ammonium citrate salts [30]. Citrate served as carbon source, while different organic amines act as surface modifier. The educts were mixed in solution, dried, and calcinated at 300°C in air for 2 h to obtain functionalized CDs. Hydrophobic CDs were prepared by using octadecyl ammonium citrate, while hydrophilic ones were obtained from 2-(2-aminoethoxy)-ethanol citrate. These CDs were characterized by a size below 10 nm, a quantum yield between 4 and 10%, and dispersibility in different solvents depending on their functionalization. When tris(hydroxymethyl)aminomethane (TRIS) is used as a carbon source and betaine hydrochloride as a surface modifier, the resulting CDs carry quaternary amine groups on their surface with a corresponding positive zeta potential of +43 mV. The particles show luminescence at λ_{max}~460 nm with a quantum yield of app. 4% and anion exchange properties [31]. Thermal decomposition is described for single precursor molecules or salts only. In this line the calcination of the complex ligand ethylenediamine-tetraacetic acid (EDTA) has turned out to be very useful. Typically, EDTA is calcinated at 400°C under nitrogen atmosphere for 2 h. Through the decomposition, especially decarboxylation, nitrogen-doped CDs are formed. These were described to have an average size of about 7.5 nm and to show blue luminescence at λ_{max}~400 nm with a quantum yield of about 40% [32–34].

Another bottom-up strategy is to perform the decomposition of molecular precursors not under dry conditions but in solution. This allows for a very homogeneous carbonization of the starting material, obtaining CDs which are already well

$$C_n(H_2O)_m \xrightarrow[\text{cat. acid/base}]{-m\ H_2O,\ \Delta T} n\ \text{„C"}$$
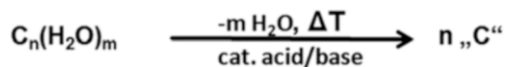
Scheme 1 Bottom-up preparation of CDs by dehydration of carbohydrates

dispersed in the solvent. One of the most popular CD preparation methods in solvents is the dehydration of carbohydrates. As implied from the name of these molecules, they formally consist of hydrated carbon so that dehydration provides pure carbon as a remnant (Scheme 1). These dehydration reactions are often catalyzed by acids or bases, ultrasound exposure [35], microwave heating [36], or hydrothermal treatment [37]. Practically, the dehydration process is not complete at all towards the end of the CD preparation, but the relative carbon content has increased considerably compared to the starting material. Under these conditions CDs are formed with delocalized electron systems and a surface decoration that stems from the functional groups of the precursor molecules. In the case of carbohydrate starting materials, surface groups are often hydroxyl-, aldehyde-, and carboxyl- groups, and the carbon to oxygen ratio depends on the dehydration rate [38]. These functional groups provide high water dispersibility on the one hand and the possibility of surface modification on the other hand.

The simplest way for the preparation of CDs from carbohydrates in aqueous solution is the acidic dehydration of glucose with concentrated sulfuric acid under stirring [39]. Following this route Peng et al. obtained "black carbonaceous powder," which was further oxidized with nitric acid in a second step and passivated with 4,7,10-trioxa-1,13-tridecanediamine (TTDDA). These CDs emit blue luminescence at λ_{max} ~440 nm with a quantum yield of 13% and an average size of 5 nm.

Modified preparation routes that basically follow the same strategy use different experimental conditions such as ultrasound exposure of the reaction mixture. A one-step route from carbohydrates to luminescent CDs using ultrasound was reported by Li et al. [35]. Typically, an aqueous glucose solution (1 M) is mixed with aqueous NaOH solution (1 M) and sonicated for 4 h. Within the reaction time the colorless solution turns gradually from yellow to dark brown due to CD formation. This preparation method does not require any passivation but provides directly blue luminescent CDs (λ_{max}~450 nm) with a size below 5 nm and a quantum yield of about 7%. A similar procedure was reported by Ma et al. who treated a mixture of glucose and ammonia with ultrasound for 24 h [40]. Those CDs had an average diameter of 10 nm with very similar optical properties.

Microwave irradiation is also a very popular technique to assist a quick and easy carbonization of carbohydrates and other precursor molecules. For example, CDs may be obtained by treating a mixture of glycerol (as carbon source) and TTDDA (as passivation agent) for only 10 min at 700 W in a microwave oven [41]. CD reparations via microwave heating have been performed using different pairs of carbon source and passivation agent such as glycerol and polyethylene imine (PEI) [42], glucose and PEG [43], amino acids and PEG [44], or citric acid and PEI [45]. Such microwave treatment of these combinations has been shown to open up a direct route to passivated CDs. It is noteworthy that passivation of CDs is not

strictly required as pyrolysis of only one precursor, sometimes acid or base cata-lyzed, has also been performed. Examples for such a synthetic route are microwave heating of glycerol [36], dextrin [46], polymers [47], citric acid [48, 49], amino acids [50], or even complex material such as egg shell membrane [51], respectively. Microwave-assisted pyrolysis is one of the most popular preparation techniques of CDs due to its high reproducibility and simplicity only outperformed with respect to the number of publications by hydrothermal synthesis.

Hydrothermal preparation of CDs offers several distinct advantages which are the reason for its popularity. First and most important, hydrothermal synthesis is rather simple. Reactions are typically carried out in stainless steel autoclaves with Teflon lining. The precursors are suspended or dissolved (mostly) in water and transferred into the autoclave, which is tightly closed afterwards. Then the auto-clave is heated in an oven or a muffle furnace. Carbonization takes place in a solution assisted by high temperature and pressure provided within the closed system. Hydrothermal synthesis is fairly mild compared to microwave treatment, for example. Accordingly, this preparation method does not require sophisticated instrumentation and provides CDs with rather high reproducibility. Please note that the experimental conditions (high temperature, high pressure) enable the carboni-zation and dehydration of rather stable materials so that a lot of different precursors can be used to prepare CDs with a broad range of chemical compositions. Synthetic routes starting from carbohydrates are the most popular ones among all published hydrothermal procedures, since carbohydrates are a low-cost, sustainable mass material. For instance, He et al. reported the hydrothermal preparation of CDs from glucose, sucrose, and starch by using several acidic/alkaline additives [37]. The obtained CDs were highly water dispersible, and their photoluminescence properties differed widely dependent on the additives in the reaction mixture. Yang et al. [38] showed that the hydrothermal formation of CDs from glucose is influenced by the addition of KH_2PO_4, affecting particle size and photolumi-nescence. N-doped CDs with amino functionalization have been obtained directly from chitosan as precursor [52]. However, not only carbohydrates may serve as precursors, several other classes of (bio-)molecules can be used in hydrothermal synthesis as well. Citric acid has been used as a carbon source which gets decarboxylated during the process providing one of the brightest CD preparations so far with a quantum yield of up to 80% (λ_{max}~450 nm). The average size of these particles was 2.8 nm [53]. Other examples for useful precursors are amino acids [54], dopamine [55], or tetrachlormethane [56]. Surprisingly not only purified molecules have been used as precursors in hydrothermal preparation of CDs, but also complex biological materials like watermelon peel [57], orange juice [58], pomelo peel [59], coffee grounds [60], or grass [61].

A meaningful comparison of the different synthetic routes to luminescent CDs requires a first categorization: *top-down* approaches need to be separated from *bottom-up* approaches. The physical approaches providing *top-down* preparation of CDs require sophisticated instrumental devices such as arc discharger or laser setups for ablation. Moreover, ablation or exfoliation of CDs from macroscopic carbon targets does not allow for doping CDs with other elements, such as nitrogen.

Table 1 Comparison and summary of different preparation methods for carbon dots (*QY*: quantum yield)

Type	Method	Advantage	Disadvantage	Typical QYs
Top-down	Arc discharge	–	Complex setup, low reproducibility	2% [16]
	Laser ablation	–	Complex setup	4–10% [23]
	Chemical oxidation	Simple (exp.)	Precursor material undefined	2–12% [18, 24, 62]
	Electrochemical exfoliation	Oxidation level easily controllable	Precursor needs to be conductive	2–12% [28, 29, 63]
Bottom-up	Ultrasonification	Degree of carbonization well controllable	Limited in choice of educts	~7% [35, 40]
	Acidic/alkaline dehydration	Simple (exp.)	Limited in choice of educts, no control of dehydration grade	~13% [39]
	Thermal carbonization	Simple when only one precursor is needed	Inhomogeneity in mixing solid educts	4–40% [30–33, 64]
	Microwave irradiation	Fast (<10 min)	Temperature range depends on solvent (aqueous solutions)	5–45% [36, 49–51]
	Hydrothermal treatment	Mild carbonization of various materials, good reproducibility	Complex optimization	Up to 80% [19, 53]

And please note that both *top-down* approaches do not provide control over the CDs' surface functionalization in contrast to *bottom-up* approaches using well-defined molecules as precursors. Precursor fragments often remain on the CDs' surface so that surface decoration can be tailored by the selection of precursors. Another big advantage of *bottom-up* procedures is the experimental option to dope CDs with other molecules or elements and their excellent reproducibility. According to the available literature, doping is the key to high luminescence, quantum yield, and functionalization for bioanalytical applications. Because of these tremendous advantages, microwave- and hydrothermal-assisted CD preparations have become the most popular among the available preparation techniques. Table 1 summarizes the established synthetic routes to luminescent CDs including individual advantages and disadvantages as well as the reported quantum yield.

3 Luminescence Properties

3.1 *Photoluminescence*

Among all properties of CDs identified and reported so far, their intrinsic luminescence is the most interesting one. Compared to organic fluorophores CDs show improved photostability, and their luminescence is stationary and non-blinking in contrast to Q-dots. Furthermore CDs possess a very broad excitation band, and it is possible to tune their emission. Even though their optical properties have been described and characterized from many different perspectives, the quantum mechanical origin of CDs' luminescence properties is far from being understood and still under intense investigation.

Typically, CDs have their absorbance maximum in the UV, and their spectrum bottoms out over the whole visible light region up into the near infrared. It is a special feature of CDs in this respect that the excitation wavelength may be varied to induce emission of differently colored light (Fig. 5). Researchers suggest two different mechanisms to explain this behavior: (i) CD preparations contain particles of different size, and these show a size-dependent luminescence. Upon excitation at a given wavelength, only a fraction of the entire population is excited and emits fluorescence [65]; (ii) multicolor photoluminescence arises from a distribution of different emissive trap sites on the particle surface [66]. To date there is no completely convincing explanation available that verifies one mechanism and excludes the other.

In the first publication about the systematic preparation of CDs, Sun et al. compared the particles' photoluminescence with that from silicon nanocrystals [23]. In this study the photoluminescence was attributed to surface energy traps which become emissive through their stabilization by surface passivation. This requirement for surface passivation is similar to that of silicon nanocrystals whose luminescence emission originates from radiative recombination of excitons [67]. The conclusions made by Sun et al. were the first attempts to explain the luminescence properties of CDs which were challenged and improved by more in-depth studies over the years.

Q-dots are often used as a reference material to compare CDs with. The luminescence of semiconducting Q-dots depends on the size of the individual crystals. The smaller the crystal, the larger is its band gap, and thus, the higher is the frequency of the emitted light after excitation. Accordingly, the color of the light shifts from red to blue (to shorter wavelengths) with decreasing size of the Q-dots [68]. However, such a strict size-dependent luminescence has not been observed in general for CDs. Lee et al. reported of a red-shift for larger CDs by exfoliation from a graphite rod after size separation of the resulting particles by column chromatography [63]. In contrast Lu et al. reported of an inverse dependency between luminescence and particle size for CDs exfoliated from graphite rods in ionic liquid [28]. Other authors claim that it is not the size but the functional
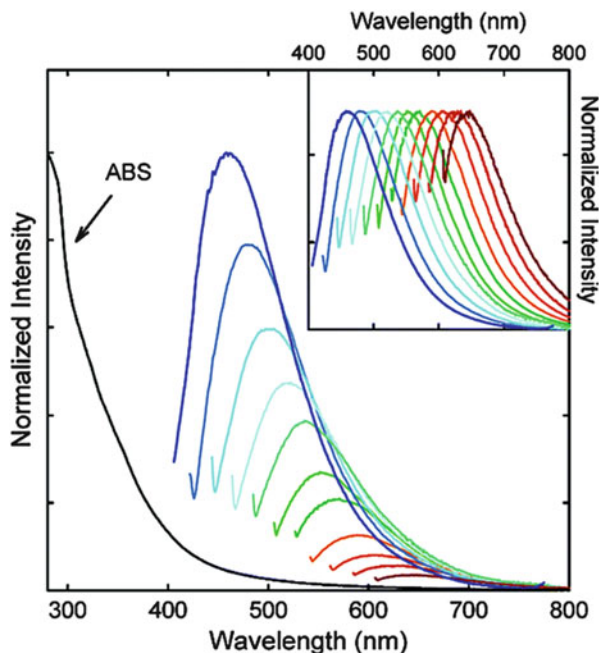
groups decorating the particle surface which has the most significant influence on
the electronic characteristics of CDs [29].

CDs have a more disordered solid state structure compared to crystalline Q-dots
or nano-sized graphene. This has to be taken into account when different
photoluminescence mechanisms are discussed [69]. A comprehensive description
and explanation of CD luminescence has to include their internal composition, any
surface functionalizations as well as the size of the particle itself. Thinking of the
structure of CDs as an amorphous or crystalline carbon core – mostly consisting of
sp^2 carbons – and an oxidized carbon shell, it is generally considered that PL is
likely to originate from the sp^2 carbon [17]. Those confined and delocalized sp^2
carbon clusters exhibit PL due to recombination of electron-hole pairs acting as
luminescence centers [70].

Yu et al. investigated the temperature-dependent luminescence of CDs from
77 to 300 K [71]. The authors observed asymmetric peaks in the luminescence
spectra at each temperature, which they attributed to a superposition of two
different luminescent species. One emission band originates from the CD core,
and another band describes emission from the particle surface. The individual
emission bands (I and II) have been fitted with two Gaussian functions, resulting
in a low and a high energy band peak (Fig. 6). Furthermore, the authors demon-
strated that CDs show rather weak electron-phonon scattering, as there is only a
very small red shift of the band gap for increasing temperatures. Since bands I and II
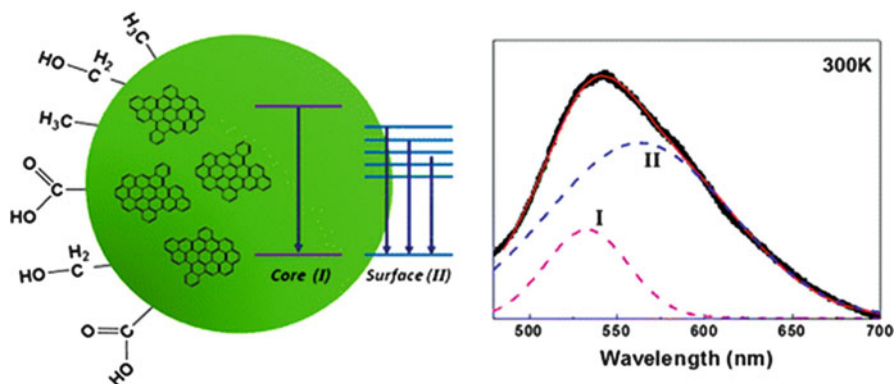
Fig. 6 *Left*: CD luminescence originates from two different luminescent species: CD core and surface. *Right*: fitting of CD photoluminescence spectra peak by two Gaussians attributed to either core or surface, respectively. With permission from [71]

are virtually temperature independent, mostly electron-electron scattering processes dominate the luminescence mechanism.

Other groups directed their research on the influence of surface states on CD luminescence [72]. As such, CDs were examined in different oxidation states. Zheng et al. used CDs prepared from soot which were oxidized with nitric acid before spectral characterization. Then these CDs were treated with the reducing agent $NaBH_4$ to bring all surface moieties to their reduced state. The spectroscopic properties of both particle types were compared to each other [73]. While the original CDs showed only weak PL at a wavelength of 520 nm with a quantum yield of 6%, the reduced CDs emitted at 440 nm with a drastically increased quantum yield of about 60% (cp. Fig. 7). The $NaBH_4$-based reduction process was found to be reversible by oxidation. Switching between reduced and oxidized states has been repeatedly performed in several cycles. The authors attribute the increase in quantum yield found for the reduced species to the increase of hydroxyl groups on the surface of the CDs, since hydroxyl groups act as electron donors. Moreover, the emission of green luminescence is associated with the existence of surface energy traps [23], while blue emission arises from so-called zigzag sites on the reduced CDs [32, 74]. *Zigzag sites* are pathways along the C-skeleton that go *zigzag* ("/\/\") in comparison to others that describe an armchair shape ("_/"). It is noteworthy that the enhancement of PL through chemical reduction is not a unique phenomenon for one individual CD preparation, but it has also been reported for other preparation methods as well [75, 76].

The oxidation state of CDs is only tuned by chemical reduction, but also by electrochemical means. Bao et al. exfoliated CDs from carbon fibers applying different potentials resulting in CDs with potential-dependent spectroscopic properties [29]. The higher the applied potential, the higher is the oxidation state of the resulting CDs and the more red shifted is the emission peak. The authors attributed their observation to a change in the distribution of oxygen-containing emissive sites
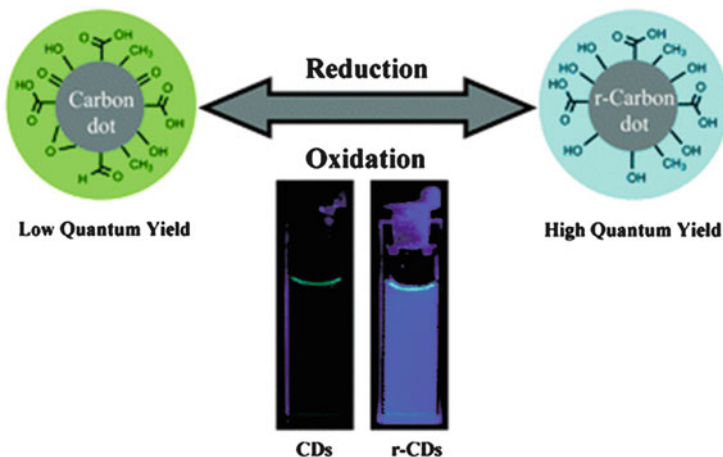
Fig. 7 Preparation of reduced state CDs (r-CDs) with blue luminescence from original CDs. *Inset*: photographs of aqueous suspensions of the CDs (*left*) and the r-CDs (*right*) under UV light (360 nm). With permission from [73]

on the surface. Very similar observations were made by Long et al., who used carbon paste electrodes for the electrochemical fabrication of CDs [27]. They were able to control the CD surface to either show spectral red shifting of their luminescence or not.

Although many aspects of the CD PL have been worked out, the mechanism is still not fully understood. It may arise from a combination of emissive traps, excitons of carbon, quantum-confinement effects, free zigzag sites, edge defects, and/or aromatic/oxygen-containing functional groups. A full understanding of the photophysical mechanisms is still in its infancy and requires further research endeavors [21].

3.2 Electrochemiluminescence

In addition to their photoluminescence, CDs also show electrochemiluminescence (ECL) similar to Q-dots [77] and silicon nanocrystals [78]. According to the other nanostructures, the mechanism of CD ECL was explained as follows: exposing CDs to a repeatedly cycling electrochemical potential, the oxidized state $(R^{\cdot}+)$ and the reduced state $(R^{\cdot}-)$ of CDs are formed. Undergoing electron transfer annihilation of these two oppositely charged carriers leads to the excited state (R^*). Eventually the excited CDs return to the ground state under emission of photons [79] (Fig. 8). Electrochemically released CDs from graphite were shown to produce ECL when the electrochemical potential is cycled between -1.5 and $+1.8$ V [26]. The ECL emission maximum peaked at 535 nm, while the peak of the PL was at about 455 nm. The authors claim that the energy gaps between ground and
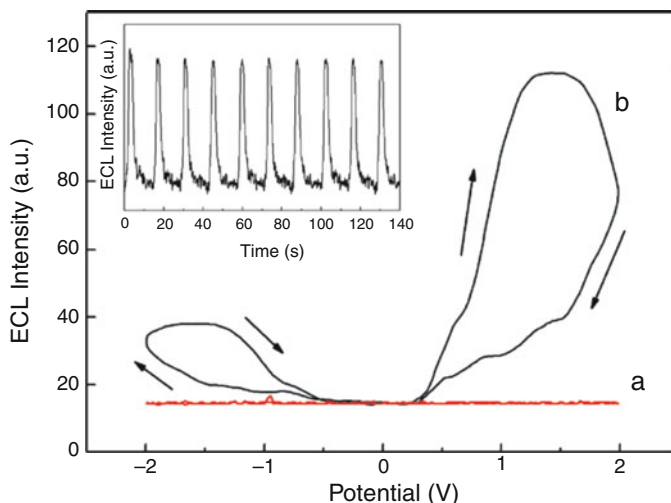
Fig. 8 Typical ECL response (*a*) without and (*b*) with CDs at an ITO electrode in 0.1 M PBS (pH 7.0). Inset: anodic ECL response during a continuous potential scan, $v = 0.1$ V s^{-1}. With permission from [79]

excited states are smaller for emissive sites on the CD surface (which is responsible for ECL emission) than the band gaps of emissive sites in the CD core (which determines the PL emission). This fits very well to the observations from other semiconducting nanomaterials, since their ECL was shown to originate from surface states and it is mostly red shifted from the PL peaks due to defect states in the band gap [78, 80].

3.3 Upconversion Photoluminescence

Probably the most interesting optical feature of CDs is their ability for *upconversion photoluminescence* (UCPL), i.e., low energy excitation followed by high energy light emission. The use of low energy radiation – mostly near-infra red photons (NIR) – as excitation source offers several advantages, especially in bioanalytical applications like (i) increased tissue penetration depth (>500 μm), (ii) low autofluorescence and self-absorption within the matrix, (iii) reduced photodamage and photobleaching, as well as (4) the possibility of localized excitation [81].

UCPL of CDs was demonstrated very early after their first well-defined preparation using laser ablation of a carbon target in the year 2007 by Sun et al. [82]. The resulting CDs emit visible light upon excitation with an argon-ion laser (458 nm) as well as upon two-photon excitation with a femtosecond-pulsed laser emitting in the NIR (800 nm). The authors demonstrated that both emissions arise from the same CDs by overlaying the individual luminescence images. Other groups made similar

observations, so that UCPL was more and more described as a rather general phenomenon associated with CDs derived from sources according to different preparation schemes including microwave-treated mixtures of citric acid/PEI [45] and ultrasonicated mixtures of glucose and ammonia [40] to CDs from an alkali-assisted electrochemical exfoliation [63]. UCPL of CDs is often attributed to multiphoton processes that involve surface or trap states [20]. Regarding the fact that the luminescence of CDs may arise from defect states on the particles' surface, CDs and Q-dots probably share common upconversion mechanisms [83].

4   CDs as Tools in Bioanalytics

Luminescent nanoparticles, for instance, Q-dots, have found widespread and multiple different applications in modern bioanalytics, and they helped to solve several experimental challenges. QDs have been used in several ways as a label in optical imaging in vitro and in vivo due to their unique spectroscopic properties [84]. However, Q-dots often contain toxic heavy metals that may leach out from the particle, and moreover QDs have been recognized as being phototoxic [85]. CDs by contrast are an entirely organic material with no heavy metals involved, but they share very similar optical properties with QDs such as general photoluminescence, high photostability, and upconversion photoluminescence (through NIR excitation). In addition to that CDs have several advantages: non-blinking luminescence, absence of toxic elements, and high water dispersibility [20]. Considering all those properties CDs are obviously very promising candidates to be used as labels in optical imaging. The next paragraphs provide an overview over CDs' biocompatibility and published applications as a contrast agent in optical microscopy.

4.1   Cytotoxicity

In order to use CDs as a label for live-cell imaging in vitro or as tracer in living organisms during in vivo imaging, these particles need to be inert and biocompatible with no significant cytotoxicity. Even though CDs mostly consist of the nontoxic element carbon, their surface is decorated with a complex mixture of functional groups arising from oxidation or passivation processes. Thus, biocompatibility of CDs has become an import issue, and it has been addressed very prominently.

   As CD preparations and the individual experimental conditions differ widely, the resulting particles are most likely not perfectly alike with respect to their physicochemical properties and also with respect to their biocompatibility/cytotoxicity. So it is no surprise that many groups have studied CD cytotoxicity. Amino-functionalized CDs prepared through hydrothermal treatment of chitosan [52] were prepared and tested for their cytotoxicity using *A549 human lung adenocarcinoma*

Fig. 9 Viability of *Hep-G2* after exposure to CDs. Viability was measured by the established MTT assay. Mean ± SD, $n = 3$. With permission from [41]
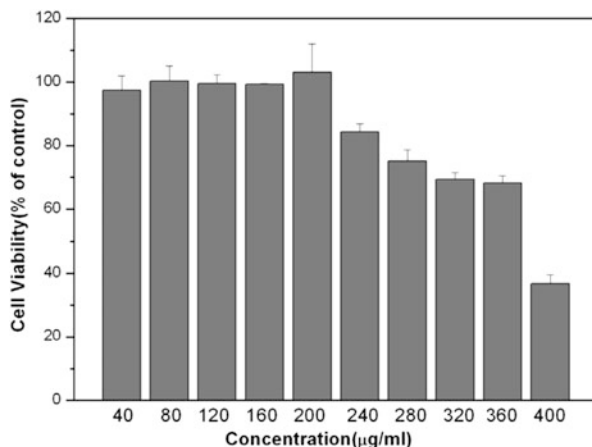
cells and the well-established MTT assay [86]. MTT assays read the metabolic activity of living cells and are therefore well suited to indicate any cytotoxic effect. The authors concluded from their experiments that CDs can be categorized as a material with low cytotoxicity. However, this study was confined to concentrations smaller or equal 200 μg/mL, which is low compared to other reports. Similar observations were made by Liu et al. who incubated human liver carcinoma cells (*Hep-G2*) with passivated CDs from microwave heating of glycerol and TTDDA [41]. MTT assays revealed cell viability of about 100% for concentrations below 240 μg/mL. Higher concentrations of CDs, however, induced a significant cytotoxic response (Fig. 9).

By contrast, Hsu et al. prepared CDs through calcination of coffee ground and evaluated the impact of these particles on the viability of pig kidney cells (*LLC-PK1*) for concentrations between 0 and 2.4 mg/mL [60]. The authors reported about uncompromised cell viability (>95%) as long as CD concentrations were below 1.8 mg/mL which renders them more biocompatible than Q-dots which get toxic beyond 100 μg/mL [87, 88]. Other CDs like those exfoliated from graphite electrodes were shown to be nontoxic up to concentrations of 400 μg/mL for human kidney cells (*293T*) [65], and a similar threshold concentration was reported for CDs from citric acid and ethylene diamine (hydrothermally) [53]. Yang et al. [89] performed a comprehensive analysis of CD cytotoxicity (Fig. 10) and concluded that CDs are "nontoxic and high-performance fluorescence imaging agents."

In this study human breast cancer cells (*MFC-7*) and human colorectal adenocarcinoma cells (*HT-29*) were incubated with PEG_{1500N}-passivated CDs from laser ablation [23]. The cellular response was evaluated in terms of proliferation, mortality, and viability via MTT assay. As a control the authors treated the same cells with PEG molecules alone under otherwise identical conditions. The results suggest that cell physiology is barely affected by CDs in comparison to the PEG molecules alone (Fig. 10). The toxic effect at high concentrations arises from the passivation agent itself which is known to induce cell fusion above certain threshold
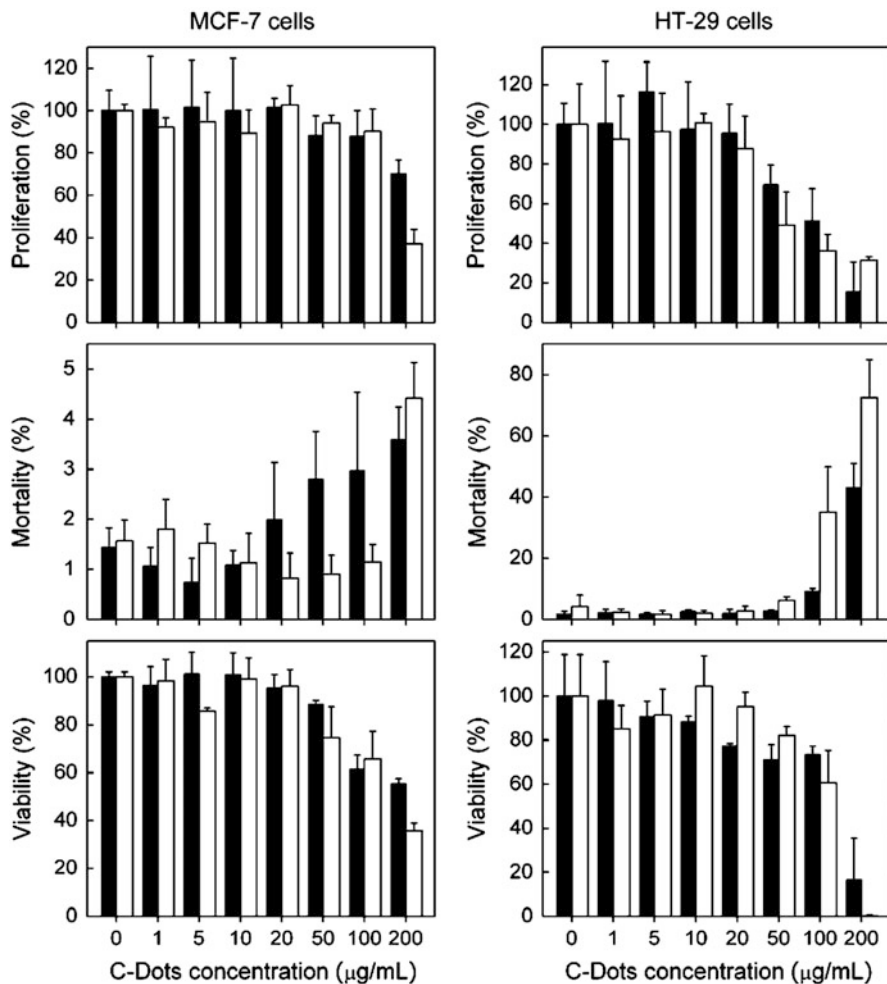
Fig. 10 Cytotoxicity evaluation for the incubation of *MCF-7* and *HT-29* cells with PEG-passivated CDs (*filled bars*) or PEG_{1500N} alone (*open bars*) for 24 h. All readings are based on the MTT assay in different experimental settings. Mean $\pm$ SD, $n = 4$. With permission from [89]

concentrations. As live-cell imaging works well with lower concentrations of CDs and requires significantly shorter exposure times, CDs were considered as nontoxic for those applications, especially in comparison to Q-dots. Similar studies with Q-dots revealed a decrease in cell viability of about 25% for human epidermal keratinocytes after exposure to PEG-passivated CdSe/CdS Q-dots (10 nM) for 24 h [90]. For comparison, viability of cells derived from the proximal tubules of a porcine kidney was compromised by 50% after a similar exposure to PEG-passivated CdSe/ZnS Q-dots [91].

   In conclusion, it is difficult to make a general statement about the cytotoxicity of CDs for multiple reasons: (i) The term "CDs" defines a rather broad class of materials with very different individual particles dependent on the educts and the preparation process. Polymer-passivated CDs may be almost inert, while CDs produced by oxidation processes have rather complex surfaces which may induce toxic effects or not dependent on the individual surface composition. (ii) Cytotoxicity studies have been performed with a wide variety of different cell lines. Some of these cell lines are less sensitive and tolerate more xenobiotic impact than others. Accordingly, a general judgment on CD cytotoxicity requires an endless number of studies pairing all the different CDs with all kinds of different cell lines. CDs share this problem with all other nanomaterials that are considered for biomedical applications. (iii) Cytotoxicity studies using higher concentrations of CDs may be affected by low molecular weight pyrolysis products that are difficult to separate from freshly prepared CDs. It is almost impossible to rule out that these contaminants are inherently included in CD suspensions.

   But the most severe cytotoxic effects have been observed for concentrations higher than required for biomedical imaging applications. Thus, CDs can be considered as useful tools for labeling cells in live-cell imaging or as tracers for in vivo studies. At the appropriate concentration they don't seem to be significantly more harmful to cells than regular organic fluorophores and fluorescent probes, but they are less invasive and of better biocompatibility than Q-dots.

4.2   In Vivo Biocompatibility

The "systematic safety evaluation on photoluminescent carbon dots" (2013) by Wang et al. studied the in vivo biocompatibility of CDs prepared through nitric acid oxidation of raw carbon soot after passivation with PEG_{2000N} [92]. Acute toxicity was evaluated after a single intravenous injection of 51 mg/kg CDs into mice (*BALB/c*). For a period of 14 days, no obvious clinical symptoms of toxicity could be observed. Biochemical serum parameters as, for instance, levels of *glutamic oxaloacetic transaminase* (GOT), *glutamate pyruvate transaminase* (GPT), urea, cholesterol, triacylglyceride (TG), blood glucose, albumin, and creatinine (CR) were all similar to levels of the control groups. Subacute toxicity was investigated on *Wistar* rats in three test groups after intravenous injection of 0.2, 2, and 20 mg/kg CDs, respectively. Within an observation time of four weeks, no symptoms of toxicity were detected. Biochemical and hematological tests were performed at day 1, 3, 7, and 28. The hematological tests included the following parameters: number of white blood cells, number of red blood cells, number of platelets, number of lymphocytes, number of neutral cells, number of other cells, hemoglobin concentration, and hematocrit (HCT). All blood-related parameters of treated animals were similar compared to the control groups (cp. Fig. 11). The concentration of blood-borne biochemicals confirmed this analysis. The data in Fig. 12 shows no relevant difference for animals that were exposed to CDs
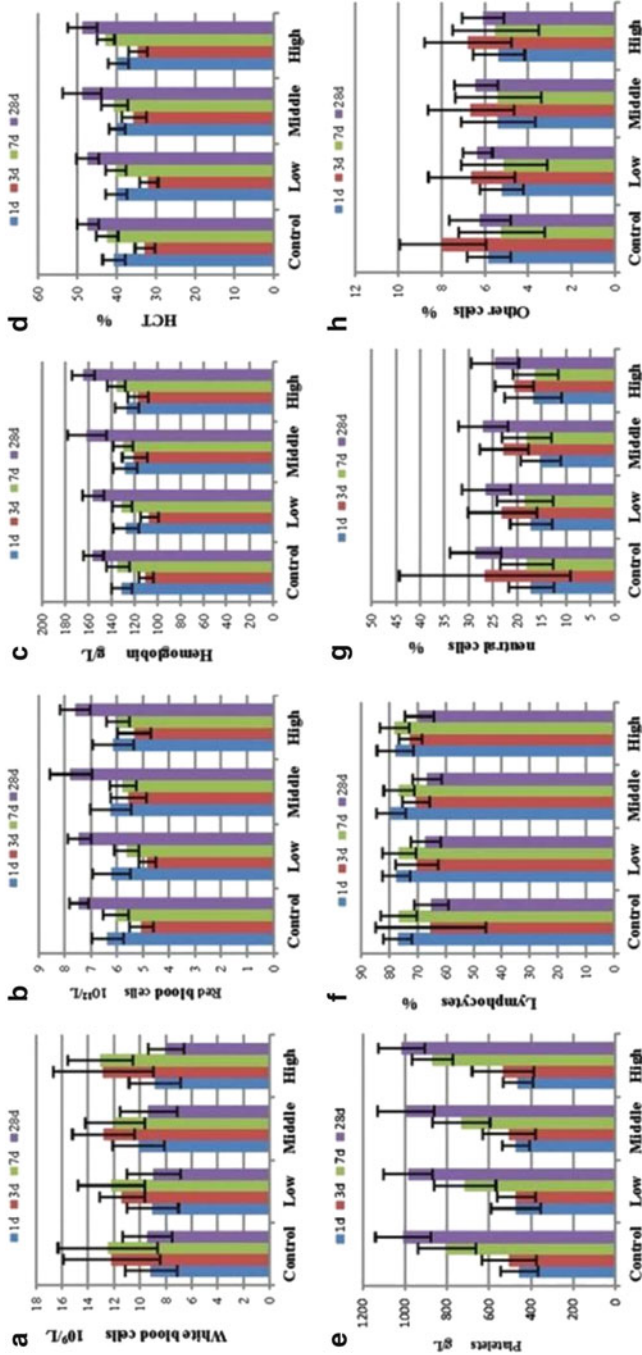
Fig. 11 Hematological analysis of rats treated with CDs in doses of 0.2 (*low*), 2 (*middle*), and 20 mg/kg (*high*) after 1, 3, 7, and 28 days. (**a**) White blood cells; (**b**) red blood cells; (**c**) hemoglobin; (**d**) hematocrit (*HCT*); (**e**) platelets; (**f**) lymphocytes; (**g**) neutral cells; (**h**) other cells. With permission from [92]
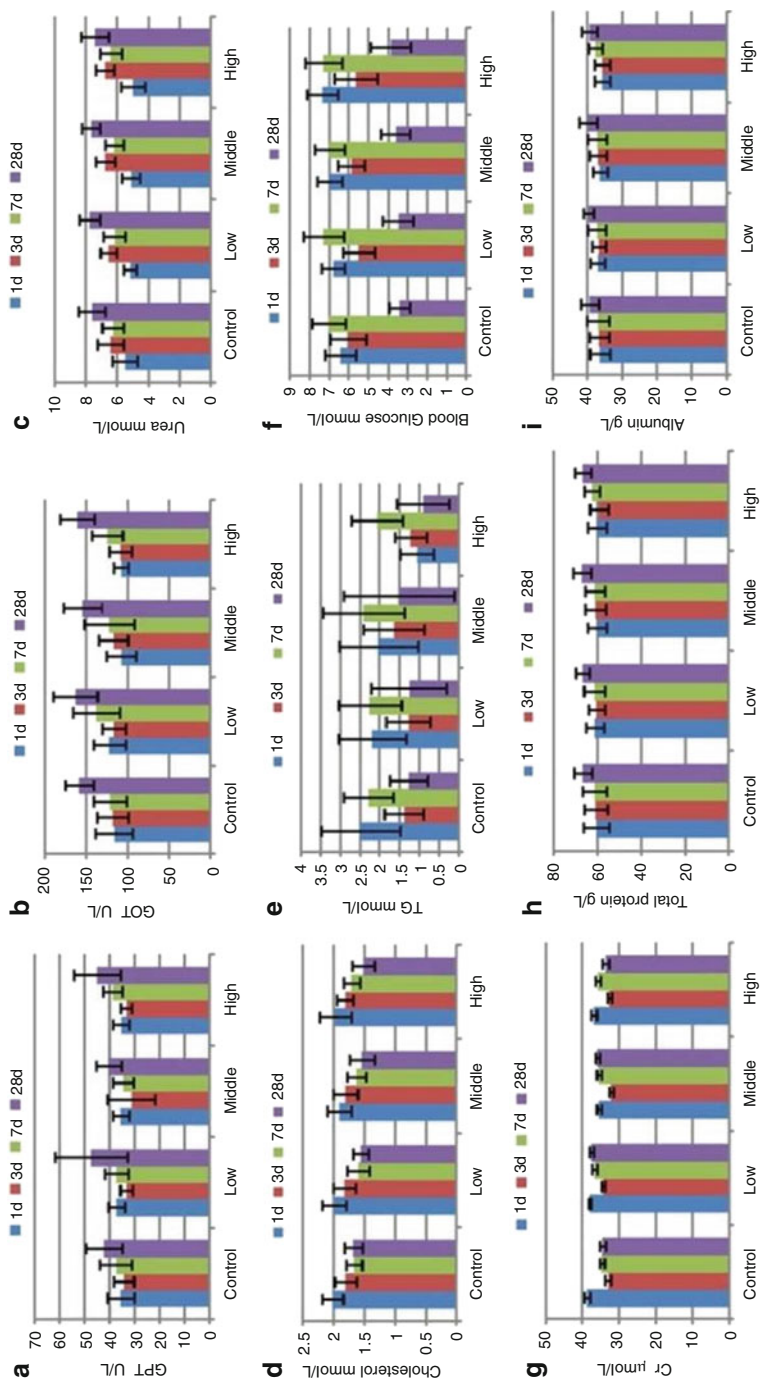
Fig. 12 Concentration or activity of blood-borne biochemicals in rats treated with CDs in doses of 0.2 (*low*), 2 (*middle*), and 20 mg/kg (*high*) after 1, 3, 7, and 28 days. (**a**) Glutamat-Pyruvat-Transaminase, GPT = ALT; (**b**) Glutamate-Oxaloacetate-Transaminase, GOT = AST; (**c**): urea; (**d**): cholesterol; (**e**) thyroglobulin = TG; (**f**) blood glucose; (**g**) Cr; (**h**) total protein; (**i**) albumin. With permission from [92]
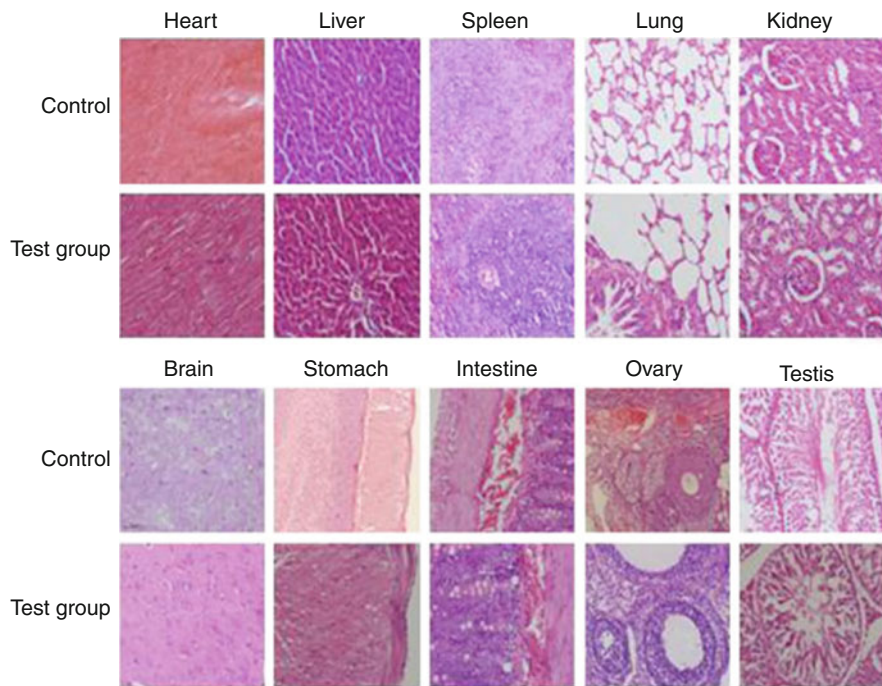
Fig. 13 Histopathological analysis of rats 30 days after treatment with 20 mg/kg CDs. With permission from [92]

compared to untreated controls. From a purely statistical viewpoint, some biochemical parameters showed a significant difference between the treated group and control, but the authors could not conclude on any biological impact. After 30 days the rats exposed to the highest dose of 20 mg/kg CDs were histopathologically examined. Histological inspection comprised the heart, liver, spleen, stomach, kidneys, lungs, brain, stomach, intestine, ovaries, and testes. As shown in Fig. 13, no obvious organ damage or abnormality from the control group was observed. Accordingly, this in-depth analysis of CD biocompatibility did not find any significant toxic effects of the CDs under test.

Tao et al. studied biodistribution and in vivo toxicology of CDs in mice [93]. Experimentally ^{125}I-labeled CDs prepared from multiwalled carbon nanotubes were injected intravenously, and the accumulation of the particles in the organs was examined. It turned out that CDs mainly accumulate in the organs of the reticuloendothelial system, such as liver and spleen. Moreover CDs were found to reach the kidneys rather rapidly, pass through the glomeruli filter, and get excreted via the urine. In vivo toxicology using a dose of 20 mg/kg provided no indication for a biological response of the animals within 90 days of observation time. The mice did neither die nor loose weight. Biomarkers of liver (Alanine Transaminase, ALT; Aspartate Transaminase, AST; Alkaline Phosphatase, ALP;

Albumin/Globulin ration, A/G) and kidney function (blood urea nitrogen, BUN) did not show any significant change due to the exposure to CDs. Thus, CDs were characterized as being nontoxic to the liver and kidney. The results have been supported by histopathology of the liver, spleen, kidney, and heart which showed no indication for a tissue response to CDs.

In a similar study PEG_{1500N}-passivated CDs with a ^{13}C-enriched core were injected intravenously into mice applying doses of 8 or 40 mg/kg, respectively [89].

Along an observation time of 28 days, no clinical symptoms have been observed. In contrast to the results described above, the authors found a rather low accumulation of CDs in the liver, spleen, and kidneys as determined from the isotope ratio $(^{13}C/^{12}C)$ in mass spectra of the tissue. Comparing the concentration or activity of blood-borne chemicals like (i) ALT and AST as liver markers or (ii) uric acid (UA), BUN or Cr as kidney markers did not show any significant impact of CDs relative to untreated controls. Histopathology of the liver, spleen, and kidney did not provide any indication of tissue damage and thereby confirmed the biocompatibility of CDs.

Thus, the yet uncontested biocompatibility of CDs is a major advantage compared to Q-dots [22]. In this respect CDs are even competitive to FDA-approved organic fluorophores like indocyanine green, which has an LD_{50} value of 60 mg/kg for intravenous injection in mice [94]. Accordingly, CDs may also become important as a contrast agent for biomedical imaging in vivo.

4.3   Live-Cell Imaging

Since CDs show a unique photoluminescence, outstanding photostability, and yet uncontested biocompatibility, they used labels and probes in live-cell imaging applications. The first approach in this respect was reported in 2006 by Sun et al. [23]. The authors incubated *Escherichia coli* ATCC 25,922 bacteria with PEG_{1500N}-passivated CDs by adding the particles to the bacteria suspension. After 18 h of incubation the suspension was centrifuged, the bacteria got washed and resuspended before they were examined by confocal laser scanning microscopy (CLSM, Fig. 14a). Similarly mammalian cells (*Caco-2*) were incubated with PPEI-EI-coated CDs by adding the particles to the culture medium. After 1.5 h the cells were washed with PBS and examined via CLSM (Fig. 14b). The labeling of both, bacteria and human cells, was clearly visible and attributed to the incorporation of the particles into the cytoplasm. Remarkably, the nuclei of most human Caco-2 cells remained dark, indicating that CDs may not be able to enter the nucleus. Likewise, Liu et al. incubated *E. coli* bacteria and *Murine P19 progenitor* cells with their CDs that were prepared through carbonization of resols. The authors reported about similar observations as described above with respect to uptake and distribution of CDs in prokaryotic and eukaryotic cells [66].

CDs prepared according to the same procedure of laser ablation and passivation via PPEI-EI have also been described and tested as multiphoton luminophores for live-cell imaging [82]. The authors incubated MCF-7 cells with the particles for 2 h
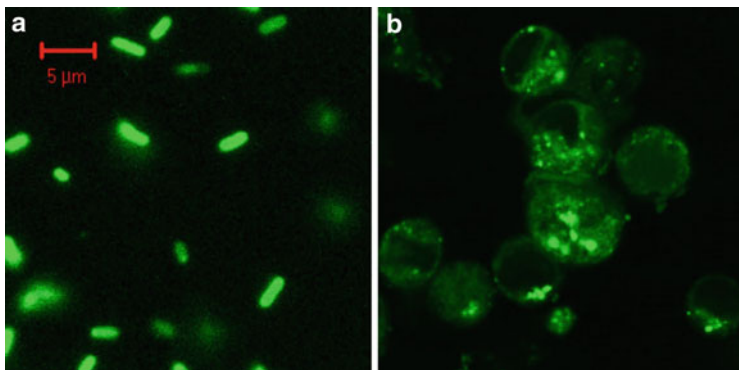
Fig. 14 Optical z-sections recorded by CLSM (488 nm exc.) through (**a**) *Escherichia coli* and (**b**) *Caco-2* cells after incubation with CDs for 18 or 1.5 h, respectively. With permission from [23]
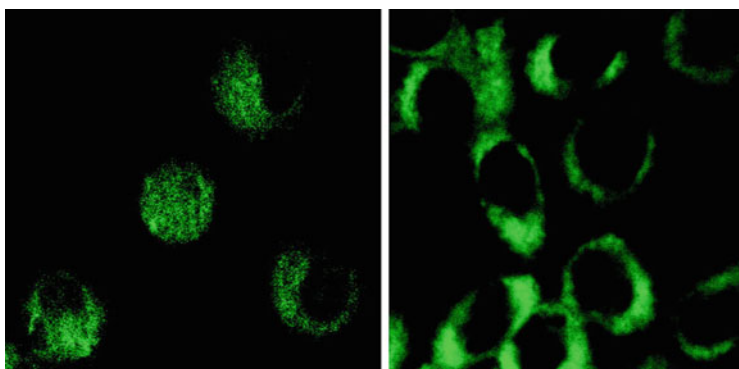
Fig. 15 Optical sections through *MCF-7* cells with internalized CDs upon excitation with a femtosecond laser pulse at 800 nm. With permission from [82]

at 37°C and examined the cells under two-photon excitation with a femtosecond laser pulse at 800 nm. Under these conditions the cells exhibited bright green luminescence in their cytoplasm with almost completely dark nuclei (Fig. 15). In contrast, Ray et al. observed a homogeneous staining of the whole cell when Ehrlich ascites carcinoma cells (*EAC*) were exposed to CDs from carbon soot [95].

Moreover, the uptake mechanism for CDs into the cytoplasm of mammalian cells has been addressed. Here, cells were incubated with CDs at 37°C and 4°C, respectively. All other experimental parameters except temperature were kept constant. Upon cooling the cells down to 4°C, endocytosis-mediated particle uptake is disabled. Accordingly the authors did not observe any significant luminescence inside the cells indicating that endocytosis is the most-likely mechanism for the internalization of CDs into cells.

With new preparation methods for CDs coming up providing similar but not identical particles, several different unique species were analyzed with respect to

Fig. 16 Intracellular fluorescence intensity of *HeLa* cells incubated with CDs in copresence of different inhibitors of endocytosis. (NS = No statistic difference). With permission from [100]
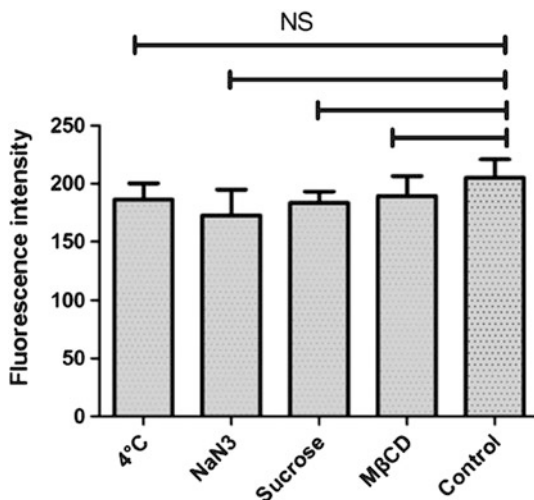
their potential as a contrast agent for live-cell imaging. Zhu et al. prepared CDs hydrothermally from graphene oxide and dispersed this material in cell culture medium for uptake experiments [96]. Internalized CDs showed bright green luminescence upon laser excitation at 405 and 488 nm from inside the cytoplasm of human bone osteosarcoma cells (*MG-63*). However, the authors also reported about a different, more complex uptake mechanism when a murine pre-osteoblast cell line (*MC3T3*) was used in such uptake experiments.

To gain further insight into the question whether or not, CDs are taken up by endocytosis HeLa cells and were incubated with CDs in presence of several different molecular inhibitors of endocytosis. Since endocytosis is an energy-dependent cellular activity, low temperatures [97] and NaN$_3$ [98] are known to suppress this process. Moreover, it is well known that the addition of sucrose or Methyl-β-cyclodextrin (MβCD) inhibits clathrin-mediated or caveolae-mediated endocytosis, respectively [99]. However, analysis of intracellular fluorescence intensity after CD exposure in presence of the various inhibitors did not show any significant difference indicating that endocytosis may not be involved (Fig. 16).

Taken together, there are conflicting results regarding the uptake mechanism of CDs into adherent mammalian cells. The same is true for other nanomaterials as well as whose uptake route has not been identified unequivocally [97, 101, 102]. Since CDs are extremely small, a non membrane-mediated, passive diffusion of the particles across the membrane along their concentration gradient is not entirely ruled out but awaits further experimental support.

The distribution of CDs after internalization in vitro has been extensively studied by Li et al. [100]: human cervical carcinoma cells (*HeLa*) were incubated with CDs and the luminescence distribution inside the cells was analyzed. According to these experiments the CDs were primarily entrapped in endosomes, multivesicular bodies, and lysosomes with aggregation at the perinuclear region, which usually results

from nanoparticle endocytosis. Such an intracellular distribution across different organelles might explain the inhomogeneous CD luminescence intensity observed in fluorescence micrographs with local intensity maxima. In a follow-up experiment, HeLa cells were incubated with CDs, and the lysosomes/endosomes, Golgi apparatus, mitochondria, and endoplasmic reticulums were counterstained with specific, fluorescent organelle markers. Merging the fluorescence images of both, the CDs and the organelle-specific dyes provided a more precise intracellular localization of the particles. Besides diffuse distribution across the cells, a significant fraction of the internalized particles has been localized to the lysosome/endosome compartment. However, CD luminescence was never found exclusively in one organelle just preferentially.

Although the internalization of CDs is not completely understood, the particles can certainly be used for imaging applications and replace existing labels whenever they perform better. Fang et al. compared the photostability of CDs with that of CdTe Q-dots, fluorescein isothiocyanate (FITC), and *Hoechst 33342* inside human embryonic kidney cells (*HEK 293*) [103]. After 25 min of continuous observation in the fluorescence microscope (CLSM), the CD label inside the cells was still detectable, whereas the luminescence of the reference materials was not. Thus, CDs obviously provide a significantly improved photostability compared to well-established fluorescence labels. Another interesting feature and added value of CDs is their multicolor emission which is dependent on the details of the experimental procedures [41, 46, 53, 66, 104]. For instance, Liu et al. incubated *Hep-G2* cells with TTDDA-passivated CDs (0.1 mg/mL) for 24 h and examined the cells via CLSM afterwards [41]. As summarized in Fig. 17, the cells showed blue (a), green (b), and red (c) luminescence upon laser excitation at 405, 488, or 543 nm, respectively.

As the surface of CDs is decorated by a variety of functional groups that arise from the oxidation or passivation steps during synthesis. These functional groups have been used as anchors to attach CDs to biomolecules or indicator dyes. The whole set of established bioconjugation techniques can be used to couple and functionalize CDs with other molecules such as N-hydroxysuccinmide (NHS) or 1-ethyl-3-(3-dimethyl-aminopropyl)-carbodiimide (EDC) chemistry. Biofunctionalization of CDs may enable the particles (i) to report on the concentration of intracellular analytes when coupled to indicators, (ii) to be targeted preferentially to predefined intracellular structures when coupled to recognition sequences, or (iii) to label individual cell types by interaction with their unique cell surface receptors when coupled to the corresponding ligands. Several examples for bioanalytical applications of CDs that are based on a preceding biofunctionalization of their surface have been described already. Selected examples are highlighted below.

One of the first modifications of CDs to comply with a given bioanalytical strategy has been reported by Li et al. in 2010 [105]. PEG-passivated CDs with amino termini were conjugated to *transferrin* via EDC chemistry to specifically target cancer cells. *transferrin* is a serum glycoprotein that is internalized by receptor-mediated endocytosis using the *transferrin* receptor. The *transferrin* receptor is commonly overexpressed by cancer cells so that it may serve as a
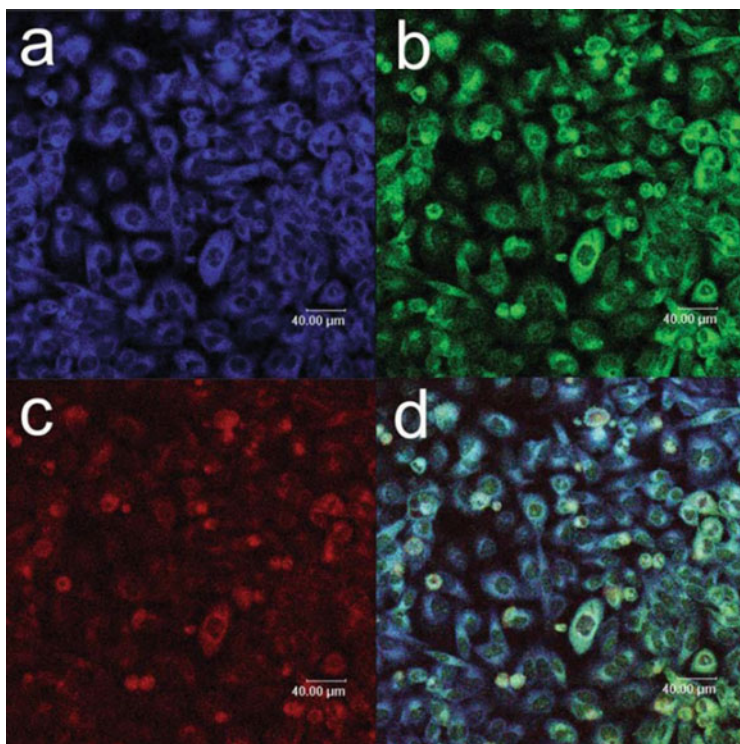
Fig. 17 Optical sections through *Hep-G2* cells after incubation with CDs. Cells show *blue* (**a**, exc 405 nm), *green* (**b**, exc. 488 nm), and *red* (**c**, 543 nm) luminescence dependent on the excitation wavelength. (**d**) Three-color overlay from (**a**), (**b**), and (**c**). With permission from [41]

label to preferentially address cancer cells but ignore non cancer cells [106]. According to this study *transferrin*-conjugated CDs showed a significantly stronger internalization into HeLa cells than non-conjugated CDs within identical exposure times. Moreover, the authors demonstrated that the uptake was mediated by *transferrin* receptors, since HeLa cells pre-saturated with *transferrin* did not show any internalization of CDs. A similar targeting strategy for cancer cells was pursued by Song et al. who conjugated CDs with folic acid (FA) [107]. The CDs themselves were prepared via microwave treatment of an aqueous solution of glucose and TTDDA. Conjugation of FA with amino groups present on the CD surface was achieved using NHS chemistry as shown in Scheme 2.

FA-conjugated CDs were used to distinguish between normal and cancer cells, based on the overexpression of folate receptors on the surface of cancer cells. In a proof-of-concept study, a mixture of human cervical carcinoma cells (*HeLa*) and non-transformed mouse fibroblasts (*NIH-3T3*) was incubated with the FA-conjugated CDs. As shown in Fig. 18 luminescence and thus, internalization of CDs was only observed for the cancerous *HeLa* cells (Fig. 18a). Receptor-mediated endocytosis was confirmed as the primary uptake mechanism by

Scheme 2 Conjugation of folic acid to the amino groups on the surface of TTDDA-passivated CDs by NHS-chemistry. Adapted from [107]
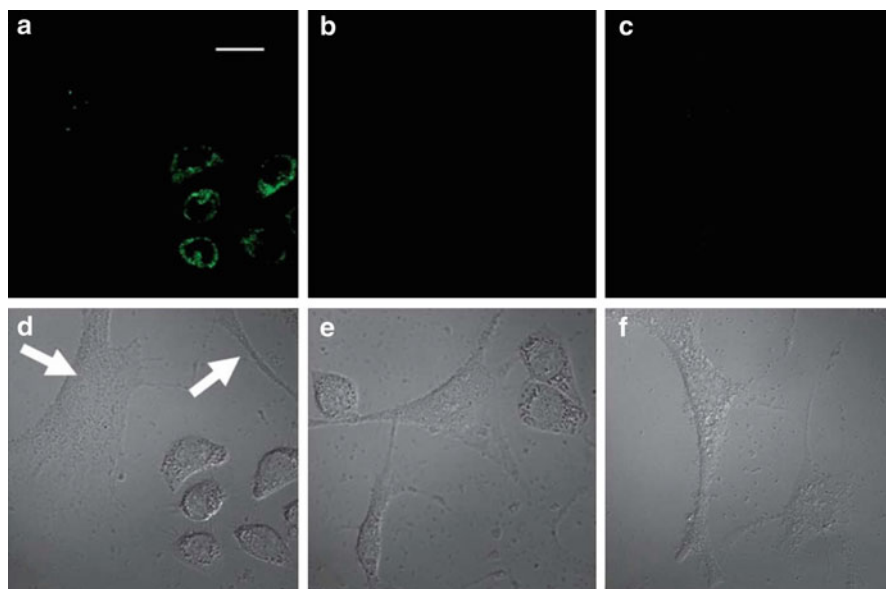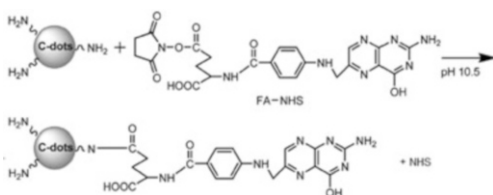
Fig. 18 Fluorescence micrographs of a mixture *of NIH-3T3* and *HeLa* cells (**a**) after incubation with FA-conjugated CDs (50 μg/mL) for 6 h or in the absence of the particles (**b**). Exposure of *NIH-3T3* alone to FA-conjugated CDs (50 μg/mL) did not provide any indication for particle uptake. (**d–f**) Phase contrast micrographs that correspond to fluorescence micrographs in (**a–c**). (**d**) *White arrows* mark *NIH-3T3* cells. *Scale bar*: 20 μm. With permission from [107]

pre-saturation of the *HeLa* folate receptors with free FA. These particular samples showed no luminescence inside the cells after incubation with FA-conjugated CDs.

Other CD surface modifications were aiming for the detection of analytes inside living cells. One of them uses modified CDs for a ratiometric measurement of the intracellular pH [108]. Here CDs were prepared from citric acid and TTDDA. As shown in Scheme 3, the particles were then conjugated to the pH-sensitive fluorescein-isothiocyanate (FITC) and the pH-insensitive reference dye rhodamine B isothiocyanate (RBITC). The pH-sensitive CD probe was used to quantify the intracellular pH of *HeLa* cells, while the latter was manipulated by the H^+/K^+ ionophore *nigericin*. Nigericin integrates into the plasma membrane and makes it permeable for protons such that the cytosol equilibrates with the pH of the extracellular medium [109]. As shown in Fig. 19, the intensity of the green luminescence

Scheme 3 Preparation of dual-label CDs (*DLCDs*). (**a**) TTDDA, 220°C, 3 h; (**b**) FITC, RBITC, room temperature, overnight. With permission from [108]
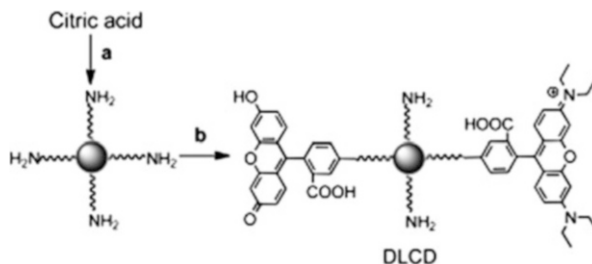
(FITC channel) increases with pH, while the intensity of the red luminescence (RBITC channel) remains roughly unaffected. The ratio of those two fluorescence intensities allows generation of a calibration curve for the intracellular pH value. Applying this calibration allows measuring the intracellular pH of HeLa cells that was determined to be 7.4 ± 0.2. The intracellular pH value of MCF-7 cells was found to be 7.2 ± 0.2. Both pH values agree favorably with the results recorded with a commercially available pH probe (SNARF-1).

Zhu et al. used a dual emission nanohybrid of CDs and Q-dots in order to image the concentration of copper ions [110]. These ratiometric nanohybrid probes consist of silica-coated CdSe Q-dots that are conjugated with CDs. While the CD fluorescence is quenched by copper ions, the Q-dot emission is inert and serves as reference. The probe was successfully applied for the imaging of Cu^{2+} concentrations in *HeLa* cells. After exposing the cells to exogenous copper by adding Cu^{2+} ions to the culture medium, the fluorescence emission of the probe turned from green yellow to red.

Yu et al. developed a ratiometric probe for hydrogen sulfide (H_2S) through modification of CDs for a *Förster resonance energy transfer* (FRET)-based readout [111]. The H_2S sensor is based on a naphthalimide-azide which was covalently attached to the surface of amino-terminated CDs via EDC chemistry. In the absence of H_2S, the CDs emit blue light at 425 nm. The presence of H_2S leads to the reduction of the azide, inducing a FRET from the CDs' emissive states to the naphthalimide and the emission shifts from blue to green at 526 nm. The CD-based probe was successfully applied to detect H_2S in living cells, namely, *HeLa* and murine aneuploid fibrosarcoma cells (*L929*). As a proof-of-concept H_2S was added to the culture medium and the luminescence inside the cells shifted from blue to green.

CDs have also been shown to assist the delivery of extracellular substances across the plasma membrane into adherent cells. Liu et al. reported about polyethylene imine (PEI)-passivated CDs for imaging and as nano-carriers for gene delivery [42]. Due to their PEI-coating, these CDs have a highly positive surface charge, which enables electrostatic interactions between the CDs and DNA. These CD-DNA-complexes were used for plasmid transfection into COS-7 cells and Hep-G2 cells. The subsequent expression of the reporter gene encoded on the plasmid was similar compared to the transfection of the same plasmid with PEI25k. As an added value the carrier CDs were used for optical imaging of the
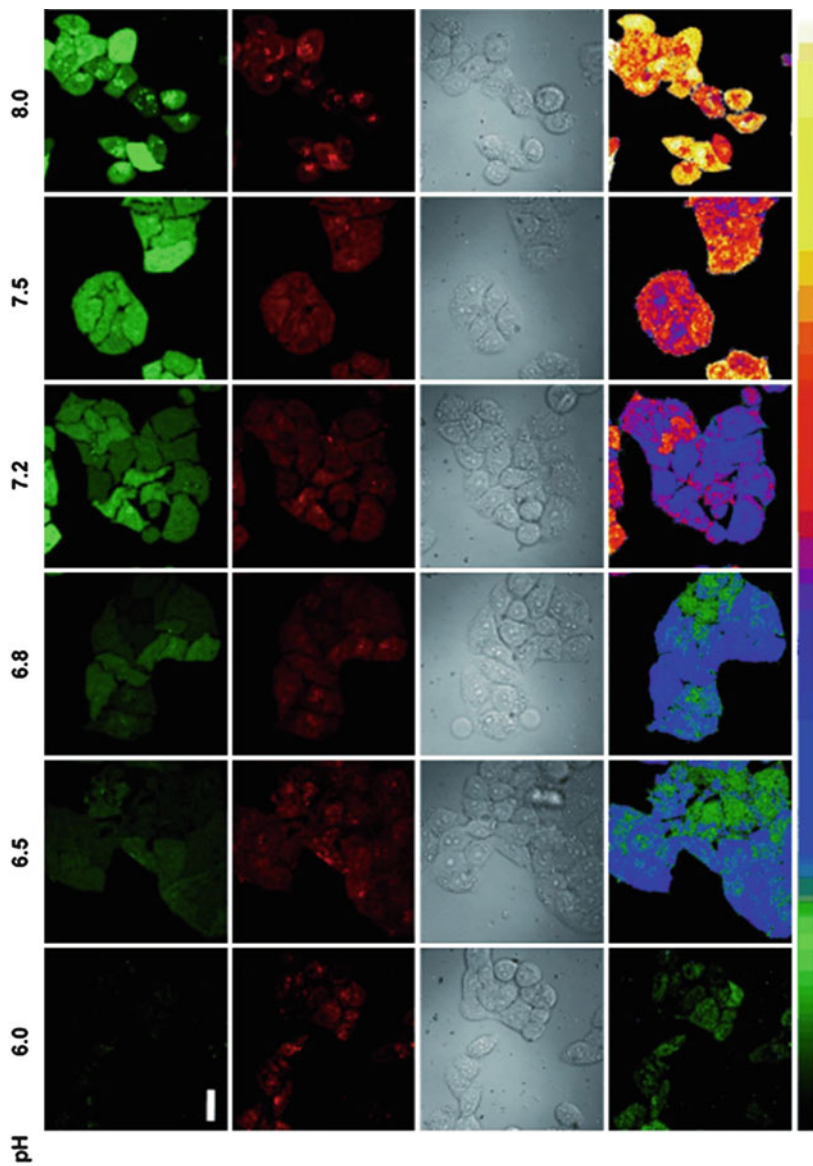
Fig. 19 Fluorescence images of *HeLa* cells at pH 6.0, 6.5, 6.8, 7.2, 7.5, and 8.0, respectively. The images of the *first column* (FITC channel) and the *second column* (RBITC channel) were recorded with filters that pass light of 510–550 or 570–610 nm, respectively. The *third column* shows the corresponding phase contrast images. Images in the *fourth column* represent the emission ratio in false colors generated by Olympus software (FV10-ASW). *Color code* given on the *very right* represents the pseudo-color change with pH. Scale bar: 20 μm. With permission from [108]
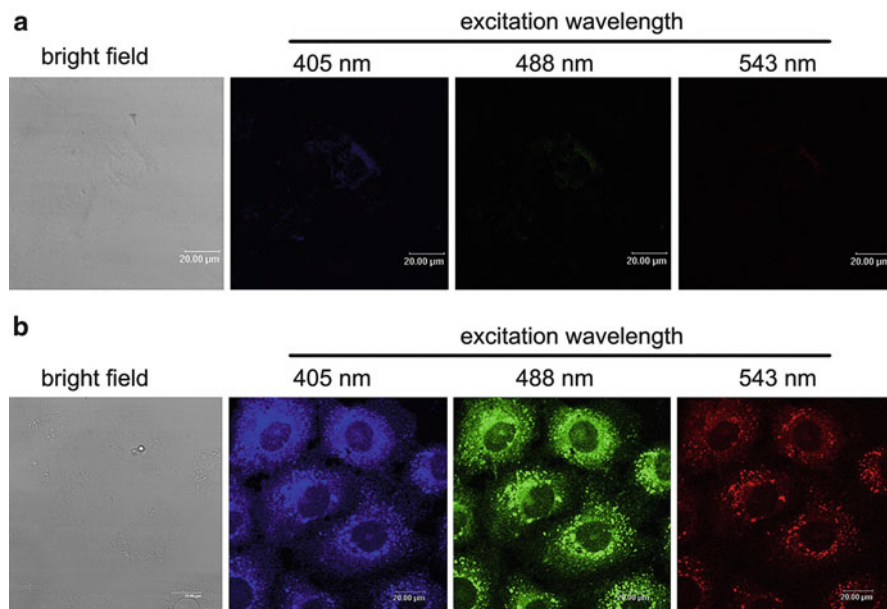
Fig. 20 Optical sections through COS-7 cells recorded by CLSM. (**a**) Non-transfected cells as negative controls and (**b**) transfected cells. CD emission was recorded upon excitation at 405, 488, and 543 nm, respectively. All scale bars correspond to 20 μm. With permission from [42]

transfected cells, as shown in Fig. 20. The CDs emit blue, green, and red luminescence upon laser excitation at 405, 488, or 543 nm, respectively. In this study the CDs were found to be predominantly localized in endosomes without entering the nucleus.

Another set of CD-based drug delivery experiments was conducted by Lai et al. using CDs incorporated inside mesoporous silica particles (CDs@mSiO$_2$) [112]. These nano-composites were prepared via the calcination of glycerol inside mSiO$_2$ particles. The resulting CDs@mSiO$_2$ were subsequently passivated by PEG and loaded with the anticancer drug *doxorubicin*. Exposing *HeLa* cells to these particles revealed that the particle-mediated incubation was more toxic for the cancer cells than incubation with free *doxorubicin*, indicating a delivery into the cells. Moreover, the blue emission of the CDs inside the mesoporous silica particles together with the red emission of doxorubicin provided the opportunity to track the drug release from the particles inside the cells.

In conclusion, existing studies have identified that CDs have a considerable potential as a flexible and versatile contrast agent in live-cell imaging. As their surfaces are accessible for established bioconjugation chemistry, they can be easily modified, tailored, and customized for specific bioanalytical applications. Even though CD research is still in its infancy, these particles have the potential to become a standard fluorescence label for bio assays, maybe even replacing

Q-dots in selected applications. However, CDs are commonly not as bright as their inorganic counterparts, so that laser-based excitation is required. So it is obvious that a wider use of CDs as a contrast agent in microscopic imaging requires improvements in specific absorbance and quantum yield.

4.4   In Vivo Imaging

Besides their application in live-cell imaging, CDs have also been used as a contrast agent for in vivo imaging aiming for new concepts in image-based diagnostics and even therapy (photodynamic therapy, PDT). However, the controlled use of nanoparticles in living organisms is a highly complex issue that has many different facets: distribution inside the organism, metabolic conversion or modification, and excretion. The first application of CDs as a fluorescence contrast agent in vivo was reported by Yang et al. in 2009 [113]. Among others the authors used PEG_{1500N}-passivated CDs from oxidized carbon soot in aqueous solution for the injection into mice. Subcutaneous injection of the CDs led to easily detectable green or red emission in the injection region. Intravenous injection was performed as the next step to determine the distribution of the CDs after circulation through the whole body. Whole body imaging showed the bladder to be brightly fluorescent. Within 3 h after injection, the urine became luminescent as shown in Fig. 21. The results suggest that CDs are primarily excreted via the urine following intravenous injection. This pathway has been reported for other PEG-passivated nanoparticles, such as Q-dots, before [114]. The organs were harvested for analysis ex vivo 4 h after injection. Significant luminescence was only found in the kidneys and in the liver (cp. Fig. 21). As the primary excretion pathway is from the kidney into the urine, luminescence was the brightest here. The marginal intensity detected inside the liver was considered as an indication of low-level accumulation of CDs in the organism. These observations are in contrast to those reports describing significant hepatic uptake of nanoparticles and nanotubes [115]. Probably, the rather low accumulation of CDs can be attributed to the surface passivation with PEG which is known to reduce interactions with proteins and other biomolecules.

Tao et al. performed similar in vivo studies using CDs that were prepared through acidic oxidation of multiwall carbon nanotubes [93]. Here, a nude mouse was subcutaneously injected with CDs at three different spots as shown in Fig. 22a. Afterwards the mouse was analyzed via fluorescence imaging using blue, green, yellow, orange, red, deep red, and NIR light with wavelengths of 455, 523, 595, 605, 635, 661, and 704 nm, respectively. The background autofluorescence (green) has spectrally subtracted the CD fluorescence in the injection spots (red), as these were seen at all excitation wavelengths. The resulting signal-to-background ratio was best at higher wavelengths (595 nm and above) due to the decreased tissue autofluorescence background. Although CD luminescence decreases for higher wavelength excitation, the background autofluorescence is even weaker leading to an increased signal-to-noise ratio under red light and NIR excitation. Optical
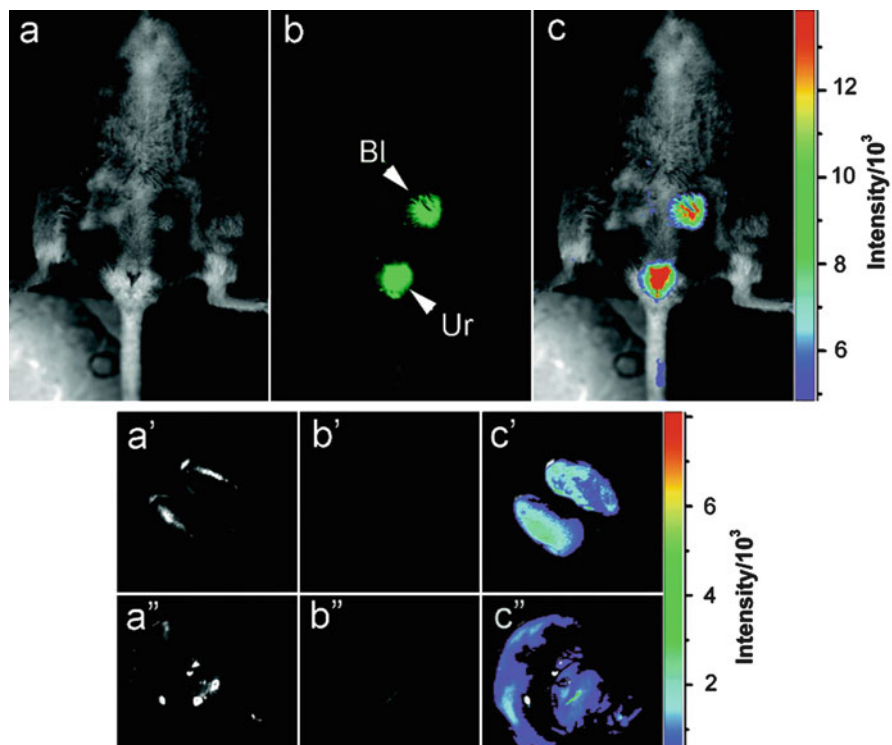
Fig. 21 In vivo imaging after intravenous injection of CDs into a mouse: (**a**) bright field, (**b**) fluorescence (*Bl*: bladder; *Ur*: urine), and (**c**) pseudo-color images encoding luminescence intensity. Bright field, fluorescence, and pseudo-color micrographs of the kidneys (a′ − c′) or the liver (a″ − c″) ex vivo. With permissions from [113]

imaging in vivo is commonly performed at higher wavelengths due to the improved tissue penetration and reduced background fluorescence [116]. Since CDs are readily excited in the NIR, they are well suited as a contrast agent for in vivo imaging.

Li et al. performed ex vivo imaging after tail injection of blue luminescent CDs into mice using a 405 nm excitation source [100]. Blue luminescence was observed in all organs, including the heart, liver, spleen, lung, kidney, intestine, and brain at 6, 16, and 24 h after injection. Among the various organs, the spleen showed the brightest luminescence due to accumulation of CDs. Interestingly, significant fluorescence was also observed in the brain indicating that non-functionalized CDs may cross the blood-brain barrier. This observation is noteworthy since delivery of Q-dots into the brain requires a surface decoration with TAT [117]. TAT stands for *trans-activating transcriptor*, and it is a small peptide, which enables nanoparticles to pass the blood-brain barrier after conjugation [118].

A direct comparison between CDs and Q-dots in fluorescence imaging application in vivo has been provided by Cao et al. [119]. CDs prepared through oxidation
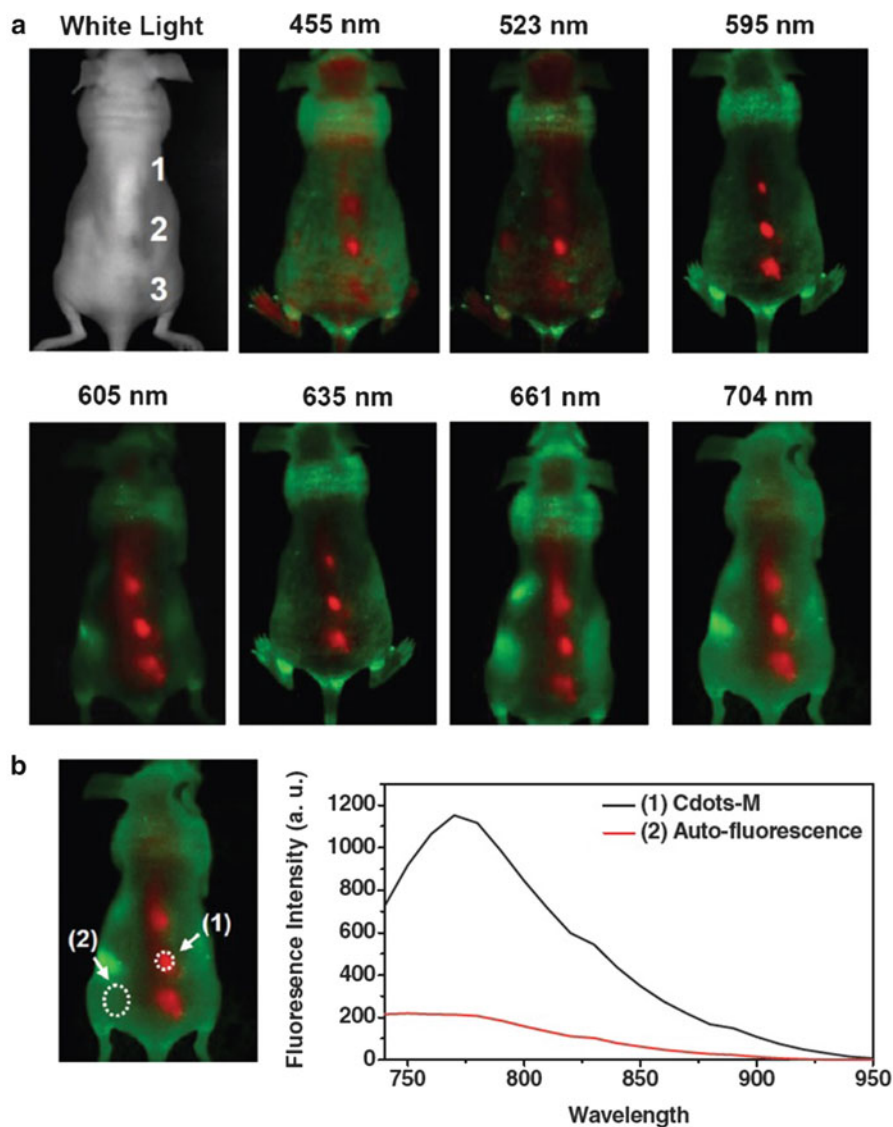
Fig. 22 (**a**) In vivo fluorescence images of a mouse after injection of CDs upon excitation at 455, 523, 595, 605, 635, 661, and 704 nm, respectively. *Red* and *green* are the fluorescence signals of CDs or the tissue autofluorescence, respectively. (**b**) Signal-to-background ratio of the spectral image taken upon NIR (704 nm) excitation. With permission from [93]

of raw carbon nanoparticles were passivated with PEG_{1500N}. For a fair comparison CdSe/ZnS Q-dots were also passivated by PEG. Both particle types were subcutaneously injected into mice. The aqueous suspensions had similar optical densities, and the subsequent fluorescence imaging was performed using band-pass filters

centered at 470 nm for excitation and 525 nm for emission. Both injection spots showed similar luminescence intensity. According to this comparison CDs may serve as an alternative to Q-dots for in vivo imaging. Their organic nature devoid of heavy metals makes them particularly attractive.

The results of the in vivo imaging studies using CDs clearly show their potential in this field. Injected CDs are easily detectable in the organisms under study. Concerning their luminescence properties in fluorescence imaging, they do not seem to be inferior to Q-dots. Moreover, CDs are water dispersible; they can be readily modified by surface conjugation chemistry and exhibit lower toxicity. Since CDs are excitable for luminescence by NIR sources, they are capable of providing information from deeper layers of the tissue with a good signal-to-background ratio. However, more work needs to be done to clarify the distribution of CDs in the organisms under study. It is very likely that there is no general rule about tissue distribution. The outcome will probably be dependent on the details of particle composition and synthesis. But there are good chances that the zoo of different CDs will contain a few species that bring together all physicochemical properties to serve as an in vivo contrast agent for a range of imaging applications.

5 Summary

In summary, chances that CDs will evolve into a routine and widely accepted tool for imaging biological specimens are promising and justified based on the existing literature. The preparation of the particles CDs is straightforward and performed under simplest experimental conditions. Low-cost and sustainable mass materials, for instance, carbohydrates, have been successfully used as precursor material. Processing of precursors and raw materials does not require any sophisticated and expensive instrumentation. The key step of CD preparation is a simple carbonization procedure. The resulting nanoparticles are highly stable, between 1 and 10 nm in diameter, and do not contain any heavy metals like Q-dots.

CDs feature astonishing optical properties like an extremely broad range of suitable excitation wavelengths from ultraviolet light (UV) to visible (VIS) and further on to the near infrared (NIR). In particular NIR excitation and upconverting photoluminescence (UCPL) are of predominant interest for in vivo imaging as both phenomena synergistically increase tissue penetration and decrease the tissue's autofluorescence. The emissive properties of CDs can be tuned and customized for a given application. Electrochemiluminescence (ECL), based on potential-dependent changes of the emissive sites on the particles' surfaces, paves the way for using CDs as reporters in redox assays and sensors.

The interaction of CDs with living cells has been intensively studied throughout the last years. It has been found that CDs are easily internalized into the cell interior. The exposure time required for CD uptake tends to be shorter than for other nanomaterials. The ease with which CDs enter the cell interior makes them interesting base materials for intracellular probes after surface functionalization.

Even though the uptake process has been attributed mechanistically to classical endocytosis, the full explanation seems to be more complex with other mechanisms involved. The existing cytotoxicity studies for carbon dots need to be handled with care and a good sense of proportion, as CDs are often prematurely described as *low-toxic* imaging reagents. As long as they are applied in reasonably low concentrations that are, however, sufficient for in vitro and in vivo imaging, the material is indeed harmless. But cell viability was shown to be affected for concentrations much higher than needed for bioassays. When CDs were tested for their suitability as contrast agent for in vivo imaging, they showed similar imaging characteristics compared to the well-established Q-dots with no significant evidence of toxicity. As the number of studies using CDs as tracers in living organisms is still low, their broad application in this respect awaits further characterization. Taken together, the long-range prognosis for CDs to become a standardized label and fluorescence marker in biomedical assays and similar applications are euphoric and optimistic.

References

1. Fortina P et al (2005) Nanobiotechnology: the promise and reality of new approaches to molecular recognition. Trends Biotechnol 23(4):168–173
2. Whitesides GM (2003) The 'right' size in nanobiotechnology. Nat Biotechnol 21 (10):1161–1165
3. Thurn KT et al (2007) Nanoparticles for applications in cellular imaging. Nanoscale Res Lett 2(9):430–441
4. Warnement MR, Tomlinson ID, Rosenthal SJ (2007) Fluorescent imaging applications of Quantum Dot probes. Curr Nanosci 3(4):273–284
5. Brus L (1991) Quantum crystallites and nonlinear optics. Appl Phys A Mater Sci Process 53 (6):465–474
6. Gao XH et al (2005) In vivo molecular and cellular imaging with quantum dots. Curr Opin Biotechnol 16(1):63–72
7. Gerion D et al (2001) Synthesis and properties of biocompatible water-soluble silica-coated CdSe/ZnS semiconductor quantum dots. J Phys Chem B 105(37):8861–8871
8. Medintz IL et al (2005) Quantum dot bioconjugates for imaging, labelling and sensing. Nat Mater 4(6):435–446
9. Derfus AM, Chan WCW, Bhatia SN (2004) Probing the cytotoxicity of semiconductor quantum dots. Nano Lett 4(1):11–18
10. Clarke SJ et al (2006) Photophysics of dopamine-modified quantum dots and effects on biological systems. Nat Mater 5(5):409–417
11. Kroto HW et al (1985) C-60–Buckminsterfullerene. Nature 318(6042):162–163
12. Greiner NR et al (1988) Diamonds in detonation soot. Nature 333(6172):440–442
13. Iijima S (1991) Helical microtubules of graphitic carbon. Nature 354(6348):56–58
14. De Jong KP, Geus JW (2000) Carbon nanofibers: catalytic synthesis and applications. Catal Rev Sci Eng 42(4):481–510
15. Novoselov KS et al (2004) Electric field effect in atomically thin carbon films. Science 306 (5696):666–669
16. Xu XY et al (2004) Electrophoretic analysis and purification of fluorescent single-walled carbon nanotube fragments. J Am Chem Soc 126(40):12736–12737
17. Baker SN, Baker GA (2010) Luminescent carbon nanodots: emergent nanolights. Angew Chem Int Ed 49(38):6726–6744

18. Tian L et al (2009) Nanosized carbon particles from natural gas soot. Chem Mater 21 (13):2803–2809
19. Dong Y et al (2013) Carbon-based dots co-doped with nitrogen and sulfur for high quantum yield and excitation-independent emission. Angew Chem Int Ed 52(30):7800–7804
20. da Silva JCGE, Goncalves HMR (2011) Analytical and bioanalytical applications of carbon dots. TrAC Trends Anal Chem 30(8):1327–1336
21. Li HT et al (2012) Carbon nanodots: synthesis, properties and applications. J Mater Chem 22 (46):24230–24253
22. Luo PJG et al (2013) Carbon "quantum" dots for optical bioimaging. J Mat Chem B 1 (16):2116–2127
23. Sun YP et al (2006) Quantum-sized carbon dots for bright and colorful photoluminescence. J Am Chem Soc 128(24):7756–7757
24. Liu HP, Ye T, Mao CD (2007) Fluorescent carbon nanoparticles derived from candle soot. Angew Chem Int Ed 46(34):6473–6475
25. Li XY et al (2011) Preparation of carbon quantum dots with tunable photoluminescence by rapid laser passivation in ordinary organic solvents. Chem Commun 47(3):932–934
26. Zheng LY et al (2009) Electrochemiluminescence of water-soluble carbon nanocrystals released electrochemically from graphite. J Am Chem Soc 131(13):4564–4565
27. Long YM et al (2012) Shifting and non-shifting fluorescence emitted by carbon nanodots. J Mater Chem 22(13):5917–5920
28. Lu J et al (2009) One-pot synthesis of fluorescent carbon nanoribbons, nanoparticles, and graphene by the exfoliation of graphite in ionic liquids. ACS Nano 3(8):2367–2375
29. Bao L et al (2011) Electrochemical tuning of luminescent carbon nanodots: from preparation to luminescence mechanism. Adv Mater 23(48):5801–5806
30. Bourlinos AB et al (2008) Surface functionalized carbogenic quantum dots. Small 4 (4):455–458
31. Bourlinos AB et al (2012) Luminescent surface quaternized carbon dots. Chem Mater 24 (1):6–8
32. Pan DY et al (2010) Observation of pH-, solvent-, spin-, and excitation-dependent blue photoluminescence from carbon nanoparticles. Chem Commun 46(21):3681–3683
33. Zhou L et al (2012) Carbon nanodots as fluorescence probes for rapid, sensitive, and label-free detection of Hg^{2+} and biothiols in complex matrices. Chem Commun 48(8):1147–1149
34. Deng YH et al (2013) Long lifetime pure organic phosphorescence based on water soluble carbon dots. Chem Commun 49(51):5751–5753
35. Li HT et al (2011) One-step ultrasonic synthesis of water-soluble carbon nanoparticles with excellent photoluminescent properties. Carbon 49(2):605–609
36. Wang XH et al (2011) Microwave assisted one-step green synthesis of cell-permeable multicolor photoluminescent carbon dots without surface passivation reagents. J Mater Chem 21(8):2445–2450
37. He XD et al (2011) Water soluble carbon nanoparticles: hydrothermal synthesis and excellent photoluminescence properties. Colloids Surf B Biointerfaces 87(2):326–332
38. Yang ZC et al (2011) Intrinsically fluorescent carbon dots with tunable emission derived from hydrothermal treatment of glucose in the presence of monopotassium phosphate. Chem Commun 47(42):11615–11617
39. Peng H, Travas-Sejdic J (2009) Simple aqueous solution route to luminescent carbogenic dots from carbohydrates. Chem Mater 21(23):5563–5565
40. Ma Z et al (2012) One-step ultrasonic synthesis of fluorescent N-doped carbon dots from glucose and their visible-light sensitive photocatalytic ability. New J Chem 36(4):861–864
41. Liu CJ et al (2011) One-step synthesis of surface passivated carbon nanodots by microwave assisted pyrolysis for enhanced multicolor photoluminescence and bioimaging. J Mater Chem 21(35):13163–13167
42. Liu CJ et al (2012) Nano-carrier for gene delivery and bioimaging based on carbon dots with PEI-passivation enhanced fluorescence. Biomaterials 33(13):3604–3613

43. Liu JM et al (2012) Highly selective and sensitive detection of Cu^{2+} with lysine enhancing bovine serum albumin modified-carbon dots fluorescent probe. Analyst 137(11):2637–2642
44. Lin Z et al (2012) Classical oxidant induced chemiluminescence of fluorescent carbon dots. Chem Commun 48(7):1051–1053
45. Salinas-Castillo A et al (2013) Carbon dots for copper detection with down and upconversion fluorescent properties as excitation sources. Chem Commun 49(11):1103–1105
46. Puvvada N et al (2012) Synthesis of biocompatible multicolor luminescent carbon dots for bioimaging applications. Sci Tech Adv Mat 13(4)
47. Mitra S et al (2012) Rapid microwave synthesis of fluorescent hydrophobic carbon dots. RSC Adv 2(32):12129–12131
48. Qu SN et al (2012) A biocompatible fluorescent ink based on water-soluble luminescent carbon nanodots. Angew Chem Int Ed 51(49):12215–12218
49. Du FK et al (2013) Carbon dots-based fluorescent probes for sensitive and selective detection of iodide. Microchimica Acta 180(5–6):453–460
50. Jiang J et al (2012) Amino acids as the source for producing carbon nanodots: microwave assisted one-step synthesis, intrinsic photoluminescence property and intense chemiluminescence enhancement. Chem Commun 48(77):9634–9636
51. Wang Q et al (2012) Microwave-assisted synthesis of carbon nanodots through an eggshell membrane and their fluorescent application. Analyst 137(22):5392–5397
52. Yang YH et al (2012) One-step synthesis of amino-functionalized fluorescent carbon nanoparticles by hydrothermal carbonization of chitosan. Chem Commun 48(3):380–382
53. Zhu SJ et al (2013) Highly photoluminescent carbon dots for multicolor patterning, sensors, and bioimaging. Angew Chem Int Ed 52(14):3953–3957
54. Hsu PC, Chang HT (2012) Synthesis of high-quality carbon nanodots from hydrophilic compounds: role of functional groups. Chem Commun 48(33):3984–3986
55. Qu KG et al (2013) Carbon dots prepared by hydrothermal treatment of dopamine as an effective fluorescent sensing platform for the label-free detection of Iron(III) ions and dopamine. Chem Euro J 19(22):7243–7249
56. Zhang YQ et al (2012) One-pot synthesis of N-doped carbon dots with tunable luminescence properties. J Mater Chem 22(33):16714–16718
57. Zhou JJ et al (2012) Facile synthesis of fluorescent carbon dots using watermelon peel as a carbon source. Mater Lett 66(1):222–224
58. Sahu S et al (2012) Simple one-step synthesis of highly luminescent carbon dots from orange juice: application as excellent bio-imaging agents. Chem Commun 48(70):8835–8837
59. Lu WB et al (2012) Economical, green synthesis of fluorescent carbon nanoparticles and their use as probes for sensitive and selective detection of Mercury(II) ions. Anal Chem 84(12):5351–5357
60. Hsu PC et al (2012) Synthesis and analytical applications of photoluminescent carbon nanodots. Green Chem 14(4):917–920
61. Liu S et al (2012) Hydrothermal treatment of grass: a low-cost, green route to nitrogen-doped, carbon-rich, photoluminescent polymer nano-dots as an effective fluorescent sensing platform for label-free detection of Cu(II) ions. Adv Mater 24(15):2037–2041
62. Qiao ZA et al (2010) Commercially activated carbon as the source for producing multicolor photoluminescent carbon dots by chemical oxidation. Chem Commun 46(46):8812–8814
63. Li HT et al (2010) Water-soluble fluorescent carbon quantum dots and photocatalyst design. Angew Chem Int Ed 49(26):4430–4434
64. Bourlinos AB et al (2008) Photoluminescent carbogenic dots. Chem Mater 20(14):4539–4541
65. Zhao QL et al (2008) Facile preparation of low cytotoxicity fluorescent carbon nanocrystals by electrooxidation of graphite. Chem Commun 41:5116–5118
66. Liu RL et al (2009) An aqueous route to multicolor photoluminescent carbon dots using silica spheres as carriers. Angew Chem Int Ed 48(25):4598–4601

67. Wilson WL, Szajowski PF, Brus LE (1993) Quantum confinement in size-selected, surface-oxidized silicon nanocrystals. Science 262(5137):1242–1244
68. Alivisatos AP (1996) Semiconductor clusters, nanocrystals, and quantum dots. Science 271 (5251):933–937
69. Fischer SA, Isborn CM, Prezhdo OV (2011) Excited states and optical absorption of small semiconducting clusters: Dopants, defects and charging. Chem Sci 2(3):400–406
70. Robertson J (1996) Recombination and photoluminescence mechanism in hydrogenated amorphous carbon. Phys Rev B 53(24):16302–16305
71. Yu P et al (2012) Temperature-dependent fluorescence in carbon dots. J Phys Chem C 116 (48):25552–25557
72. Ding C, Zhu A, Tian Y (2014) Functional surface engineering of C-dots for fluorescent biosensing and in vivo bioimaging. Acc Chem Res 47(1):20–30
73. Zheng HZ et al (2011) Enhancing the luminescence of carbon dots with a reduction pathway. Chem Commun 47(38):10650–10652
74. Pan DY et al (2010) Hydrothermal route for cutting graphene sheets into blue-luminescent graphene quantum dots. Adv Mater 22(6):734–738
75. Shen R et al (2012) Dramatic fluorescence enhancement of bare carbon dots through facile reduction chemistry. ChemPhysChem 13(15):3549–3555
76. Zhu BC et al (2013) Preparation of carbon nanodots from single chain polymeric nanoparticles and theoretical investigation of the photoluminescence mechanism. J Mat Chem C 1(3):580–586
77. Bae Y, Myung N, Bard AJ (2004) Electrochemistry and electrogenerated chemiluminescence of CdTe nanoparticles. Nano Lett 4(6):1153–1161
78. Ding ZF et al (2002) Electrochemistry and electrogenerated chemiluminescence from silicon nanocrystal quantum dots. Science 296(5571):1293–1297
79. Zhu H et al (2009) Microwave synthesis of fluorescent carbon nanoparticles with electrochemiluminescence properties. Chem Commun 34:5118–5120
80. Myung N, Ding ZF, Bard AJ (2002) Electrogenerated chemiluminescence of CdSe nanocrystals. Nano Lett 2(11):1315–1319
81. Kim HM, Cho BR (2009) Two-photon probes for intracellular free metal ions, acidic vesicles, and lipid rafts in live tissues. Acc Chem Res 42(7):863–872
82. Cao L et al (2007) Carbon dots for multiphoton bioimaging. J Am Chem Soc 129 (37):11318–11319
83. Chen W, Joly AG, McCready DE (2005) Upconversion luminescence from CdSe nanoparticles. J Chem Phys 122(22):224708
84. Jaiswal JK et al (2004) Use of quantum dots for live cell imaging. Nat Methods 1(1):73–78
85. Cho SJ et al (2007) Long-term exposure to CdTe quantum dots causes functional impairments in live cells. Langmuir 23(4):1974–1980
86. Mosmann T (1983) Rapid colorimetric assay for cellular growth and survival: application to proliferation and cytotoxicity assays. J Immunol Methods 65(1–2):55–63
87. Hardman R (2006) A toxicological review of quantum dots: toxicity depends on physico-chemical and environmental factors. Environ Health Perspect 114(2):165–172
88. Rosenthal SJ et al (2011) Biocompatible quantum dots for biological applications. Chem Biol 18(1):10–24
89. Yang ST et al (2009) Carbon dots as nontoxic and high-performance fluorescence imaging agents. J Phys Chem C 113(42):18110–18114
90. Zhang LW et al (2008) Biological interactions of quantum dot nanoparticles in skin and in human epidermal keratinocytes. Toxicol Appl Pharmacol 228(2):200–211
91. Stern ST et al (2008) Induction of autophagy in porcine kidney cells by quantum dots: a common cellular response to nanomaterials? Toxicol Sci 106(1):140–152
92. Wang K et al (2013) Systematic safety evaluation on photoluminescent carbon dots. Nanoscale Res Lett 8:122–130

93. Tao HQ et al (2012) In vivo NIR fluorescence imaging, biodistribution, and toxicology of photoluminescent carbon dots produced from carbon nanotubes and graphite. Small 8 (2):281–290
94. Lutty GA (1978) Acute intravenous toxicity of biological stains, dyes, and other fluorescent substances. Toxicol Appl Pharmacol 44(2):225–249
95. Ray SC et al (2009) Fluorescent carbon nanoparticles: synthesis, characterization, and bioimaging application. J Phys Chem C 113(43):18546–18551
96. Zhu SJ et al (2011) Strongly green-photoluminescent graphene quantum dots for bioimaging applications. Chem Commun 47(24):6858–6860
97. Verma AO et al (2008) Surface-structure-regulated cell-membrane penetration by monolayer-protected nanoparticles. Nat Mater 7(7):588–595
98. Schmid SL, Carter LL (1990) ATP is required for receptor-mediated endocytosis in intact cells. J Cell Biol 111(6):2307–2318
99. Anderson RGW (1998) The caveolae membrane system. Annu Rev Biochem 67:199–225
100. Li N et al (2012) Biodistribution study of carbogenic dots in cells and in vivo for optical imaging. J Nano Res 14(10):1177–1185
101. Geiser M et al (2005) Ultrafine particles cross cellular membranes by nonphagocytic mechanisms in lungs and in cultured cells. Environ Health Perspect 113(11):1555–1560
102. Lajoie P, Nabi IR (2007) Regulation of raft-dependent endocytosis. J Cell Mol Med 11 (4):644–653
103. Fang YX et al (2012) Easy synthesis and imaging applications of cross-linked green fluorescent hollow carbon nanoparticles. ACS Nano 6(1):400–409
104. Xu Y et al (2013) Nitrogen-doped carbon dots: a facile and general preparation method, photoluminescence investigation, and imaging applications. Chem Euro J 19(7):2276–2283
105. Li Q et al (2010) Photoluminescent carbon dots as biocompatible nanoprobes for targeting cancer cells in vitro. J Phys Chem C 114(28):12062–12068
106. Qian ZM et al (2002) Targeted drug delivery via the transferrin receptor-mediated endocytosis pathway. Pharmacol Rev 54(4):561–587
107. Song YC et al (2012) Fluorescent carbon nanodots conjugated with folic acid for distinguishing folate-receptor-positive cancer cells from normal cells. J Mater Chem 22 (25):12568–12573
108. Shi W, Li XH, Ma HM (2012) A tunable ratiometric pH sensor based on carbon nanodots for the quantitative measurement of the intracellular pH of whole cells. Angew Chem Int Ed 51 (26):6432–6435
109. Tafani M et al (2002) Regulation of intracellular pH mediates bax activation in HeLa cells treated with staurosporine or tumor necrosis factor-alpha. J Biol Chem 277(51):49569–49576
110. Zhu AW et al (2012) Carbon-dot-based dual-emission nanohybrid produces a ratiometric fluorescent sensor for in vivo imaging of cellular copper ions. Angew Chem Int Ed 51 (29):7185–7189
111. Yu CM et al (2013) Carbon-dot-based ratiometric fluorescent sensor for detecting hydrogen sulfide in aqueous media and inside live cells. Chem Commun 49(4):403–405
112. Lai CW et al (2012) Facile synthesis of highly emissive carbon dots from pyrolysis of glycerol; gram scale production of carbon dots/$mSiO_2$ for cell imaging and drug release. J Mater Chem 22(29):14403–14409
113. Yang ST et al (2009) Carbon dots for optical imaging in vivo. J Am Chem Soc 131 (32):11308–11309
114. Choi HS et al (2007) Renal clearance of quantum dots. Nat Biotechnol 25(10):1165–1170
115. Li SD, Huang L (2008) Pharmacokinetics and biodistribution of nanoparticles. Mol Pharm 5 (4):496–504
116. Helmchen F, Denk W (2005) Deep tissue two-photon microscopy. Nat Methods 2 (12):932–940

117. Santra S et al (2005) Rapid and effective labeling of brain tissue using TAT-conjugated CdS:
     Mn/ZnS quantum dots. Chem Commun 25:3144–3146
118. Rao KS et al (2008) TAT-conjugated nanoparticles for the CNS delivery of anti-HIV drugs.
     Biomaterials 29(33):4429–4438
119. Cao L et al (2012) Competitive performance of carbon "quantum" dots in optical bioimaging.
     Theranostics 2(3):295–301

Nanoparticles in Biomedical Applications

Jacqueline Maximilien, Selim Beyazit, Claire Rossi, Karsten Haupt, and Bernadette Tse Sum Bui

Abstract Due to readily adaptive sizes, shapes, compositions and large surface area to volume ratios, nanoparticles (NPs) are increasingly prevalent in biomedical applications. In recent times, a plethora of NPs have been investigated specifically regarding how they can be exploited for drug delivery, bioimaging agents and theranostic tools. In this article, lipid-based, inorganic, dendrimeric and polymeric nanoparticles serving these applications are described. The ease of synthesis of these NPs, coupled with an enhanced stability, reduced toxicity and ability to conjugate with diverse molecules (peptides, proteins, antibodies, aptamers) for biocompatibility and biotargeting, indicates that all the key components are being met for their advances towards approved therapies. For their successful applications as drug delivery systems, smart polymeric NPs responding to stimuli such as heat, pH and light to provide controlled release have been introduced. Upconverting nanoparticles and molecularly imprinted polymers, often termed plastic antibodies because of their high affinity and selectivity towards their target molecules, are further discussed as novel bioimaging materials.

Keywords Drug delivery • Molecularly imprinted polymers • Nanoparticles • Theranostics • Smart materials

Contents

J. Maximilien, S. Beyazit, C. Rossi, K. Haupt (✉), and B. Tse Sum Bui (✉)
Sorbonne Universités, Université de Technologie de Compiègne, CNRS Laboratory for Enzyme and Cell Engineering, CS60319, 60203 Compiègne Cedex, France
e-mail: karsten.haupt@utc.fr; jeanne.tse-sum-bui@utc.fr

1   Introduction

Nanotechnology is a rapidly developing field which incorporates the use of materials with submicron dimensions, usually between 1 and 100 nm in size although some schools of thought accept particles that have dimensions less than 1,000 nm. This confers them a high surface area to mass ratio, which make them valuable tools in biology and medicine when combined with well-engineered surface characteristics and functionalities. The amalgamation of polymer science and pharmaceutical sciences has therefore focused on the design and development of novel drug delivery and theranostic systems based on such materials.

As pertains to nanotechnology in the food and pharmaceutical industries, it is interesting to note that there is no 'official' Food and Drug Administration (FDA: US regulatory body) definition of a nanoparticle. Nevertheless, nanoparticles of various sources have been and are currently being used in a number of biomedical applications (Fig. 1). Their advantages include the ability to target specific organs and/or cells, when conjugated to biologically relevant ligands. Moreover, they can improve the pharmacokinetic profile of the encapsulated drug by protecting the drug from degradation and/or early release. This increases the concentration of the drug at the site of action. A lower toxicity profile is also anticipated as there should be minimal systemic exposure of the drug.

Ideally, nanoparticles for use in biomedical applications should possess reduced cytotoxicity profiles, long-term physical stabilities and high loading capacities. The efficacy of nanomaterials is often linked to their ability to penetrate the plasma membrane and be internalised in cells following administration using the parenteral, oral, ocular, mucosal or dermal delivery routes. However, due to the complex and heterogeneous nature of functional nanoparticles, it is difficult to predict behaviours in vitro. Nevertheless, overwhelming opportunities for precise particle engineering and the renewed drive towards personalised medicines is currently steering nanoparticles to the forefront of biomedical and biotechnological research. In this article, a number of nanoscale materials and their applications in the biomedical field, more particularly as drug delivery, bioimaging and theranostic tools, will be reviewed.
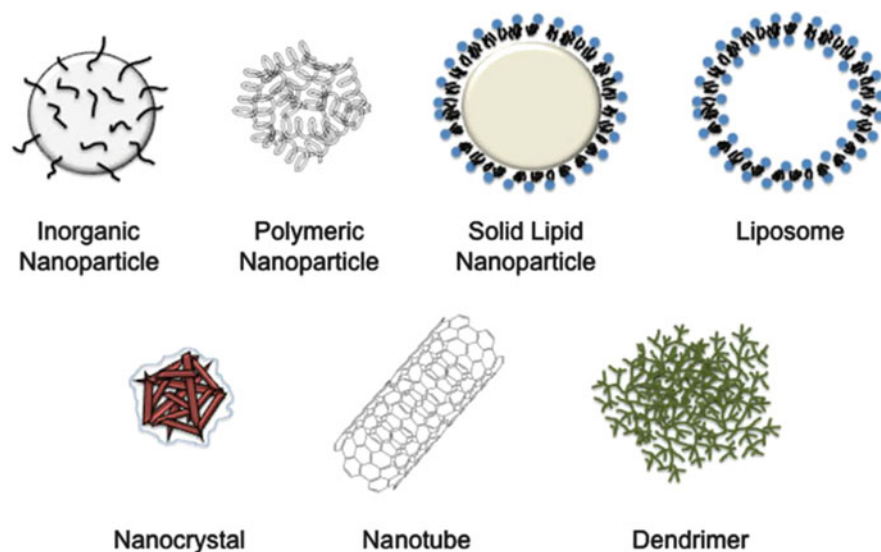
Fig. 1 Various types of nanomaterials used for biomedical and drug delivery applications (Reproduced with permission from [1])

2 Lipid-Based Nanoparticles

The first nanoparticles used for drug delivery were lipid-based nanoparticles; two well-explored examples are discussed here.

2.1 Solid Lipid Nanoparticles and Nanostructured Lipid Carriers

Solid lipid nanoparticles (SLNs) are lipophilic colloidal nanoparticles made from *solid* lipids (i.e. their phase transition temperature is higher than 37°C). They are commonly used as drug delivery systems with the first patents being published in 1993 and 1996 [2, 3]. Second-generation SLNs known as nanostructured lipid carriers (NLCs) are fabricated with a blend of *solid* and *liquid* lipids, this blend staying solid at room and body temperature. The formation of a crystalline structure with more imperfections resulted in higher drug loading (Fig. 2a) [4, 5].

The production process is identical for SLNs and NLCs; they are prepared mainly by high-pressure homogenisation or microemulsion technology. The high-pressure homogenisation method is analogous to the oil/water emulsion methods used for parenteral administration. Two basic production methods are used: hot homogenisation and cold homogenisation. In both instances, the drug is dissolved or solubilised in the lipid which is heated to 5–10°C above its melting temperature.
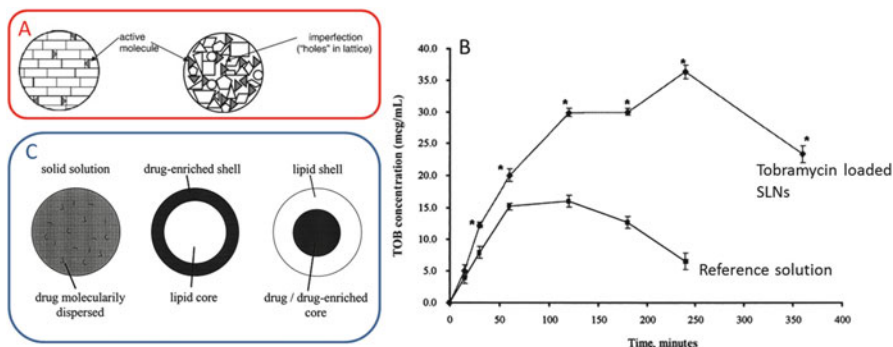
Fig. 2 (**a**) Graphical representation of crystallisation of lipids in SLNs (*left*) and NLCs (right) [4]. (**b**) Concentration profiles of the drug tobramycin when administered as eye drops in form of tobramycin-loaded SLNs (*filled diamonds*) compared to a reference solution (*filled squares*) [6]. (**c**) Three drug incorporation methods which depend on the saturation solubility of incorporated drugs at the recrystallisation temperature of the lipid [7]. Adapted from [4, 6, 7]

Using the hot homogenisation technique, the drug is dissolved directly in the melted lipid before it is added to a hot aqueous surfactant solution. The pre-emulsion is then homogenised under high pressure. The resulting oil in water emulsion is cooled to room temperature and the lipid recrystallises to yield solid lipid nanoparticles. For the cold homogenisation method, the drug containing lipid melt is mechanically ground to produce microparticles which are then suspended in a cold surfactant solution and finally homogenised at or below room temperature. This method is more suitable for temperature labile drugs.

SLNs have been used to deliver hydrophilic, hydrophobic, small molecules and biomacromolecules. SLNs loaded with the antibiotic tobramycin used to treat bacterial infections (2.5% drug loading with respect to lipid weight) were assessed as an ocular delivery system and proved to provide higher bioavailability than reference eye drops (Fig. 2b) [6]. Almeida et al. demonstrated SLNs' suitability for peptide delivery and further reported that the lipid matrix improved their stability, avoided proteolytic degradation and facilitated controlled release [8]. Since then, further reports have confirmed the incorporation of biomacromolecules in SLNs [9, 10]. Immediate or controlled release of drugs can be tailored by the lipid matrix, surfactant concentration, homogenisation parameters and final particle size [11].

SLNs are widely used in drug delivery because they have adopted GRAS (generally regarded as safe) status. Thus, their large-scale production can be facilitated by manufacturing units currently available for parenteral drugs. Indeed, a very comprehensive review by the Müller group focused entirely on the use of solid lipid nanoparticles for parenteral drug delivery [12]. Their disadvantages include the potential partitioning of hydrophilic drugs in the aqueous phase during the preparation process, therefore leading to poor drug loading and/or the expulsion of drugs from the matrix following polymorphic transition during storage (Fig. 2c).

2.2   Liposomes

Liposomes are artificial vesicles composed of phospholipids. The word vesicle is derived from the Latin *vesicula* which means small bladder. Small unilamellar vesicles (SUVs, 30–50 nm), large unilamellar vesicles (LUVs, 100–200 nm) and giant unilamellar vesicles (GVs, 5–50 μm) [13] have been studied extensively as carriers of both small molecules [14, 15] and biologically relevant macromolecules [14, 15]. Liposomal delivery of pharmaceutically relevant compounds has also been the subject of numerous patents [16, 17] and it has experienced exponential growth in recent times.

Following their initial report discussing the diffusion of univalent ions across phospholipid bilayers [18], Bangham et al. further presented the preparation and use of liposomes as membrane models in 1974 [19]. The amphiphilic nature of phospholipids allows them to self-aggregate in aqueous solutions and form spherical structures. Liposomes are described as unilamellar or multilamellar, depending on the number of phospholipid bilayers present, and they can incorporate hydrophilic compounds in their aqueous compartment(s) and hydrophobic compounds in their lipid bilayer(s).

Liposomes are produced mainly by sonication, extrusion and reverse-phase evaporation. The original liposome preparations by Bangham et al. [19] were the basis for the development of sonication methods used for unilamellar vesicle preparation. Here, the lipid(s) being used are dissolved in an organic solvent and then dried to a thin film under an inert atmosphere. The thin film is then rehydrated with the aqueous phase and ultimately probe- or bath-sonicated to yield unilamellar vesicles. The sonication method can yield vesicles with sizes smaller than 50 nm. However, such small vesicles are dramatically limited in terms of the encapsulation capacity of aqueous space per mole lipid, which is often in the range of 0.1–1% [20]. The extrusion of lipid suspensions through polycarbonate membranes was reported to yield liposomes with a well-defined size and distribution [21]. Typically, the process follows that of the previously explained sonication method up to the rehydration step. The rehydrated lipids are then extruded through polycarbonate membranes in order of decreasing pore size so that unilamellar vesicles can be obtained between 50 and 5,000 nm. Liposomes can also be produced by reverse-phase evaporation where the phospholipids are dissolved in an organic solvent; an aqueous buffer is then added to the phospholipid containing solvent and the solvent is subsequently evaporated under reduced pressure [22, 23]. This method was offered as a means to obtain larger aqueous lumens for higher aqueous loading capacity.

The physicochemical properties of liposomes are regularly exploited for drug delivery. Liposomes have been used to encapsulate small molecules [25–28] and macromolecules [29–31]. Composed of phospholipid building blocks, they are biodegradable and easily modifiable to render them more biocompatible or facilitate specific cell targeting. Liposomal charge can be easily tuned by changing the lipid(s) or lipid ratios, and pH-sensitive release [32, 33] can be achieved by the
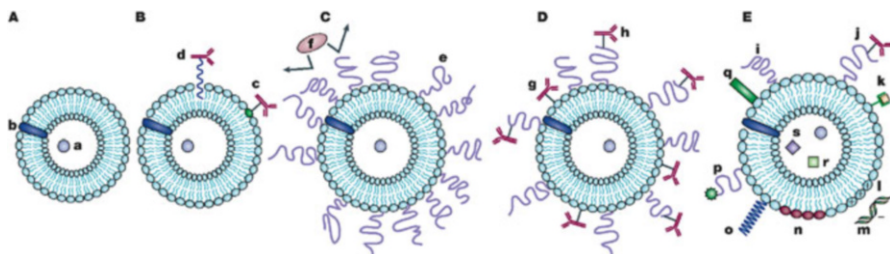
Fig. 3 Evolution of liposomes from simple lipid-based structures (**a**) to more complex vesicles which (**b**, **d**, **e**) incorporate antibodies for targeting of specific cells, (**c**, **d**, **e**) are decorated by PEG to improve biocompatibility or (**e**) are designed with an increased lumen size for higher cargo capacity (**e**) (Reproduced with permission from [24])

incorporation of pH-sensitive components in the lipid bilayer. There have also been reports of temperature- [28, 34] and photo-sensitive [35] liposomes. Long circulating liposomes (Fig. 3c) are usually surface-modified with natural or biocompatible polymers, such as poly(ethylene glycol) [36, 37] to shield them from opsonin interactions, hence prolonging the circulating time and increasing the possibility that they will deliver their cargo before being trafficked out of the circulatory system or degraded. Additionally, liposomes can be functionalised with surface-attached ligands such as oligonucleotides [38], biotin, aptamers [39], lectins [40] and antibodies [41] for biorecognition and binding to cells of interest.

The first FDA-approved nanodrug was Doxil® in 1995 [42], a PEGylated liposome formulation which contained doxorubicin·HCl mostly in the aqueous core, for the treatment of solid tumours. Doxorubicin is an anticancer drug which retards or prohibits the growth of solid tumours by intercalating into the DNA. It is, however, extremely cardiotoxic. The use of PEGylated liposomes, 80–90 nm in diameter, was proven to prolong drug circulation time while concurrently avoiding clearance by the reticuloendothelial system and reducing the cardiotoxicity of the free drug. Two factors were recognised to positively influence Doxil as an efficient drug delivery system: (1) high and stable remote loading of doxorubicin and (2) the physical state of the lipids used in the liposome. The lipid composition (egg phosphocholine/cholesterol/methyl poly(ethyleneglycol)–distearoylphosphatidyl ethanolamine) ensured the liposome to be in the 'liquid-ordered' phase. Doxil® passively targeted tumours using the enhanced permeation effect.

Interestingly, it took almost three years after the expiration of Doxil-related patents (March 2010) for the first generic form of Doxil to get FDA approval. There are a number of reasons for this. Foremost, it is the challenge of understanding each nanoparticle-drug system to the extent where critical physicochemical characteristics can be identified and exploited to achieve the desired in vivo effect. Secondly, there is the need to establish adequately specific analytical techniques to characterise in vitro and in vivo properties and thirdly the cost associated with bringing liposomal formulations to market. Another important consideration is the increasing use of multifunctional and multicomponent liposomes. The complexities of

(1) site-specific targeting, (2) inclusion of biomarker and imaging capabilities, (3) tailored delivery against the backdrop of increased importance of combinatorial therapies, mean that the development and manufacturing of liposomal formulations are becoming more and more complex. Increased complexity relates to increased developmental costs and higher regulatory standards regarding quality control and even extended timelines due to the intellectual property limitations.

The FDA's latest approved liposome formulation was Marqibo® in 2012, a sphingosomal/cholesterol (58:42 mol/mol) encapsulation of vincristine sulphate for the treatment of Philadelphia chromosome-negative (Ph-) acute lymphoblastic leukaemia. The therapy is available to heavily pretreated patients and consists of a once-a-week injection of liposomes (~115 nm) by a healthcare professional.

Parenteral administration, and in particular intravenous administration, is the preferred route of administration for liposomal formulations, although ocular and transdermal routes have also been exploited. Oral delivery is generally not considered due to gastrointestinal degradation of the carrier and poor bioavailability of associated drugs. This consequently limits the therapeutic areas where liposomal formulations will be considered as most patients are not amenable to self-injections.

Yet, considering that liposomes have been scientifically explored for more than four decades, there are only a limited number of liposomal drugs approved for clinical use or in clinical trials [24]. The restrictions regarding liposomal delivery include their miniscule encapsulation space, short half-life, leakage, fusion of encapsulated drug molecules and high production costs. This highlights the fact that gains in liposomal formulations relate more to reduced toxicity than improved efficacy. An excellent example is the previously discussed doxorubicin, where liposomal encapsulation of the drug results in a significant reduction in the irreversible cardiotoxicity of free doxorubicin. Moreover, the encapsulation of nucleic acids requires the use of cationic lipids for efficient association of the cargo with liposomes. However, the toxic effects of cationic liposomes rapidly became apparent, and due to the large size of the DNA–lipid complexes and its high surface charge, they get rapidly cleared from the circulatory system [43].

3 Inorganic Nanoparticles

3.1 Iron Oxide

Inorganic colloidal nanoparticles have been extensively used in imaging systems because they possess size-dependent electronic, optical and magnetic properties. As an example, superparamagnetic iron oxide nanoparticles (SPIONs) attracted attention due to their high potential in a number of biomedical applications, namely, tissue repair, drug delivery, magnetic resonance imaging, hyperthermia and cell labelling [44]. As far as their preparation is concerned, the co-precipitation of Fe^{2+}

and Fe^{3+} ions from aqueous salt solutions in the presence of a base allows for better control over size, composition and shape as compared to physical methods such as gas phase deposition and electron beam lithography [45]. Magnetite nanoparticles obtained by different synthetic protocols may exhibit very different magnetic properties. One of the major practical disadvantages of such nanoparticles is that anisotropic dipolar attraction causes them to aggregate to large clusters unless large quantities of surfactant are added to stabilise them in suspension. However, it is obvious that high concentrations of surfactant are not compatible with applications in life sciences or in the presence of living cells. Additionally, it has been shown that the reactivity of iron oxide particles increases significantly when their geometrical dimensions are reduced. On the other hand, smaller particles undergo more rapid biodegradation in biological environments than bigger ones. Hence, various strategies have been developed for the fabrication of iron oxide nanoparticles and their surface modification with various inert materials that improve biocompatibility and interactive functions at the particle surface. Coating materials include synthetic polymers, natural polymers and silica. Natural polymers such as dextran, poly (D,L-lactide) [46] and chitosan [47] are known to stabilise ferrous colloidal solutions and improve bioavailability by enhancing blood circulation time. Dextran-coated iron oxide nanoparticles have been used as magnetic resonance imaging (MRI) contrast agents for many years [48]. Two SPION agents are clinically approved: ferumoxides (marketed as Endorem in Europe and Feridex in the USA ever since it has been approved in 1995) and ferucarbotran (marketed as Resovist) for MRI of the liver. Endorem® is composed of superparamagnetic iron oxide nanoparticles coated with dextran or carboxydextran. The final size of the particles is between 120 and 180 nm. They are administered as a slow infusion of 11.2 mg of Fe/mL which renders these formulations only suitable for delayed-phase imaging. Resovist® has a particle size of about 60 nm and can be administered as a rapid bolus so that it is used for both dynamic and delayed imaging. In the liver, these particles are sequestered by phagocytic Kupffer cells as part of the normal reticuloendothelial system, but they are not retained in lesions lacking Kupffer cells.

The development of a facile means of functionalising dextran-stabilised iron oxide nanoparticles [49] paved the way to covalently bind various biomolecules such as antibodies, proteins, peptides, polysaccharides and aptamers to the particle surface meant to enhance cell targeting.

Theranostic applications of SPIONs coated with mesoporous silica layers [50, 51] are also receiving widespread attention. Surface silanol groups that can easily react with alcohols and silane coupling agents [52] stabilise the dispersions in nonaqueous solutions and provide the possibility to covalently attach ligands of interest. Mesoporous silica possesses large pores which can be exploited to physically trap drugs, as investigated by Vallet-Regi et al. [53]. These authors demonstrated that mesoporous silica of type MCM-41 was loaded with up to 30% (w/w) Ibuprofen [53]. Lu et al. [54] further described a sol–gel approach for the coating of SPIONs with uniform shells of amorphous silica. Here, fluorescent dyes were incorporated in the shell by covalent coupling with the sol–gel precursor. The shell thickness was controlled by varying the concentration of the sol–gel solution.
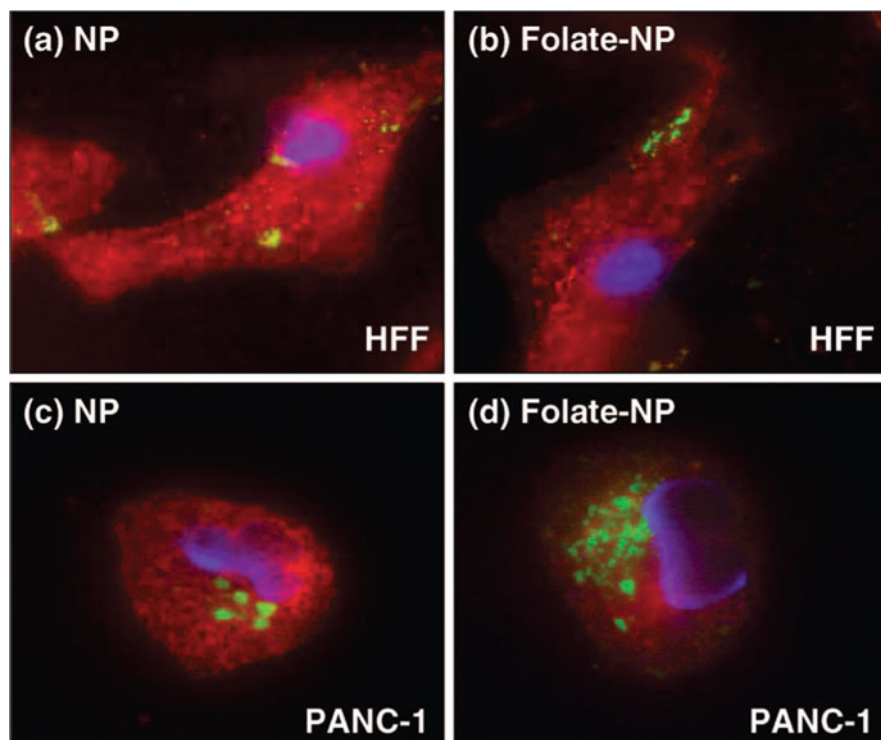
Fig. 4 Internalisation of folic acid-modified NPs (*green fluorescence*). Cell nuclei were stained by DAPI (*blue*) and cell membranes were stained with wheat germ agglutinin (*red*). *Top images*: human foreskin fibroblasts (HFF) treated with NPs (*left*) and folate-modified NPs (*right*). *Bottom images*: human pancreatic cancer cells (PANC-1) treated with NPs (*left*) and folate-modified NPs (*right*). The figure has been reproduced with permission from [55]

In a very interesting report, drug delivery, magnetic resonance and fluorescence imaging, magnetic manipulation and cell targeting were all simultaneously achieved using mesoporous silica nanoparticles [55]. Briefly, mesoporous silica spheres were synthesised around iron oxide nanocrystals using a condensation method. Fluorescein isothiocyanate was incorporated into the pore walls and the particle surface to minimise any increase in particle size due to the loading process. Drug cargo was loaded by soaking the particles in a concentrated drug–dimethyl-sulphoxide solution followed by a purifying centrifugation before the particles were resuspended in aqueous solution. Moreover, folic acid was immobilised on the particle surface to target cancer cells which overexpress the α-folate receptor. Finally, confocal scanning laser microscopy was used to visualise the internalisation of these particles into human pancreatic cancer cells.

The images on the left of Fig. 4 show internalisation of iron oxide nanocrystals (green fluorescence) coated with mesoporous silica by both human foreskin fibroblasts (HFF) and human pancreatic cancer cells (PANC-1). Functionalisation of

nanoparticles with folic acid resulted in enhanced accumulation in PANC-1 cells which overexpress α-folate receptor. This finding confirms a molecularly specific delivery of the multifunctional particles to their target cells.

An example for a clinical application of these materials is Rienso® (ferumoxytol), available in Europe for the treatment of iron deficiency-based anaemia in adult patients with chronic kidney disease. Rienso® is made from carbohydrate-coated superparamagnetic iron oxide nanoparticles [56]. Available as a preparation for intravenous injection, the total dose of 1,020 mg is administered over about 10 days. Ferumoxytol also shows potential as a theranostic tool as there is currently a clinical trial recruitment process to examine whether administration of ferumoxytol at the time of magnetic resonance imaging can aid in cancer detection [57]. Long-term clinical trials will unravel potential long-term effects of this therapy but the most common adverse effects reported so far occurred at the site of injection and include bruising and erythema. Furthermore less than 2% of patients reported additional adverse effects such as dizziness, nausea and headaches. These reports are encouraging for the clinical application of iron-based nanoparticles.

3.2 Quantum Dots

Quantum dots (QDs) are colloidal nanocrystals with size ranging from 2 to 20 nm. They are made from semiconductor materials (chalcogenides of metals, e.g. CdSe, CdS, CdTe) which exhibit very unique properties as their photo- and electroluminescence can be tuned by simply changing the crystallite size (Fig. 5) [58]. QDs present a better alternative to traditional organic fluorescent dyes because their excited state lifetime (20–50 ns) is almost one order of magnitude longer than that of organic dyes (2–5 ns) and they are less sensitive to photobleaching.

Monodisperse QDs ranging from 2.3 to 5.5 nm can be synthesised via the pyrolysis of organometallic precursors (e.g. dimethylcadmium and trioctylphosphine selenide) in a coordinating solvent like trioctylphosphine oxide (TOPO). The precursors are injected at temperatures between 340 and 360°C and initially form seeds which are allowed to grow at temperatures between 290 and 300°C. These CdSe dots are collected as powders using size-selective precipitation. They are redispersed in TOPO and trioctylphosphine (TOP). For the ZnS shell, diethylzinc and hexamethyl-disilathiane are commonly used as Zn and S precursors, respectively. Equimolar amounts of each are dissolved in TOP under an inert atmosphere and then this shell precursor solution is added dropwise to the CdSe cores which were heated under an inert atmosphere to 140–220°C. The higher the temperature at which the precursors are added, the larger the final diameter of the CdSe/ZnS core-shell QDs [58].

While their widespread use is limited due to toxicity concerns, various capping strategies are currently being employed to minimise this. The first involves 'cap exchange' where native TOP/TOPO is replaced by bifunctional ligands. The second capping strategy employs inert silica in the form of silica shells which can further
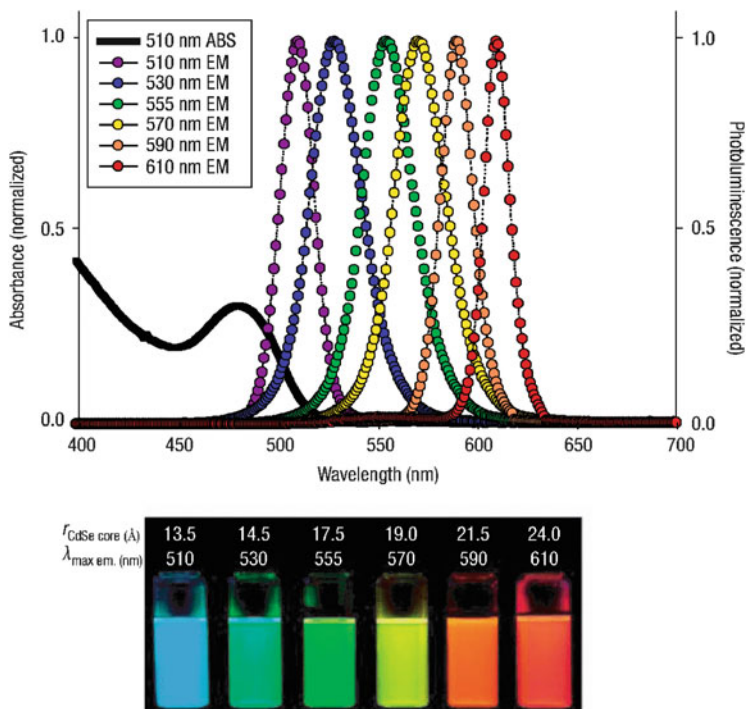
Fig. 5 Different emission spectra of QDs depending on the size of the CdSe core (Reproduced with permission from [59])

be functionalised. Finally, the conjugation of 'diblock' and 'triblock' copolymers and phospholipids to TOP/TOPO on QDs' surfaces is used for shielding the core of the particle from the environment. The capping strategy of choice depends on the final application of the QDs and takes into consideration the individual limitations of each method. For instance, while silica and organic polymer shells confer a greater stability onto quantum dots, they also substantially increase the particle diameter. CdSe/ZnS coated with siloxane shells is still modifiable by surface functionalisation using thiol and/or amine groups to mention just two [60].

Derfus et al. [61] reported that QDs' toxicities are enhanced when they have prolonged exposure to oxidative environments which could lead to the release of free cadmium. They proposed the use of strategies which prevent surface oxidation and the storage of QDs under an inert atmosphere. In addition, they showed that CdSe quantum dots which were capped with 1–2 monolayers of ZnS, coated with methacrylic acid and further rendered biocompatible with the conjugation of bovine serum albumin, provided a reduced toxicity compared with bare CdSe QDs.

In another study, core-shell CdSe/ZnS QDs were protected by both TOPO and an amphiphilic triblock copolymer (Fig. 6). The hydrophobic interactions between TOPO and the polymer hydrocarbon backbone are strong enough to resist hydrolysis and enzymatic degradation. Moreover, the triblock copolymer was found to
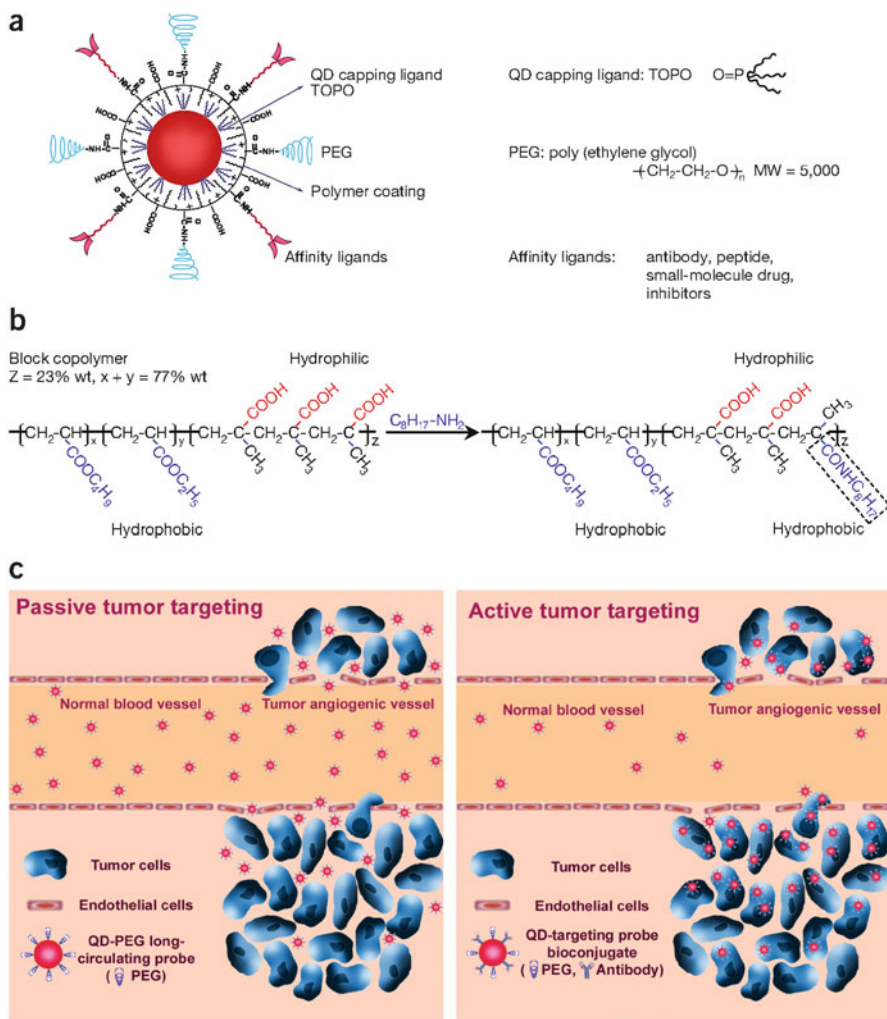
Fig. 6 Methods of functionalising QDs to render them biocompatible and facilitate active targeting (Reproduced with permission from [62])

prevent aggregation of QDs [62]. In addition, QDs were further surface-modified with antibodies to target the prostate-specific membrane antigen (PSMA) and polyethyleneglycol (PEG) to improve biocompatibility and increase blood circulation time. In vivo, it was found that encapsulation with PEG improved the circulation time of conjugated QDs but decreased the rate of organ uptake, while conjugation with PSMA resulted in the delivery and retention of QDs in tumour xenografts.

One major disadvantage of QDs is their blinking. Blinking occurs when a fluorophore's emission intensity fluctuates between bright and dark states. The "quantum jump" theory proposed by Niels Bohr goes as follows: since electrons

cannot reside between states, they must undertake instantaneous leaps from one state to another [63]. In experiments on single fluorescent molecules, the occurrences of these quantum jumps are seen as interruptions of the fluorescence signal. Although all factors that contribute to blinking frequency and duration are not completely understood yet, there have been moves to design fluorophores with suppressed or no blinking. Mahler et al. [64] reported the fabrication of a novel type of CdSe/CdS core-shell QD with a 5 nm crystalline CdS shell which exhibited suppressed blinking at frequencies lower than 33 Hz in 68% of the nanoparticle population. Blinking was monitored using a CCD camera and analysis was based on images acquired continuously over 5 min.

3.3   Upconverting Nanoparticles

Upconverting nanoparticles (UCNPs) are lanthanide-doped nanocrystals. Lanthanide ions are unique materials that can convert infrared excitation light to shorter UV/visible light by a process which is known as photon upconversion. Contrarily to the conventional fluorescence process which involves one ground state and one emission state, the upconverting process relies on the existence of multiple intermediate states to accumulate the low-energy excitation photons [65]. Efforts to apply UCNPs as bioimaging and diagnostic tools have proven their versatility as fluorescent probes and are reflected by a significantly improved and facilitated fabrication process. This provides better quality UCNPs that are small and homogeneous. UCNPs have distinctive superior properties compared to other fluorophores. For instance, organic dyes have broad emission spectra unsuitable for multiplex biolabelling and they often suffer from photodegradation on exposure to external illumination. Quantum dots offer great features like large molar extinction coefficients, high quantum yields, narrow emission bandwidths, size-dependent tunable emissions and high photostability. Nevertheless toxicity concerns of QDs based on the potential leakage of toxic components from the particles under certain conditions remain a matter of debate. Organic dyes and QDs are excited by UV or visible light. Absorption of UV/Vis light by biological samples is often associated by autofluorescence that interferes with the signal obtained from the fluorophore. In addition, UV exposure can cause photodamage and DNA mutation. UCNPs avoid all these drawbacks due to their near infrared excitation where biological matrices have no photoactivity. Moreover, they have sharp emission bandwidth, long lifetime, tunable emission, high photostability and low cytotoxicity.

There is increasing interest in the use of UCNPs as theranostic agents due to their improved fluorescence and toxicity profiles compared to quantum dots. Figure 7 reports loading and release studies of doxorubicin (DOX) from PEG-functionalised UCPs [65]. The authors reported pH-dependent loading and release of the encapsulated drug.
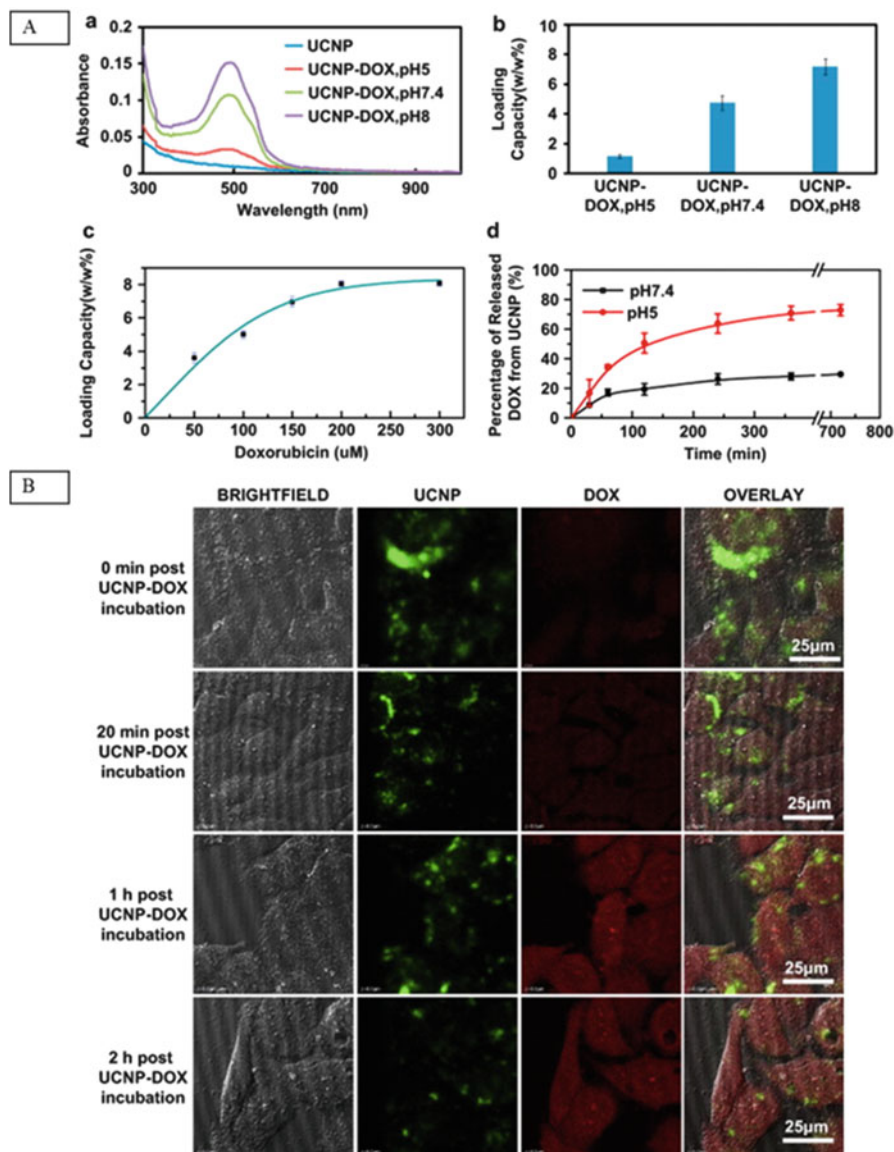
Fig. 7 (**A**) Drug loading and release using a UCNP-DOX carrier system. (*a*) UV–Vis spectra of UCNPs loaded with DOX at different loading pH values. (*b*) Quantification of DOX loading at different pHs. (*c*) Quantification of DOX loading at different DOX concentrations (loading at pH 8). (*d*) DOX release from UCNPs over time in buffers at pH 5 and 7.4. (**B**) HeLa cells incubated for 2 h with UCNP-DOX at 37°C prior to washing. Confocal images have been taken at indicated time points after washing (adapted from [65])

All of the aforementioned examples reinforce the use and importance of natural and synthetic polymers to create biocompatible shells around inorganic nanoparticles which can improve their toxicity profiles [66] and enable the multifunctional use of these nanoparticles [66–69].

4   Dendrimers

Dendrimers are highly branched, globular macromolecules with many arms emanating from a central core. They are fabricated via a stepwise process which yields molecules possessing a core, interior layers composed of repeating units, and an exterior with terminal functionalities attached to the outmost generations. The first article using the term 'dendrimer' was published in 1984 from the company Dow Chemicals, detailing the synthesis of monodisperse poly(amidoamine) (PAMAM) dendrimers [70], after the initial report by Vögtle's group in 1978 reporting the 'cascade-chain-like' synthesis of molecules [71].

Figure 8 shows a comparison of Starburst™ PAMAM dendrimers of generations four ($G = 4.0$) to seven ($G = 7.0$) with various biomacromolecules. The number of assembled β-alanine monomers is 3, 9, 21, 45, 93, 189, 381, 765 and 1,533 for dendrimers from generations 0 to 8, and the mass is expected to double from generation to generation [70].

Fig. 8 Comparison of the structure of Starburst PAMAM dendrimers from generations 4 to 7 with a variety of biomacromolecules including proteins, DNA and a typical lipid bilayer (Reproduced with permission from [72])

Fig. 9 Structures of adriamycin (*left*) and methotrexate (*right*)

In recent years, several advantages of dendritic molecular architecture have been identified as relevant for use in drug delivery applications. Namely, the controlled multivalency of dendrimers can be used favourably to attach several drug molecules, and the low polydispersity that is obtained for the synthesis of dendrimers is advantageous for reproducible pharmacokinetic profiles. Therapeutic agents can be loaded either in the branched interior by electrostatic interactions, hydrogen bonding or hydrophobic interactions. Alternatively, they might be attached to the dendrimer surface by electrostatic or covalent bonds. Various reviews and articles have reported the functionalisation of dendrimers for the transport of macromolecules and hydrophobic drugs such as doxorubicin [73] and as contrast agents for magnetic resonance imaging [74].

Cationic PAMAM dendrimers were complexed with DNA and efficient transfection of cells was shown to be related to the dendrimer/DNA ratio, dendrimer diameter and the conjugation of a water-soluble, membrane-destabilising protein onto the exterior surface of the dendrimer [75].

In another study, polyethylene glycol monomethyl ether chains of 550 and 2,000 dalton molecular weight were attached to third- and fourth-generation PAMAM dendrimers via urethane bonds. The authors used adriamycin and methotrexate (MTX) (Fig. 9) as test molecules, as they are known as efficient, hydrophobic cancer drugs fitting nicely in the hydrophobic interior part of the PAMAM dendrimer. External PEG units provided biocompatibility. Although the main driving force for encapsulation of the drug is hydrophobic interaction, the length of the PEG units also plays a role on the encapsulation efficiency. Fourth-generation PAMAM, conjugated with PEG_{2000}, showed better encapsulation than the corresponding PEG_{550}. The authors claimed that longer PEG units surround the dendrimer better and prevent leakage of the drug from the interior part of the dendrimer. The other explanation could be the conformation change of the PAMAM after PEG conjugation as longer PEG chains can make the inner part of the dendrimer larger. Encapsulation behaviours of fourth-generation PAMAM-PEG_{2000} for adriamycin and methotrexate provided the best encapsulation efficiency. In average, 6.5 adriamycin and 26 methotrexate molecules were encapsulated per dendrimer [76].

The release profile of adriamycin from the fourth-generation PAMAM PEG_{2000} was compared to that of free adriamycin in PBS buffer by dialysis. Both profiles

Fig. 10 Release of MTX
from fourth-generation
PAMAM-PEG$_{2000}$. The
MTX-loaded fourth-
generation PAMAM-
PEG$_{2000}$ (*circles*) or free
MTX (*triangles*) dissolved
in 1 mM Tris–HCl buffer,
pH 7.4 containing (*open
symbols*) or not containing
(*closed symbols*) 150 mM
NaCl upon dialysis against
the same solution
(Reproduced with
permission from [76])
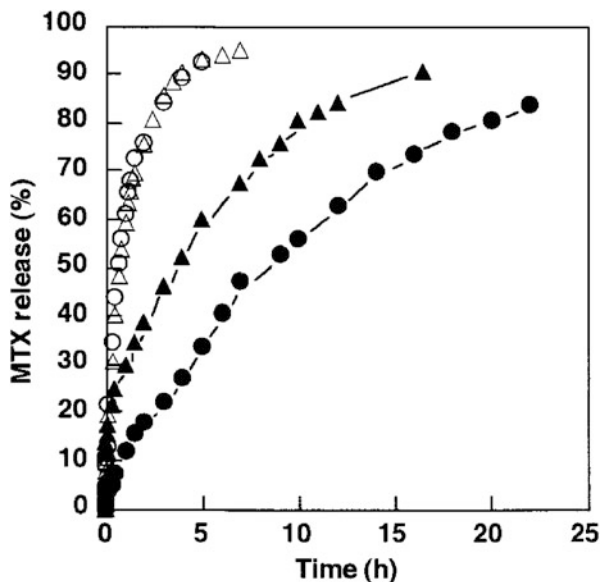
were not significantly different. This was explained by weak hydrophobic interactions between PAMAM and adriamycin. The same behaviour was also observed for a third-generation PAMAM-PEG$_{2000}$ carrier. In the case of methotrexate, the drug was tightly bound to the dendrimer by electrostatic interactions, causing its slower release as compared to that of a free drug. However, in the presence of 150 mM NaCl, the same release rate was observed for free drug and the drug encapsulated in dendrimer (Fig. 10), indicating the role of electrostatic interactions between drug and dendrimer.

Table 1 provides a brief summary of some of the aforementioned nanoparticles which are currently approved by the FDA as drug delivery systems or diagnostic tools. Engineering of new nanoparticles for well-controlled and defined delivery of therapeutic drugs is an exciting and rapidly developing field in which polymeric nanoparticles are becoming increasingly relevant.

5 Polymeric Nanoparticles

Polymers are very large molecules comprised of smaller building block units called 'monomers'. Two main groups can be distinguished: natural and synthetic polymers. Natural polymers include polysaccharides (agarose, chitosan and hyaluronic acid) or protein-based polymers (collagen, albumin and gelatin). Synthetic polymers are particularly attractive as they offer the opportunity to specifically engineer materials with a given set of properties for one particular application.

Table 1 Examples of nanocarrier-based drugs and diagnostics on the market or in clinical trials

Compound	Commercial name	Composition	Indications	Approved by FDA
Doxorubicin	Doxil®/ Caelyx	Injectable PEG-liposomes	Recurrent breast cancer, ovarian cancer, refractory Kaposi's sarcoma	1995
Ferumoxides	Endorem/ Feridex	Superparamagnetic iron oxide nanoparticles	MRI contrast agents	1996
IL2 fused to diphtheria toxin	Ontak (Denileukin diftitox)	Immunotoxin (fusion protein)	Cutaneous T-cell lymphoma	1999
Paclitaxel	Abraxane	Albumin-bound paclitaxel nanoparticles	Metastatic breast cancer	2005
Ferumoxytol	Feraheme	Carbohydrate-coated superparamagnetic iron oxide nanoparticles	Iron deficiency anaemia Chronic kidney disease	2009
Vincristine	Marqibo®	Liposomes	Philadelphia chromosome-negative (Ph-) acute lymphoblastic leukaemia	2012
Docetaxel	Docetaxel PNP	Injectable polymeric nanoparticle	Solid tumours	Phase 1

Adapted from Peer et al. 2007 [77] and FDA.gov [78]

5.1 Natural Polymers

Natural polymers have undergone extensive studies due to their inherent biocompatibility and their low toxicity.

5.1.1 Natural Cationic Polymers

Natural cationic polymers are attractive candidates for therapeutic applications as they are generally non-toxic, biocompatible and biodegradable and possess low immunogenicity. Very often they also carry chemical moieties that are suitable for conjugation chemistry to improve targeting or bioavailability. Consequently, they are the subject of enormous research focus, particularly with respect to non-viral gene delivery systems due to their flexible properties, easy synthesis, robustness and potential for efficient gene delivery. They exhibit unique physicochemical properties for enhanced targeting and bioavailability and form electrostatic complexes with anionic biomacromolecules, like nucleic acids and proteins. When used as gene delivery vehicles, they mediate genetic transfection of cells via the complexation of nucleic acids, and they protect the cargo from enzymatic degradation and facilitate cellular uptake. Commonly used natural cationic polymers include

chitosan and poly-L-lysine, both of which have inherent positive charges. Further interesting candidates include dextran derivatives after chemical introduction of cationic moieties.

Chitosan

Chitosan is a polycationic, natural polymer composed of D-glucosamine and *N*-acetyl-D-glucosamine linked by β-(1,4)-glycosidic bonds (Fig. 11). Industrially, it is obtained by hydrolysing the aminoacetyl groups of chitin from crabs or shrimps in aqueous alkaline solution. Since the term chitosan is applied to chitins in various stages of deacetylation and depolymerisation, it is not easily defined in terms of exact composition. Its degradation by enzymes such as lysozyme and chitosanase into oligomers and further to N-glucosamine, which is endogenous to the human body, renders it non-toxic [79]. Often described as biocompatible, chitosan also possesses mucoadhesive [80] and antimicrobial properties, chelates toxic metals (e.g. mercury, cadmium, lead) and shows good coagulation ability and immunostimulating activity [81]. The fact that chitosan can be sterilised adds to its list of attributes and explains why it has been used as a pharmaceutical excipient in oral formulations and in cosmetics.

The high charge density of chitosan at pH below its pK_a of around 6.5 [81, 82] aids polyelectrolyte formation and a low charge density around neutral pH reduces its cytotoxicity. However, the low charge density also results in diminished solubility, aggregate formation and poor stability of chitosan-based formulations. It has been shown that the degree of deacetylation of chitosan nanoparticles has a greater influence on cellular uptake and cytotoxicity than its molecular weight. Indeed chitosan nanoparticle uptake decreased by 26% when the polymer molecular weight was reduced from 213,000 to 10,000 daltons and by 46% when the degree of deacetylation was reduced from 88% to 46% [83].
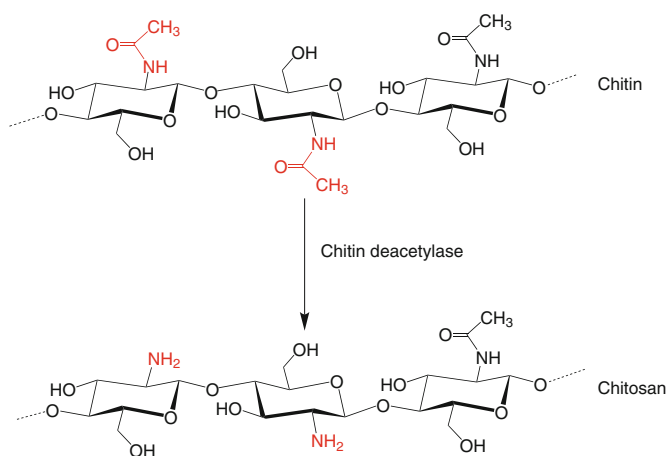
Fig. 11 Chemical structures of chitin and its deacetylated derivative, chitosan

Chitosan has a strong electrostatic affinity for anionic biomacromolecules such as DNA and RNA in saline or acetic acid solution. It spontaneously forms microspheres via complex coacervation [84]. This drug delivery system is advantageous as it has the added benefit of protecting DNA and RNA from degradation and it enables the controlled release of therapeutic compounds [85–88]. The transfection efficiency of chitosan–DNA complexes is quite low in comparison with viral vectors and is shown to depend on numerous factors including the structure of the polycations used, the cell type being transfected and nanoparticle size and composition, in addition to the previously mentioned poor solubility at physiological pH. Free amino groups in chitosan have been used to improve transfection of chitosan–DNA complexes and to graft various ligands and complexes including folic acid [89], transferrin and protein conjugates [90].

Quaternisation of chitosan is a strategy which has been used by many research groups to control the cationic character of the polymer without altering its pH independency. One way of achieving this is to react the amino groups of chitosan with aldehydes to form a Schiff-base intermediate; this Schiff base is then reacted with methyl iodide to yield quaternised chitosan [91]. This process improves the mucoadhesive properties of chitosan, depending on the degree of quaternisation [92]. Moreover, chitosan hydrogels have been investigated as drug delivery vehicles for immediate and sustained release of therapeutic compounds [93]. The use of a hydrogel allows the incorporation of rigidifying linkages within the polymer matrix which reduces rapid swelling and immediate release of the payload. It was noted that addition of drugs before or after cross-linking and the degree of cross-linking contributed to the resulting release profile of the encapsulated drugs [94].

Cationic Dextran

Dextran is an FDA-approved highly water-soluble branched polysaccharide composed of glucose units mainly linked by α-(1,6)-glycosidic bonds. It is biodegradable, its solubility is not affected by pH and it is easy to modify and widely available. Cationic dextran derivatives have been developed as a delivery vehicle for nucleic acids. Dextran–spermine-based conjugates are prepared by the reductive amination between oxidised dextran and spermine. Spermine is a naturally occurring linear oligoamine which is a polycation at physiological pH. In a study comparing more than 300 different polycations prepared from polysaccharides and oligoamines having two or four amino groups, it was found that the dextran–spermine conjugate displayed the highest transfection rate in perfused rat lungs [95]. Data showed that changes in spermine content and the extent of grafting can have a severe impact on the DNA-compaction properties, which in turn impacts the effectiveness of cell transfection [96]. Moreover, low percentages of PEGylation of the dextran–spermine gene carrier were studied for improved functionality. It turned out that 3 and 5% PEGylation of the dextran–spermine gene carriers showed the highest transfection rates.

5.1.2 Anionic Natural Polymers

Anionic polymers have the ability to form ionic complexes with cationic biomolecules, basic peptides and blood proteins for several therapeutic indications. However, the number of literature reports is smaller for the use of anionic polymers compared to cationic polymers.

5.2 Synthetic Polymers

Nature has long been the major inspiration behind extraordinary advances in science. The investigation and elucidation of the role and mechanism of action of natural polymers have propelled interest and growth in the synthetic polymer field. It is now widely accepted that synthetic polymers are a versatile group of materials applicable to various fields of research. In particular, polymer-based nanoparticles (NPs) have attracted increasing attention from the scientific community in recent years because they show promising applications in in vitro and in vivo diagnostics, as drug delivery vehicles, bioanalytical probes and imaging tools. Synthetic polymers offer flexibility in terms of different polymer architectures, physical states, shape, size and surface properties [97] and are divided into two main groups: biodegradable and non-biodegradable polymers. They can be engineered as mono-, co- or oligo-polymers with repeating units of one, two or more monomer units, respectively.

Biodegradable synthetic polymers include poly(glycolic acid) (PGA), poly(lactic acid) (PLA) and their copolymer poly(lactic acid-co-glycolic acid) (PLGA), poly(p-dioxanone) as well as copolymers of trimethylene carbonate and glycolide. In the synthetic polymer family, polyesters are particularly attractive in biomedical applications due to their ease of degradation by hydrolysis of ester linkages. Their structure can be tailored to alter degradation rates and moreover the degradation products are sometimes precursors in metabolic pathways.

Nondegradable biocompatible polymers have a long history in medical applications. The spectrum of use includes but is not limited to coatings on devices, implants, catheters, membranes and porous scaffolds for tissue regenerative applications, injectable drug delivery and imaging systems [98]. Implanon™ is a non-biodegradable, etonogestrel-containing single sterile rod implant approved by the FDA as a contraceptive in 2006 [99]. Each Implanon™ rod consists of an ethylene vinyl acetate (EVA) copolymer core containing 68 mg of etonogestrel, surrounded by an EVA polymer skin. The release rates are 60–70 μg/day in the first 6 weeks, 35–45 μg/day at the end of the first year and 25–30 μg/day at the end of the third year.

One of the most attractive features of synthetic polymers is the ability to engineer them in such a way that allows stimuli responsiveness. This may be

critical for encapsulation of molecules of interest or may play a role in drug-release mechanisms. The key parameter defining a responsive or 'smart' polymer is that it has a non-linear response to an external signal and by judiciously choosing or designing monomers, one can synthesise polymers which are responsive to a number of physical (temperature, ultrasound, light and electricity) or chemical (pH, ionic strength) or even biological stimuli (antigens).

5.2.1 Thermoresponsive Polymers

Temperature sensitivity arises from the balance between hydrophobic and hydrophilic segments of a polymer. Typically, most solutes and solvents are miscible if the temperature is higher than the so-called *upper critical solution temperature* (UCST).

   If the temperature is below the UCST, the system exhibits a phase transition and the solute precipitates. A number of polymers show contrasting behaviour in aqueous solution, where they are soluble in aqueous solution until the temperature exceeds a critical point where they become insoluble (Fig. 12a). This *lower critical solution temperature* (LCST) corresponds to the region in the phase diagram at which the enthalpic contribution of water, hydrogen-bonded to the polymer chain, becomes less than the entropic gain of the system as a whole and is therefore largely dependent on the hydrogen-bonding capabilities of the constituent monomer units. Examples include poly (N-isopropylacrylamide) (pNIPAM), poly(vinyl-methyl-ether) and poly(vinyl-methyl-oxazolidione) with LCSTs of ~32°C, 34 °C and 40 °C, respectively [101]. It should be noted that for polymer gel systems, the volume-phase transition temperature is widely used to describe the transition instead of LCST since such polymers swell instead of dissolving in solution. In cases where the polymer is only soluble above a certain critical temperature, this critical point is known as the upper critical solution temperature (UCST) (Fig. 13).

   The most widely studied synthetic, thermally responsive polymer is pNIPAM. pNIPAM is soluble in water below its LCST because of the predominance of hydrophilic interactions, mainly hydrogen bonds between amide groups and water; these water molecules are released from the polymer hydration layer into the bulk water as the temperature increases past the LCST; hence the polymer becomes insoluble and phase separation occurs (Fig. 12b). The LCST can also be 'tuned' by the addition of hydrophobic or hydrophilic co-monomers and/or by controlling the molecular weight of the polymer. Hydrophilic monomers such as acrylic acid induce an increase in the LCST of pNIPAM while the opposite is true for hydrophobic monomers. This provides versatility in the choice of co-monomers which can be tailored to achieve controlled release close to the body temperature of 37°C [103–105].

   While it has been well established that the NIPAM monomer is cytotoxic, in vitro [106] and in vivo [107], assessments using pNIPAM indicate that the polymer is neither toxic to endothelial, epithelial, fibroblast or smooth muscle cells nor to mice. However, further studies regarding cytotoxicity are required to investigate short- and long-term effects of the polymers and copolymers before their full potential in pharmaceutical formulations can be exploited.

Fig. 12 Schematic of 'smart' polymer response to temperature (Reproduced with permission from [100])

5.2.2 pH-Responsive Polymers

Within the human body, there are many regions with differential pH gradients. While the pH of body tissue is maintained around 7.4, the pH of gastric acid in the stomach is between 1.5 and 3.5. In the small intestine, the pH ranges from 6 in the duodenum to 7.4 in the terminal ileum and 5.7 in the caecum. It is also well established that tumour microenvironments are hypoxic and acidic [108], features which can be exploited to design therapeutics which are more effective at targeting harmful tumour cells. Intracellularly, pH ranges from ~7.4 in the cytosol to 6.0–6.5

Fig. 13 Schematic showing phase transition associated with lower critical solution temperature (LCST) and upper critical solution temperature (UCST). The dark blue line represents the phase separation boundary which produces a cloud point in solution (Reproduced with permission from [102])

in early endosomes and 4.5–5.5 in late endosomes and lysosomes. Since most polymeric nanoparticles between 100 and 200 nm are thought to be internalised via endocytosis, this is an important consideration in drug delivery design to avoid premature release of cargo or expulsion from cells.

Ionisable moieties such as carboxylic acid, amine, phenylboronic acid, imidazole, sulphonamide and thiol groups can confer pH sensitivity. Acrylic acid and its corresponding polymers are commonly used as pH-sensitive synthetic polymers, because at pH values above its pK_a (~4.5), acrylic acid is deprotonated and becomes reactive. For example, poly(propylacrylic acid) (PPAA) is not haemolytic at pH 7.4 but displays pH-dependent haemolytic behaviour that rises dramatically as the pH drops below 6.5 [109]. It was further reported that the conjugation of targeting ligands onto the polymer did not alter its pH-responsive character. Dong et al. 1991 reported the fabrication of hydrogels based on poly(hydroxyethyl-methacrylate-co-acrylic acid) and poly(acrylamide-co-acrylic acid) which were sensitive to both temperature and pH [110]. In vitro drug-release studies performed using indomethacin showed negligible release at pH 1.4 in 24 h but more than 90% release at pH 7.4 over 5 h. Nanospheres of cross-linked networks of methacrylic acid grafted with poly(ethylene glycol) and acrylic acid grafted with poly(ethylene glycol) showed a pH-dependent increase in size from 200 nm at pH 2.0 to 2,000 nm at pH 6.0. Insulin was entrapped in the nanospheres at pH 3.0 and released at pH 7.0 and in vivo studies with diabetic rats indicated a successful lowering of serum glucose levels for those treated with insulin-loaded polymers compared with the control group [111].

The selective reversal of surface charge of copolymers formulated from PLGA nanoparticles (d ~70 nm) in the acidic environment of endosomes was determined to promote interaction of nanoparticles with endo-lysosomal membranes which ultimately facilitated escape from the trafficking/recycling vacuoles into the cytosol

in less than 10 min [112]. This has important implications for the effective delivery of cargo into cells and holds a potential disadvantage. pH-sensitive polymers need to be effective at very narrow pH ranges or they run the risk of inducing severe toxic effects due to drug burst or poor therapeutic efficacy by incomplete drug release at a target site.

5.2.3 Photoresponsive Polymers

Photoresponsive polymers have attracted attention due to their ability to change their chemical or physical properties upon exposure to light of a given wavelength. Applications include optical storage elements, biosensors, drug delivery and bioactivity switching of proteins [113].

The three main categories of photoresponsive molecules are (1) photoisomerisation, (2) photodimerisation and (3) photocleavage. Photoisomerisation can be performed, for instance, with azobenzenes which undergo fully reversible isomerisation when irradiated by a suitable light source. Azobenzene-containing polymers are well-studied systems which undergo significant changes in geometry and polarity due to transitions between the *trans-* and *cis*-conformations (Fig. 14).

The conformation change is accompanied by a fast and complete change of structure, geometrical shape and polarity. For instance, while the more stable *trans*-azobenzene has no dipole moment, the *cis*-form is quite polar, having a dipole moment of 3 debye. Azobenzene moieties can be used to control the hydrophobicity/hydrophilicity of a polymer chain. In addition to polarity, a change in the conformation of the azobenzenes can induce steric hindrance that results in a change of polymer morphology.

Kros and co-workers reported the synthesis of a supramolecular gel for controlled protein release [114]. First, maleimide moieties were grafted onto dextran, a natural polymer as described above. Then, maleimide-grafted dextrans were functionalised with either cyclodextrin or azobenzene moieties separately. The two resulting linear polymers were used as building blocks of supramolecularly cross-linked hydrogels for the light controlled release of proteins. As stated before, *trans*-azobenzene is hydrophobic and can be trapped in the central cavity of cyclodextrins. Upon irradiation with UV light, the conformation changes from *trans-* to *cis*-conformation causing deformation of the physically cross-linked gels and the simultaneous release of proteins (Fig. 15).

Fig. 14 Reversible transformation of *trans-* to *cis*-azobenzenes
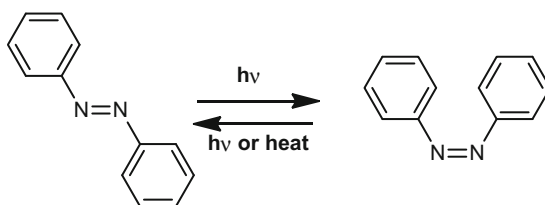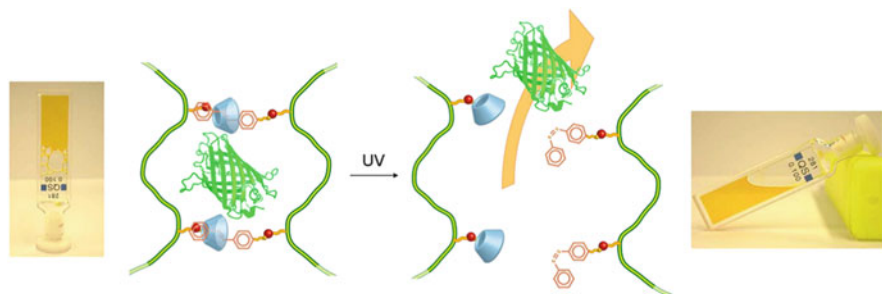
Fig. 15 Photoresponsive protein release from a hydrogel composed of *trans*-azobenzene-modified dextran and cyclodextrin-modified dextran (Reproduced with permission from [114])

Gupta and co-workers used a similar method to obtain nanogels for drug delivery [115]. Instead of using azobenzene–cyclodextrin complexes as supramolecular cross-linker, they used hydrophobic interactions between azobenzene moieties. Aspirin-loaded nanogels were irradiated with UV light and hydrophobic interactions were weakened by conformation change. The resulting loose structure provided the release of aspirin. In addition, they showed the effect of pH on the release profile of the nanogels. The drug was released almost two times faster at pH 9.0 than pH 4.0. Cytotoxicity studies revealed that nanogels were toxic to cells above 1 mg/mL.

6   Molecularly Imprinted Polymers

Molecularly imprinted polymers (MIPs) are tailor-made synthetic receptors, obtained by co-polymerisation of functional and cross-linking monomers in the presence of a molecular template. The template can be the target molecule or a derivative thereof. After removal of the template from the polymer, binding sites are accessible that allow binding of the target molecule with a very high specificity and affinity, comparable to that of natural receptors [116, 117]. MIPs have considerable advantages over biological recognition materials such as enzymes and antibodies, as they are more easily prepared and cheaper and they possess greater chemical, thermal and mechanical stability. Due to these advantages they have become serious alternatives to biomolecules in solid-phase extraction (SPE) [118, 119], as recognition elements in sensors [120, 121], as substitutes of antibodies in immunoassays [122, 123] and, more recently, in drug delivery [124, 125], as therapeutic drugs [126, 127] and for bioimaging [128].

MIPs are interesting for drug delivery applications as the drug's attractive interactions with the memory cavities within the polymer network should slow down its release (sustained release). Sustained release is needed when a drug is toxic above a certain critical concentration. The water compatibility of MIPs is essential for their application in the human body. Preparation of water-compatible

MIPs with high binding specificity still remains a big challenge; however successful examples have been described. MIP-based soft contact lenses, which have been used as drug delivery carriers in vivo, is one of the most elegant examples. The first application of imprinted therapeutic contact lenses in vivo was reported in 2005 [124]. Poly(MAA-co-DEAA-co-EGDMA) MIP lenses were prepared in the presence of timolol, a drug used in the treatment of glaucoma, without any porogen and a very low degree of cross-linking. The resulting lens had a diameter of 14 mm and a thickness of 80 μm. Timolol release studies carried out in rabbits showed that the soft contact lenses provided measurable timolol concentrations in the tear fluid for 2.0- to 3.0-fold longer times than the non-imprinted contact lenses and eye drops, respectively. The time of release, however, did not pass beyond 90 min. Later, in 2012, Byrne and co-workers improved the MIP protocol and obtained a MIP contact lens (100 μm thickness and diameter 12 mm) which can deliver a steady, effective concentration of the drug for an extended period of time of 26 h, which is longer than the time of daily lens wear [129]. The imprinted poly(HEMA-co-AA-co-AM-co-NVP-co-PEG$_{200}$DMA) contact lenses could controllably deliver a sustained four-fold and fifty-fold higher concentration of ketotifen fumarate, an antihistamine, than the non-imprinted polymer (NIP) and eye drops respectively.

Recently, we described a sol–gel MIP and demonstrated its potential as drug delivery device for the controlled release of salicylic acid (SA) [125]. Sol–gel MIPs, obtained by molecular imprinting in silica-based matrices, are synthesised in the presence of water, such that the recognition sites have a better chance to bind the ligand in an aqueous environment. Moreover, silica-based materials are biocompatible and non-toxic [130]. SA is frequently used as a topical treatment for skin inflammatory disorders like acne, psoriasis and seborrheic dermatitis. The main side effects caused by this treatment are acute irritation and moderate chemical burns. One way to control this problem would be to control the delivery of SA. Sol–gel-based MIPs for SA were hence prepared using the functional monomers 3-(aminopropyl)triethoxysilane and trimethoxyphenylsilane as well as the cross-linker tetraethyl orthosilicate. The loading capacity was 12 mg of SA per gram of MIP – or 1.2% of SA – complying with dermatological formulations. Practically no SA was bound to the non-imprinted polymer (NIP), showing the remarkable specificity of the sol–gel polymers. In vitro release profiles of the polymers in water are shown in Fig. 16. Almost quantitative release was observed after 30 h.

Very recently, we demonstrated the application of MIPs for cell and tissue imaging [128]. As a demonstration for the detection of glycosylations on cell surfaces, fluorescent MIP-NPs for glucuronic acid were synthesised. Epifluorescence and confocal microscopy showed that the MIPs were able to localise and quantify hyaluronan on the surface of human keratinocytes. Hyaluronan is a polysaccharide composed of repeating units of glucuronic acid and N-acetylglucosamine and it serves as a biomarker of certain cancers. Figure 17 shows the confocal microscopy image to localise glucuronic acid MIP-NPs on human keratinocytes. A more innovative approach using UCNPs-MIP NPs for bioimaging [131] is on-going in our laboratory.
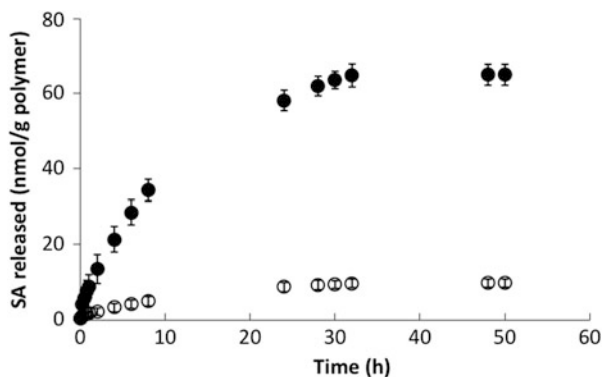
Fig. 16 Release profile of salicylic acid-loaded sol–gel MIP (*filled circle*) and control polymer (*open circle*) in water at room temperature (Reproduced with permission from [125])
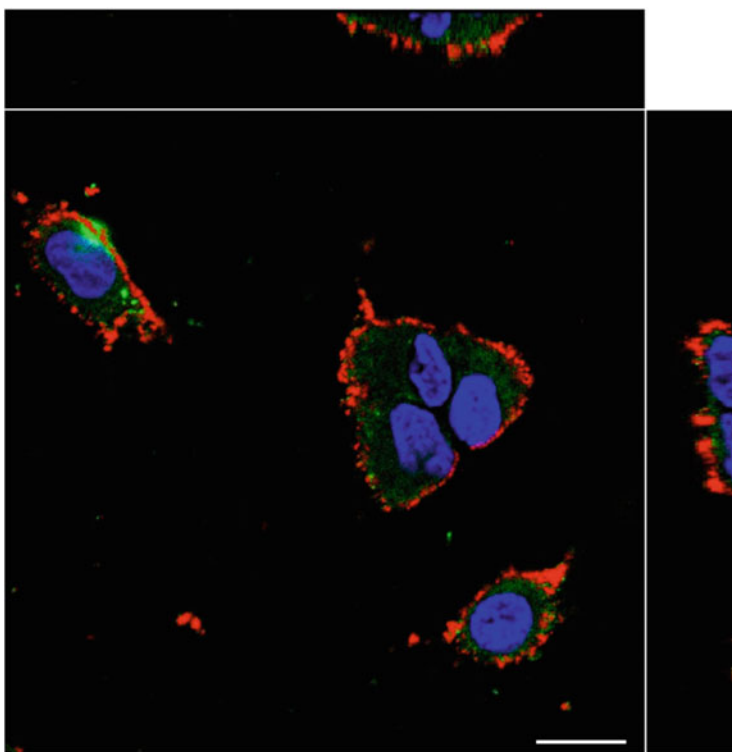
Fig. 17 Confocal micrograph of rhodamine-labelled MIP-NPs specific for glucuronic acid after binding to human keratinocytes. The merge image of three colour channels consists of the *blue* DAPI signal from the cell nucleus, the green 3,3'-dioctadecyloxacarbocyanine perchlorate signal labelling the cell membrane and the red rhodamine signal of MIPs on the cell surface. Scale bar: 20 μm. Adapted with permission from [128]

In conclusion, while this chapter provides a brief and global overview of nanoparticles in biomedical applications, the list examined here is by no means complete. Colloidal gold nanoparticles, gold–silver mixed nanoclusters and carbon nanotubes are also of interest. It is hoped that from this summary of current trends, the reader grasps some of the challenges but also exciting developments in the field of advanced nanoscale materials used in biomedical applications.

References

1. Faraji AH, Wipf P (2009) Nanoparticles in cellular drug delivery. Bioorg Med Chem 17 (8):2950–2962
2. Gasco MR (1993) Method for producing solid lipid microspheres having a narrow size distribution. US5250236A, USA
3. Müller RH, Lucks JS (1996) Medication vehicles made of solid lipid nanoparticles (SLN). EP0605497 B1, Germany
4. Müller RH (2007) Nanostructured lipid carriers (NLC) in cosmetic dermal products. Adv Drug Deliv Rev 59(6):522–530
5. Fang JY et al (2008) Lipid nanoparticles as vehicles for topical psoralen delivery: solid lipid nanoparticles (SLN) versus nanostructured lipid carriers (NLC). Eur J Pharm Biopharm 70 (2):633–640
6. Cavalli R et al (2002) Solid lipid nanoparticles (SLN) as ocular delivery system for tobramycin. Int J Pharm 238(1):241–245
7. Müller RH, Mäder K, Gohla S (2000) Solid lipid nanoparticles (SLN) for controlled drug delivery–a review of the state of the art. Eur J Pharm Biopharm 50(1):161–177
8. Almeida AJ, Runge S, Müller RH (1997) Peptide-loaded solid lipid nanoparticles (SLN): influence of production parameters. Int J Pharm 149(2):255–265
9. Almeida AJ, Souto E (2007) Solid lipid nanoparticles as a drug delivery system for peptides and proteins. Adv Drug Deliv Rev 59(6):478–490
10. Hu F, Hong Y, Yuan H (2004) Preparation and characterization of solid lipid nanoparticles containing peptide. Int J Pharm 273(1):29–35
11. zur Mühlen A, Schwarz C, Mehnert W (1998) Solid lipid nanoparticles (SLN) for controlled drug delivery–drug release and release mechanism. Eur J Pharm Biopharm 45(2):149–155
12. Wissing S, Kayser O, Müller R (2004) Solid lipid nanoparticles for parenteral drug delivery. Adv Drug Deliv Rev 56(9):1257–1272
13. Menger FM, Keiper JS (1998) Chemistry and physics of giant vesicles as biomembrane models. Curr Opin Chem Biol 2(6):726–732
14. Hwang SY et al (2012) Effects of operating parameters on the efficiency of liposomal encapsulation of enzymes. Colloids Surf B Biointerfaces 94:296–303
15. He J et al (2013) Hydrodynamically driven self-assembly of giant vesicles of metal nanoparticles for remote-controlled release. Angew Chem 125(9):2523–2528
16. Apple MA, Hunt CA, Yanagisawa H. (1981) Bis-anthracycline nucleic acid function inhibitors and improved method for administering the same US4263428A, USA
17. Deamer DW (1985) Method for encapsulating materials into liposomes US4515736 A.
18. Bangham AD, Standish MM, Watkins JC (1965) Diffusion of univalent ions across the lamellae of swollen phospholipids. J Mol Biol 13(1):238–252

19. Bangham AD, Hill MW, Miller NGA (1974) Methods in Membrane Biology, Ch 1, Vol 1, Ed. Korn ED, Springer US

20. Szoka JR, Papahadjopoulos FD (1980) Comparative properties and methods of preparation of lipid vesicles (liposomes). Annu Rev Biophys Bioeng 9(1):467–508

21. Olson F et al (1979) Preparation of liposomes of defined size distribution by extrusion through polycarbonate membranes. Biochim Biophys Acta Biomembr 557(1):9–23

22. Szoka F, Papahadjopoulos D (1978) Procedure for preparation of liposomes with large internal aqueous space and high capture by reverse-phase evaporation. Proc Natl Acad Sci U S A 75(9):4194–4198

23. Szoka F et al (1980) Preparation of unilamellar liposomes of intermediate size (0.1–0.2 μm) by a combination of reverse phase evaporation and extrusion through polycarbonate membranes. Biochim Biophys Acta Biomembr 601:559–571

24. Torchilin VP (2005) Recent advances with liposomes as pharmaceutical carriers. Nat Rev Drug Discov 4(2):145–160

25. Knudsen NØ et al (2012) Calcipotriol delivery into the skin with PEGylated liposomes. Eur J Pharm Biopharm 81(3):532–539

26. Verma D et al (2003) Liposomes increase skin penetration of entrapped and non-entrapped hydrophilic substances into human skin: a skin penetration and confocal laser scanning microscopy study. Eur J Pharm Biopharm 55(3):271–277

27. Beukelman C et al (2008) Anti-inflammatory properties of a liposomal hydrogel with povidone-iodine (Repithel®) for wound healing in vitro. Burns 34(6):845–855

28. Needham D et al (2000) A new temperature-sensitive liposome for use with mild hyperthermia: characterization and testing in a human tumor xenograft model. Cancer Res 60 (5):1197–1201

29. Kundu AK et al (2012) Stability of lyophilized siRNA nanosome formulations. Int J Pharm 423(2):525–534

30. Weissig V, Whiteman KR, Torchilin VP (1998) Accumulation of protein-loaded long-circulating micelles and liposomes in subcutaneous Lewis lung carcinoma in mice. Pharm Res 15(10):1552–1556

31. Lurquin PF (1981) Binding of plasmid loaded liposomes to plant protoplasts: validity of biochemical methods to evaluate the transfer of exogenous DNA. Plant Sci Lett 21(1):31–40

32. Torchilin VP, Zhou F, Huang L (1993) pH-sensitive liposomes. J Liposome Res 3 (2):201–255

33. Yatvin M et al (1980) pH-sensitive liposomes: possible clinical implications. Science 210 (4475):1253–1255

34. Dromi S et al (2007) Pulsed-high intensity focused ultrasound and low temperature–sensitive liposomes for enhanced targeted drug delivery and antitumor effect. Clin Cancer Res 13 (9):2722–2727

35. Gerasimov OV et al (1999) Cytosolic drug delivery using pH-and light-sensitive liposomes. Adv Drug Deliv Rev 38(3):317–338

36. Zalipsky S (1993) Synthesis of an end-group functionalized polyethylene glycol-lipid conjugate for preparation of polymer-grafted liposomes. Bioconjug Chem 4(4):296–299

37. van der Meel R et al (2014) Extracellular vesicles as drug delivery systems: lessons from the liposome field. J Control Release 195:72–85

38. Patolsky F, Lichtenstein A, Willner I (2000) Amplified microgravimetric quartz-crystal-microbalance assay of DNA using oligonucleotide-functionalized liposomes or biotinylated liposomes. J Am Chem Soc 122(2):418–419

39. Cao Z et al (2009) Reversible cell-specific drug delivery with aptamer-functionalized liposomes. Angew Chem Int Ed 48(35):6494–6498

40. Lehr CM (2000) Lectin-mediated drug delivery: the second generation of bioadhesives. J Control Release 65(1):19–29

41. Allen TM et al (1995) A new strategy for attachment of antibodies to sterically stabilized liposomes resulting in efficient targeting to cancer cells. Biochim Biophys Acta Biomembr 1237(2):99–108
42. FDA (1995) U.S. Doxil®. http://www.accessdata.fda.gov/drugsatfda_docs/label/2012/050718s043lbl.pdf
43. Allen TM, Cullis PR (2013) Liposomal drug delivery systems: from concept to clinical applications. Adv Drug Deliv Rev 65(1):36–48
44. Gupta AK, Gupta M (2005) Synthesis and surface engineering of iron oxide nanoparticles for biomedical applications. Biomaterials 26(18):3995–4021
45. Jana NR, Chen Y, Peng X (2004) Size-and shape-controlled magnetic (Cr, Mn, Fe, Co, Ni) oxide nanocrystals via a simple and general approach. Chem Mater 16(20):3931–3935
46. Ruiz JM, Benoit JP (1991) In vivo peptide release from poly (DL-lactic acid-co-glycolic acid) copolymer 5050 microspheres. J Control Release 16(1):177–185
47. Khor E, Lim LY (2003) Implantable applications of chitin and chitosan. Biomaterials 24 (13):2339–2349
48. Na HB, Song IC, Hyeon T (2009) Inorganic nanoparticles for MRI contrast agents. Adv Mater 21(21):2133–2148
49. Perez JM, Josephson L, Weissleder R (2004) Use of magnetic nanoparticles as nanosensors to probe for molecular interactions. ChemBioChem 5(3):261–264
50. Chen JF et al (2004) Preparation and characterization of porous hollow silica nanoparticles for drug delivery application. Biomaterials 25(4):723–727
51. Arruebo M et al (2007) Magnetic nanoparticles for drug delivery. Nano Today 2(3):22–32
52. Ulman A (1996) Formation and structure of self-assembled monolayers. Chem Rev 96 (4):1533–1554
53. Vallet-Regi M et al (2001) A new property of MCM-41drug delivery system. Chem Mater 13 (2):308–311
54. Lu Y et al (2002) Modifying the surface properties of superparamagnetic iron oxide nanoparticles through a sol-gel approach. Nano Lett 2(3):183–186
55. Liong M et al (2008) Multifunctional inorganic nanoparticles for imaging, targeting, and drug delivery. ACS Nano 2(5):889–896
56. Schwenk MH (2010) Ferumoxytol: a new intravenous iron preparation for the treatment of iron deficiency anemia in patients with chronic kidney disease. Pharmacotherapy 30 (1):70–79
57. ClinicalTrials.gov (2015) Using Ferumoxytol-enhanced MRI to measure inflammation in patients with brain tumors or other conditions of the CNS
58. Dabbousi BO et al (1997) (CdSe) ZnS core-shell quantum dots: synthesis and characterization of a size series of highly luminescent nanocrystallites. J Phys Chem B 101 (46):9463–9475
59. Medintz IL et al (2005) Quantum dot bioconjugates for imaging, labelling and sensing. Nat Mater 4(6):435–446
60. Gerion D et al (2001) Synthesis and properties of biocompatible water-soluble silica-coated CdSe/ZnS semiconductor quantum dots. J Phys Chem B 105(37):8861–8871
61. Derfus AM, Chan WC, Bhatia SN (2004) Probing the cytotoxicity of semiconductor quantum dots. Nano Lett 4(1):11–18
62. Gao X et al (2004) In vivo cancer targeting and imaging with semiconductor quantum dots. Nat Biotechnol 22(8):969–976
63. Stefani FD, Hoogenboom JP, Barkai E (2009) Beyond quantum jumps: blinking nanoscale light emitters. Phys Today 62(2):34–39
64. Mahler B et al (2008) Towards non-blinking colloidal quantum dots. Nat Mater 7(8):659–664
65. Wang C, Cheng L, Liu Z (2011) Drug delivery with upconversion nanoparticles for multifunctional targeted cancer cell imaging and therapy. Biomaterials 32(4):1110–1120
66. Kim J et al (2008) Designed fabrication of a multifunctional polymer nanomedical platform for simultaneous cancer-targeted imaging and magnetically guided drug delivery. Adv Mater 20(3):478–483

67. Park YI et al (2009) Nonblinking and nonbleaching upconverting nanoparticles as an optical imaging nanoprobe and T1 magnetic resonance imaging contrast agent. Adv Mater 21 (44):4467–4471
68. Lee PW et al (2010) Multifunctional core-shell polymeric nanoparticles for transdermal DNA delivery and epidermal Langerhans cells tracking. Biomaterials 31:2425–2434
69. Erogbogbo F et al (2010) Biocompatible magnetofluorescent probes: luminescent silicon quantum dots coupled with superparamagnetic iron (III) oxide. ACS Nano 4(9):5131–5138
70. Tomalia DA, Naylor AM, Goddard WA (1990) Starburst dendrimers: molecular-level control of size, shape, surface chemistry, topology, and flexibility from atoms to macroscopic matter. Angew Chem Int Ed 29(2):138–175
71. Buhleier E, Wehner W, Vogtle F (1978) Cascade-chain-like and nonskid-chain-like syntheses of molecular cavity topologies. Synthesis 2:155–158
72. Tomalia DA, Fréchet JMJ (2002) Discovery of dendrimers and dendritic polymers: a brief historical perspective. J Polym Sci A Polym Chem 40(16):2719–2728
73. Lee CC et al (2006) A single dose of doxorubicin-functionalized bow-tie dendrimer cures mice bearing C-26 colon carcinomas. Proc Natl Acad Sci U S A 103(45):16649–16654
74. Fischer M, Vögtle F (1999) Dendrimers: from design to application—a progress report. Angew Chem Int Ed 38(7):884–905
75. Haensler J, Szoka FC (1993) Polyamidoamine cascade polymers mediate efficient transfection of cells in culture. Bioconjug Chem 4(5):372–379
76. Kojima C et al (2000) Synthesis of polyamidoamine dendrimers having poly (ethylene glycol) grafts and their ability to encapsulate anticancer drugs. Bioconjug Chem 11 (6):910–917
77. Peer D et al (2007) Nanocarriers as an emerging platform for cancer therapy. Nat Nanotechnol 2(12):751–760
78. FDA (2014) Drugs and medical devices search. http://www.fda.gov/
79. Gebelein CG, Dunn RL (1990) Progress in biomedical polymers. Springer-Verlag New York Inc.
80. Berscht PC et al (1994) Incorporation of basic fibroblast growth factor into methylpyrrolidinone chitosan fleeces and determination of the in vitro release characteristics. Biomaterials 15(8):593–600
81. Agnihotri SA, Mallikarjuna NN, Aminabhavi TM (2004) Recent advances on chitosan-based micro-and nanoparticles in drug delivery. J Control Release 100(1):5–28
82. Samal SK et al (2012) Cationic polymers and their therapeutic potential. Chem Soc Rev 41 (21):7147–7194
83. Huang M, Khor E, Lim LY (2004) Uptake and cytotoxicity of chitosan molecules and nanoparticles: effects of molecular weight and degree of deacetylation. Pharm Res 21 (2):344–353
84. Leong K et al (1998) DNA-polycation nanospheres as non-viral gene delivery vehicles. J Control Release 53(1):183–193
85. Felt O, Buri P, Gurny R (1998) Chitosan: a unique polysaccharide for drug delivery. Drug Dev Ind Pharm 24(11):979–993
86. Mi FL et al (1999) Chitosan–polyelectrolyte complexation for the preparation of gel beads and controlled release of anticancer drug I effect of phosphorous polyelectrolyte complex and enzymatic hydrolysis of polymer. J Appl Polym Sci 74(7):1868–1879
87. Mi FL et al (1999) Chitosan–polyelectrolyte complexation for the preparation of gel beads and controlled release of anticancer drug II effect of pH-dependent ionic crosslinking or interpolymer complex using tripolyphosphate or polyphosphate as reagent. J Appl Polym Sci 74(5):1093–1107
88. Mi FL et al (1999) Porous chitosan microsphere for controlling the antigen release of Newcastle disease vaccine: preparation of antigen-adsorbed microsphere and in vitro release. Biomaterials 20(17):1603–1612

89. Mansouri S et al (2006) Characterization of folate-chitosan-DNA nanoparticles for gene therapy. Biomaterials 27(9):2060–2065

90. Mao HQ et al (2001) Chitosan-DNA nanoparticles as gene carriers: synthesis, characterization and transfection efficiency. J Control Release 70(3):399–421

91. Jia Z, Xu W (2001) Synthesis and antibacterial activities of quaternary ammonium salt of chitosan. Carbohydr Res 333(1):1–6

92. Stepnova EA et al (2007) New approach to the quaternization of chitosan and its amphiphilic derivatives. Eur Polym J 43(6):2414–2421

93. Bhattarai N, Gunn J, Zhang M (2010) Chitosan-based hydrogels for controlled, localized drug delivery. Adv Drug Deliv Rev 62(1):83–99

94. Shi XY, Tan TW (2002) Preparation of chitosan/ethylcellulose complex microcapsule and its application in controlled release of Vitamin D_2. Biomaterials 23(23):4469–4473

95. Azzam T et al (2002) Polysaccharide-oligoamine based conjugates for gene delivery. J Med Chem 45(9):1817–1824

96. Hosseinkhani H et al (2004) Dextran–spermine polycation: an efficient nonviral vector for in vitro and in vivo gene transfection. Gene Ther 11(2):194–203

97. Marchyk N et al (2014) One-pot synthesis of iniferter-bound polystyrene core nanoparticles for the controlled grafting of multilayer shells. Nanoscale 6(5):2872–2878

98. Shastri AP (2003) Non-degradable biocompatible polymers in medicine: past, present and future. Curr Pharm Biotechnol 4(5):331–337

99. FDA (2009) U.S. Implanon™ (etonogestrel implant). http://www.accessdata.fda.gov/drugsatfda_docs/label/2009/021529s004lbl.pdf.

100. de las Heras Alarcón C, Pennadam S, Alexander C (2005) Stimuli responsive polymers for biomedical applications. Chem Soc Rev 34(3):276–285

101. Fujishige S, Kubota K, Ando I (1989) Phase transition of aqueous solutions of poly (N-isopropylacrylamide) and poly (N-isopropylmethacrylamide). J Phys Chem 93 (8):3311–3313

102. Gibson MI, O'Reilly RK (2013) To aggregate, or not to aggregate? considerations in the design and application of polymeric thermally-responsive nanoparticles. Chem Soc Rev 42 (17):7204–7213

103. Chun SW, Kim JD (1996) A novel hydrogel-dispersed composite membrane of poly (N-isopropylacrylamide) in a gelatin matrix and its thermally actuated permeation of 4-acetamidophen. J Control Release 38(1):39–47

104. Kidchob T, Kimura S, Imanishi Y (1998) Thermoresponsive release from poly(Glu(OMe))-block-poly(Sar) microcapsules with surface-grafting of poly(N-isopropylacrylamide). J Control Release 50(1–3):205–214

105. Eeckman F, Moës AJ, Amighi K (2002) Evaluation of a new controlled-drug delivery concept based on the use of thermoresponsive polymers. Int J Pharm 241(1):113–125

106. Cooperstein MA, Canavan HE (2013) Assessment of cytotoxicity of (N-isopropyl acrylamide) and Poly (N-isopropyl acrylamide)-coated surfaces. Biointerphases 8(1):19–30

107. Malonne H et al (2005) Preparation of poly(N-isopropylacrylamide) copolymers and preliminary assessment of their acute and subacute toxicity in mice. Eur J Pharm Biopharm 61 (3):188–194

108. Schornack PA, Gillies RJ (2003) Contributions of Cell Metabolism and H+ Diffusion to the Acidic pH of Tumors. Neoplasia 5(2):135–145

109. Kyriakides TR et al (2002) pH-sensitive polymers that enhance intracellular drug delivery in vivo. J Control Release 78(1):295–303

110. Dong LC, Hoffman AS (1991) A novel approach for preparation of pH-sensitive hydrogels for enteric drug delivery. J Control Release 15(2):141–152

111. Foss AC et al (2004) Development of acrylic-based copolymers for oral insulin delivery. Eur J Pharm Biopharm 57(2):163–169

112. Panyam J et al (2002) Rapid endo-lysosomal escape of poly (DL-lactide-co-glycolide) nanoparticles: implications for drug and gene delivery. FASEB J 16(10):1217–1226

113. Roy D, Cambre JN, Sumerlin BS (2010) Future perspectives and recent advances in stimuli-responsive materials. Prog Polym Sci 35(1):278–301
114. Peng K, Tomatsu I, Kros A (2010) Light controlled protein release from a supramolecular hydrogel. Chem Commun 46(23):4094–4096
115. Patnaik S et al (2007) Photoregulation of drug release in azo-dextran nanogels. Int J Pharm 342(1-2):184–193
116. Alexander C et al (2006) Molecular imprinting science and technology: a survey of the literature for the years up to and including 2003. J Mol Recognit 19(2):106–180
117. Haupt K et al (2012) Molecularly imprinted polymers. In: Molecular imprinting. Springer, pp 1–28
118. Tse Sum Bui B, Haupt K (2010) Molecularly imprinted polymers: synthetic receptors in bioanalysis. Anal Bioanal Chem 398(6):2481–2492
119. Haupt K (2001) Molecularly imprinted polymers in analytical chemistry. Analyst 126 (6):747–756
120. Ton XA et al (2013) A versatile fiber-optic fluorescence sensor based on molecularly imprinted microstructures polymerized in situ. Angew Chem Int Ed 52(32):8317–8321
121. Fuchs Y et al (2013) Holographic molecularly imprinted polymers for label-free chemical sensing. Adv Mater 25(4):566–570
122. Vlatakis G et al (1993) Drug assay using antibody mimics made by molecular imprinting. Nature 361(6413):645–647
123. Ye L, Haupt K (2004) Molecularly imprinted polymers as antibody and receptor mimics for assays, sensors and drug discovery. Anal Bioanal Chem 378(8):1887–1897
124. Hiratani H et al (2005) Ocular release of timolol from molecularly imprinted soft contact lenses. Biomaterials 26(11):1293–1298
125. Li B et al (2014) Water-compatible silica sol–gel molecularly imprinted polymer as a potential delivery system for the controlled release of salicylic acid. J Mol Recognit 27 (9):559–565
126. Hoshino Y et al (2010) Recognition, neutralization, and clearance of target peptides in the bloodstream of living mice by molecularly imprinted polymer nanoparticles: a plastic antibody. J Am Chem Soc 132(19):6644–6645
127. Cutivet A et al (2009) Molecularly imprinted microgels as enzyme inhibitors. J Am Chem Soc 131(41):14699–14702
128. Kunath S et al (2015) Cell and tissue imaging with molecularly imprinted polymers as plastic antibody mimics. Adv Healthcare Mater 4:1322–1326
129. Tieppo A et al (2012) Sustained in vivo release from imprinted therapeutic contact lenses. J Control Release 157(3):391–397
130. Díaz-García ME, Laíñño RB (2005) Molecular imprinting in sol–gel materials: recent developments and applications. Microchim Acta 149(1-2):19–36
131. Beyazit S et al (2014) Versatile synthesis strategy for coating up converting nanoparticles with polymer shells by localized photopolymerization using the particles as internal light sources. Angew Chem Int Ed 53:8919–8923

Index